KEM-19b
Evaluation of post-abandonment fluid migration and seismic hazard assessment in the southwest aquifer of Groningen

Part 1

Energy & Materials Transition
www.tno.nl
+31 88 866 42 56
info@tno.nl

TNO 2025 R10452 – 20 June 2025
KEM-19b
Evaluation of post-abandonment fluid migration and seismic hazard assessment in the southwest aquifer of Groningen

Part 1

Author(s)	S. Osinga, E. Peters, P. Fokker; D.A. Kraaijpoel, C.R. Geel, M. van Unen, J. Foeken, S. Peeters, S. Bottero
Classification report	TNO Public
Title	TNO Public
Report text	TNO Public
Appendices	TNO Public
Number of pages	154 (excl. front and back cover)
Number of appendices	5
Sponsor	The Dutch Ministry of Economic Affairs and Climate
Programme name	Kennisprogramma Effecten van Mijnbouw - KEM program
Project name	KEM-19b

Managementsamenvatting

Aan de zuidwestelijke grens is het Groningen gasveld verbonden met een groot aquifer (watervoerende laag) in de zuidelijke Lauwerszee Trog. Door de gasproductie uit het Groningen gasveld en een reeks kleine gasvelden aan de westkant van de trog, heeft deze aquifer te maken met nog steeds voortdurende drukverlaging. Het doel van deze studie is om onze kennis te vergroten over deze voortdurende drukverlaging en het potentieel voor toekomstige seismische activiteit in de aquifer als gevolg van deze drukverlaging.

Om dit te bereiken is een ensemble van geologische en dynamische simulatiemodellen van de aquifer gemaakt, inclusief de kleine gasvelden aan de westkant en een deel van de Groningen en Bedum velden aan de oostkant. Voor het ensemble werden compactie en bodemdaling gesimuleerd. Op basis van de overeenkomst met waargenomen druk in de kleine gasvelden en bodemdaling boven de aquifer, werd een subset van het ensemble geselecteerd om de drukverlaging en compactie in de aquifer van 2024 tot 2100 te voorspellen. In sommige gebieden van de aquifer, met name de aquifer net ten westen van Harkstede en van Ten Boer, werd de onzekerheid in de voorspelde drukverlaging aanzienlijk verminderd op basis van de waargenomen bodemdaling. De aquifer tussen het Roden veld en het Harkstede gebied ervoer duidelijk drukverlaging door gaswinning uit zowel het Roden als het Groningen veld, met name door de productie nabij Harkstede.

De voorspellingen van druk en compactie werden gebruikt als input om seismiciteit en seismische dreiging (grondbeweging) te bepalen voor de komende decennia. Hiervoor wordt de TNO Model Chain workflow, oorspronkelijk ontwikkeld voor het Groningen veld (TNO, 2020), toegepast op de zuidwestelijke aquifer. Deze toepassing vereist de uitbreiding van de twee belangrijkste bouwstenen: (1) het seismische bronmodel (SSM) en (2) het grondbewegingsmodel (GMM). Voor de Groningen modelketen zijn beide componenten specifiek ontworpen en gekalibreerd voor het Groningen veld. Een uitbreiding van de keten, om de zuidwestelijke aquifer op diepte en een groter blootgesteld gebied aan het oppervlak op te nemen, vereist zowel het in beeld brengen van nieuwe (meer) gegevens als een (her)kalibratie.

Ondanks de aanzienlijke onzekerheid met betrekking tot de aquiferdrukken, tonen de seismische voorspellingen gebaseerd op de verschillende ensembleleden, eenmaal gekalibreerd, allemaal zeer beperkte seismische activiteit in de zuidwestelijke aquifer in vergelijking met de verwachte voortdurende seismische activiteit in het Groningen veld. Dit is een belangrijk resultaat, omdat het aangeeft dat de aanzienlijke onzekerheid in de drukvoorspellingen niet vertaalt naar aanzienlijke onzekerheid met betrekking tot seismische activiteit. Ten slotte, vanwege de lage hoeveelheid voorspelde seismische activiteit in de zuidwestelijke aquifer, is er een zeer beperkte impact van deze nieuw gemodelleerde seismische activiteit op de seismische dreiging boven de zuidwestelijke aquifer. We concluderen dat de seismische dreiging blijft afnemen met toenemende afstand van het Groningen gasveld en dat de seismische activiteit van de zuidwestelijke aquifer zeer beperkt is en dit algemene beeld niet significant verandert.

Executive Summary

On its southwest border, the Groningen gas field is connected to an extensive aquifer in the southern Lauwerszee Trough. Due to the gas production from the Groningen gas field and a series of small gas fields on the west side of the trough, this aquifer has experienced, (and is still experiencing) pressure depletion. The objective of this study is to increase our knowledge on the ongoing pressure depletion in the aquifer and the potential for future seismic activity.

To achieve that, an ensemble of geological and dynamic simulation models has been created of the southwest (SW) aquifer including on the west side the small gas fields and on the east side a part of the Groningen and Bedum fields. For the ensemble, compaction and subsidence were also simulated. Based on the fit to observed pressure in the small gas fields and subsidence above the aquifer, a subset of the ensemble was selected to forecast the depletion and compaction in the aquifer from 2024 to 2100. In some areas of the aquifer, most notably the aquifer just west of Harkstede and of Ten Boer, the uncertainty in the forecasted depletion was considerably reduced based on the observed subsidence. The aquifer between the Roden field and the Harkstede area clearly experienced depletion due to gas exploitation from both the Roden and the Groningen fields, in particular from the production near Harkstede.

The forecast of pressure and compaction was used as input to produce seismicity forecasts and seismic hazard (ground motion) assessments for the coming decades. For this purpose, the TNO Model Chain workflow developed for the Groningen field (TNO, 2020) is applied to the SW aquifer. This application requires the extension of the two main building blocks: (1) the seismic source model (SSM) and (2) the ground motion model (GMM). For the Groningen model chain both components have been designed and calibrated specifically for the Groningen field. An extension to include the SW aquifer at depth, and a larger exposed area at the surface, requires both taking into account new (more) data, as well as a (re)calibration.

Despite the considerable uncertainty related to the pressures, once calibrated, the seismicity forecasts of the individual pressure model ensemble members all show very limited seismicity in the SW aquifer when compared to the expected ongoing seismicity in the Groningen field. This is an important result, as it indicates that the significant uncertainty in the pressure forecasts does not translate to significant uncertainty with regards to seismicity. Finally, due to the low level of forecasted seismicity in the SW aquifer, there is a very limited impact of this newly modelled seismicity on the seismic hazard above the SW aquifer. We have identified that the seismic hazard continues to decrease with increasing distance from the Groningen gas field and that the seismicity of the SW aquifer itself is very limited and does not significantly change this general picture.

Contents

Contents

1 Introduction

The Groningen gas field has been producing since the 1960's and the resulting pressure depletion has caused many induced seismic events. Due to the pressure depletion in the Groningen gas field, some of the surrounding aquifers are also depleting in pressure. Some of these aquifers extend quite far beyond the gas reservoir. One of these depleting aquifers is the SW aquifer of the Groningen gas field which is situated in the southern Lauwerszee Trough (Figure 1-1), a region where small-scale seismicity has been observed in recent times, likely caused by pressure depletion in the aquifer. The depletion in the aquifer is attributed not only to gas production from the Groningen gas field, but also to the small gas fields on the west side of the Lauwerszee Trough, in particular the Roden gas field (Molen et al., 2020).

The specific objective of this project is to focus on the aquifer in the southern Lauwerszee Trough and investigate the pressure depletion as well as the future potential seismic activity in the aquifer.

This project is a follow-up of the KEM-19 study "Evaluation of post-abandonment fluid migration and ground motion risks in subsurface exploitation operations in the Netherlands" carried out by TNO and Deltares and completed in 2022 (TNO-Deltares 2022).
In the KEM-19 study, the pressure depletion in the aquifers surrounding the Groningen gas field was investigated for the coming centuries. It was concluded, that the Groningen gas field is too large to be repressurized by its connected aquifers and that the connected aquifers will continue to decline in pressure, albeit at a slow pace.

This study focuses on the following research questions:
1. What will be the pressure depletion of the southwestern aquifer taking into account the depletion of Groningen gas field as well as the smaller gas fields in the Lauwerszee Trough?
2. What are the locations of smaller faults, and their orientation and throw in the southwestern aquifer?
3. What is the expected induced seismicity in the coming decades?
    a. What is the seismic hazard?
    b. How does this compare to the seismic hazard of the Groningen gas field?

This study aims to address key research questions through a modelling approach.
In KEM-19 project, a regional reservoir model was developed, encompassing the SW aquifer of the Groningen gas field in the Lauwerszee Trough. However, it did not include the smaller gas fields on the southwestern side of the Lauwerszee Trough. As a result, the KEM-19 model could not fully capture the aquifer's depletion, as it only reflected the pressure changes from the Groningen gas field. Additionally, the limited number of wells in the aquifer led to significant uncertainty.

In this follow-up project a local model is created that includes the SW aquifer, the surrounding small gas fields and a part of the Groningen field. Due to the lack of direct pressure measurements in the aquifer, subsidence is modelled for the area of interest and compared to observed subsidence. This approach is expected to significantly improve the quantification of the current pressure depletion and its evolution in the future, including associated uncertainties. To characterize uncertainties, an ensemble of models is used instead of a single

model. Special focus is on the characterization of smaller and larger scale faults, including fault orientation and throw, to be able to include them in a geological model and in the seismic source model. In order to produce seismic hazard (ground motion) estimates, the Ground Motion Model (GMM-V7) for Groningen is extended to cover the SW aquifer. Due to the similar structure of the deep subsurface, the main effort regarding the GMM update concerns extending the site-response model with an additional 81 spatial zones to account for the site-amplification characteristic of the shallow subsurface, which is highly variable in composition and structure.

The report is structured to address the research questions of this study. Following the introduction, in Chapter 2 the creation of the ensemble of geological (static) reservoir models is detailed, including the development of the reservoir's geometry and properties such as porosity, permeability and net-to-gross (NtG). Chapter 3 describes how the ensemble of geological models is extended to an ensemble of dynamic models to simulate the pressure history. It also covers the modeling of subsidence for the ensemble of models and the selection of a subset based on the fit to observed subsidence and pressures to forecast aquifer pressure. In Chapter 4, the required extension of the Ground Motion Model and Seismic Source Model is described. The extended version of the TNO Model Chain workflow developed for the Groningen field (TNO, 2020) is then applied to the SW aquifer. Finally, Chapter 5 presents the conclusions and recommendations derived from the study.
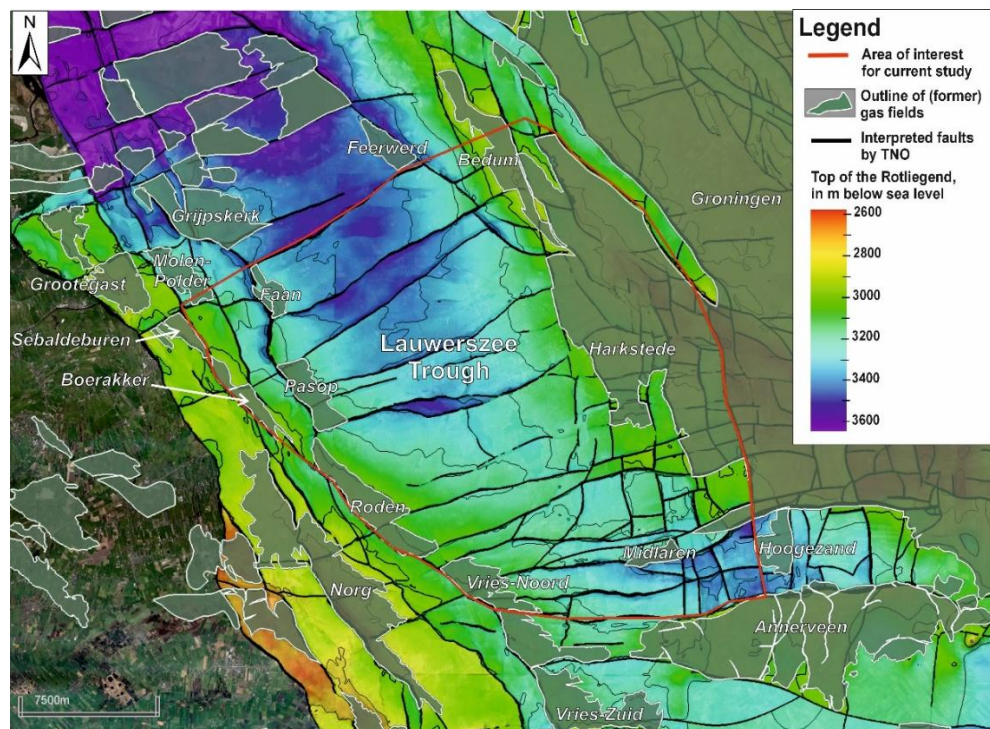

Figure 1-1 Overview image displaying the area of interest outlined in red and the locations of gas fields projected onto a depth map of the Rotliegend formation (warmer colors indicate shallower depths). The interpreted faults, shown in black, are based on TNO's (2023) internal geological model for the broader Groningen region.

2 Improved geological model SW aquifer of the Groningen field

2.1 Introduction

The main objective of this part of the study was to create an ensemble of geological models of the aquifer located southwest of the Groningen Field (Figure 2-1, Figure 2-2 and Figure 2-3) including the small gas fields on the west side and a relevant part of the Groningen gas field on the east. Special emphasis was placed on the characterization of both small and large-scale faults, including fault orientation and throw, and incorporating them in a geological reservoir model of the SW aquifer, which comprises the Slochteren Formation of the Groningen field.

The approach was as follows:
〉 Existing reservoir models and data sets were used as much as possible to model known reservoir characteristics and fault trends. To cover this point, first an introduction is given regarding the geological background, including the stratigraphy (paragraph 2.1.1), reservoir architecture (paragraph 2.1.2) and the structural development of the wider Groningen area (paragraph 2.1.3). Subsequently, the data and existing reservoir models are described that were used to construct the model for the current study (paragraph 2.2);
〉 The boundaries for the model are described and faults that were missing from the previous models were newly interpreted on 3D seismic data. Based on these additional fault interpretations, a new base case structural model was built (paragraph 2.3);
〉 A petrophysical analysis was done for the wells in the small gas fields on the west side of the Lauwerszee Trough (paragraph 2.4)
〉 An ensemble of geological models with properties was created using Gaussian simulation. First the methods regarding the property modelling are described (paragraph 2.5). Finally the modelling results are shown (paragraph 2.6).
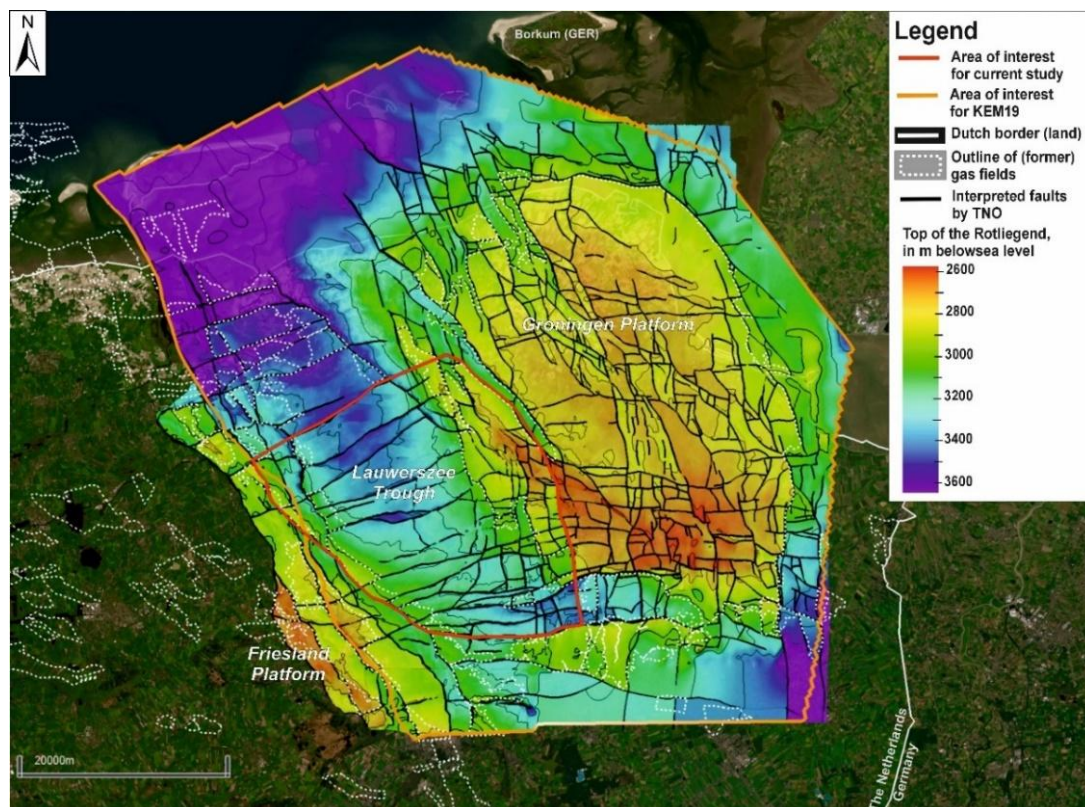
Figure 2-1 Area of Interest (red polygon) of the KEM-19b project projected onto a depth map of the Top of the Rotliegend (=Base Zechstein) with a fault interpretation by TNO. Warmer colours mean shallower depths, cooler colours mean larger depths. The thin black lines are contour lines which are present every 200 m. The interpreted faults (in black) are from TNO (2023) internal geological model for the wider Groningen area.
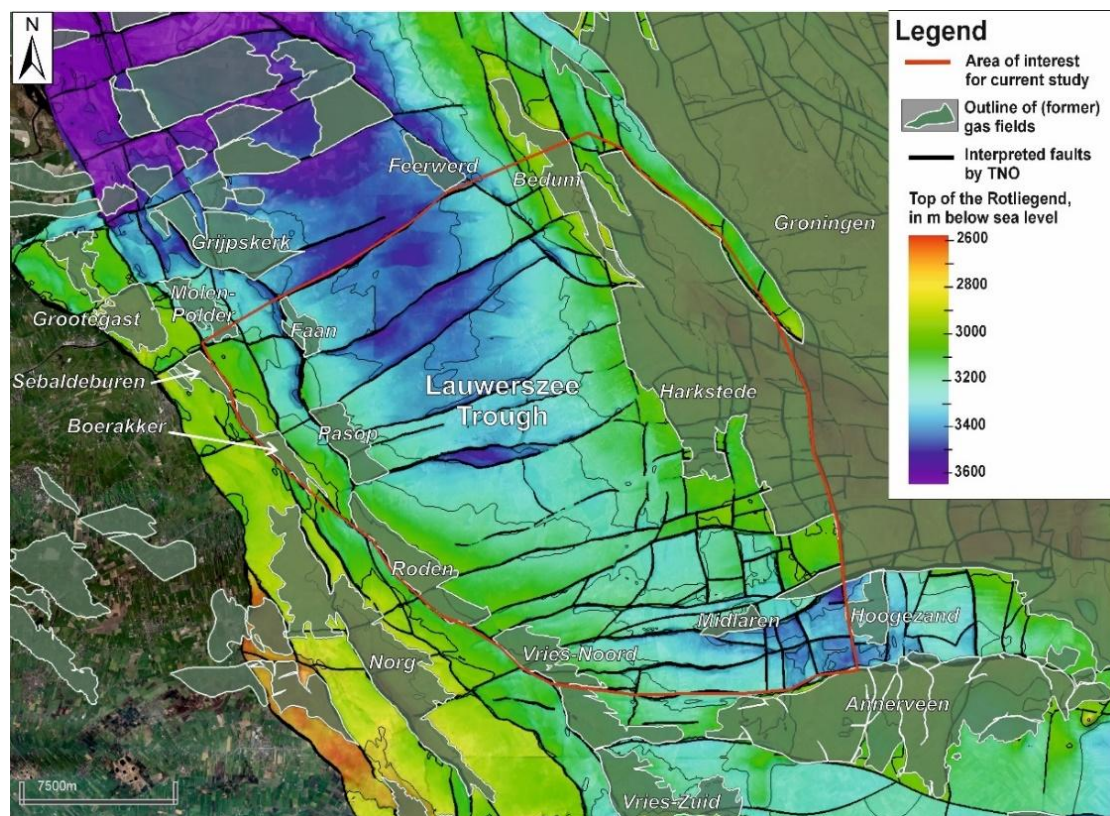
Figure 2-2 Overview picture showing the names and locations (green) of the gas fields in the area of interest projected on a depth map of the top of the Rotliegend (warmer colours indicate shallower depth). The red outline is the area of interest. The interpreted faults (in black) are from TNO (2023) internal geological model for the wider Groningen area.

Figure 2-3 Overview picture showing the well names in the area of interest projected on a depth map of the top of the Rotliegend (warmer colours indicate shallower depth). The red outline is the area of interest. For the EKL cluster, only well EKL-1 is plotted for clarity. The dashed white lines indicate the outline of the gas fields. See Figure 2.2 for a clearer image of the position of the gas fields. The interpreted faults (in black) are from TNO (2023) internal geological model for the wider Groningen area.
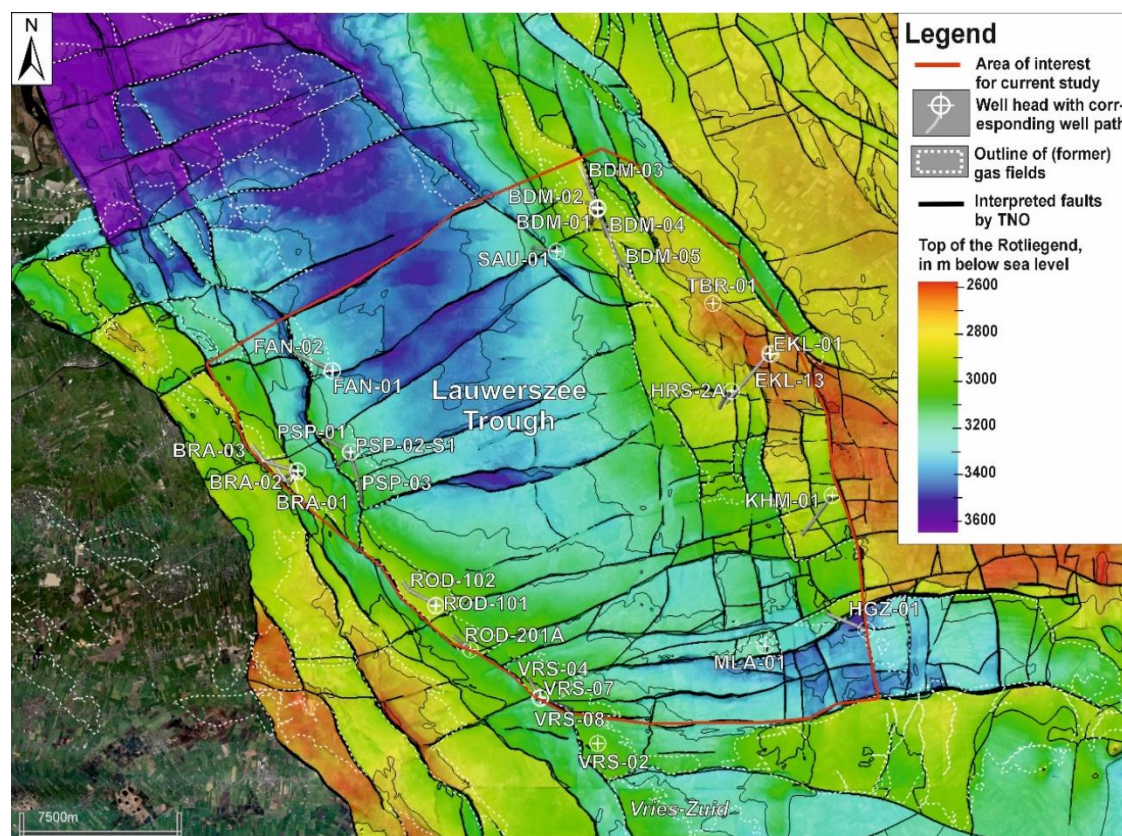
2.1.1 Regional geological background and stratigraphy

The Late Permian sandstones of the Upper Rotliegend group comprise the Slochteren Formation, which can be subdivided into the Lower Slochteren and the Upper Slochteren Members (Figure 2-4). Around 80% of all the Dutch natural gas has historically been produced from more than 200 fields within this interval, including the large Groningen gas field (e.g. Kortekaas et al., 2023, see also Figure 2-2). The Upper Rotliegend siliciclastic sediments were deposited along the fringes of the Southern Permian Basin (SPB), which was an endorheic[1] basin during the Late Permian that stretched from the UK in the west towards Poland in the east (e.g. Fryberger et al., 2011, Figure 2-5). During deposition of the Upper Rotliegend Group, the SPB generally underwent gentle thermal subsidence (Ziegler, 1990; van Wees et al., 2000, Geluk, 2007). This gentle period of subsidence followed after a tectonic pulse, causing crustal thinning, widespread uplift, wrench tectonics and associated magmatism during the Latest Carboniferous and Early Permian (Ziegler, 1990; van Wees et al., 2000, Geluk, 2007). This tectonic phase is expressed in the current SPB-area as the Base Permian Unconformity (BPU), which reflects a hiatus in the geological record of around 40-60 million years between the sediments of the Late Carboniferous and the overlying Upper Rotliegend sediments (Geluk, 2007; Reijmer et al., 2017). Towards the south of SPB, continental collision occurred along the

---

[1] An endorheic basin is a self-contained basin that allows no water outflow to other bodies of water (such as rivers and oceans). Instead, the water drainage flow in an endorheic basin equilibrates through evaporation. Modern day examples of endorheic basins are the Caspian basin and the Dead Sea basin.

Rheic suture during roughly the same time period, leading to major uplift and the formation of the Variscan orogenic belt (e.g. Ziegler, 1990; Smit et al., 2018).

When the Upper Permian sands were deposited, the SPB was positioned around 20° N, causing an arid climate at the time (e.g. Glennie; 1972. Howell, and Mountney, 1997; Fryberger et al., 2011). Within this arid climate, sediments were transported by ephemeral river systems and by strong (generally easterly trade) winds, leading to a variety of lithofacies including fluvial, playa and aeolian deposits (e.g. Fryberger et al., 2011; de Jager & Visser, 2017; Bouroullec and Geel, in press). Aeolian deposits are generally considered the best reservoirs with an average porosity that exceeds 20% (e.g. De Jager & Visser, 2017; Kortekaas et al., 2023). The main source of sediments was the Variscan orogenic belt towards the south of the SPB, from which sediments were transported generally from south-southeast towards the north-northwest (e.g. Geluk, 2007; Fryberger et al., 2011, Van Ojik et al., 2012; Figure 2-6).

The overall subsidence of the SPB and the influx of sediments caused a progressive basal onlap configuration onto de paleo basin margins, where younger strata were deposited increasingly further southwards (e.g. Fryberger et al., 2011, De Jager & Visser, 2017, Figure 2-4). Overall, the sediments along the southern rim of the SPB, display a typical proximal to distal trend which is characterised by a shaling out towards the north ((e.g. Fryberger et al., 2011, De Jager & Visser, 2017, Kortekaas et al., 2023, Figure 2-7). Along the most proximal southern parts of the SPB, conglomerates are abundantly present, while further towards the north, the sandstones get increasingly intermixed with mudstones (Fryberger et al., 2013; De Jager & Visser, 2017, Figure 2-7). The distal deposits that are time-equivalent to the Slochteren. Fm. are part of the Silverpit Formation (e.g. Kortekaas et al., 2023, Figure 2-4, Figure 2-6 and Figure 2-7). A significant mudstone interval, which can be found also in more proximal parts of the SPB and represents a base level highstand, is formed by the Ameland Claystone Member, which separates the Lower Slochteren from the Upper Slochteren Members (Kortekaas et al., 2023, Figure 2-4 and Figure 2-7). Another base level highstand led to the deposition of the Ten Boer Claystone Member, which overlies either the Upper Slochteren Mb or the Slochteren Formation (Kortekaas et al., 2023, Figure 2-4 and Figure 2-7). In the most distal parts of the SPB (also referred to as the Silverpit Basin, Figure 2-6), also evaporites were deposited.

At the very end of the Permian, an abrupt flooding of the SPB occurred, leading to the deposition of the Kupferschiefer Formation. This flooding marks the end of the Upper Rotliegend Group and the onset of the deposition of the Zechstein Group, during which alternations of carbonates, evaporites and siliciclastics were deposited in several reoccurring cycles (e.g. Geluk, 2007; Patruno et al., 2017; Peeters et al., 2023). During deposition of the Zechstein Group, vast amounts of evaporites were deposited in the Groningen area. These evaporites were remobilised into a variety of salt structures during Mesozoic rifting (e.g. Ten Veen et al., 2012; Bouroullec et al., 2018). The presence of Zechstein salt also decouples the sub-salt deformation from the supra salt deformation in the wider Groningen area (Ten Veen et al., 2012; Bouroullec et al., 2018).
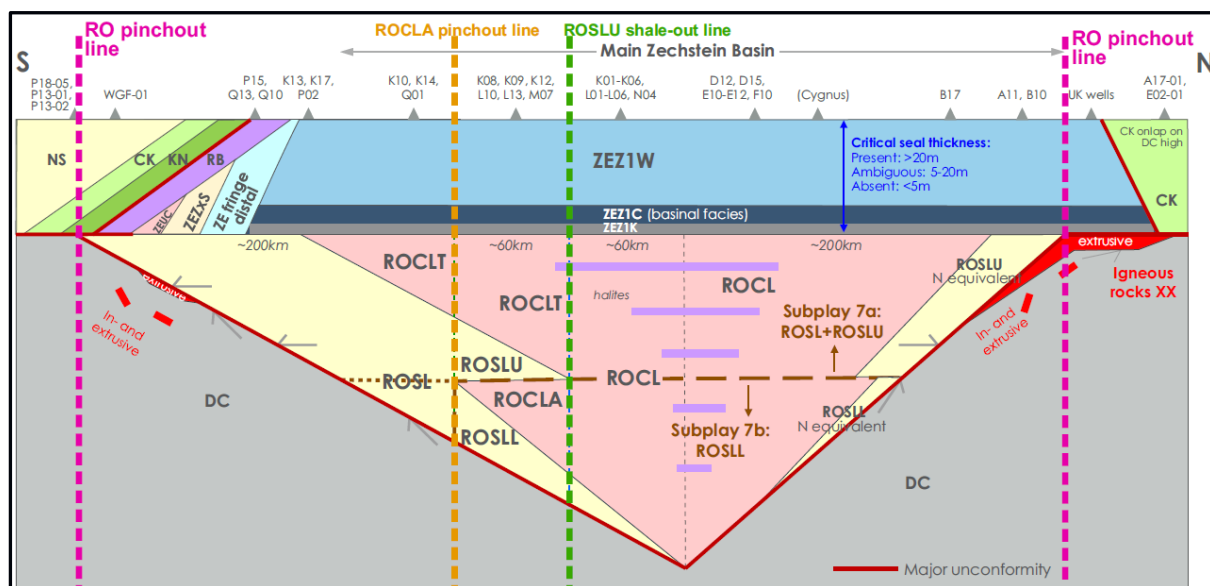
Figure 2-4 Stratigraphic scheme illustrating the vertical and lateral distribution of the Rotliegend Upper-, and Lower Slochteren sandstones. Abbreviations used: NS; North Sea Groups, CK; Chalk Group, KN; Rijnland Group, RB; Lower Germanic Trias Group, ROSL; Slochteren Fm. (sandstones), ROSLU; Upper Slochteren Mb., ROSLL; Lower Slochteren Mb., ROCLT; Ten Boer Claystone Mb., ROCLA; Ameland Claystone Mb., ROCL; Silverpit Formation (claystones), ZE; Zechstein Group; ZEZ1K; Coppershale Mb., ZEZ1C; Z1 Carbonate Mb., ZEZ1W; Z1 Anhydrite Mb., ZEZxS; Zechstein Fringe Sandstone Members (Z1-Z4), ZEUC; Zechstein Upper Claystone Mb. See the dashed black line in Figure 2-5 for the approximate location of this stratigraphic scheme. Figure from Kortekaas et al., 2023.
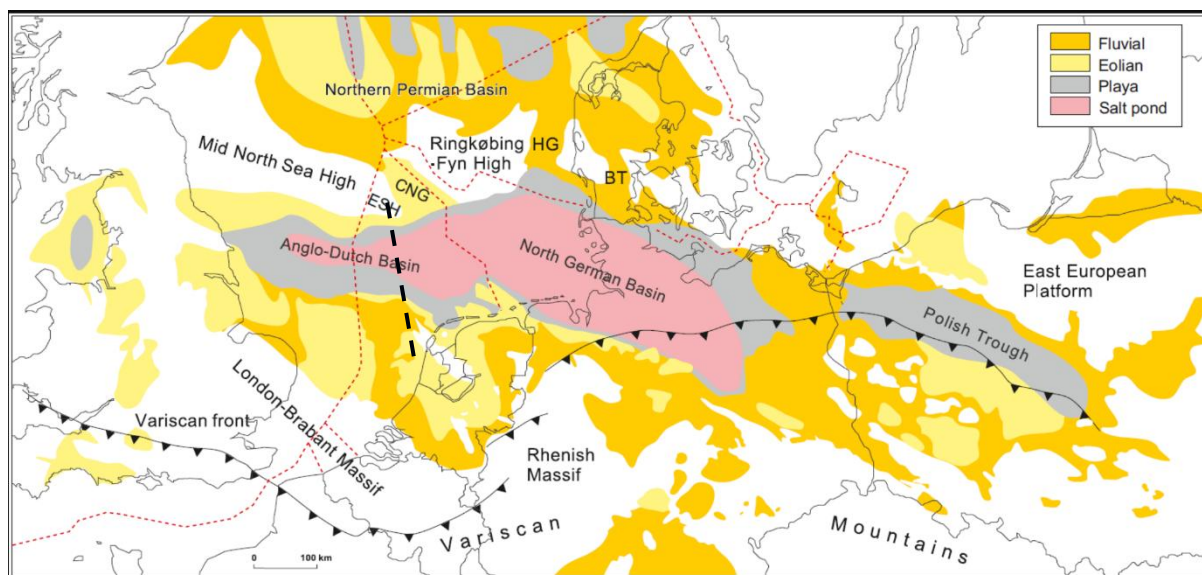
Figure 2-5 Generalised Gross Depositional environment map on the European scale, illustrating the outline of the Southern Permian Basin, which stretched from the UK in the west towards Poland in the east. Figure from Bouroullec and Geel, in press.
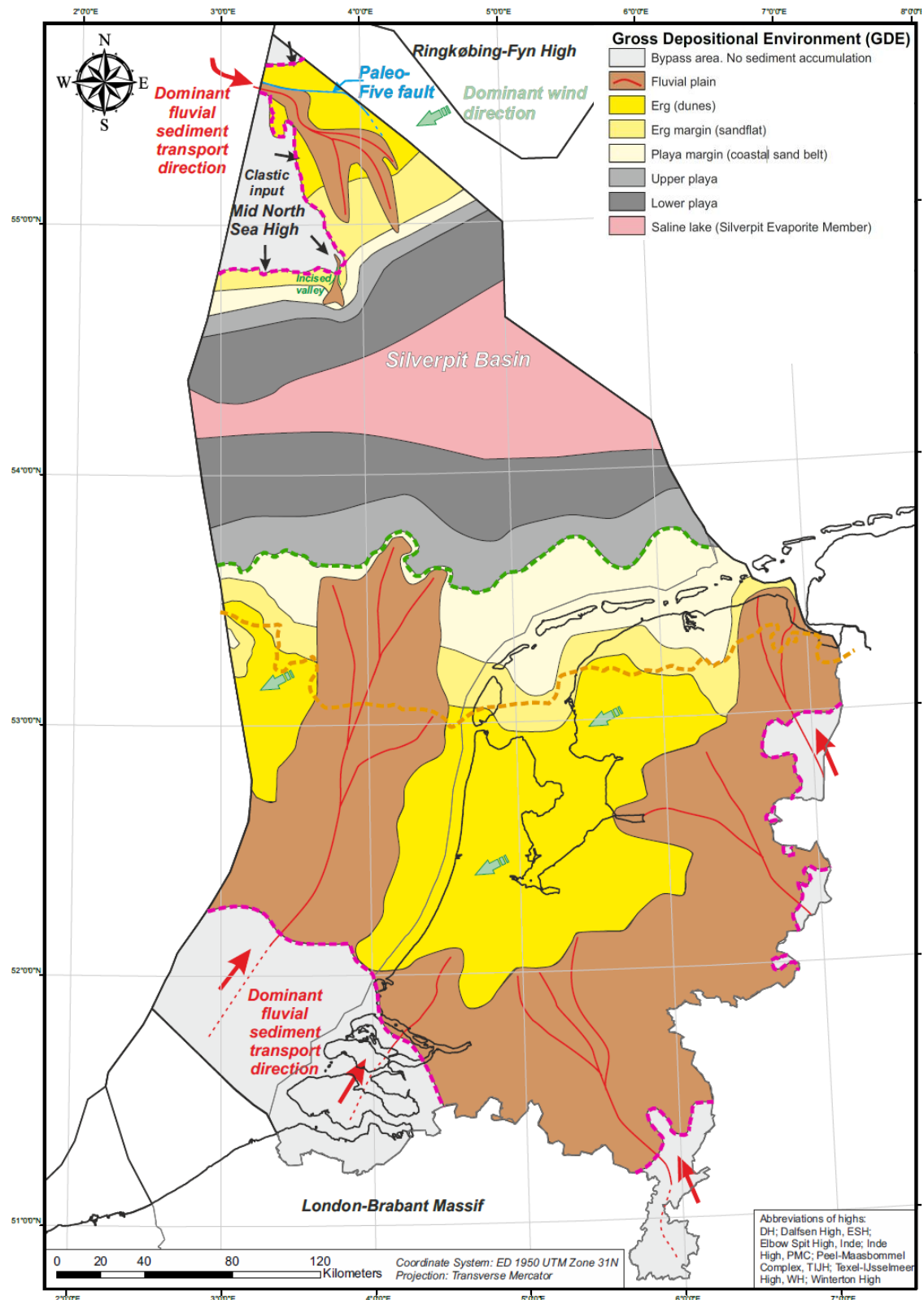
Figure 2-6 Generalised gross depositional environment (GDE) map for the Upper Slochteren Member of the Netherlands. Note that the fluvio-eolian reservoirs were deposited along the margins of Southern Permian Basin, while in the distal part of the SPB (referred to as Silverpit Basin), mainly mudstones and evaporites were deposited. General transport direction was from south to north. Figure from Kortekaas et al., 2023.

Figure 2-7 Lithological cross section displaying a proximal to distal trend from the offshore G17-1 well in the Silverpit basin (distal part of the system), towards the onshore wells in the wider Groningen area (proximal part of the system). Note that in the well SLochteren-9, Norg-Zuid-1, Appelscha-1 and Emmen-7, the Ameland Claystone Member is no longer present and the Upper and Lower Slochteren Members merge into a single succession of sand, which is then defined as the Slochteren Fm.. See also Figure 2.4. *Figure from Gast et al., 2010.*

2.1.2 Reservoir architecture in the wider Groningen area

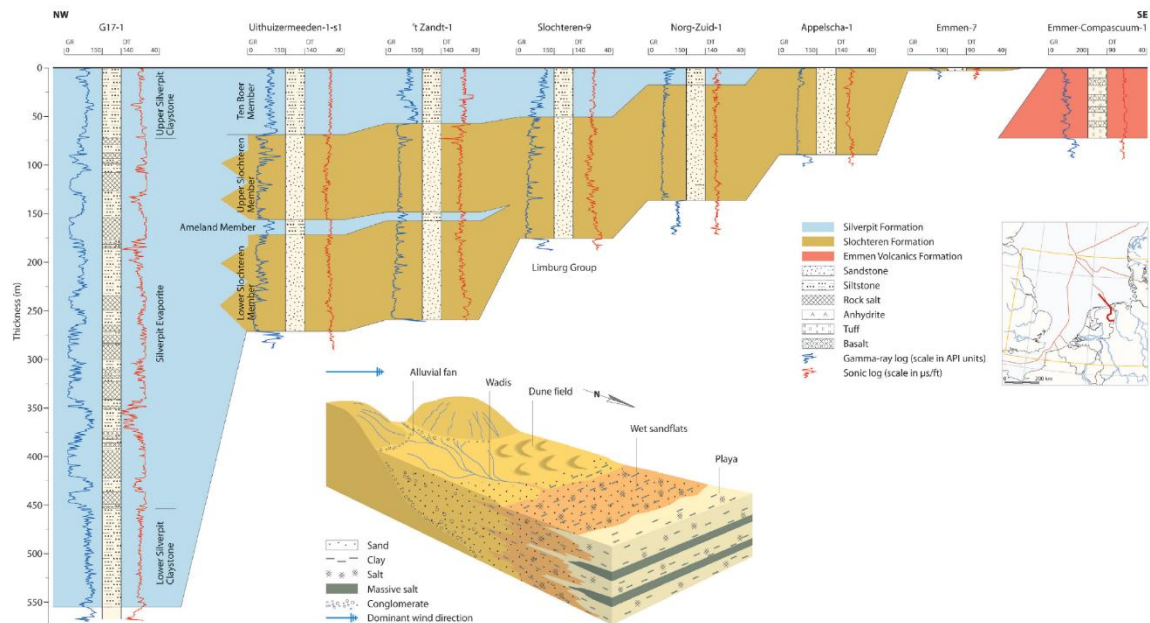The reservoir quality of the Slochteren reservoirs has been extensively studied in the wider Groningen area via thousands of core plugs (De Jager & Visser, 2017). Porosities vary typically from 10 to 24% and permeabilities generally vary between 1 to 1000 mD (Visser, 2012; De Jager & Visser, 2017). Attempts have been made for the extensively studied Groningen field to distinguish different facies within the sandstones, such as fluvial, aeolian and mixed fluvial-eaolian (e.g. Vissers et al., 2016; De Jager & Visser, 2017). Although the purely aeolian sandstones are characterised by the best reservoir properties, they only account for 1.5% of the sandstone facies, which has been attributed to repeated erosion of aeolian deposits, leading to a high degree of sorting but a low degree of preservation in the sedimentary record (Vissers et al., 2016). It is noted that when the degree of sorting is lower and some small amounts of finer-grained sediments are intermixed with the coarser-grained sediments, this only has a limited effect on the average porosities (De Jager & Visser, 2017). On the field scale, the best reservoir qualities can generally be found in the central part of the field. Towards the south, conglomeratic facies become more abundant and towards the north, the interval becomes more prone to mudstone intercallations that are interbedded with the sandstone intervals (e.g. Gast et al., 2010 Fryberger et al., 2011, De Jager & Visser, 2017, Figure 2-4). Besides the paleo depositional environment, also the diagenetic history usually exerts a major control on the reservoir quality. For the Groningen field, diagenesis generally did not have a significant negative impact on the reservoir quality (De Jager & Visser, 2017). Other Rotliegend fields are sometimes affected by early diagenetic processes such as the secondary precipitation of anhydrite or dolomite (Amthor and Okkerman, 1998; Van Hulten, 2006). Amthor and Okkerman (1998) found for the southern margin of the SPB that the combined

volume of dolomite and anhydrite cementation increases from south to north, following roughly the proximal to distal trend present in the paleo depositional environment (Figure 2-6). This is likely related to an increase in salinity and wetness of the system (i.e. episodically higher groundwater tables) from south to north (Amthor and Okkerman (1998). Although the current study area is positioned in a proximal part of the system, the risk for secondary precipitation of anhydrite and/or dolomite might increase northward.

Another diagenetic process that may (partly) plug the reservoir pores and deteriorate the reservoir quality is the formation of fibrous illite (Bjørlykke et al., 1995; Van Hulten, 2006; Gaupp and Okkerman, 2011). Illite occurs both as an authigenic clay mineral within the Upper Permian Rotliegend interval (e.g. Seemann, 1979), but may also form due to illitization of kaolinite, derived from Zechstein brines (Almon, 1979, Lanson et al., 1996, Van Hulten, 2006). The occurrence of fibrous illite occurs later in the diagenetic history at relatively higher temperatures and has been link to major phases of tectonic activity (e.g. Mesozoic rifting and/or Late Cretaceous/Early Cenozoic inversion), allowing Zechstein brines to be introduced in the Rotliegend system after faulting (Lanson et al., 1996). The majority of the Groningen field has been largely protected from fibrous illite formation, likely because of its limited maximum burial depth and/or early charge of gas (Gaupp & Okkerman, 2012; De Jager & Visser, 2017). For the current study area, this means that especially away from the Groningen field and the Groningen platform in general and into the Lauwerszee Trough, this secondary clay precipitation such as fibrous illlite precipitation may have had a negative impact on the reservoir quality.

2.1.3 Structural development of the wider Groningen area

The current study area covers the central part of the Lauwerszee Trough, the very eastern tip of the Friesland platform and the southwestern part of the Groningen platform (Figure 2-1). The Lauwerszee Trough was likely already a paleo low during the Early Carboniferous, when platform carbonates developed onto the adjacent Friesland and Groningen Highs (Kombrink et al., 2010; Van Hulten, 2012). At present, The Zechstein and Rotliegend Groups are positioned at greater depths within the Lauwerszee Trough than on the adjacent Groningen and Friesland platforms. The difference is generally around 400 - 800 meters (see Figure 2-1). The overlying space is mostly filled with a relatively thick interval of Triassic within the Lauwerszee Trough compared to the platform areas (GDN-v5). The Jurassic interval is absent both within the Lauwerszee Trough and on the platform areas and also the Cretaceous and Cenozoic intervals don't display any clear thickness trends (GDN-v5).

Like the rest of the current southern North Sea Area, the wider Groningen area has been affected by multiple deformation phase. Younger deformation phases often reactivated older structures, resulting in the complex fault pattern that is present today (See Figure 2-1). The main deformation phases within the area are:
- An Early Carboniferous phase of extensional tectonics, during which the approximately NW-SE oriented main bounding fault systems of the Lauwerszee Trough where active (e.g. Smit et al., 2018)
- A phase of Late Carboniferous-Early Permian inversion, widespread uplift, magmatism and wrench tectonics, resulting in the formation of the BPU (e.g. Geluk, 2007; Reijmer et al., 2017)
- A phase of Early Permian rifting, which created narrow syn-depositional grabens in Germany and possibly affected also the Ems Graben just east of the Groningen field

(De Jager & Visser, 2017). Syn-depositional faulting within the Groningen area has not been demonstrated for the Upper Rotliegend sediments (De Jager & Visser, 2017).

- Mesozoic extension and rifting. During the Triassic, a general east-west extension was present within the Southern North Sea Area. The thickness trend within the Lauwerszee Trough suggest that the main bounding fault systems were possibly active during this time (DGM V-5, Triassic thickness map). Mesozoic extension also triggered major halokinesis of the Zechstein evaporites (e.g. Bouroullec et al., 2018). It is most likely that, during this phase, faults at the Rotliegend level were most active, and created the patchwork of fault blocks that is observed at present (De Jager & Visser, 2017, Figure 2-1).
- A Late Cretaceous to Early Cenozoic phase of inversion, caused by Alpine compression. This phase mainly affected the Mesozoic rift Basin in the Southern North Sea Area, but some effect is present on the platforms area, including the wider Groningen area. Within the wider Groningen area, some fault reactivation of pre-existing trends can be observed, resulting in narrow pop-up and pull-apart blocks formed by NW-SE to more W-E striking faults (De Jager & Visser, 2017). Additionally, thinning of the upper part of the Paleogene over the Groningen field indicates that inversion during the Cenozoic to some extent also affected the Groningen platform (De Jager & Visser, 2017).

2.2 Data collection

The data collection started with a review of existing, publicly available, and in-house 3D reservoir models that cover the area of interest or are adjacent to it. The available models are:

- NAM reservoir model Groningen Field (2019) - a detailed, complex 3D reservoir model of the Groningen Field
- TNO KEM-19 – a relatively simple 3D reservoir model based on NAM and TNO-GDN.
- TNO internal model – NAM 3D reservoir model extended with additional seismic interpretations west of the Groningen Field.
- TNO ThermoGIS - a layer based model with reservoir properties for various aquifers, among which the Slochteren Formation (Lower Slochteren Member - ROSLL, Upper Slochteren Member - ROSLU), Ameland Member (ROCLA) and Ten Boer Member (ROCLT).

Figure 2-8 shows top views of three of these models with faults and the base of the Zechstein. Shortcomings and missing features of each model for the current project are readily identified. In the NAM reservoir model (2019) an area is missing on the western side and therefore it doesn't cover the full extent of the current study area. In addition, the faults that cross the Lauwerszee Trough do not extend far enough into the area of Interest. Additionally, not enough faults were interpreted in the Lauwerszee Trough in order to fully cover the objectives of the current study.
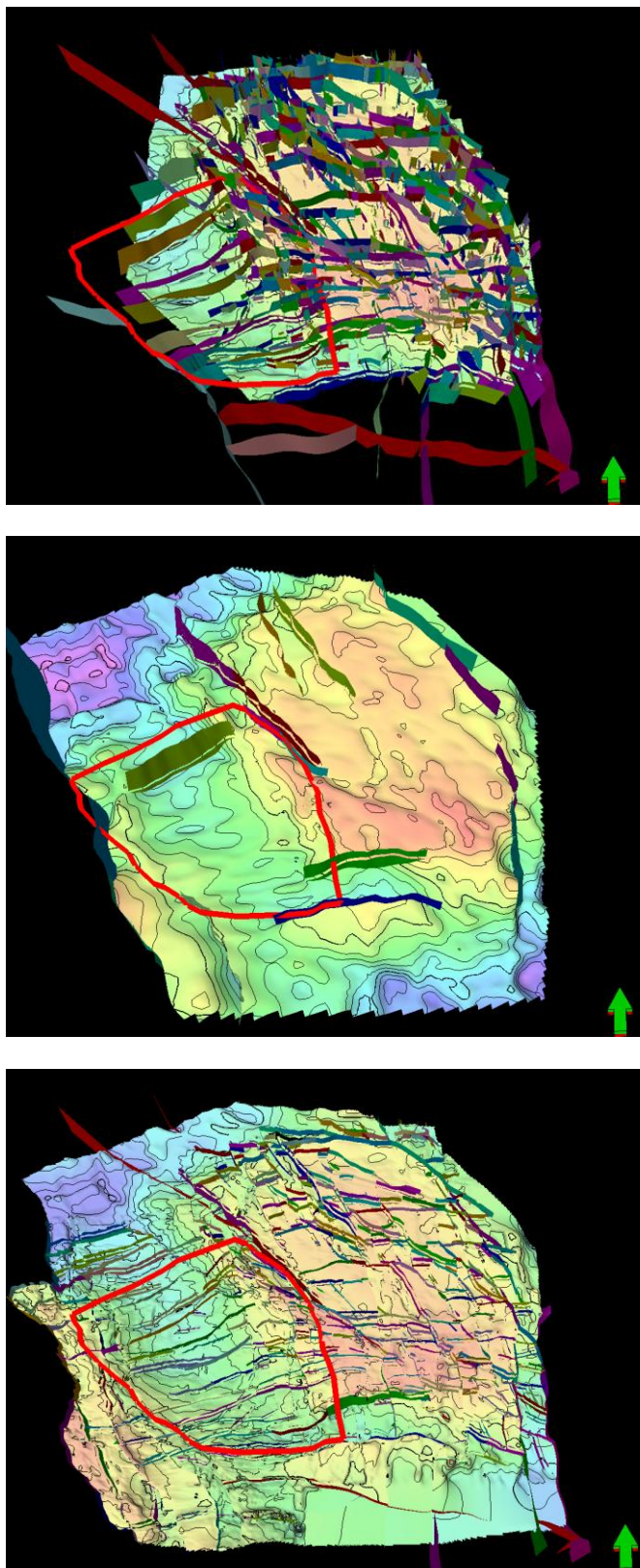
Figure 2-8 Low angle bird's-eye view, which enables to compare the extend and details of the existing models. For an impression of the scale see Figure 2-1 to Figure 2-3. Upper: NAM reservoir model (2019). Middle: TNO KEM-19 reservoir model (2021). Lower: TNO internal reservoir model (2023). The red polygon is the outline of the current area of interest. Green arrow indicates north.

The TNO KEM-19 reservoir model (2021) contains only a handful of faults (middle image in Figure 2-8), and lacks the detail needed within the Lauwerszee Trough. The TNO internal reservoir model (2023) was based on NAM's (2019) model for the area on the Groningen platform and had been extended toward the west, thereby covering also large parts of the Lauwerszee Trough and a minor part of the Friesland platform. This model is generally detailed enough and it covers the current area of interest. A limited number of smaller scaled faults in the Lauwerszee Trough is not incorporated in this model (Figure 2-8 bottom picture and Figure 2-14). Another point of attention for the TNO (2023) internal model is that its reservoir properties are likely too optimistic in the water zone since the simulation of the properties do not take into account differences in reservoir quality between the water and gas phase and changes with depth.

The model of choice to use as a starting point was TNO's internal model (2023) (Figure 2-9). The geometry (horizons, faults, grid cell size) was largely fit for purpose, but a few challenges remained. First of all, the set of faults needed to be checked on seismic and some smaller scaled faults needed to be added. Also the model boundaries needed to be selected before creating the static model. Subsequently a model grid was created via pillar gridding. In addition, a part of the Carboniferous underlying the Lower Slochteren Member needed to be added to the bottom of the model. This is needed to allow pressure depletion in the underlying Carboniferous interval (see also chapter 2.3).
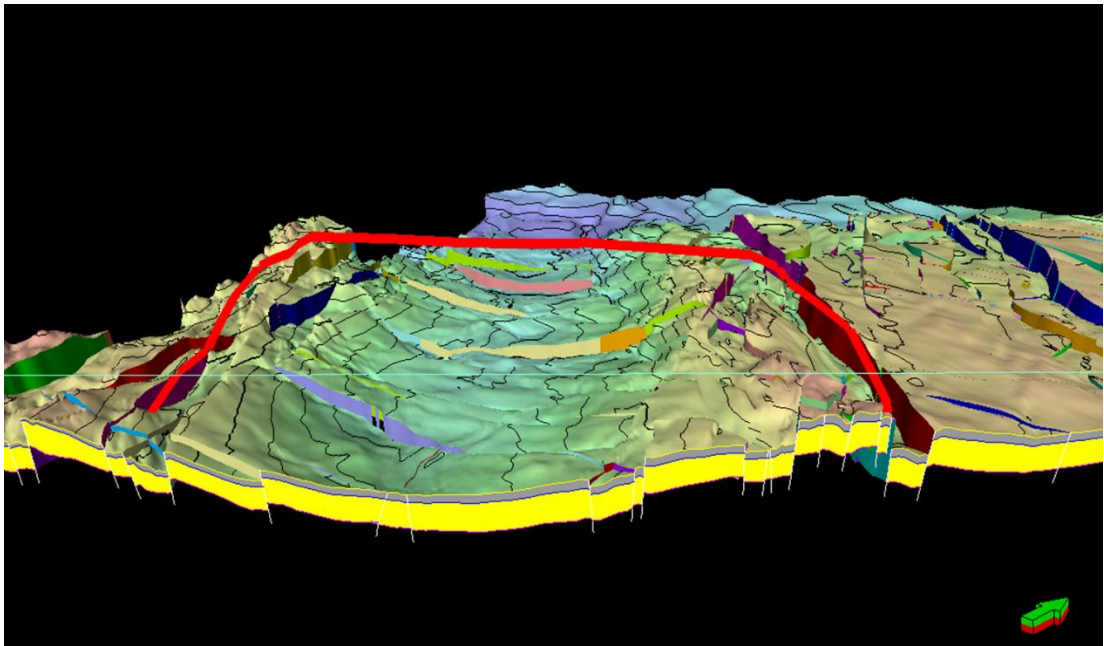
Figure 2-9 3D bird's-eye view of the geometry of the TNO internal model that was used as a starting point for the KEM-19b model. Yellow colour on the cross-section denotes the sandstones of the Slochteren Formation, the overlying grey represents the shaly Ten Boer Member. Note that the Ameland Member is not present this far south. Green arrow indicates north.

2.3   Construction of the fault model and grid

From the geological model (also called static reservoir model), a dynamic reservoir model will be created, which will be used to simulate the pressure depletion in this aquifer. This has a strong impact on the choice of the model area and boundaries, which will be discussed below. Ultimately, an ensemble of models will be created by varying reservoir properties. The geometry (i.e. faults and reservoir configuration) of the model, which is discussed in the

current chapter 2.3, will not be varied. The creation of the ensemble will be discussed in section 2.5.

Since there are no wells in the aquifer within the Lauwerszee Trough, the information for the aquifer needs to come from the gas fields on both sides of the aquifer: the Groningen and Bedum fields on the east and a series of small gas fields in the west (Figure 2-2 and Figure 2-3). These gas fields and the wells associated with it need to be included in the model to constrain the reservoir properties (porosity and permeability), to simulate the pressure depletion in the aquifer resulting from these small gas fields and to simulate the subsidence. As mentioned in the introduction, observed subsidence is used to reduce the uncertainty. The workflow of how this is done is explained at the start of Chapter 3. Only a small part of the Groningen field will be included to keep the size of the model limited and to allow a sufficiently detailed grid near the small gas fields. Keeping the size of the model limited is important because the uncertainty will be addressed by using an ensemble of models rather than a single model. Preferably the boundary of the model is located at faults with large offset which act as no flow boundaries, but that was not always possible. Below the detailed choices for the boundaries are described, based on the geological settings and the requirements for the dynamic model. The boundaries are no flow boundaries except when indicated otherwise.

The boundaries of the model were selected as follows:
- In the north, a large fault with large offset separating the northern part of the Lauwerszee Trough from the southern part is used as the main part of the boundary (Figure 2-2 and Figure 2-10). On the northwest side, the model boundary is formed by a number of faults bounding the Faan and Boerakker gas fields. In the north-east no suitable faults were available and the boundary of the model is in the Bedum field (Figure 2-2 and Figure 2-10). Therefore the Bedum field will be implemented as a pressure boundary condition.
- On the east side, two connected faults with large offsets separating the western periphery from the Groningen main field are selected as boundary. The offset of the faults is well visible in Figure 2-9 (i.e. the red fault and the purple fault) and Figure 2-10. The included part of the Groningen field will be implemented as a pressure boundary.
- To the south, the position of the boundary is taken as the south bounding fault of the graben between Groningen and Annerveen on the east side and on the west side by faults separating Vries North from Vries Central. The Annerveen field itself is not included in the model (Figure 2-2 and Figure 2-10), because it is not directly connected to the SW aquifer due to the deep graben.
- On the west side, the boundary is formed by a series of faults which close the small gas fields on the west and mostly have large offsets (Figure 2-2, Figure 2-9 and Figure 2-10).

The implementation of the Groningen and Bedum fields as pressure boundary conditions and the values used for the pressure will be discussed in more detail in paragraph 3.2. As top boundary condition, the base Zechstein is selected. For the bottom boundary, a part of the Carboniferous underlying the Lower Slochteren Member needed to be added to the bottom of the TNO model. This was done to allow pressure depletion in these layers. In the model area, the Lower Slochteren Member is underlain by various formations of the Limburg Group. This is simplified in the model.
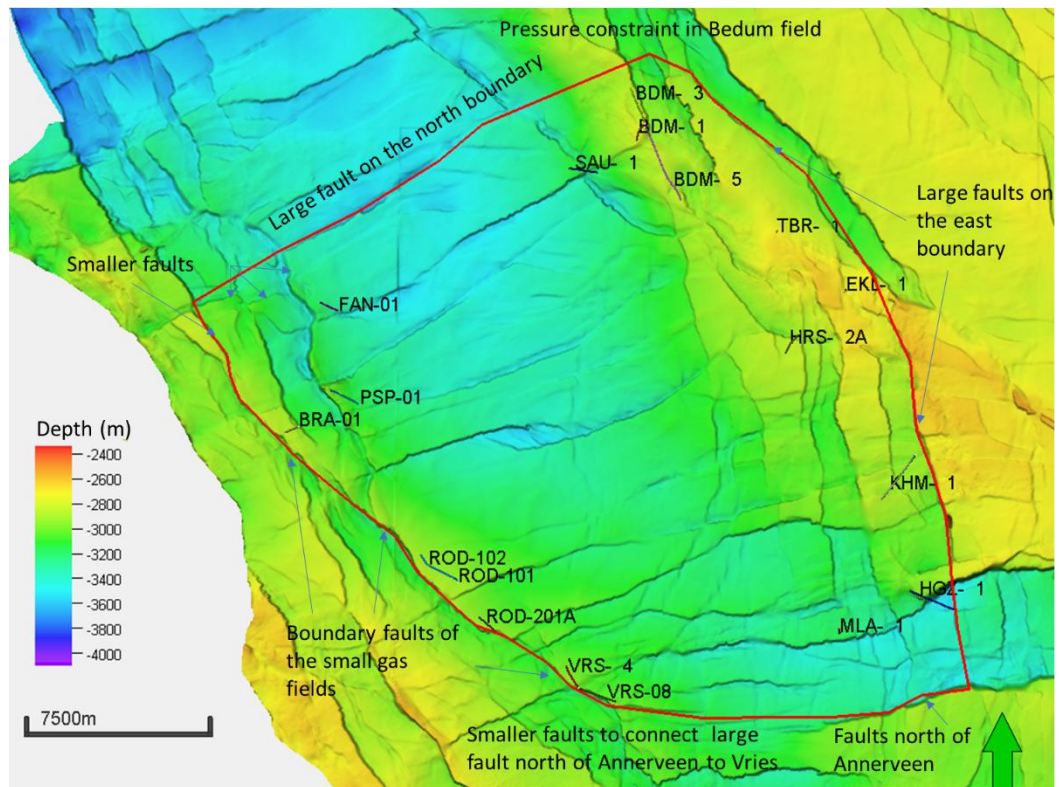
Figure 2-10 Top of the Rotliegend depth map. Red line is the outline of the area of interest. Green arrow indicates north.

As stated above, additional work on the faults was necessary. A check on the faults from TNO's internal model against a Variance cube (a seismic attribute that is frequently used to map faults) resulted in the identification of a number of minor, small scaled faults (i.e. both in terms of offset and lateral continuity) that are not incorporated in the TNO internal model (Figure 2-11). The majority of these faults have an approximately east-west strike that is oblique to the strike of the larger faults in the Lauwerszee Trough, which is generally WSW-ENE (Figure 2-12). These minor faults are most likely Riedel shear faults, which resulted from strike-slip movements. It is noted that not all minor faults have been incorporated in the current model. This is due to gridding limitations, and not due to seismic quality as the seismic quality is good.

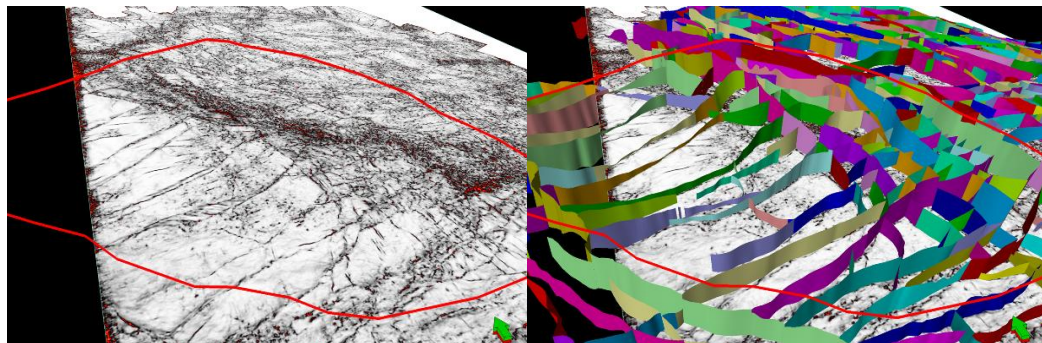
Figure 2-11 **Left:** Bird's-eye view showing a depth slice of the 3D Groningen seismic survey at ~3500 m depth. Right: the same time slice overlain by faults from TNO's internal model (2023). Note that some smaller faults are missing from the model. The red polygon is the outline of the area of interest.
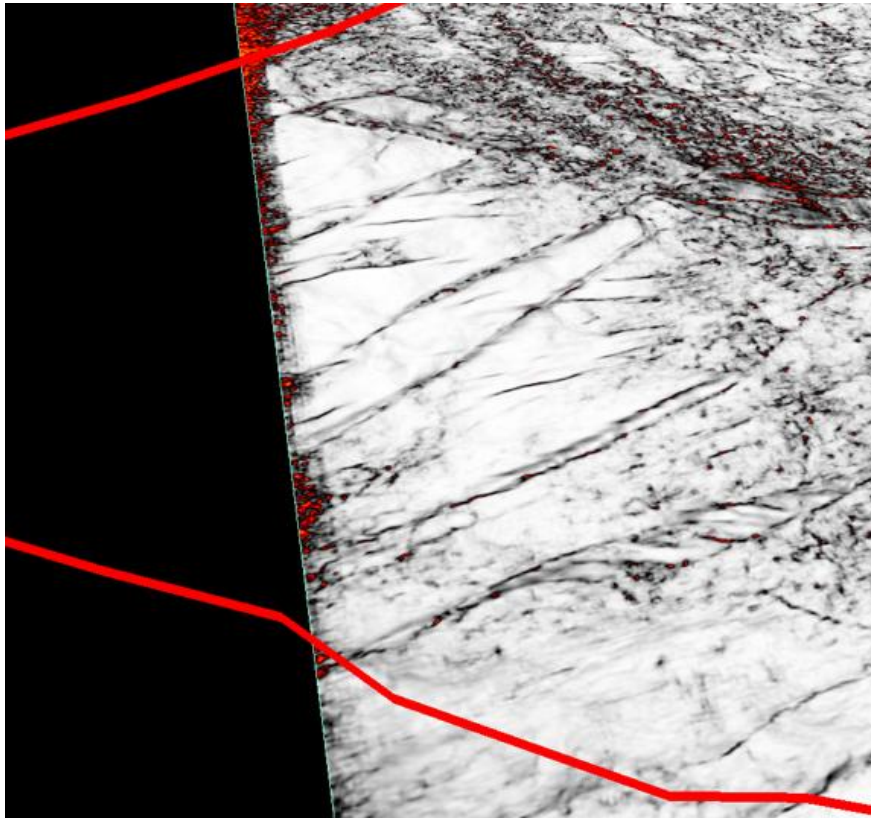
Figure 2-12 Detail of Figure 2-11 left, showing the oblique strike of the smaller faults with respect to the larger faults, most likely the result of strike-slip movements. A mall pull-apart structure is present the foreground. The red polygon is the outline of the area of interest.

In addition to fault interpretation on the Groningen seismic cube, additional faults needed to be interpreted on seismic cubes west of the Groningen cube. Figure 2-13 shows a map with the outlines of all seismic cubes that cover the area of interest. Apart from the Groningen cube, these include 5 seismic surveys:

- Grootegast L-123 (1985)
- Grootegast L-128 (1985)
- Lauwerszee (1983)
- Broek (1992)
- Eext (1992)

Figure 2-13 Overview of seismic surveys and wells in the area of interest (white polygon). Green arrow indicates north.

For the area of interest, a pillar grid with increment of approximately 150x150 m (Figure 2-14, top map) was created. The pillar grid is a 3D grid based on the fault information (the fault model) and is structured based on the pillars describing the fault 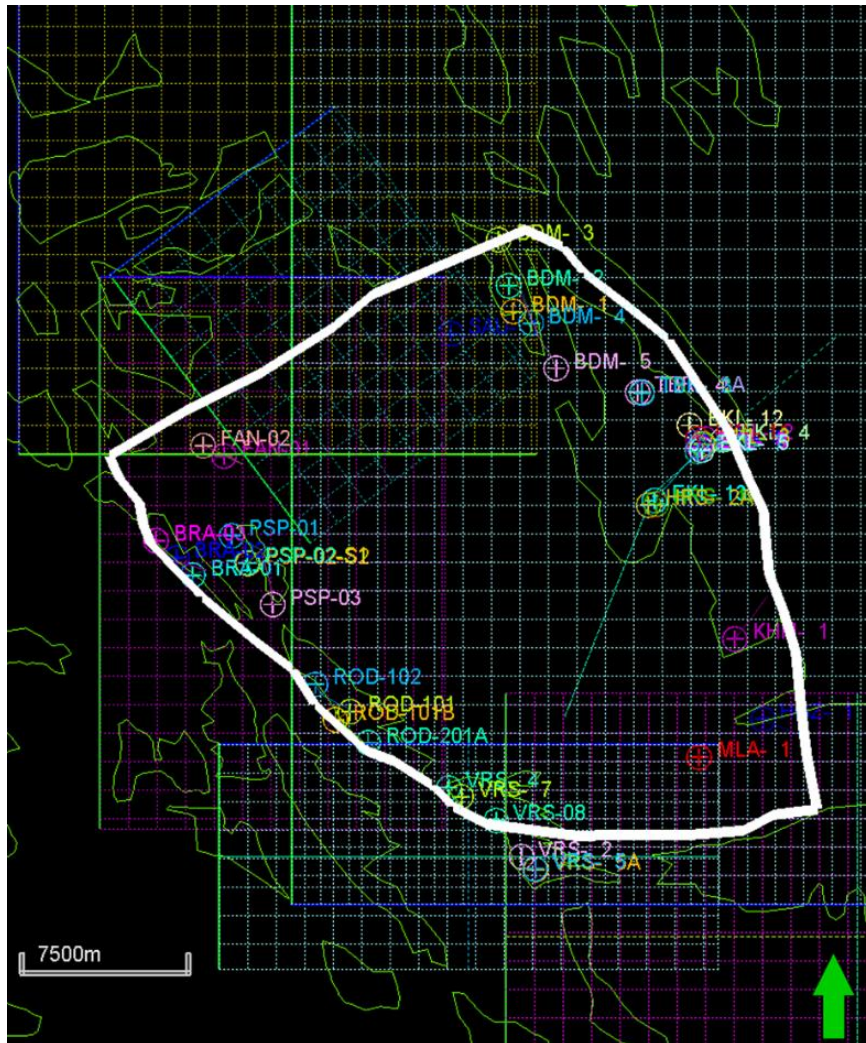geometry. The selected horizontal resolution of ~150 x 150 m is a compromise between the accurate representation of the faults and the small gas fields on the one hand and a feasible number of grid cells required for the reservoir simulations in WP 2. To create the 3D grid to be used for reservoir simulations, the pillar grid is combined with information from the relevant horizons. The top of the model is the top of the Ten Boer Member (ROCLT). The other horizons are the top of the Upper Slochteren Member (ROSLU), the Ameland Member (ROCLA) and top and base of the Lower Slochteren Member (ROSLL). The bottom of the model is 60 m below the base of the Lower Slochteren Member to allow pressure depletion in the underlying formations from the Limburg Group of the Carboniferous. This is less than the thickness of the Limburg Group that is included in the NAM Groningen model. However in the south of the Groningen field, these units are gas bearing and are known to be connected to the gas bearing units of ROSLL above. This is not the case in the aquifer area and lower permeability and connectivity is expected.

Figure 2-14 Top Figure: Map view of the pillar grid of the area of interest resulting from the combination of existing large fault model and some newly interpreted small faults in the current project. Bottom Figure: Map view of the fault pattern in a pillar gridding configuration of the internal TNO (2023) project. The bold (light) red polygon indicates the outline for the area of interest for the current project.

The horizons are created based on a combination of seismic interpretation and well tops. The top of the Rotliegend was derived from seismic interpretation performed during the modelling of the NAM geological model (2019; for the Groningen platform area) and during the TNO internal modelling (2023; for the Lauwerszee Trough and the most eastern part of the Friesland platform). The intra-Rotliegend layering was based on well tops, which were adopted from the NAM geological model (2019) and the TNO's internal geological (2023). These well tops were picked based on well-log data during the modelling of the aforementioned models. It is noted that the following wells were not incorporated in the TNO internal (2023) geological model: FAN-01, FAN-02, PSP-02, PSP-03 and VRS-08. The well data from these wells, including well logs, well deviation paths, and well tops, were downloaded from nlog.nl, imported into the Petrel project and subsequently used for the update of the geological model.

To achieve a consistent grid, the model construction was undertaken by adding the thickness of the individual zones (derived from well tops) to the top of the model (i.e., the top of the Ten Boer Member (ROCLT), derived from seismic interpretation). The zone layering is presented in Table 2-1. Because most gas is produced from the Upper Slochteren Member (ROSLU), this zone has the highest resolution (i.e. average thickness of 8 m per layer, see Table 2-1). The Ameland Member (ROCLA) is a relatively thin, largely mudrock-dominated interval layer. The ROCLA pinches out towards the south, which reduces the average thickness of the layer. Nevertheless, it was modelled explicitly because it can affect the communication between Upper and Lower Slochteren Members.

Table 2-1 Overview of the layering of the geological 3D grid

Zone	Number of layers	Average thickness of the layers
ROCLT	2	27 m
ROSLU	15	8 m
ROCLA	1	3 m
ROSLL	5	11 m
Carboniferous	2	31 m

In total the geological 3D grid has 143 x 160 x 25 grid cells resulting in 572,000 cells.

In the centre of the model there were a few cells with negative volume due to pinching out of cells near faults. This has been solved for the simulation grid by setting these cells to inactive. Because the cells are in the aquifer the impact of the volume is not relevant. The connectivity is marginally reduced, but because these cells are located near low-permeable fault, the impact is negligible.

2.4 Review petrophysical properties and update

2.4.1 Data and methods

The NAM Groningen reservoir model (2019) does not contain wells outside the Groningen Field. Therefore, in order to populate the extended model with reservoir properties (porosity, net-to-gross, permeability), a petrophysical evaluation of selected wells in the southern

part of the Lauwerszee Trough and on the eastern side of the Friesland platform has been conducted (Figure 2-2 and Figure 2-9).

Table 2-2 provides an overview of the selected wells with available log data. Main target intervals for the evaluation are the Ten Boer, the Slochteren and the underlying Carboniferous formations. For some wells, porosity (ϕ), permeability (k) and net-to-gross (NtG) data are available from ThermoGis_v2.2 (a single averaged ϕ, k or NtG over the (entire) Slochteren Formation).

Table 2-2 Selected wells for petrophysical evaluation with available log data. Reported property data (NtG, ϕ, k) are adopted from ThermoGIS_v2.2 and represent the average Slochteren (ROSL) reservoir interval.

Field	Well name	Alternative well name	Usable logs	Evaluated [Y/N]	Comment	ThermoGis_v2.2 Eff. porosity [%] ROSL	ThermoGis_v2.2 permeability [mD] ROSL	ThermoGis_v2.2 NtG [%] ROSL
Roden	ROD-101		GR, DENS, Sonic, Resistivity	Y	Ten Boer, Slochteren (RO) & Maurits (DC) formations evaluated	16.7	25	95.3
	ROD-101-S1		no logs available	N	Undifferentiated below Zechstein, RO-DC well tops not interpreted			
	ROD-101-S2		GR, Sonic, Resistivity	N	No density logs	20.0		
	ROD-102		GR, NEU, DENS, Sonic, Resistivity	Y	Ten Boer, Slochteren (RO) & Maurits (DC) formations evaluated	18.3		74.1
	ROD-201		-	N	well TD in Ommelanden-Chalk			
	ROD-201-S1		GR, NEU, DENS, Sonic, Resistivity	Y	Ten Boer, Slochteren (RO) & Maurits (DC) formations evaluated	16.8		
Vries*	VRS-4	VRS-401	GR, NEU, DENS, Sonic, Resistivity	Y	Ten Boer, Slochteren (RO) & Limburg Group (DC) formations evaluated	16.4		82.6
	VRS-7	VRS-402	GR, NEU, DENS, Sonic, Resistivity	Y	Ten Boer & Slochteren (RO) formations evaluated. TD in Slochteren	16.3		75.0
	VRS-8	VRS-403	GR, NEU, DENS, Sonic, Resistivity	Y	Ten Boer & Slochteren (RO) formations evaluated. TD in Slochteren			
Pasop	PSP-01		GR, DENS, Sonic	Y	Ten Boer, Slochteren (RO) & Ruurlo (DC) formations evaluated	17.5	33	89.6
	PSP-02		GR	N	Undifferentiated below Zechstein, RO-DC well tops not interpreted			
	PSP-02-S1		GR, DENS, Sonic	Y	Ten Boer, Slochteren (RO) & Limburg Group (DC) formations evaluated			
	PSP-02-S2		GR	N	No density logs	17.1		
	PSP-03		GR, Sonic	N	No density logs			
Boerakker	BRA-01		GR, DENS, Sonic	Y	Ten Boer, Slochteren (RO) & Ruurlo (DC) formations evaluated	18.1		81.4
	BRA-02		GR, DENS, Sonic	Y	Ten Boer & Slochteren (RO) formations evaluated. TD in Slochteren	16.9		67.0
	BRA-03		GR, DENS, Sonic	Y	Ten Boer & Slochteren (RO) formations evaluated. TD in Slochteren	16.7		86.0
Faan	FAN-01		GR, DENS, Sonic, Resistivity	Y	Ten Boer & Slochteren (RO) formations evaluated. TD in Slochteren			
	FAN-02		GR, Sonic	N	Ten Boer & Slochteren (RO) formations evaluated. TD in Slochteren			

* VRS-02, VRS-05, VRS-09, VRS-10 are outside the study area

Because the Slochteren formation is a nearly pure sandstone formation, porosity is calculated from the Density log without applying a shale correction:

$$\varphi = \frac{\rho_{matrix} - \rho_{bulk}}{\rho_{matrix} - \rho_{fluid}}$$

with ρ_bulk = RHOB log, ρ_matrix=2.66 g/cm^3, ρ_fluid = 1.05 g/cm^3.

Porosity was calculated using the Petrel calculator. Permeability was calculated in each well based on the porosity log and by applying a poro-perm relationship. In ThermoGIS a standard, countrywide poro-perm relationship is used to calculate permeability from porosity (https://www.thermogis.nl/porositeit-en-permeabiliteit). However, for the wells in the present study, poro-perm relationships were derived (where possible) for each field using poro-perm data reported in the NLOG core plug database (https://www.nlog.nl/sites/default/files/thematische_data/nlog_poroperm.xlsx). Both a porosity correction (0.92) as well as a Juhasz correction (Juhasz, 1986) on permeability data have been applied.

The core-plug data is also used to test whether different porosity-permeability relationships are required for either gas or water bearing intervals in the Slochteren formations.

For each evaluated well a net-to-gross (NtG) was determined using cut-offs on the GR and porosity in line with NAM . Net reservoir is taken as GR<60 gapi and porosity > 0.04.

2.4.2 Petrophysical evaluations

2.4.2.1 Ten Boer and Slochteren formations

Log evaluations have been conducted for the wells listed in Table 2-2. Evaluated results have been, where porosity-permeability measurements are available, cross checked with the core plug data (Figure 2-15). Generally a good match was achieved between the density derived porosity data and the coreplug data. In 0, the porosity-permeability log data per well is provided.

In order to check how the density derived porosities compare to porosities from the NAM Groningen reservoir model, two random wells (EKL-04 and AMR-01) were selected from the Groningen model. In each well, the porosity was calculated based on the density log only, and compared to existing porosity logs in the Groningen model. It is hereby assumed that in the Groningen model a full integrated petrophysical evaluation has been conducted for the wells using all available logs (GR, NEU-DENS, sonic, density). For well EKL-04, also the Ten Boer formation porosities were re-calculated in order to check if the effect of not incorporating a shale correction in the porosity determination of the wells in Table 2-2.

Density derived porosities generally compare well to those derived from the Groningen reservoir model (Figure 2-16). For porosities > 15%, the density porosity generally slightly overestimate the porosity by ~10% (Figure 2-16 A and C). Differences in porosity > 15% may be related to regional and depth variation, sand/shale distribution in the wells but are generally considered negligible when the logs are upscaled for the reservoir model.
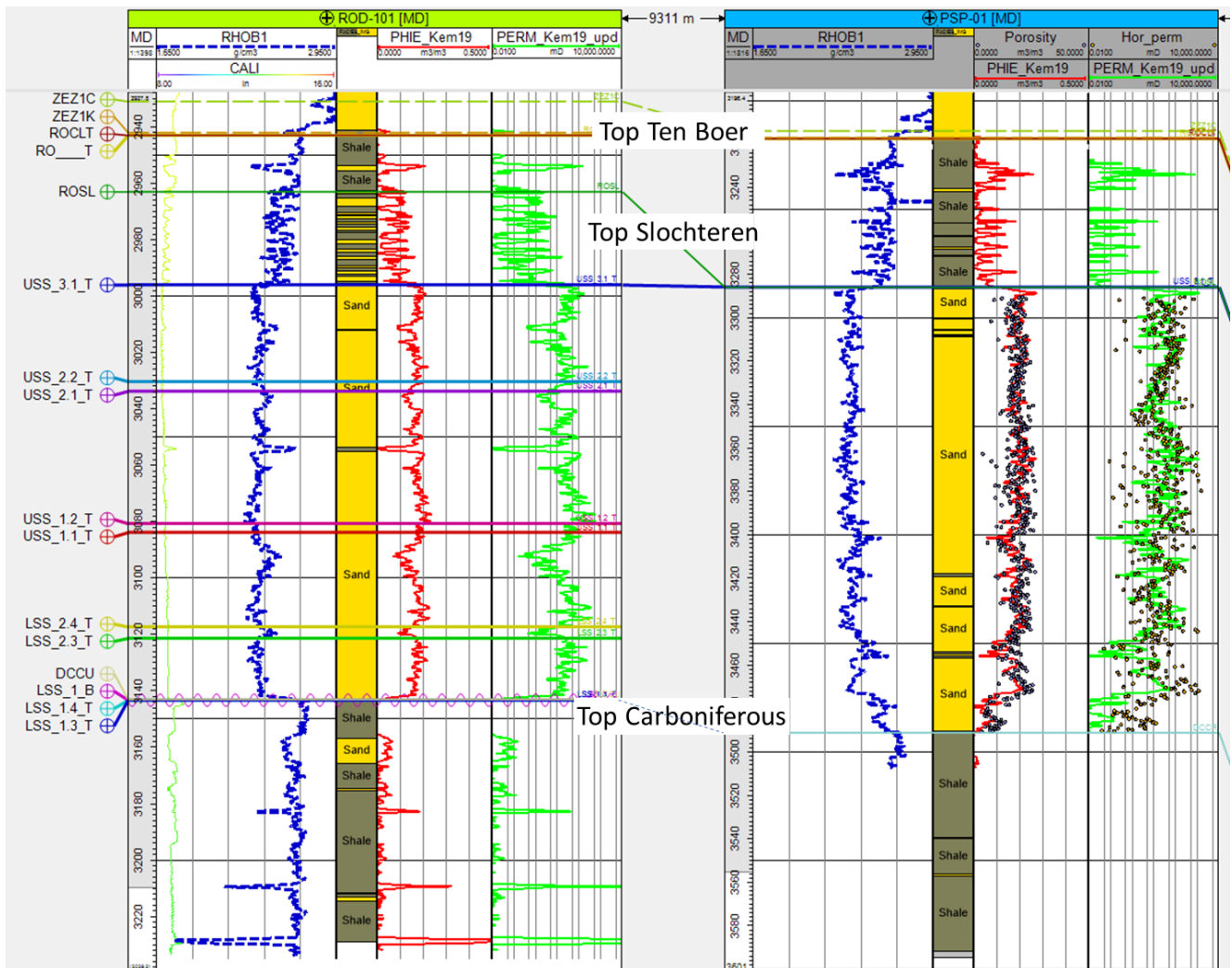
Figure 2-15 Well corelation panel with examples of evaluation results of well ROD-101 and PSP-01. ROSL coreplug measurements (https://www.nlog.nl/sites/default/files/thematische_data/nlog_poroperm.xlsx) are shown for PSP-01 to compare to calculated porosity and permeability logs.

In order to assess whether the assumption to neglect the shale correction is valid, the Ten Boer porosities in well EKL-04 were calculated using the density log and compared to the Groningen reservoir log values. In the Groningen model, cut-offs are applied to the porosity data (if φ <0.04 and if φ>0.34 then porosity is set to undefined), hence only the more sandy intervals are present in the Groningen model in the Ten Boer interval. Despite this, also the Ten Boer density derived porosities compare well to the Groningen model porosity data in this well. For porosities > 15%, the density porosity generally slightly overestimate the porosity by ~10% (Figure 2-16 B).
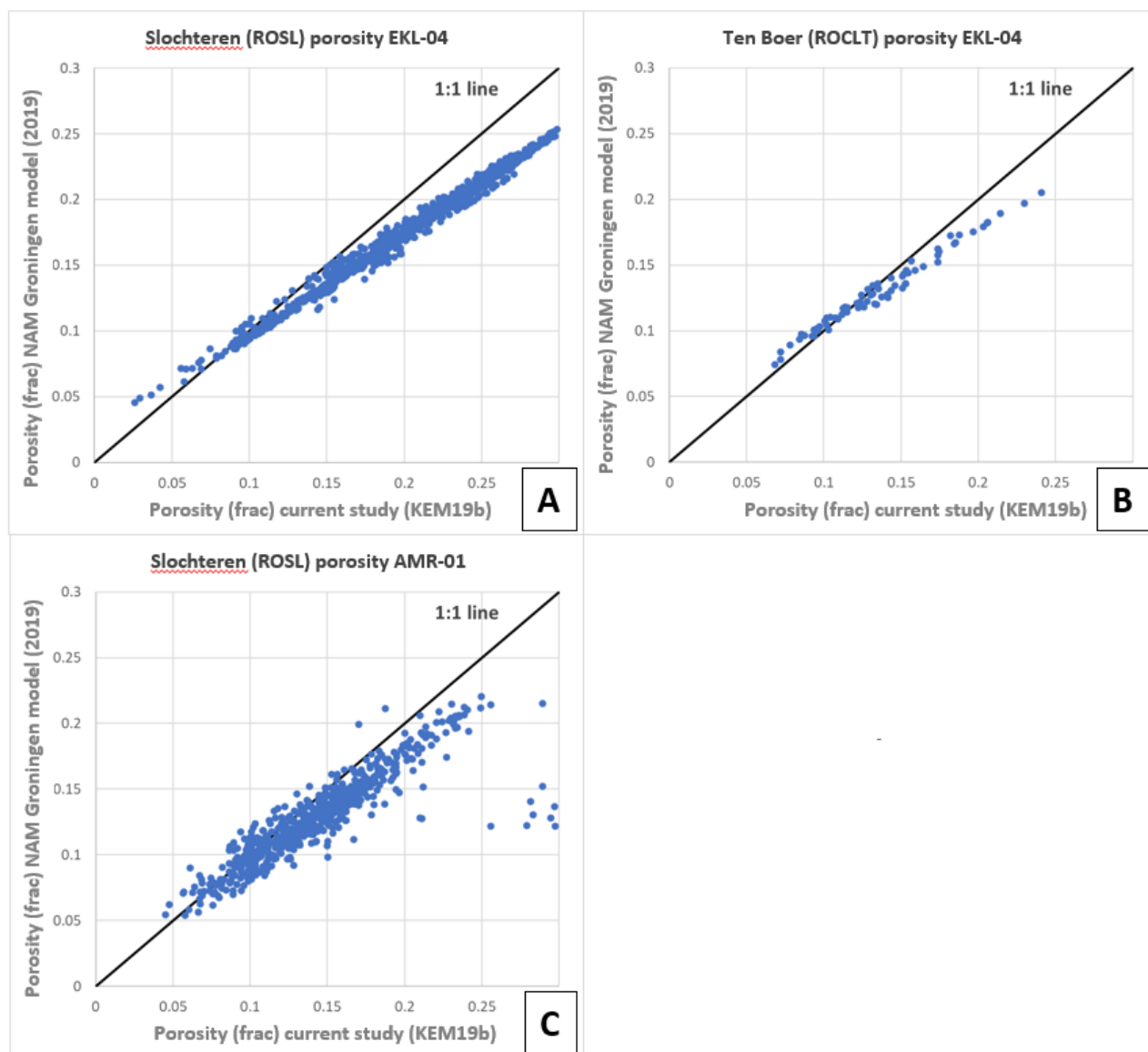
Figure 2-16 Comparison between porosities derived from the NAM Groningen reservoir model (2019) and porosity calculated based on density logs for two randomly selected wells from the Groningen Field. A and B are for well ERK-04 for respectively Slochteren (ROSL) and the Ten Boer (ROCLT) formations. C for well AMR-01 (only Slochteren interval).

Permeability was calculated from the density derived porosity logs using a field-specific poro-perm relationship for Pasop (PSP-01) and Roden (ROD-101 & ROD-202-S1), see Figure 2-17 and Table 2-3.

Wells from the Vries field had only a limited number of coreplug measurements (n = 6) for the Slochteren interval. In some of the Vries wells, a significant amount of coreplug data from the Ten Boer Formation was available, however using these data for the Slochteren interval would underestimate the poro-perm relationship. For wells in the Boerakker and Faan fields, no coreplug data is available. For the evaluated wells in these fields, the poroperm relationship from PSP-01 was used (Table 2-3).
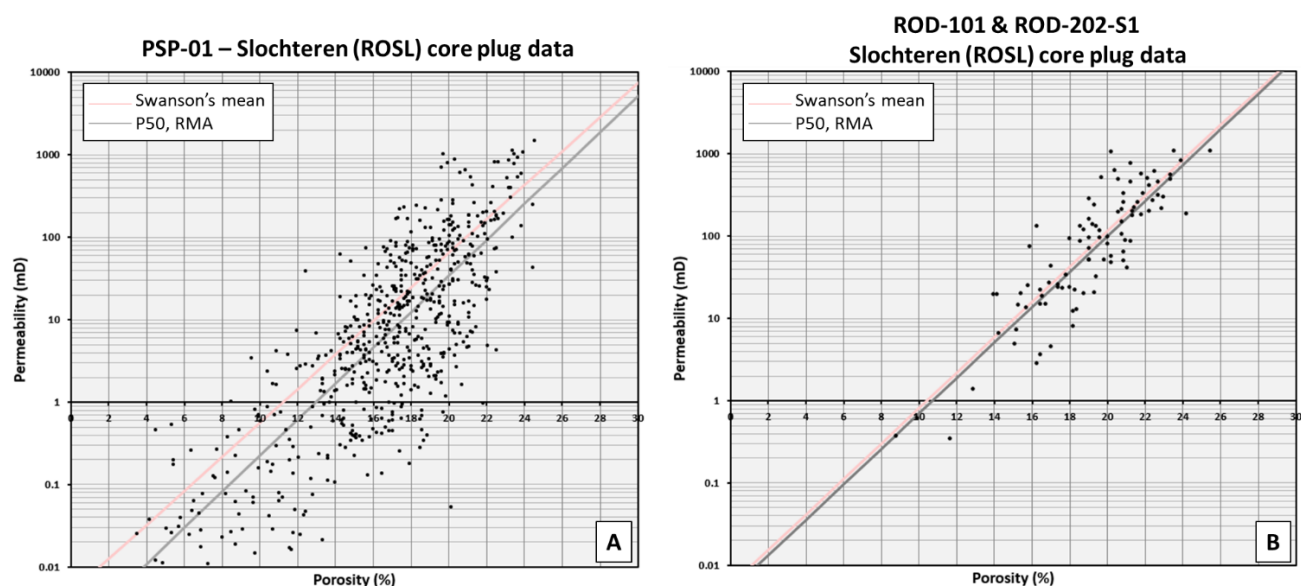
Figure 2-17 Slochteren (ROSL) porosity-permeability plot based on coreplug data from well PSP-01 (A) and wells ROD-101 & ROD-202-S1 (B). For all calculated poro-perm relationships, the P50 – reverse mean average (RMA) was adopted. A Juhasz (1986) correction and a porosity correction of 0.95 have been applied to all coreplug data.

Table 2-3 Derived porosity-permeability relationship for wells in the study area.

Well	Poro-perm relationship	Formation
PSP-01	k = 0.001477 * exp^(0.5020*PHIE)	ROSL
ROD-101	k = 0.0060275 * exp^(0.4839*PHIE)	ROSL
ROD-201-S1		
Vries	6 coreplug measurements in ROSL; PSP-01 poro-perm used	ROSL
Faan	Insufficient coreplug data; poro-perm relationship of PSP-01 was	
Boerakker		

In order to assess the effect of water versus gas bearing intervals on the calculated permeability, the coreplug data from PSP-01 (most coreplug dense well in the study area) is plotted above and below the Gas-Water Contact (GWC, Figure 2-18. The GWC in PSP-01 resides at 3123 m (m NAP) or 3443 m MD.

No clear distinction between porosity-permeability data from below and above the GWC is observed (Figure 2-18). Separate porosity-permeability relationships were derived based on coreplug data below and above the GWC. The resulting calculated permeabilities show minimal differences and have negligible (<5%) effect on the calculated permeabilities.
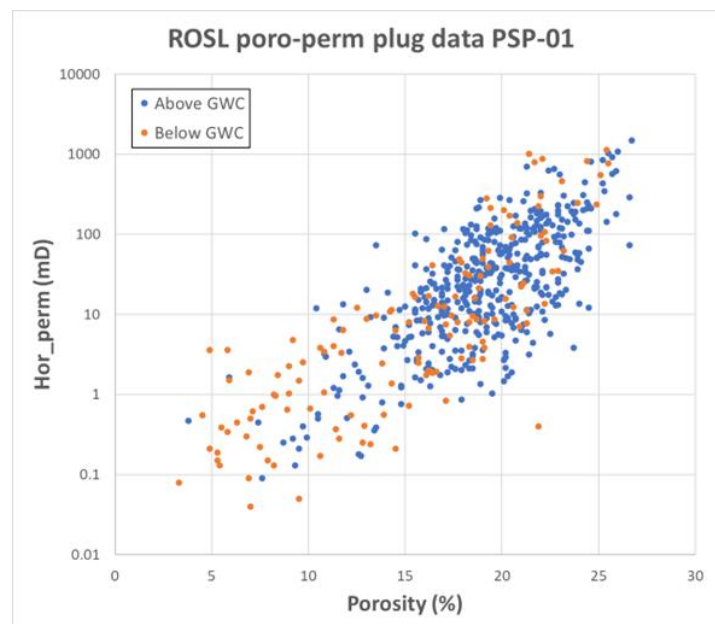
Figure 2-18 Slochteren coreplug data from well PSP-01 separated into above and below the Gas-Water contact (GWC) at 3123 m (m NAP) or 3443 m MD.

2.4.2.2 Carboniferous formations

The aquifer properties of the Carboniferous units directly underlying the Slochteren formations (Pasop and Boerakker: Ruurlo Formation; Vries: De Lutte Formation; Roden: Maurits Formation) were assessed by incorporating core plug data alone. Often log coverage over these Carboniferous intervals is poor to absent, hence it is not possible to do a meaningful evaluation.

Coreplug data from wells in the study area are only available for the Pasop field (PSP-01). Plug data from the Vries Field is available for one well outside the study area (VRS-101). To further expand the plug database for the Carboniferous units, two wells from nearby fields were selected (Grijpskerk: GRK-03 and Saaksum: SSM-02).

A summary of available plug data is provided in Table 2-4.

NtG cannot be calculated from the coreplug and/or available log data. Therefore, following the NAM Groningen reservoir model, a constant NtG of 0.2 is adopted.

Table 2-4 Summary of available coreplug data for Carboniferous units in and in close proximity to the study area.

Field	Well	Unit	ϕ - porosity (%)					k - permeability (mD)				
			min	max	avg	median	nr coreplugs	min	max	avg	median	nr coreplugs
Grijpskerk	GRK-03	DC	2.4	19.3	8.1	8	19	0.02	5.94	0.94	0.06	16
Saaksum	SSM-02											
Pasop	PSP-01	Ruurlo	4.2	7.8	6.08	6.3	26	0.03	0.53	0.17	0.08	5
Vries	VRS-101	De Lutte	3.3	13.8	8.94	9.3	36	0.3	26.0	6.64	3.00	29

2.5   Property modelling

The result of property modelling will be an ensemble of geological models representing the uncertainty in the reservoir properties that serves as input for dynamic reservoir flow simulations. For creating the ensemble several properties are varied, namely:
- Porosity, net-to-gross and horizontal permeability
- Vertical permeability as a fraction of the horizontal permeability
- Vertical permeability of the Ameland Member (ROCLA)
- Baffle[2] for vertical flow between the Slochteren and the Carboniferous units
- Transmissivity of the faults

Porosity, net-to-gross and permeability are varied over the entire field per ensemble member using Gaussian random function simulation. The details of this will be discussed below. The details of how the other properties are varied, is discussed in Section 3.3, where the creation of the ensemble of reservoir models is discussed.

Upscaling well logs
All wells logs in the model area need to be upscaled to the resolution of the grid before they can be used for the property modelling. This applies to both the wells of the small gas field interpreted in this project and to the logs of the wells of the NAM Groningen model. For the wells interpreted in this project outliers where removed by applying cut-offs to the porosity data: if ϕ <0.04 and if ϕ>0.35 then porosity is set to undefined following the NAM workflow.

For all wells inside the model area, the logs of porosity, NtG and permeability were upscaled to the vertical resolution of the grid. For the upscaling arithmetic averaging was used for all three properties, also permeability. Since parallel flow to the well is the most relevant flow pattern, arithmetic averaging is the most appropriate upscaling method. No weighting was applied.

Porosity
Reservoir properties are based on well log data which are predominantly from the gas fields. Only two wells have been drilled in the aquifer, namely HAR-01 and SAU-01 and of these two, only SAU-01 has sufficient data to estimate porosity. Properties in the deep Lauwerszee Trough are most likely not as good as in the surrounding gas fields because of the presence of dolomite cement and illite fibers (see paragraph 2.1.2). In addition, there is generally a bias in the wells because they are targeting better quality rocks. NAM therefore has used inversion of the seismic data to improve the porosity estimates in areas with few wells (de Zeeuw and Geurtsen, 2018). It is beyond the scope of the current project to do this for the Southern Lauwerszee Trough. Instead, a porosity-depth relation will be included to ensure lower values in the deeper aquifer. This will be explained in more detail below.

As discussed in paragraph 2.1.2, there might be a decrease in reservoir properties from south to north. The small gas fields do not reflect this trend. The fields with the best reservoir quality are Roden and Pasop (see Figure 2-2 for locations of the fields), whereas Vries, which is more to the south doesn't have very good reservoir quality. This also depends however on the depth of the gas-water contact compared to the Upper and Lower Slochteren Members. Therefore

---

[2] An area that reduces or obstructs the flow, for example a layer; semi-permeable barrier.

no directional orientation has been implemented because there is not enough information to support such a decision.

Porosity is simulated using Gaussian random function simulation with the upscaled well logs as main input. A spherical variogram has been used with a sill of 1 and nugget of 0.001. The range settings used for the variogram are shown in Table 2-5. In the NAM Groningen static model, the ranges for the variogram are smaller, mostly around 3000 to 5000 m and the sill ranges from ~1 to 1.5. The reason for the larger ranges used in this project is the lack of wells in the Lauwerszee Trough.

For Ameland and Ten Boer Members, the petrophysical analysis is less appropriate because no shale correction was applied to the density log derived porosities (it is assumed that the Slochteren Formation is predominantly sandstone). The Ameland Member will be adjusted during base model tuning and is varied in the ensemble. To the north of the model area, the Ameland Member causes a clear barrier between the Upper and Lower Slochteren Members (Landman, 2023). In the model area, the thickness is mostly less than 5 m and is not expected to hydraulically separate the Upper from the Lower Slochteren.

As a result of the small number of logs penetrating the Carboniferous formations, the distribution to be used for the Gaussian simulation is taken with an average porosity of 0.08 rather than from the upscaled well logs.

Table 2-5 Settings for the Gaussian random function simulation of the porosity

	mean	Standard deviation	range	Variogram Range (major/minor/vertical)
ROCLT	From upscaled logs			15000/15000/15
ROSLU	From upscaled logs			15000/15000/30
ROCLA	From upscaled logs			15000/15000/10
ROSLL	From upscaled logs			15000/15000/15
DC	0.08	0.04	0.02-0.2	15000/15000/30

As secondary variable in the Gaussian simulation, a porosity-depth relation is used which is treated as a local varying mean (with normal score transform). The porosity-depth relation for the Upper Rotliegend members is based on the change of porosity with depth in ThermoGIS for the Upper Rotliegend and is shown in Figure 2-19. Below, insufficient information was available to derive a pore-depth curve. The curve for the modelled Carboniferous interval used and shown in Figure 2-19 is based on the available core data in Table 2-4 and the information available in (Zeeuw and Geurtsen, 2018b).
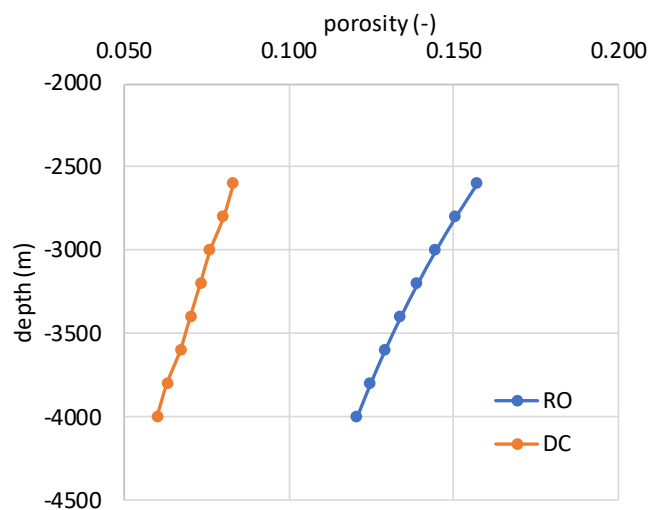
Figure 2-19 Porosity-depth relations used for the Upper Rotliegend members (RO) and Carboniferous units (DC).

Net-to-gross (NtG)

NtG is also simulated using Gaussian random function simulation with the same settings as used for porosity in Table 2-5, with the exception of the values for the Carboniferous. Due to a paucity of data, a constant value of 0.2 is used in the entire model area for all ensemble members. In addition, to avoid grid cells with very low volume which are set to inactive during the simulation, NtG was minimized on a value of 0.03.

Permeability

Permeability is simulated using Gaussian random function simulation with co-kriging of porosity as the secondary variable (using locally varying mean). In this case a lognormal distribution is used instead of the distribution from the well logs. To avoid unrealistically high permeability in some of the layers that distort the flow modelling, the maximum value is limited for some formations. See Table 2-6 for the values used.

For the Carboniferous, a normal distribution is used instead of lognormal, to reduce the occurrence of high values. The ranges of permeability are based on the NAM Groningen model (Zeeuw and Geurtsen, 2018b).

The vertical permeability is calculated as a fraction of the horizontal permeability. To determine a range of realistic values for this fraction, the NAM Eclipse model for the Groningen gas field was investigated. The NAM Eclipse model[3] has been made publicly available in 2023 through https://public.yoda.uu.nl/geo/UU01/8JYW40.html). This model shows a range of values in anisotropy because it is an upscaled model. The permeability in this model shows less anisotropy for higher permeability. For a horizontal permeability (kh) of around 1 mD, the most common value for the vertical permeability (kv) is ~0.1 mD resulting in kh/kv ~ 10. At kh = 100 mD, kv ≈ 30 mD resulting in kh/kv ~ 3. However, the grid cell height is generally less in the NAM model than in the model developed in this project, which implies higher anisotropy in this model than in the NAM model. Based on this information, a range of kh/kv from 5 to 15 for the ensemble was used (See section 3.3 for more information on the sampling for the ensemble). For the base model a value of 10 has been used.

---

[3] Dynamic model (Eclipse version) to predict the formation pressure response to gas extraction in the Groningen gas field, The Netherlands, P. Tummala, NAM, 2023.

Table 2-6 Settings for the Gaussian random function simulation of the permeability

	mean	Standard deviation	Range	Variogram Range (major/minor/vertical)
ROCLT	From upscaled logs			15000/15000/15
ROSLU	From upscaled logs		0.74 – 3000	15000/15000/30
ROCLA	From upscaled logs		0.63 – 500	15000/15000/10
ROSLL	From upscaled logs		0.03 – 1000	15000/15000/15
DC	0.3	0.2	0.02 – 50	15000/15000/30

Fault transmissivity multipliers
The fault transmissivity is calculated by the simulation software based on the juxtaposition of the formation and the permeability of these formations. However, the transmissivity of faults often differs from this value. In the Groningen area many faults are known to have very low transmissivity. Therefore, initial fault transmissivity multipliers were set to 0.1. Subsequently, for all faults for which information was available, the multipliers were set manually. Information was derived from the NAM Groningen model on the east side and the small gas fields on the west. The faults in this project were matched by name to the faults in the NAM model. The multipliers listed in different versions of the NAM Groningen dynamic model were compared and a value selected based on the different values. Also the range to be used for the ensemble sampling were based on it. Due to changes in the different NAM models over time and differences in naming, not all fault multipliers could be determined this way. In addition the NAM dynamic model has a stair-step grid and a different resolution than the model created in this project. Differences in multipliers therefore, can be expected between the two models. The remaining fault multipliers, including those on the west side of the model, were tuned in the base model (Section 3.2.2.6).

The list of multipliers per fault is presented in Appendix B (Table B-3).

2.6 Results

Figure 2-20 and Figure 2-21 show the geometry of the model in two cross-sections. The cross-section from north-west to south-east (Figure 2-20) illustrates the change in thickness of the Upper Rotliegend units. The cross-section from south-west to north-east (Figure 2-21) shows the difference in faults on the east side near Harkstede and on the west side near the Roden gas field.
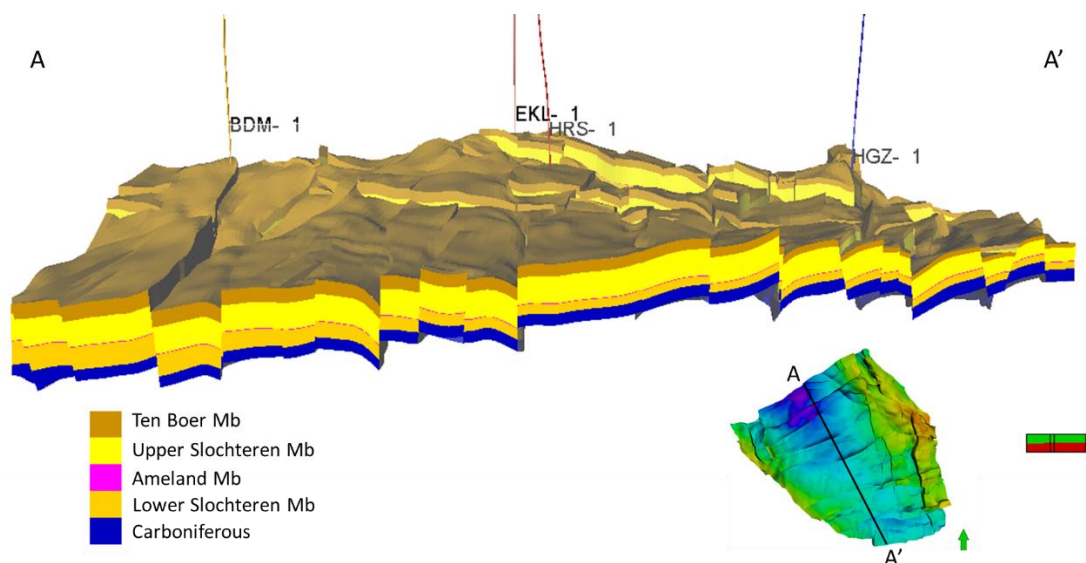
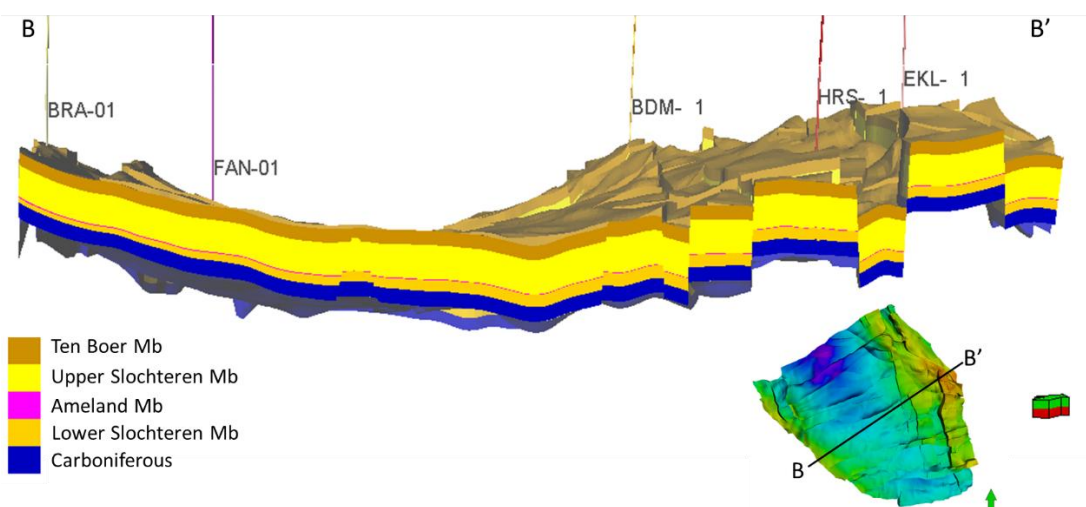Figure 2-20. North-west to south-east cross-section showing the five modelled zones.

Figure 2-21 South-west to north-east cross-section showing the five modelled zones.

In total the geological model has 177 faults, excluding the boundary faults. More than 50% of these faults have a throw of less than 40 m, but a small number of faults has large throws of more than 300 m (Figure 2-22). These are predominantly the long faults with a west-south-west to east-north-east orientation. There are also a few in the Harkstede area on the edge of the Groningen field. Please note that the faults with the largest throw are poorly visible in Figure 2-22, because the throw exceeds the total thickness of the model, especially in the south of the model. Please see for example the cross-section in Figure 2-20 to see these faults. The majority of faults added in this study are short, east-west oriented faults in the northern part of the model area (Figure 2-14). On the east side of the model area (near the Groningen field), the fault interpretation was already very complete.
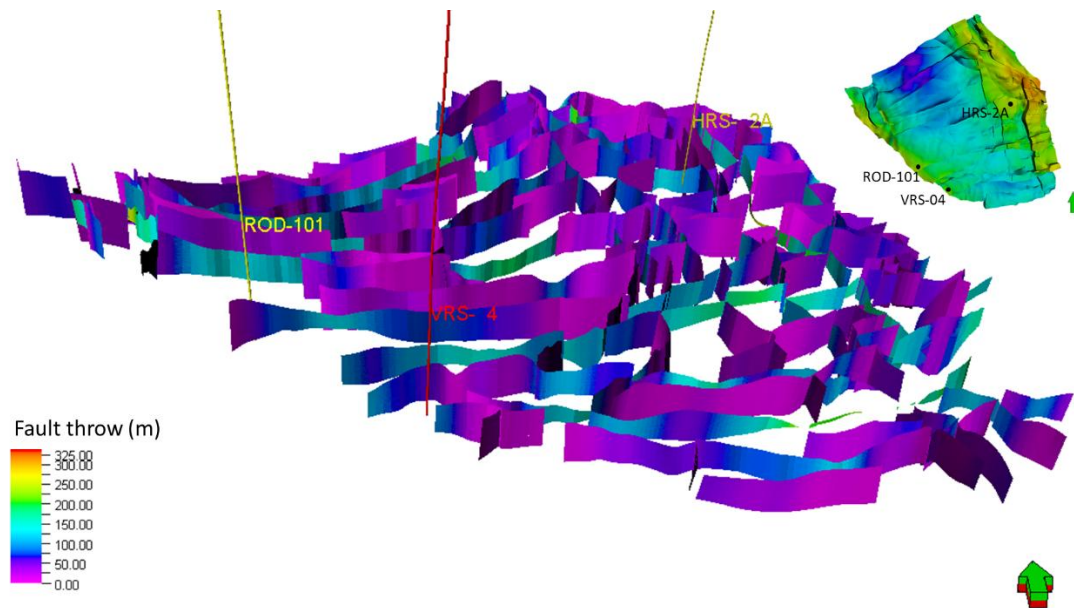
Figure 2-22 Fault throw (m) of the interpreted faults. Three wells have been added for orientation purposes. z-axis is increased by a factor of 5. Green-red arrow indicates north (green on top, red at bottom).

In Figure 2-23 an example of the porosity of the top of the ROSLU is presented as an illustration. Overall, the distribution of the properties is quite smooth as can be expected from the long ranges that were used for the variogram. Figure 2-24 shows two cross sections. One approximately south-west to north-east and the other north-west to south-east. Also shown are the grid cells around the wells which are determined by upscaling of the well logs. These values determine to a large extent the distribution of the simulated porosity. The cross section from south-west to north-east, which goes from Roden to the Groningen field, clearly shows the reduction of the porosity with depth between the gas fields. The cross section from north-west to south-east goes through the aquifer and becomes thinner in the south-east.
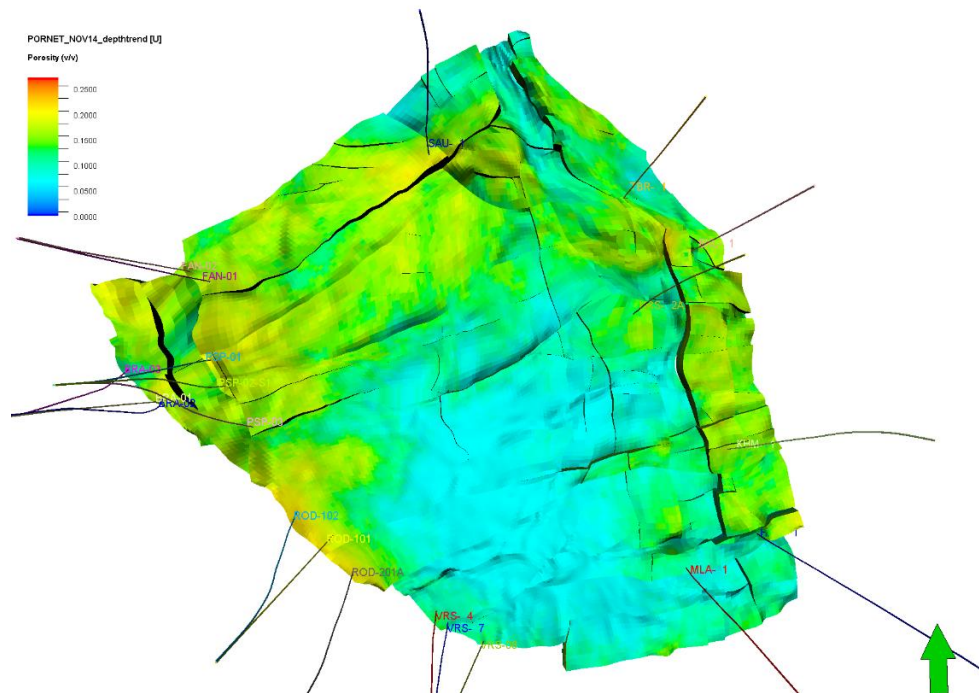
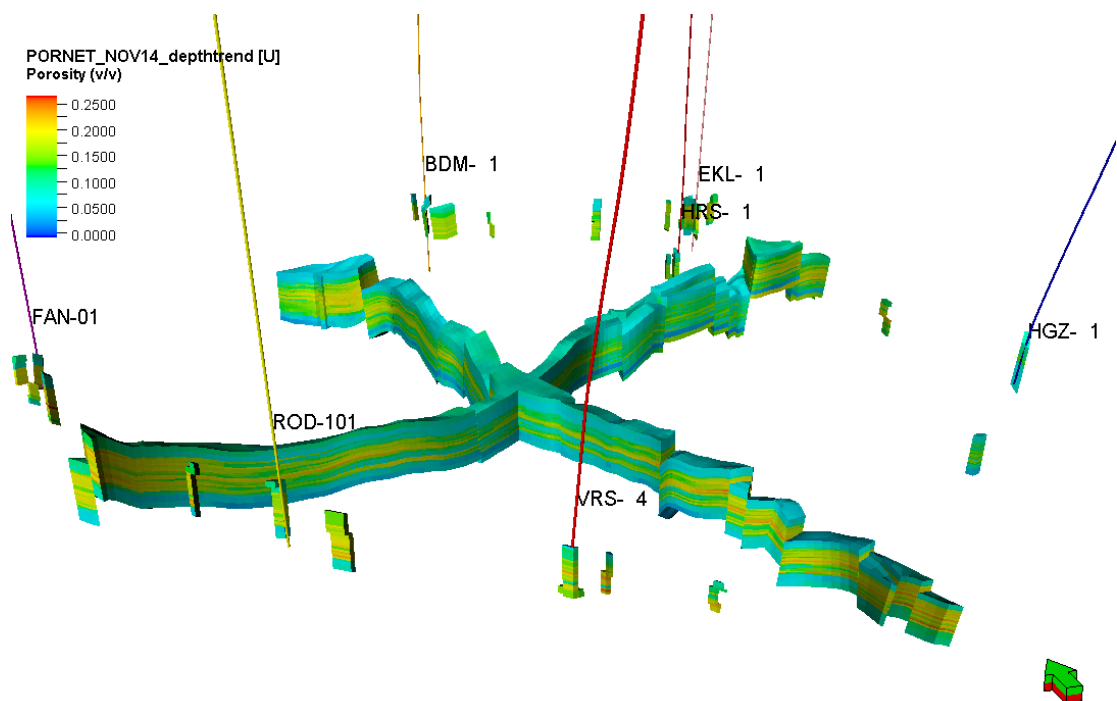Figure 2-23 Example of the porosity of the top of the ROSLU. Green arrow indicates north.

Figure 2-24 Example of the simulated porosity in two cross-sections. Also shown are the upscaled grid cells near the wells that are the input to the Gaussian simulation. For orientation a number of key wells are shown. Green-red arrow indicates north (green on top, red at bottom).

Porosity-depth trends where implemented as locally varying mean to ensure a decreasing trend of porosity with depth. Figure 2-25 shows the resulting trend lines from an example of the simulated porosity with depth. The implemented curves from Figure 2-19 have been added. This shows that the variability in the resulting trends is quite large. Porosity in the Ten Boer Member (ROCLT) is much lower, but the trend is similar. Upper Slochteren has the best properties, which decrease little with depth. The spread around the trend lines is large though: the correlation coefficient ranges from -0.23 for the Lower Slochteren Member to -0.51 for the Carboniferous units. The high porosity at shallow depth for the Carboniferous units is the result of relatively high porosity encountered in the VRS-4 well, which influences the area around the well.
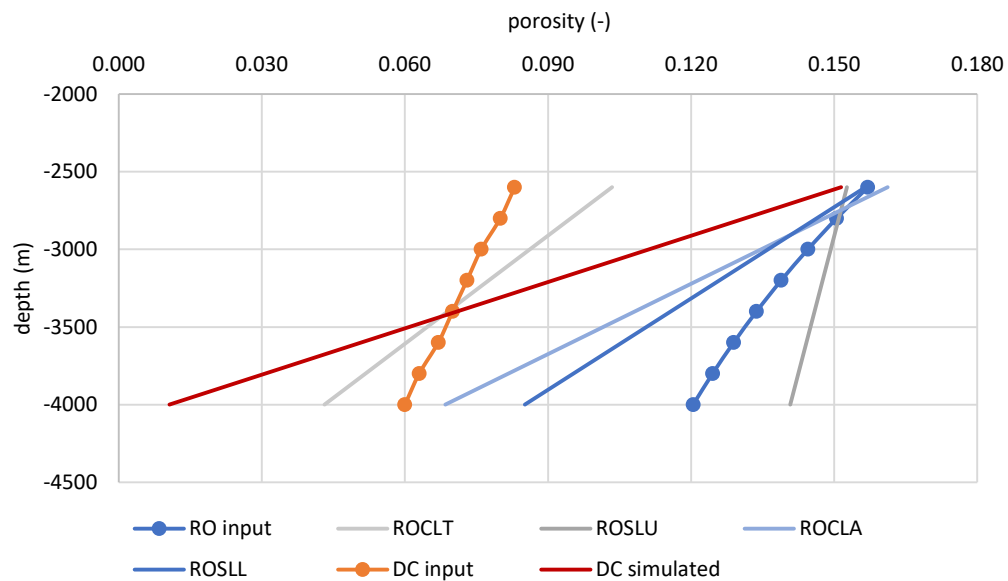

Figure 2-25 Porosity-depth trends from an example of the simulated porosity (linear trend lines of porosity versus depth) and the input porosity-depth relations used as a local varying mean for the Upper Rotliegend (RO) and Carboniferous units (DC) (curves with dots).

Permeability is simulated with co-kriging of porosity as the secondary variable and thus follows the trends of porosity, which is clear from a comparison of Figure 2-23 and Figure 2-26. The apparent variability in the aquifer is due to the logarithmic scale which enhances the variability of the small values.
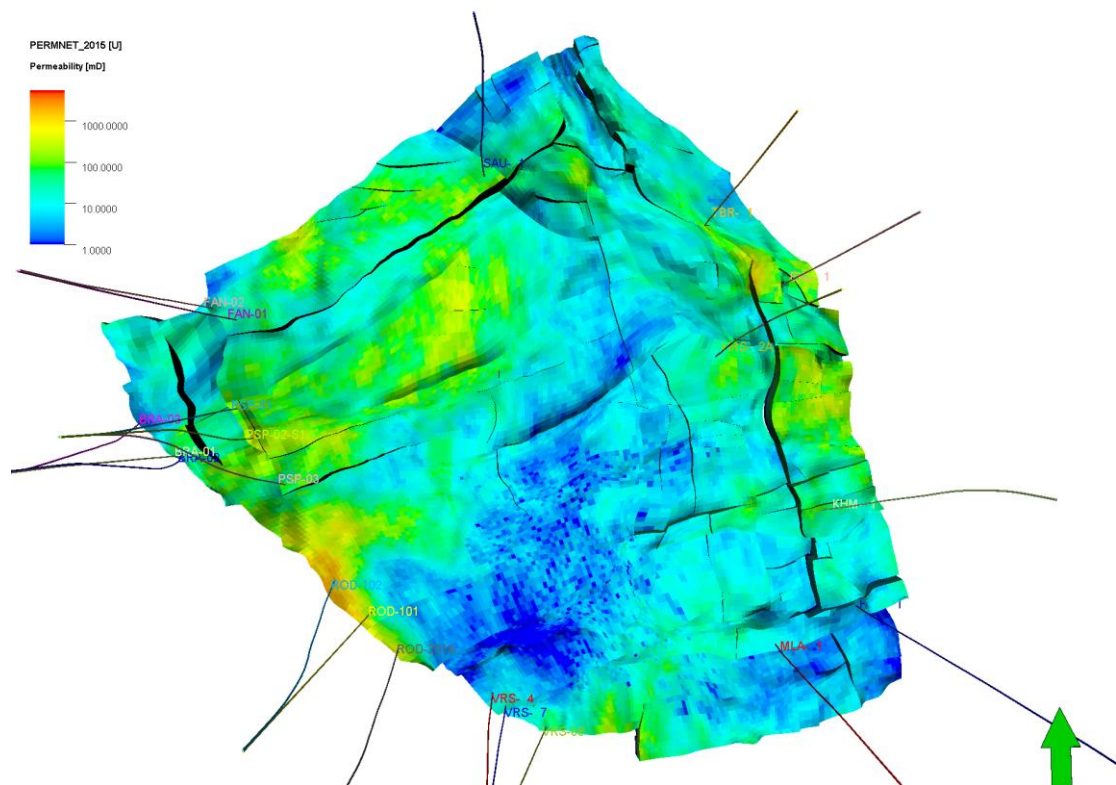
Figure 2-26 Example of the permeability of the top of the ROSLU. Green arrow indicates north.

3 Post-abandonment pressure depletion

3.1 Objectives and approach

The objective of this part of the study is to generate pressure forecasts for the SW aquifer of the Groningen gas field for the period 2024-2100. To achieve this, an ensemble of dynamic reservoir simulation models is developed based on the ensemble of geological models. The workflow is illustrated in Figure 3-1. This ensemble of dynamic models is used to simulate the pressure history based on historical production data. Subsequently, the ensemble of pressure simulations (of the historical period) is used to calculate an ensemble of compaction and subsidence simulations. Based on the match to observed pressure in the small gas fields on the west side of the aquifer and to observed subsidence, a subset of the ensemble is selected for the forecast period. Finally, the selected subset of the ensemble is simulated over the period 2024 - 2100 to provide the required forecasts of pressure and compaction.

Before creating the ensemble of reservoir models, first a base dynamic model is created. The base model uses a single geological realization with a fixed seed for the porosity, NtG and permeability.
The base model has been tuned to reflect the general behaviour of gas production and pressure at the well data. Since the primary purpose of the model is to predict pressure behaviour in the aquifer, a detailed analysis and history match of each of the small gas fields is out of scope of this study. The focus has been on reproducing typical behaviour (like pressure recovery after shutin) rather than a detailed pressure match and to focus on behaviour that impacts the aquifer rather than those only affecting pressure at the well.

In this chapter the creation and tuning of the base model is described in Section 3.2. Following this, the development and the results of the ensemble of dynamic reservoir simulation models and the simulations of compaction and subsidence are discussed in Sections 3.3 and 3.4. Finally, Section 3.5 presents the selection of the subset of ensemble members used for the forecast period and the resulting forecasts .
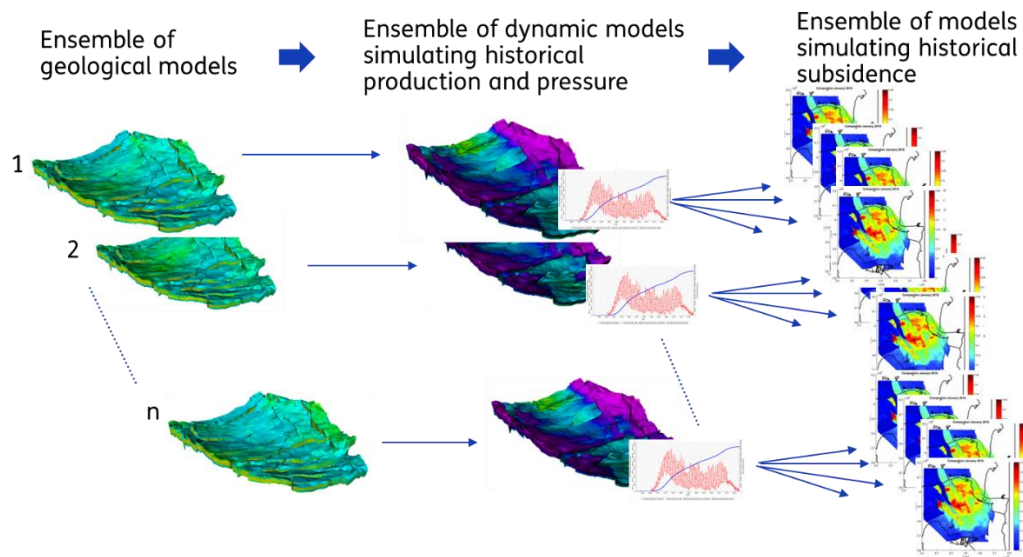
Figure 3-1 Illustration of the workflow used in this chapter. An ensemble of geological and dynamic reservoir simulation models is created, where each geological model is used to create one dynamic reservoir simulation model. The output of each dynamic model is subsequently used to create multiple simulations of compaction and subsidence.

3.2 Base reservoir model

3.2.1 Input

In this section the input used to build the base reservoir model is discussed. One of the realizations of the ensemble of geological models is used as base, which is the realization created with the following seeds (Petrel version 2022.7): 10004 for porosity, 6600 for permeability and 25114 for NtG. The porosity and permeability are illustrated in Figure 2-23 and Figure 2-26.

Capillary pressure and relative permeability
For the relative permeability and capillary pressure information, the curves from the NAM Eclipse 100 (by Schlumberger) dynamic reservoir model of the Groningen gas field have been used, but in a simplified way. NAM has made the Eclipse™ model publicly available in 2023[4] through https://public.yoda.uu.nl/geo/UU01/8JYW40.html together with a Petrel geo-model. The model is based on the existing MoReS model. The NAM Eclipse™ dynamic model has a separate set of relative permeability and capillary pressure curves for each porosity class (0.01 per class) for each formation. In this study, a single set of curves has been used, namely the curve for the average porosity of that formation:
- ROCLT and DC: average porosity is 0.08.
- ROSLU: average porosity is 0.15
- ROSLL + ROCLA: average porosity is 0.12

The curves that have been used are shown in Figure 3-2.

---

[4] Dynamic model (Eclipse version) to predict the formation pressure response to gas extraction in the Groningen gas field, The Netherlands, P. Tummala, NAM, 2023.

Two aspects of the curves are important to discuss: gas below free water level (GBFWL) and the permeability in the water zone.

In the Groningen area, gas below the free water level (GBFWL) is found in many wells. NAM included this GBFWL in the dynamic models, because it affects the pressure depletion and thus the compaction and subsidence (Zeeuw and Geurtsen, 2018b). The impact of the gas is two-fold: the permeability of the aquifer is reduced due to the presence of the gas and the effective compressibility of the aquifer is increased resulting in less pressure decline for the same flow to the gas field. The NAM Eclipse dynamic model has 2% GBFWL (i.e. gas saturation is 0.02 below FWL) in the Rotliegend formation. The same approach is followed in this study. In some of the logs in the small gas fields, also evidence was found of GBFWL, for example in ROD-102.. Therefore, in the entire model area, in the Ten Boer (ROCLT) and Upper Slochteren (ROSLU), 2% GBFWL was added for 30 m below the free water level (FWL). This is implemented in the model by assigning relative permeability curves that end at Sw=0.98. The curves from the NAM Eclipse model have been used at the average porosity of the formation (Figure 3-3). The gas is not mobile and capillary pressure is zero. It should be noted that the irreducible water saturation (at which Krw=0.2 in Figure 3-2) has changed as well. This does not affect the results, because only the end-point is used of these curves.

From information from logs and history matching in the Groningen gas field, it is known that the permeability in the water zone is generally lower than in the gas zone. This is possibly caused by continuing diagenesis in the areas where water is present compared to gas-filled zones. Because most logs used for the property modelling are from the gas zone, this is not well represented in the simulated reservoir properties in the water zone (Section 2.5). Here the approach followed by NAM is used, which is to reduce the endpoint of the relative permeability curve of water to 0.2 (Figure 3-2). This is essentially a multiplier on the permeability in the water zone. The benefit of this approach is that the multiplier is applied in one go to all relevant areas (i.e. all areas with high water saturation), also in the capillary fringe, which is the transition zone between water and gas zones.
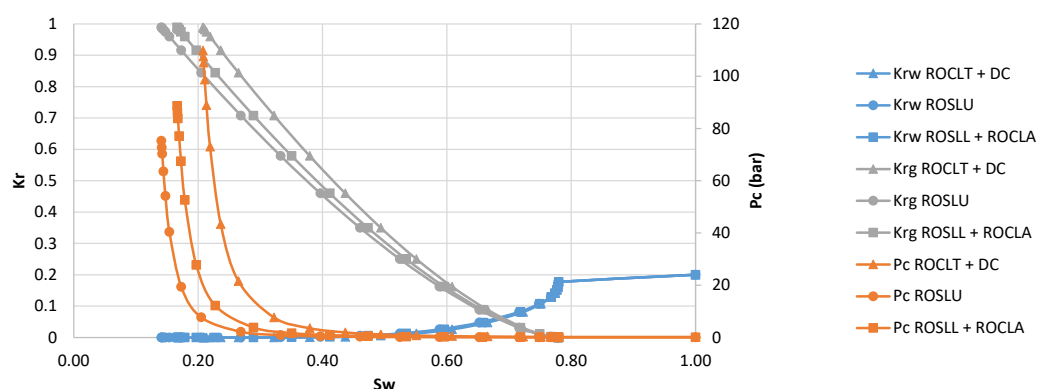

Figure 3-2 Relative permeability and capillary pressure curves used in the dynamic reservoir model.
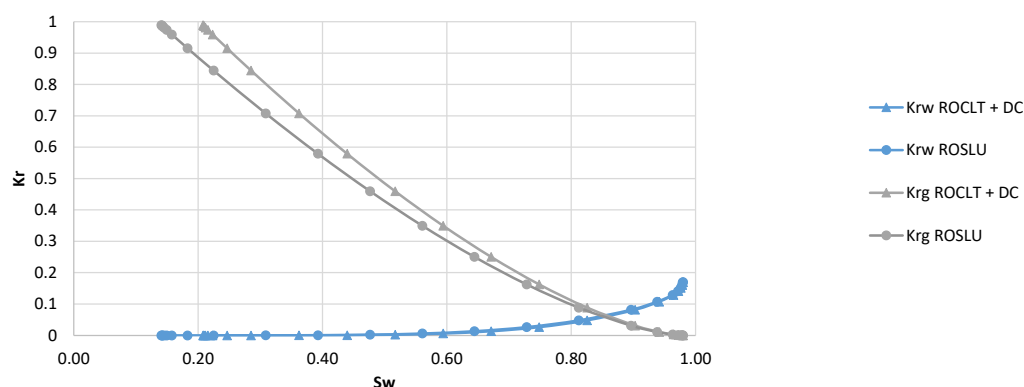
Figure 3-3 Relative permeability used in the dynamic reservoir model for the zone with GBFWL of 30 m thickness below the FWL.

Gas composition
Public information on gas composition was downloaded from nlog.nl (http://www.nlog.nl/sites/default/files/thematische_data/nlog_gascompos.xlsx). Information is available for the following wells in the area of interest: ROD-101, ROD-101-S2, ROD-102, PSP-01, BRA-01 (see Figure 2-3 for well locations). Each of the small gas fields has a different gas composition, but the available data show that Roden, Boerakker and Pasop (see Figure 2-2 for the locations of the small gas fields) have similar composition with the amount of methane in the range of 80.5 to 82.5 mol-% and an amount of N_2 of around 11 mol-%. Therefore, it was decided to use the gas composition of the Roden field for the Boerakker and Pasop fields as well. For Faan no data is available, but since it is close to Boerakker and Pasop, also the gas composition of the Roden field was used.

For Vries-North, no wells are listed in the information on nlog.nl, however, in Vries-Central, just south of Vries-North, information is given for well VRS-201. This composition has a higher methane content than the small gas fields to the north (Roden, Boerakker and Pasop) and a relatively small amount of nitrogen. The composition for well VRS-201 is used for the gas properties of Vries-North.

The composition of the Groningen gas has 86 mol-% CH_4 and 14 mol-% N_2. This is also used for Bedum, although this field has less N_2 (4 to 5 mol-%). This simplification is allowed because both fields are implemented as pressure constraints. The description of the implementation as pressure constraints is discussed later in this section under "*boundary conditions*".

The gas compositions used are given in Appendix B (Table B-1). The properties for these compositions are derived using the correlations from (Dranchuk and Abou-Kassem, 1975) for the Z-factor and (Carr et al., 1954) for gas viscosity which are the default correlations as used by Petrel v2022.7.

Water composition
For the water composition a single value for the salinity for the entire model area is used: 280.000 ppm NaCl. Molen et al. (2020) used a value of 200,000 ppm for the Roden field, but Burkitov et al (2016) used 280,000 for the Groningen field. The latter is assumed to be more accurate and more representative of the aquifer and is used for the entire model area. The viscosity and density at 100°C were used based on the Petrel default correlations: (Spivey and McCain, 2003) for density and (Kestin et al., 1981) for viscosity. The viscosity is 0.63 cP at reservoir conditions. The brine density at Eclipse standard conditions is 1215.9 kg/m³ and at

reservoir conditions (100°C and 345 bar) it is 1179 kg/m³. The compressibility is 2.8E-5 1/bar. All values are close to the values used in the NAM Eclipse model and listed in (Burkitov et al., 2016).

Pore volume compressibility
The pore volume compressibility is based on the values used for the NAM Groningen model and listed in (Burkitov et al. 2016) and depends on porosity. The same basic approach was used in later versions of the NAM model (Landman, 2023), enhanced with a multiplier estimated during the history match. The corrections based on history matching on the Groningen side of the model have not been applied. For each of the main formations (ROCLT, ROSLU etc) of model, the average porosity was determined and the pore volume compressibility estimated from Figure 42 of Burkitov et al., 2016. Because the variability was quite small for the range in average porosity from 0.08 to 0.15, a single values of 2.5E-5 1/bar has been used. Please note that this is not the value used in the modelling of compaction and subsidence in Section 3.4, where different compaction models are used (see Section 3.4.2). The impact of the pore volume compressibility on the flow simulation is small which justifies the use of a single, averaged value of compressibility.

Initial conditions
It is assumed that the entire area is in pressure communication and that the initial pressure is consistent throughout the model area. Initial water pressure is taken as 344 bar at 3000 m depth, based on the pressure in the Groningen and Roden fields. For input in the simulator the pressure is recalculated to the depth of the Free Water Level (FWL) using a density of 1178 kg/m³. The values used are listed in Appendix B.

The FWL values for the small gas fields are based on the most recent field review document of the respective fields as available on NLOG. The FWL values for the Groningen model are based on the values from Groningen dynamic model update V7 (Landman, 2023). The values for the Bedum field are based on (Geurtsen et al., 2020). See Appendix B for the values used.

The model simulations do not include thermal modelling and therefore a constant reservoir temperature of 100°C is used throughout the model, which is the estimated temperature at ~3 km depth. This mainly affects the fluid properties.

Boundary conditions
The position of the boundaries of the model was discussed in paragraph 2.3. Most boundaries can be implemented as no-flow boundaries, because they are positioned at large bounding faults, except on the east side. On the east side of the model is the Groningen gas field. Only part of the gas field is incorporated in the model, to keep the size of the model limited and allow more detail in the aquifer and small gas fields. Since the pressure in the part of the Groningen gas field that is incorporated in the model is influenced by production outside of the model, the pressure in the east part of the model will be imposed. This is done by running the production wells in this area on a pressure constraint. This means that the bottom hole pressure in the well is set and that the amount of reservoir fluids (gas and/or water) that can be produced is simulated based on the bottom hole pressure.

For the bottom hole pressure (BHP) constraint of the production wells on the east side of the model (see Figure 2-3), the simulated bottom hole pressure from the NAM Groningen MoReS dynamic model is used. These have been made available with the NAM Groningen Eclipse model. In this case the output from the MoReS model rather than the Eclipse model was used, because the Eclipse model deviates from the MoReS model in the western periphery (TNO, 2024) and the MoReS model fits the observations better. The match of the MoReS model is

within a few bar for most wells (Landman, 2023), which is sufficiently accurate for the purpose of this model. Using pressure observations rather than model output is not possible, because the observations do not cover the entire area and time period.

Wells and dynamic data
For all the wells in the small gas fields on the west side of the model area (Vries-North, Roden, Pasop, Boerakker and Faan (Figure 2-2), the following data was collected:
- Well path and completions
- Well gas and water production rates
- Static pressure measurements

Most information is available on NLOG.nl. The completions were provided by NAM, as was the gas and water production of wells prior to 2003, which are not available on NLOG. The static pressure measurements are based on public information available online: https://nam-feitenencijfers.data-app.nl/embed/component/?id=gasdruk#tab-overig, enhanced by the information in (TNO, 2023a) and in public field review documents.

The simulation model is run with annual time steps. This is sufficiently accurate for the relatively slow response of the aquifer. It does mean however that detailed pressure behaviour in the small gas fields is not represented. Please note that the static pressure measurements are approximated by the pressure in the grid block containing the top perforation. Because the model is run with annual time steps, it is not possible to simulate the reservoir pressure during a shutin explicitly. The gas production for the small gas fields is available on a monthly basis in Nm^3. For the simulation they are recalculated to sm^3 and aggregated to annual time steps.

For the wells on the east side of the model, the well paths were available in the NAM Groningen geological model that was used as input for the geological models in this project. The completions were imported from the NAM Groningen Eclipse model. As mentioned during the discussion of the boundary conditions, the BHP constraints for the production wells were taken from the NAM Groningen MoReS model. For each well on the east side, the simulated BHP is available at daily time steps for the entire model period. For the Eemskanaal-cluster (EKL, Figure 2-3) not all wells are incorporated in the model, because the interference between the wells caused numerical instability in the model. The observation wells HRS-2A, MLA-1 and SAU-1 are also included in the model. More information on these wells is provided in Section 3.2.2.6.

For all the wells in the model, the completions could not always be implemented at the depth at which they are in reality. Because the grid is relatively coarse, perforations that are placed in a (thin) layer with high permeability in reality, will be in a thicker, lower permeability layer in the model. In this case, implementing the actual perforated thickness results in underestimation of the productivity. In these cases, the length of the perforated intervals are adjusted to fit the coarser grid.

3.2.2 Tuning of the base model

To be able to tune the base model to the dynamic data, part of the data is used as input and part as observations. All the wells in the small gas fields are run on gas production targets. The static pressure measurements and, to a lesser extent, the water production are used as

observations. Because of the relative coarseness of the models compared to the size of the small gas fields, the water inflow measurements are difficult to reproduce. In particular the vertical resolution is a limiting factor, because it is chosen relatively coarse for simulation of a very large aquifer, rather than for simulation of small gas fields, where vertical details are more relevant.

The estimates of the GIIP (Gas Initially In Place) were mostly based on the field review reports ("winningsplannen"), which are available on nlog.nl for all Dutch gas fields.

3.2.2.1 Roden

The Roden gas field is the most important of the small gas fields in the context of this project: the gas field is one of the larger gas fields and has a well connected aquifer, which extends to the Groningen gas field (around Harkstede)(Figure 3-4). Also important is the fact that in the Roden south block (which is produced via well ROD-201), static pressure measurements were continued almost 30 years after production had been stopped (Figure 3-5). During this period, a significant pressure increase was observed which was attributed to aquifer inflow (Molen et al., 2020). Also in the north block considerable pressure increase was observed after production stop.

The Roden field has three wells which were producing from 1976 to 2003 (Figure 3-5). The Slochteren Formation has good reservoir properties and the connected aquifer has very few faults. The pressure has increased in the south block by around 100 bar from the time of the shutin of the well ROD-201 in 1985 to 2000. In the north block the pressure recovery after shutin is at least 88 bar. The prior estimates of the GIIP was 8 NBCM (8.5 sBCM) for the north block and 1.5 NBCM (1.6 sBCM) for the south block based on (Molen et al. 2020) and the field review of 2003.

Because of challenges in matching the observed pressure recovery, a mass balance approach was employed to estimate the required aquifer size. This estimation based on the equilibrated pressure (i.e. the pressure after the gas field and aquifer are in equilibrium again after production), the estimated GIIP and gas production. For the equilibrated pressure, the final pressure was assumed. For the south block, this resulted in an estimated size of the aquifer twice the size of the aquifer in the reservoir model. Since the uncertainty in the size of the aquifer in the reservoir model was not that large, probably the GIIP estimate is inaccurate. For the north block, the aquifer size appeared to be approximately correct if GIIP was somewhat lower than estimated.

Much better solutions could be simulated by assuming a higher GIIP in place for the south block (consistent with the static model), slightly lower GIIP for the north block (also consistent with the static (geological) model) and that part of the gas in both blocks is available as so-called 'slow gas'. This is gas that is for example located behind fault with low transmissivity or in low permeability deposits. It was investigated whether gas below FWL or gas from ROCLT (Ten Boer Member) could be responsible for this behaviour, however neither of these options had sufficient effect. After re-examining the seismic data, it was concluded that there are several locations in which low-offset faults could be present in the gas fields. Implementing these as semi-permeable baffles improved the pressure behaviour considerably. The position of the baffles is shown in Appendix B.

From the pressure behaviour it is clear that pressure communication between the north and south block is limited. This is consistent with the NAM Groningen dynamic models in which the

large SW-NE oriented faults are mostly assumed to have low permeability (e.g. Zeeuw and Geurtsen, 2019).

The results of the base model in which the above changes are implemented are plotted in Figure 3-6 and Figure 3-7. The estimated GIIP and pore volume multiplier are given in the summary table of the base model (Table 3-1).
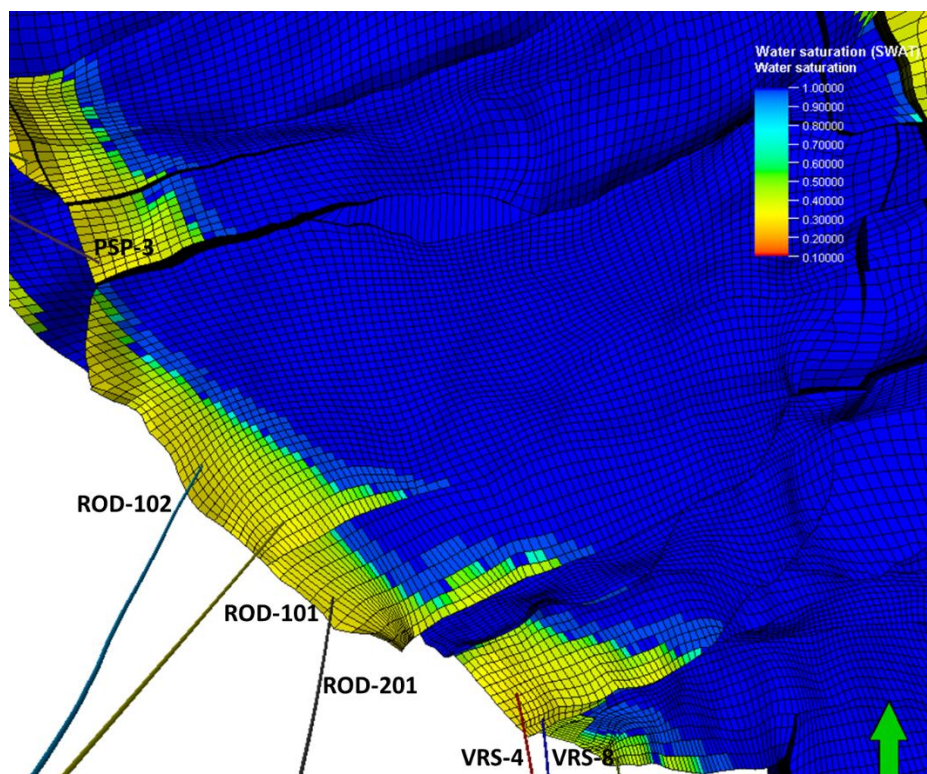

Figure 3-4 Top of the Roden gas field showing water saturation and the three wells ROD-102 and ROD-101 in Roden North and ROD-201 in Roden South. An overview of the initial water saturation in the entire model is presented in Figure 3-15.
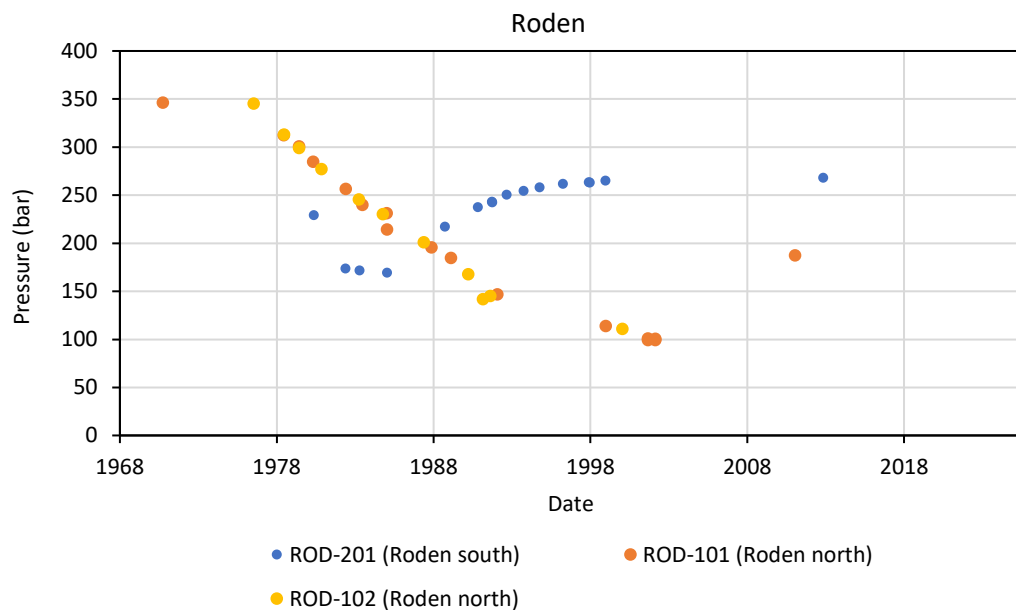
Figure 3-5 Observed static pressure in the Roden field. Roden north is produced via wells ROD-101 and ROD-102 and Roden south via well ROD-201.
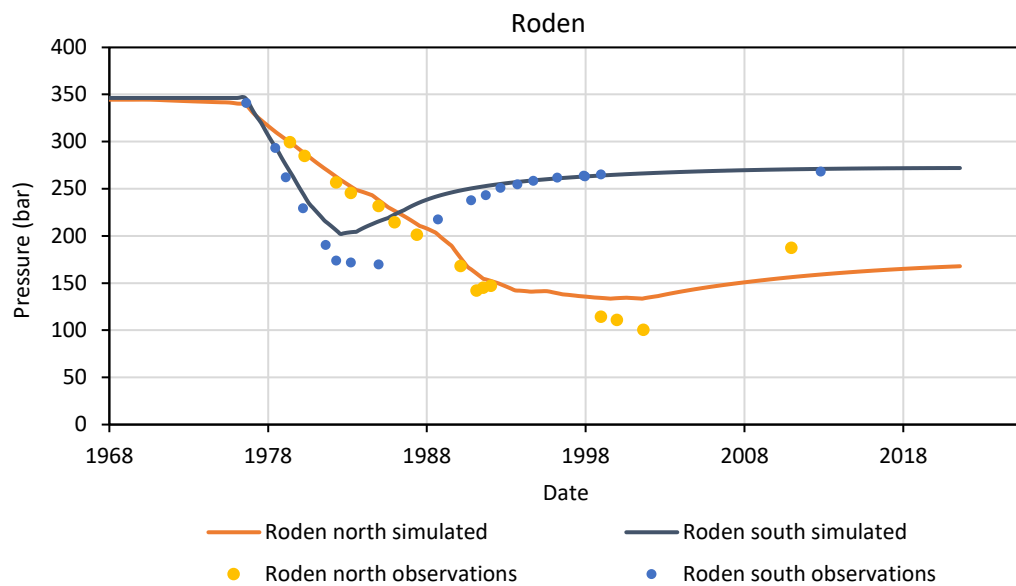
Figure 3-6 Base model results for the Roden gas field showing the static pressure observations (observations), and the simulated reservoir pressure in the grid blocks containing the wells (simulated).
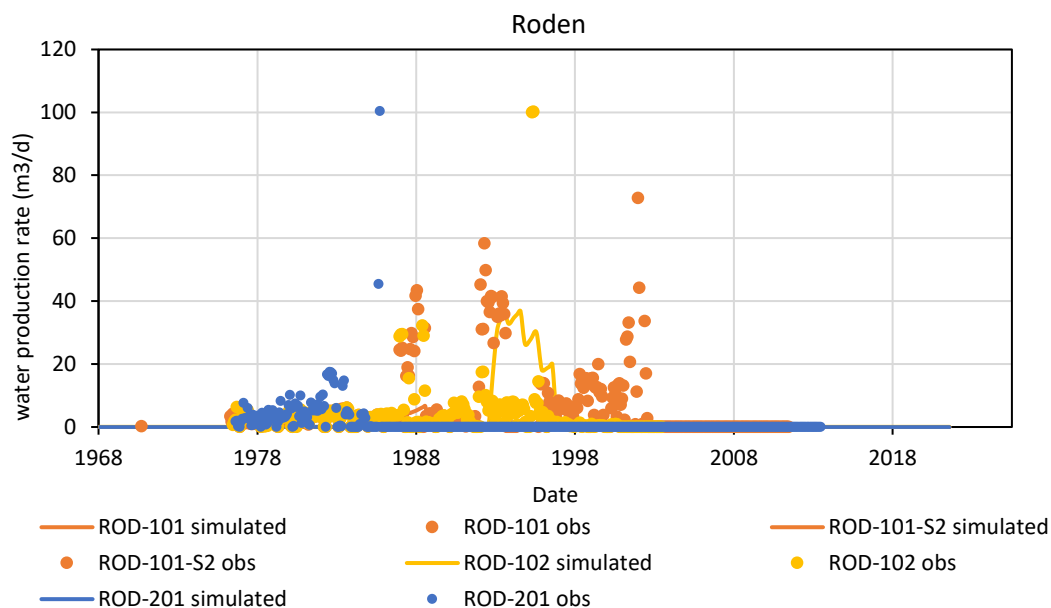
Figure 3-7 Base model results for the Roden gas field showing the water production observations and simulations per well. ROD-101 was replaced in 1989 by the sidetrack ROD-101-S2.

3.2.2.2 Vries North

The gas field Vries North is produced from three wells: VRS-4 (VRS-401 on nlog.nl), VRS-7 (VRS-402 on nlog.nl) and VRS-8 (VRS-403 on nlog.nl) and has lower productivity than the Roden field. The initial model had far too much water production and too little drawdown, indicative of an overestimation of the size of the connected aquifer. A smaller aquifer was also shown in NAM, 2021 in the model used for long term subsidence forecasts which includes the connected aquifers in a coarse way. NAM, 2021 illustrates (in their Figure 3) that the fault density is much higher in the Vries aquifer than in the Roden aquifer which might explain the lower connectivity since many faults in this area have reduced transmissivity. Because it was not feasible to include all faults, a number of baffles was implemented in the same way as in the Roden field to reduce the connectivity in the aquifer. The baffles are show in Figure B-14 in Appendix B. The position of the baffles was based on indications of the presence of faults from the seismic data and the structure map by NAM.

The static GIIP was lower than the GIIP estimate from NAM and was adjusted using a pore volume multiplier. The estimated GIIP and pore volume multiplier are given in the summary table of the base model (Table 3-1).

The results of the base model are shown in Figure 3-8 (pressure) and Figure 3-9 (water production). VRS-4 and VRS-7 are located in the same fault block and the static pressure measurements were only reported for the fault block and not for each well separately.
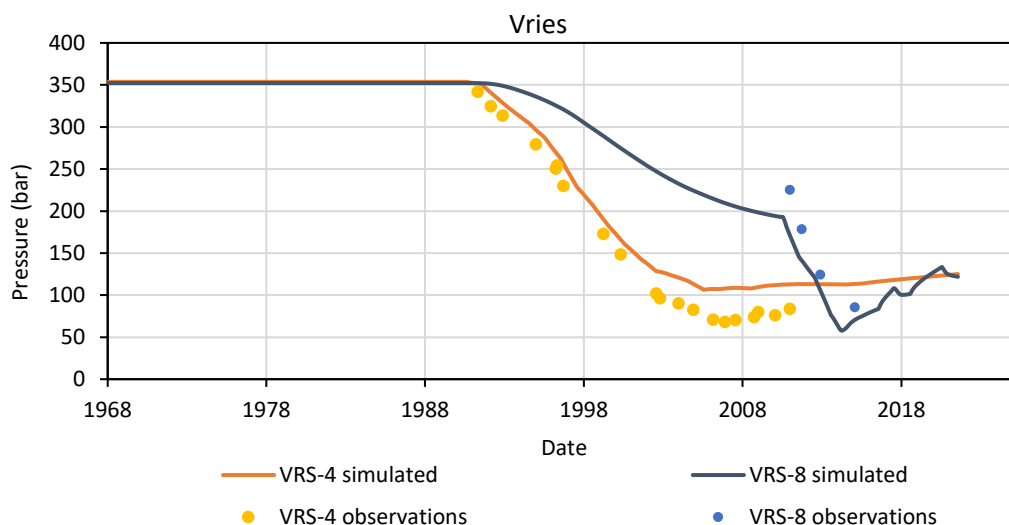
Figure 3-8 Base model results for Vries North showing the static pressure observations (observations), and the simulated reservoir pressure in the grid blocks containing the wells (simulated). VRS-7 is located in the same fault block as VRS-7.
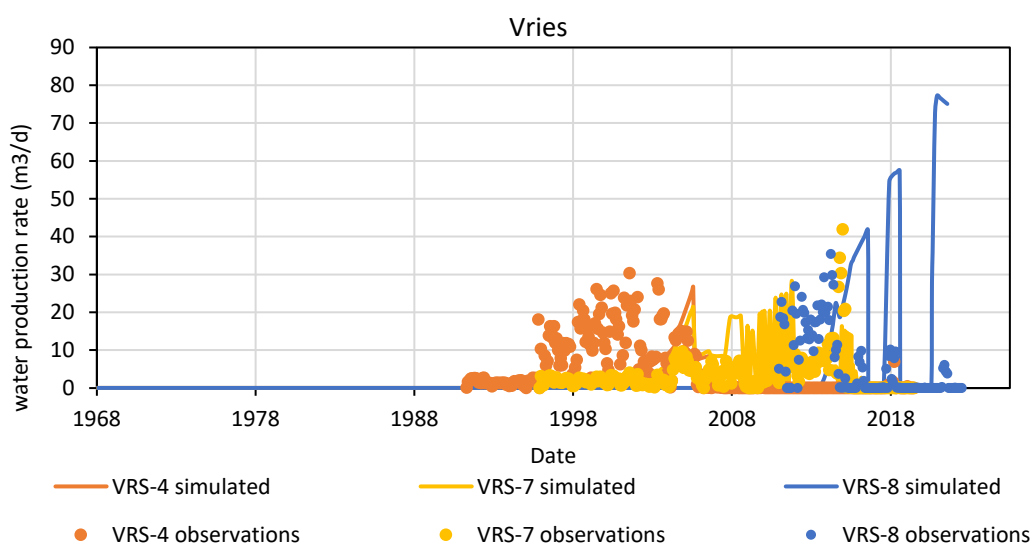

Figure 3-9 Base model results for Vries Noord showing simulated and observed water production for all three wells.

3.2.2.3 Pasop

Pasop is a small gas field just to the north of Roden. It is produced from three wells (PSP-01, PSP-02-S2 and PSP-03. The field has good productivity like Roden, but is highly compartmentalised with a ~400 m wide, high block in which the wells are located. The wells are produced intermittently to avoid formation water production. The amount of gas initially in place is too large, which could be related to the fact that not all static GIIP is accessible from the wells due to the highly compartmentalised nature of the field. It could also be related to an inaccurate representation of the details of the faults and the top of the reservoir due to

the relatively coarse grid. The GIIP is reduced via a pore volume multiplier. In addition the transmissivity of the faults is adjusted to better predict the pressure drawdown. Based on the NAM structural map, two faults were missing which were added as baffles (Figure B-14 in 0). The pressure results of the base model are shown in Figure 3-10. In the model no water production rate is simulated. Observed water production rates are substantial for PSP-01 (50 to 200 sm³/d) but only for a short period in 2006 and 2007. The model was too coarse to reproduce this.
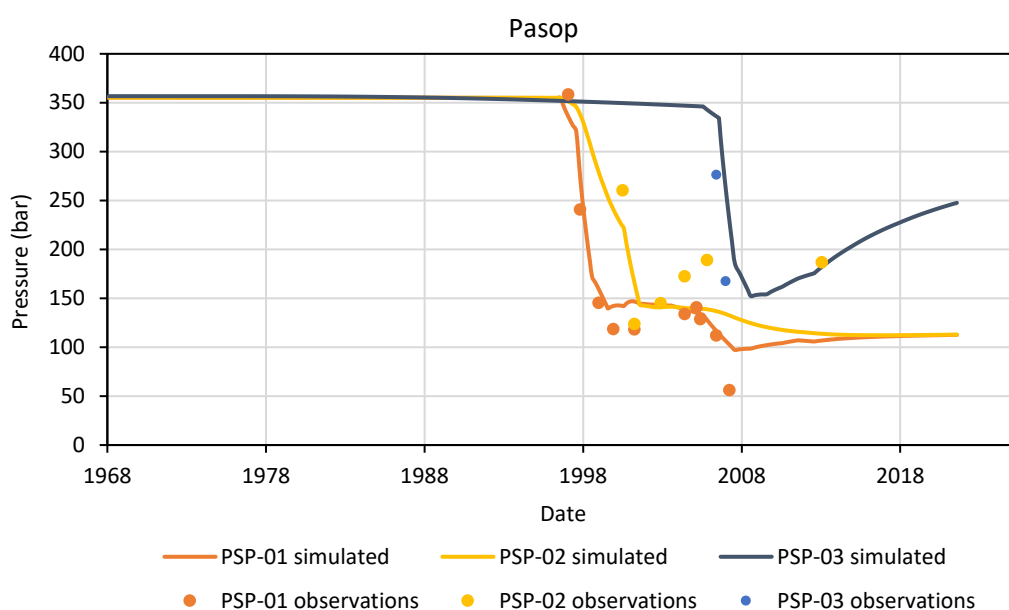

Figure 3-10 Base model results for Pasop showing the static pressure observations (observations), and the simulated reservoir pressure in the grid blocks containing the wells (simulated).

3.2.2.4 Faan

The Faan gas field is to the north of the Pasop field and produced via wells FAN-01 and FAN-02 from 2008. The field is highly compartmentalized and consists of at least three compartments. The FAN-01 well is located in the Faan main block, FAN-02 in the west block. The Faan main block is connected to the SW aquifer. In the model developed in this project, the internal faults are missing. The GIIP in the static model is considerably larger than the dynamically estimated GIIP and the pressure decline in the wells was thus predicted very poorly. The model was matched by adding baffles roughly at the locations of the missing faults and reducing the size of gas zone via a pore volume multiplier. The connection to the SW aquifer appears to be overestimated in the model and has been reduced by means of a baffle around the contact. The results for the pressure are shown in Figure 3-11. In the model no water production rate is simulated. Observed water production rates were small (max 30 sm³/d for one date).
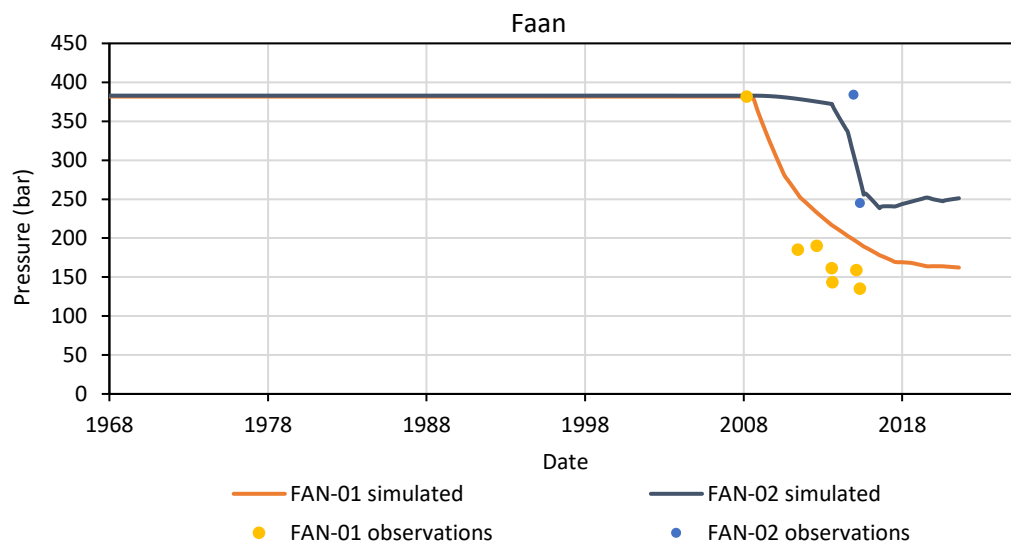
Figure 3-11 Base model results for Faan showing the static pressure observations (observations), and the simulated reservoir pressure in the grid blocks containing the wells (simulated).

3.2.2.5 Boerakker

The Boerakker gas field is located on the far north-westerly tip of the model and hardly influences the pressure in the SW aquifer, since it is not connected to it. The main reason to include it is the prediction of the subsidence: the pressure drawdown at Boerakker creates a subsidence bowl that influences the Pasop and Roden fields. The field is produced via two wells: BRA-02 and BRA-03. The static GIIP is considerably smaller than the NAM estimate (Table 3-1), which is corrected using a pore volume (PV) multiplier on the compartment containing BRA-2 and a separate PV multiplier on the block containing BRA-3. The PV multiplier on the block containing BRA-3 is 0.55 and is not varied in the ensemble. The results are shown in Figure 3-12.
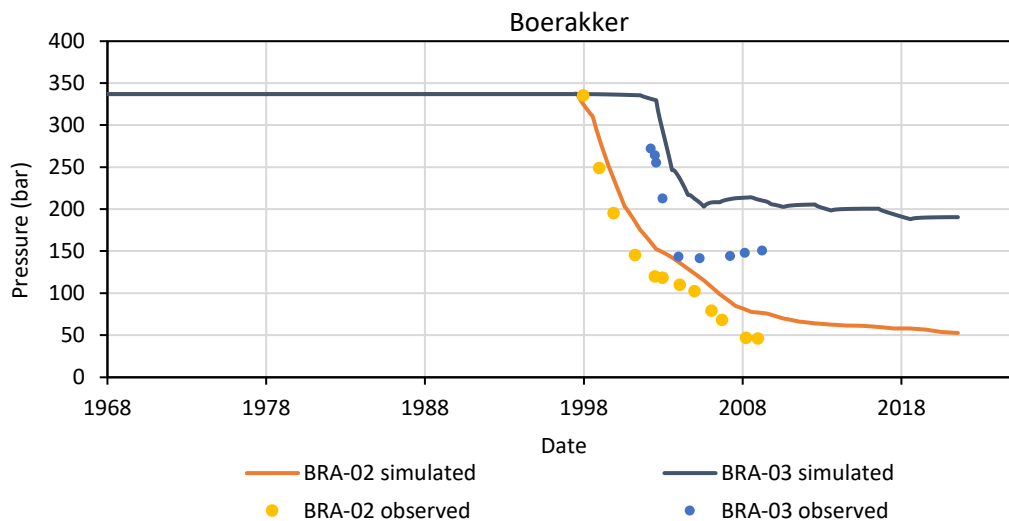
Figure 3-12 Base model results for Boerakker showing the static pressure observations (observations), and the simulated reservoir pressure in the grid blocks containing the wells (simulated).

3.2.2.6 Groningen side

On the east side of the model are the Groningen and Bedum fields in which the wells are run on pressure constraint, because the pressure is not only determined by production from the wells incorporated in the model created here, but also from outside the model area as mentioned in paragraph 2.3. Only the pressure measurements in the following wells can be used for tuning: HRS-2A, MLA-1 and SAU-1, because they are further from the boundary (Figure 2-3). The NAM Groningen MoReS model was matched using additional types of, such as PNL (Pulsed Neutron Lifetime) data which give information on the water level rise. Most of this is in the main Groningen area, but PNL data are available in the Harkstede block, which show a water level rise. This information has only been included in a qualitative way by checking if the water level rises in the base model.

The most important parameters used for tuning the model are fault transmissivity multipliers. The initial settings for the fault transmissivity multipliers are discussed in Section 2.5. These settings resulted in a slight overestimation of the pressure drawdown in the Harkstede block (well HRS-2A) prior to 2006 when well EKL-13 starts producing. A small reduction in connectivity to the EKL cluster and increased connectivity to the aquifer were sufficient to get a good match in HRS-2A (Figure 3-13). The fast pressure recovery of the NAM model after the stop of the production in early 2014, was not reproduced in the reservoir model developed in this study.

Pressure drawdown at well MLA-1 was underestimated with the initial settings. This was attributed to a lack of connectivity to the region with well HGZ-1 which depletes as a result from production in the Groningen field. An increase in the relevant fault multipliers improved the match sufficiently (Figure 3-14). Well SAU-1 was matched sufficiently well with the initial settings (367 bar compared to the observed 372 bar).

It should be noted that the south-west periphery of the Groningen field is the most complicated area of the Groningen field (Zeeuw and Geurtsen, 2019) and that a full

representation of all the behaviour is not feasible in this setting. Also NAM had difficulty matching this area. For example to achieve a history match in KHM-1 (Figure 2-3, between the EKL-cluster and HGZ-1), Landman (2023) was forced to implement time-varying fault multipliers to achieve a satisfactory history match.
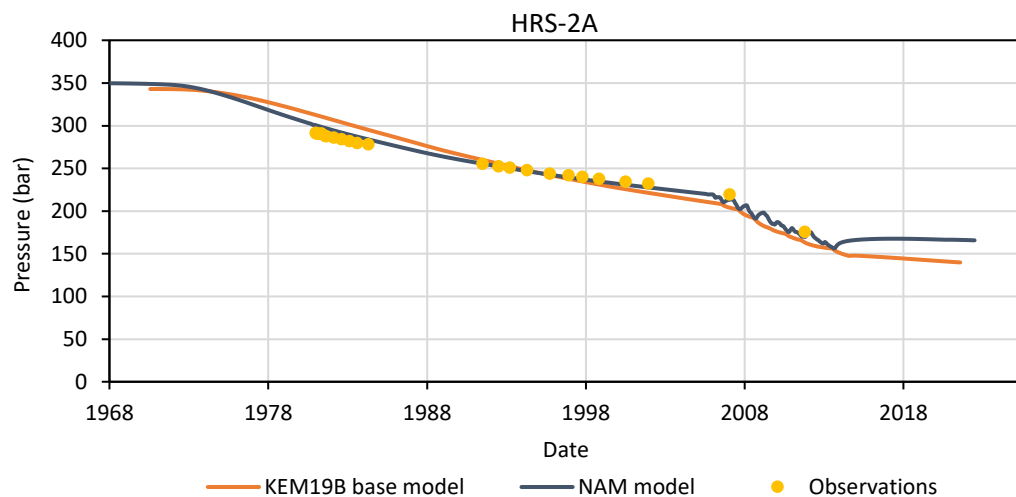

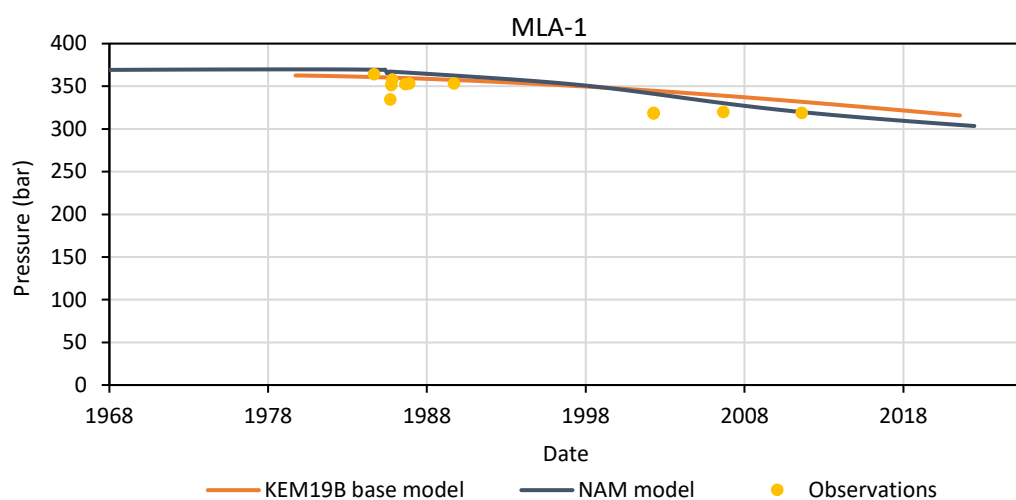Figure 3-13 Pressure at HRS-2A from the base model, from the NAM Mores model and observations.

Figure 3-14 Pressure at MLA-1 from the base model, from the NAM Mores model and observations.

3.2.3 Results base model

Table 3-1 gives an overview of the GIIP of the static base model prior to application of the pore volume multiplier, the GIIP of the dynamic base model (incl. gas BFWL which is ~5% for most fields) and estimates by NAM based on field reviews. The value listed in the table is not the mean of the ensemble, but the value of the single realization selected as base model. The

ensemble results are presented in the next section. Figure 3-16 shows the simulated pressure in the base model at the end of the historical period (1 Jan 2022 in this study). Clearly visible in blue is the depleted aquifer that is connected to Roden. The other aquifers are less depleted.

Table 3-1 Estimated GIIP values (BCM in sm^3) for the base model compared to the estimates derived from the field reviews by NAM

	Static GIIP	Pore volume multiplier	dynamic GIIIP (incl GBFWL)	NAM GIIP
Vries-Noord	3.1	1.4	4.6	4.8
Roden-Noord	7.3	1.0	7.7	8.5**
Roden-Zuid	3.2	1.17	3.9	1.6
Boerakker	2.6	1.81*	3.9	4.8
Pasop	6.4	0.61	4.1	3.9
Faan	3.7	0.3	0.9	1.4
Noordlaren	0.3	0.83	0.2	0.2

* For the main compartment containing BRA-1 and BRA-2, BRA-3 has multiplier 0.55.
** For the Roden field, NAM estimates are available for the entire field only. The division is based on (Molen et al., 2020).
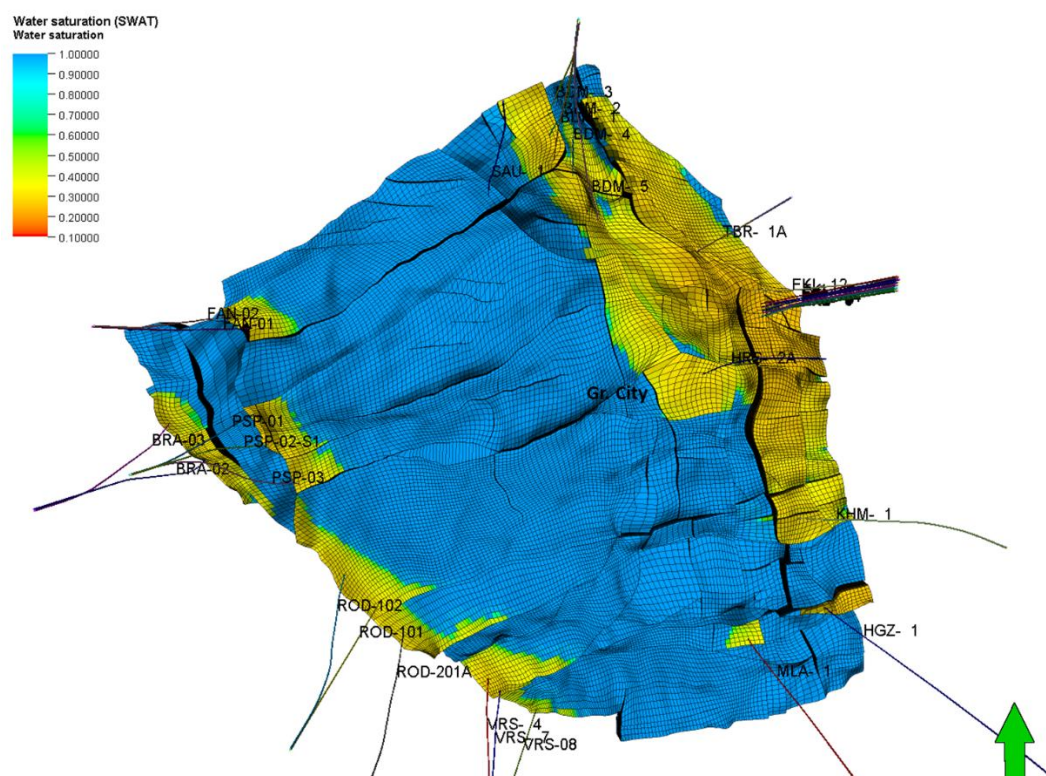

Figure 3-15 Initial water saturation distribution in the model area of the base model. Green arrow indicates north.
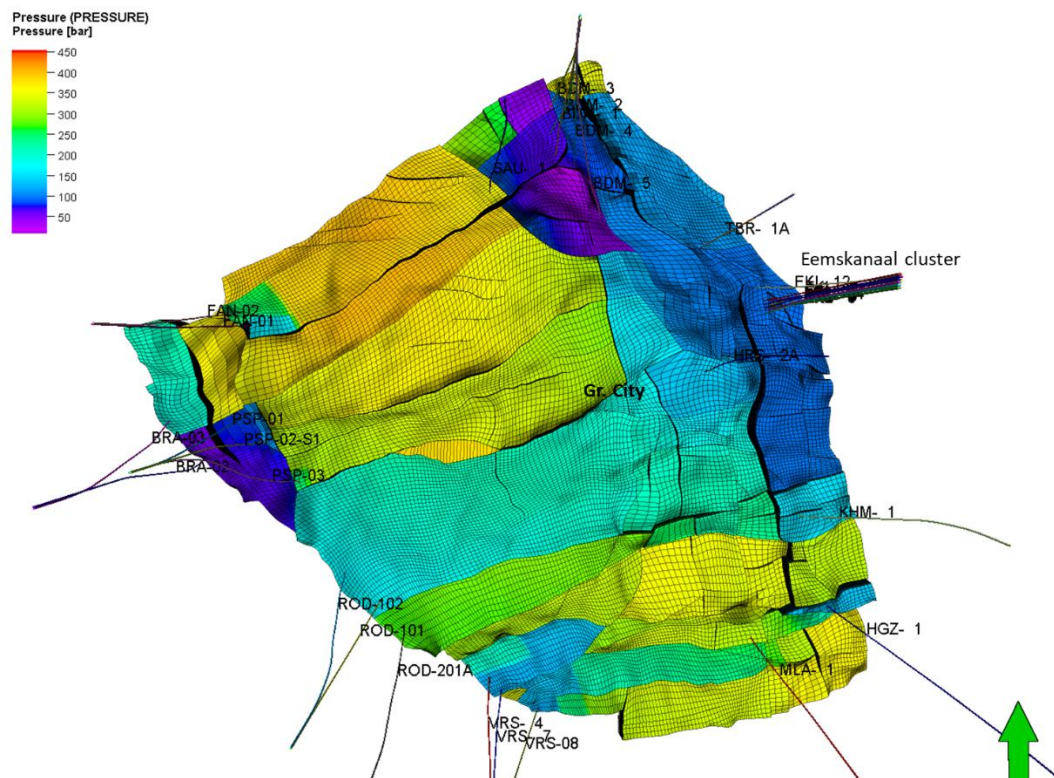
Figure 3-16 Top view of the pressure at the end of the history period (1 January 2022) for the base model. Green arrow indicates north.

3.3 Ensemble of reservoir models

3.3.1 Ensemble input settings

The following properties are varied to create the ensemble of 100 reservoir model realizations:

- NtG, porosity and permeability via Gaussian simulation (discussed in section 2.5)
- Vertical permeability as a fraction of the horizontal permeability
- Vertical permeability of the Ameland member (ROCLA)
- Multiplier on the permeability between the Slochteren and the Carboniferous formations following (Zeeuw and Geurtsen, 2018b): layer 23
- Transmissivity of the baffles to horizontal flow from the base model (faults implemented as baffles in the small gas fields)
- Fault transmissivity

Although the main sources of uncertainty have been included in the ensemble, the set is not complete. Sources of uncertainty that have not been included are for example structural uncertainty and the relative permeability. In part, such uncertainties have not been included because they are more difficult to implement, but mainly because the impact is similar to uncertainty that has been included, like structural uncertainty and porosity which both affect the GIIP.

Adjustment of the gas-initially-in-place (GIIP) for the ensemble
For the base model, pore volume multipliers per small gas field were implemented to get an acceptable GIIP and history match in the wells. Due to the variations in NtG and porosity, the GIIP is different for each member (model realization) of the ensemble. Due to these differences, application of the same pore volume multipliers as in the base model to all ensemble members does not lead to an acceptable history match for the ensemble. An alternative would be to apply a pore volume multiplier to each ensemble member that results in the same GIIP-values for all ensemble members. This is not a good alternative, because it underestimated the uncertainty. Therefore, to preserve variation in the ensemble but have the correct range, the pore volume multipliers are calculated for each ensemble member separately. The multipliers are calculated in such a way that the range from the ensemble is normalised to the expected GIIP range based on 'observations'. The 'observations' of the GIIPs are values estimated by NAM and during the tuning of the base model. Thus if a member has a GIIP of for example 10% above the minimum of the initial range, it will be adjusted to a value 10% above the minimum of the 'observed' range.

The multipliers are calculated based on the static GIIP values calculated using the porosity and NtG from the ensemble and the average gas formation volume factor from the base model. The procedure is illustrated in Figure 3-17. $GIIP_{ens}$ refers to the values from the static ensemble prior to the adjustment. $GIIP_{obs}$ refers to the range in GIIP values to which the GIIPs are corrected and which are based on the observations. Table 3-2 lists the values for the GIIPs for the small fields.
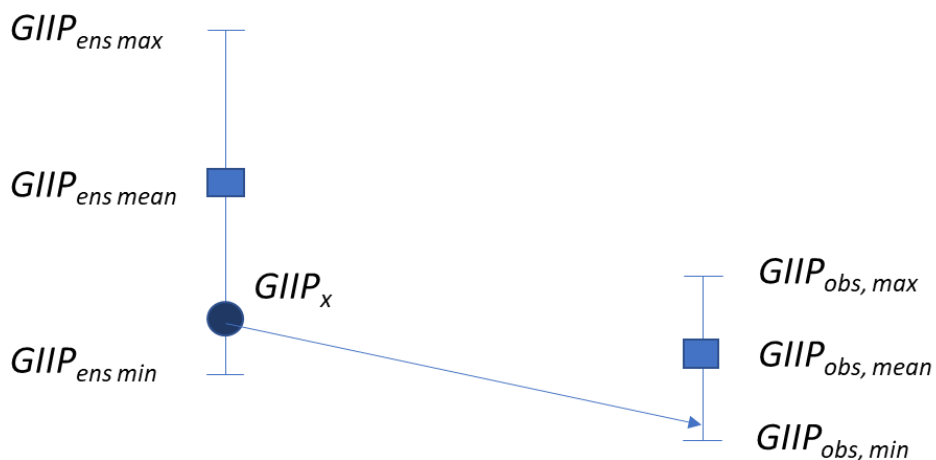

Figure 3-17 Illustration of the procedure for the adjustment of the GIIP of each of the small gas fields in the ensemble while preserving variability for ensemble member x.

Thus for each pore volume multiplier in the model, the following equation (eq. 1) is used:

$$PVMULT_x = \frac{GIIP_{obs,\ mean} + \left(\frac{(GIIP_x - GIIP_{ens,\ mean})}{GIIP_{ens,\ range}} GIIP_{obs,range}\right)}{GIIP_x} \qquad \text{eq. 1}$$

Where:

$PVMULT$: pore volume multiplier
GIIP   : Gas Initially In Place

Subscripts:
x : small gas field or sector identifier
y : ensemble member number
ens   : the static ensemble prior to the application of the multiplier
obs   : values to which the GIIPs are corrected (based on observations)
mean   : arithmetic average
range   : maximum value – minimum value

For Vries, Roden Boerakker and Noordlaren , the static GIIP estimate is close to the dynamic GIIP without GBFWL. For Faan and Boerakker, the dynamic GIIP of the base model is lower, because some changes were implemented in the tuning phase that are not in the static model.

Table 3-2 Static GIIP (sBCM) values of the ensemble prior to the adjustment using multipliers (GIIP$_{ens}$ in Figure 3-17) and which were used for determining the multipliers for the ensemble (GIIP$_{obs}$ in Figure 3-17). These GIIP values don't include the GBFWL and the manual changes to the dynamic model in the tuning phase for Boerakker and Faan.

	Static GIIP of the ensemble			Range ('obs') used to calculate the pore volume multiplier		
	min	mean	max	min	mean	max
Vries-Noord	2.8	3.1	3.6	4.1	4.3	4.7
Roden-Noord	6.7	7.5	8.3	7.1	7.4	7.9
Roden-Zuid	2.9	3.2	3.4	3.2	3.7	4.2
Boerakker	2.6	2.9	3.3	4.4	4.8	5.1
Pasop	5.6	6.4	7.0	3.4	3.9	4.4
Faan	3.6	3.9	4.3	1.0	1.1	1.3
Noordlaren	0.2	0.3	0.3	0.1	0.2	0.3

Sampling for the ensemble
The other parameters that are varied for the ensemble (except for the fault transmissivity multipliers, see below) are sampled from a uniform distribution with ranges as given in Table 3-3. The values used in the base model are added for comparison.

Table 3-3 Minimum and maximum of the range of the uniform distribution from which the parameters are sampled.

	Base model	min	max
Anisotropy (kh/kv)	10	5	15
Multiplier on kv ROCLA	0.01	0.002	0.032
Multiplier on kv layer 23	0.001	0.0002	0.0032
Baffles set 1	0.01	0.005	0.02
Baffles set 2	0.001	0.0005	0.002
Baffles set 3	0.0002	0.0001	0.0003

Fault transmissivity multipliers
The fault transmissivity multipliers have also been varied for the ensemble. The workflow is however different from the other parameters that have been varied. Like the other parameters, a value has been set in the base model for each multiplier. However for the variation in the ensemble, the faults have first been grouped in 'logical' geographical groups, like for example the group of faults that controls the flow between the Eemskanaal cluster and the Harkstede block. The division of the faults over the groups can be found in Appendix B. Group 0 is not varied in the ensemble. For all other groups of faults a random value is sampled from a uniform distribution with ranges as specified in Table B-5 in 0. The random value is raised to the power 10 before multiplying with the fault multiplier from the base model:

$$Fault\_mult_x = fault\_mult\_base * 10^{random\ value\ of\ the\ group}$$
eq. 2

Simulation
The ensemble and base model have been developed in Petrel and Eclipse (by Schlumberger NV (SLB.com)). However for simulation of the ensemble, open source simulator OPM flow (https://opm-project.org/) has been used. For the base model, it was checked that the results of OPM flow are in line with those from Eclipse.

3.3.2 Ensemble results

Table 3-4 shows the results of the dynamic GIIP of the ensemble for the small gas fields. The dynamic GIIP is calculated in the dynamic model and deviates from the static GIIP because the gas formation volume per grid cell is used instead of the average and the gas below free water level is included. Figure 3-18 and Figure 3-19 show the reservoir pressure for the Roden field and HRS-2A respectively for the ensemble as examples. Further pictures are provided in Appendix B. The spread for HRS-2A is larger than for the Roden field, because there was less pressure information to constrain it. The subsidence data will be used to select the better fitting ensemble members. The calculation of the subsidence and the workflow to select the members will be discussed in the next section.

Table 3-4 Dynamic GIIP values from the ensemble

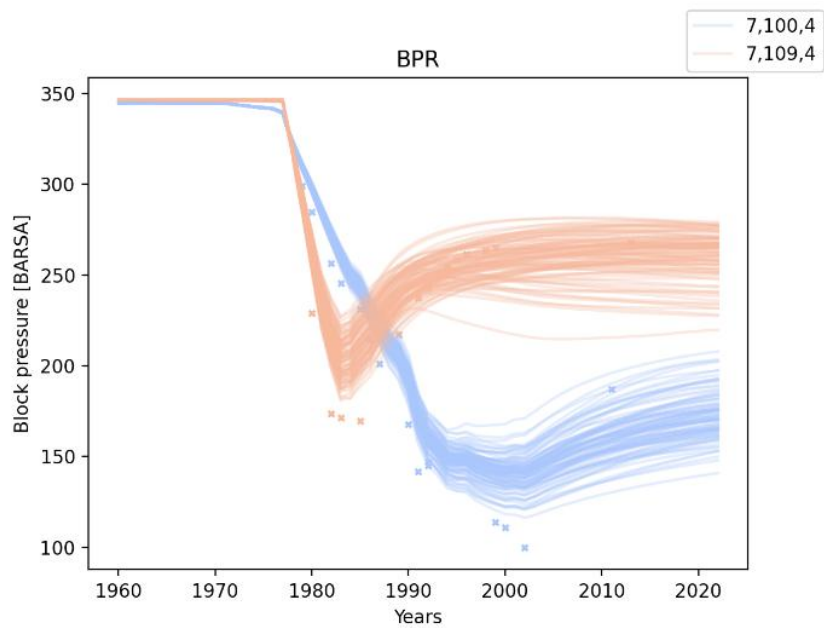| GIIP (BCM sm3)	Dynamic GIIP ensemble		
	min	mean	max
Vries-Noord	4.2	4.5	4.9
Roden-Noord	7.5	7.9	8.3
Roden-Zuid	3.5	4.0	4.5
Boerakker	3.6	4.0	4.4
Pasop	3.6	4.1	4.7
Faan	0.8	1.0	1.1
Noordlaren	0.1	0.2	0.3

Figure 3-18. Ensemble of reservoir pressures (at BHP depth) of the Roden gas field for the historical period. Blue curves represent the Roden north block and red is Roden south. Stars indicate static pressure measurements.
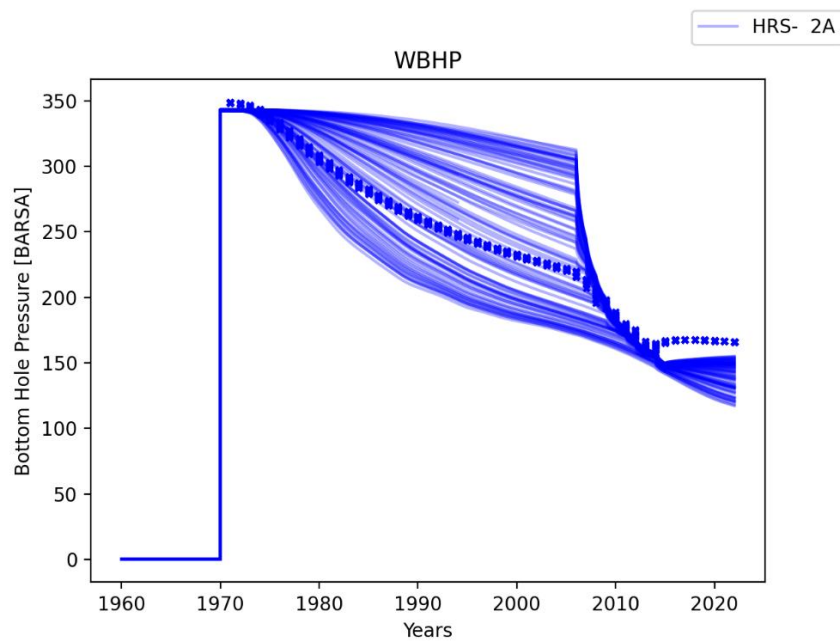

Figure 3-19 Ensemble of BHP (bottom hole pressure) for HRS-2A. Stars indicate output from the NAM MoReS model which were used as measurements.

3.4 Compaction and subsidence

Aquifer pressure changes cause compaction by the changes in effective stress associated with them. This compaction causes surface movement – which can be measured. In this Section we document how we have employed subsidence measurements to reduce the uncertainty of the pressure distribution in the aquifer and to discriminate probabilities of the ensemble members. The tool that we use is ESIP (acronym for Ensemble Subsidence Interpretation and Prediction), an inhouse tool targeted at the use of surface movement data for reservoir characterization, deploying an ensemble data assimilation approach (Candela et al, 2022).

3.4.1 Surface movement data

We have evaluated two sources of surface movement data. The first is the data provided by Rijkswaterstaat. These contain benchmark heights through time, of the primary benchmark network. However, the benchmarks located in the region above the Groningen SW aquifer are quite limited and none of them contain numbers outside the timespan 1980 – 2000.

We therefore also evaluated data provided by NAM, which are the data that they have used for their own interpretation of subsidence in the northern Netherlands. The dataset spans the time interval between 1964 and 2018 and contains more benchmarks: also the secondary benchmarks are incorporated. The secondary benchmarks have been constructed specifically for the determination of surface movement due to gas production in the region. Therefore, the network of benchmarks is much more dense. In addition, the time window at which benchmark heights have been determined is much larger and a good coverage of the complete history during the gas production of Groningen until 2018 could be provided. We have thus used the NAM data in this study.

The reservoir model output that we used for this study is the pressure decline in the SW aquifers only. We have therefore selected only the benchmarks that are not influenced by parts of the gas fields which are not in the pressure output maps. All gas-production-related surface movements in the selected benchmarks can thus be attributed to the pressures in the models detailed above. The locations of the benchmarks that were used are represented in Figure 3-20.

ESIP uses double differences of height measurements. Our input contained interpreted heights for each location. These had been produced by comparing single height differences between benchmark locations and comparing them to a benchmark that is assumed stable. Using those is equivalent to double differences under the condition that the error model is propagated and incorporated in a covariance matrix. This covariance matrix, however, was not available.

NAM have employed an adapted use of the measurement error model upon a motivation of "model error" – possible unmodeled features causing mismatches between model results and measurements (NAM report, 2021). They assume this error is larger for larger displacements; they add a variance of $\sigma_0 + \alpha \cdot dh$ to the covariance, with σ_0 of the order of 0.5 – 0.6 cm^2; α of the order of 0.03 cm and dh the modeled displacement. These numbers make the covariance matrix almost diagonal, so the NAM treatment provides a qualitative argument for using a diagonal covariance matrix. However, our inversion procedure is different from theirs: we use a "Red Flag" approach (Nepveu, Kroon et al, 2010), therefore we use the measured displacements rather than the modeled displacements for the additional variance determination. In the assimilation procedure we use height differences of subsequent times;

not the total displacements since the first measurement campaign in which that point was evaluated.

We deploy the measurements in a parameter estimation exercise. Ensemble methods like those that we use often suffer from ensemble collapse if the number of data points is large (Van Leeuwen, 2009): the spread of the outcome then is too small in view of the data uncertainty. The ensemble collapse can be removed by increasing the variance of the data considerably. We arrived at acceptable numbers of sizeable model realization probabilities with $\sigma_0 = 1\ cm^2$; $\alpha = 1\ cm$. We comment on this below.
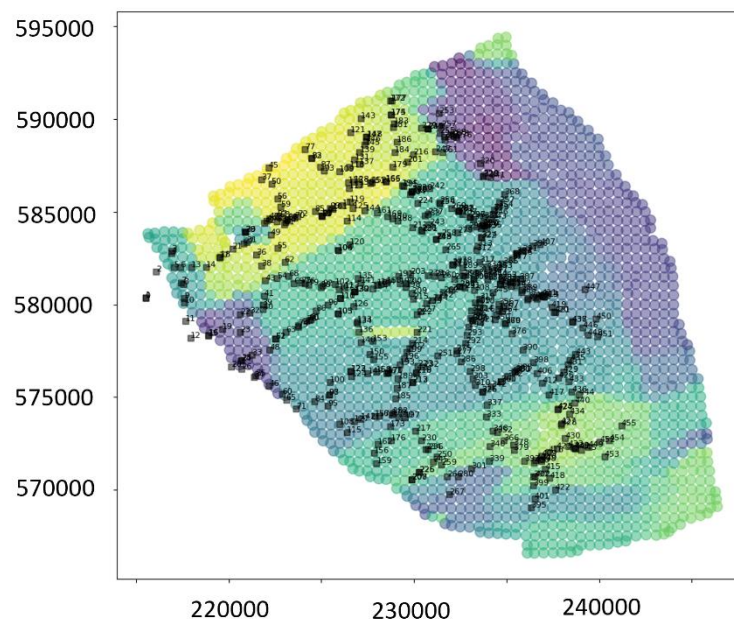
Figure 3-20 Selected benchmarks above the SW Groningen aquifer. The background color signifies the pressure depletion in the SW aquifer (darker colors indicate more decline); we see larger pressure declines towards the NE-E border, where the aquifers are bounding the Groningen field, and to the W-SW border where the aquifers bound some of the smaller fields.

3.4.2 Screening of mechanical parameters with the Red Flag method

We have deployed the Red Flag method for our parameter estimation exercise (Nepveu et al, 2010). In the Red Flag method, first an ensemble of realizations is created. Then each ensemble member is assigned a scaled probability, based on the mismatch between the ensemble's calculated subsidence and the measured subsidence.

We used four compaction models: a linear model, a bi-linear model, a time-decay model and a rate-type compaction model (Candela et al, 2022; see also the next sections). For each compaction model we construct 10 random realizations of the driving parameters within their bandwidth, for each of the 100 reservoir models. For each of the four compaction models this results in an ensemble of 1000 surface movement predictions at all locations.

For the influence function we used a Geertsma-Van Opstal function (Opstal, 1974). This function calculates the subsidence bowl for a center of compression at the depth of the compacting reservoir in a homogeneous subsurface, with an underlying rigid basement. The parameters in this function are the given depth of the compacting source, the depth of the basement, and the Poisson's ratio of the subsurface. The subsidence model calculates the total influence of all compacting grid cells of the reservoir simulator by superposition. The data with which the model realizations are compared contain 2829 differences at 457 locations.

The compaction coefficient is dependent on the porosity. The starting value for our compaction coefficient is (Candela et al, 2022)

$$c_{m0}[10^{-5}bar^{-1}] = 267.3 \cdot \phi^3 - 68.72 \cdot \phi^2 + 9.85 \cdot \phi + 0.21$$

The compaction coefficient is calculated for each grid cell in the reservoir simulation.

3.4.2.1 Linear compaction model

The thickness change of a grid cell in the linear compaction model under uniaxial strain conditions is a simple linear function of the pressure depletion:

$$\frac{\Delta V_{linear}}{V} = f_{cm} \cdot c_{m0} \cdot dP$$

With the use of the linear compaction model we apply a single multiplication factor f_{cm} to the starting value to maintain the porosity dependence. We have first have determined the range in which the compaction parameters should be. We started with a range of 0.3-1.0 for the compaction coefficient multiplication factor; for the Geertsma-Van Opstal parameters we started with 4000-7000 m depth for the rigid basement and a fixed value of 0.25 for the Poisson ratio.

The 1000 ensemble members are evaluated in the customized Red Flag algorithm, resulting in a scaled probability for each realization. The screening phase of the Red Flag method employs a variance that is increased by a factor of 10, because otherwise the exercise results in ensemble collapse with only a single realization surviving with sensible probability.

Figure 3-21 visualizes the results. In Figure 3-21a we see the probability for each realization vs the realization number. Every reservoir realization corresponds to 10 realizations in this plot, arranged with numbers 0-9; 10-19 for reservoir realizations 1, 2, etc. We see that some reservoir realization perform better than others, however, there is considerable scatter and the probability within every set of 10 for a reservoir realization is largely varying. When plotting the probabilities against the compaction parameters , we conclude, somewhat intuitively, that the f_{cm} (Figure 3-21b) should be in the range 0.5-0.6; the rigid-basement depth (Figure 3-21c) should be larger than 5000 m. Even within these ranges, the majority of the members have small probability, apparently because the corresponding reservoir realizations are suboptimal.

We reran the Red Flag algorithm with the narrower distribution of these starting values, in order to obtain a larger number of members with relatively large probability and a more precise determination of the fitness of the underlying reservoir realizations. To our reassurance, the best realizations remained largely the same ones. In Section 3.5.1 we will further discuss how we proceed to selecting cases for forecasting. The measured and modelled displacements in 20 of the 457 locations is reproduced in Figure 3-22. The

assignment of probabilities based on the match of ensemble member predictions with the data indeed improves the fit considerably. This was also the case for the benchmarks not shown here.
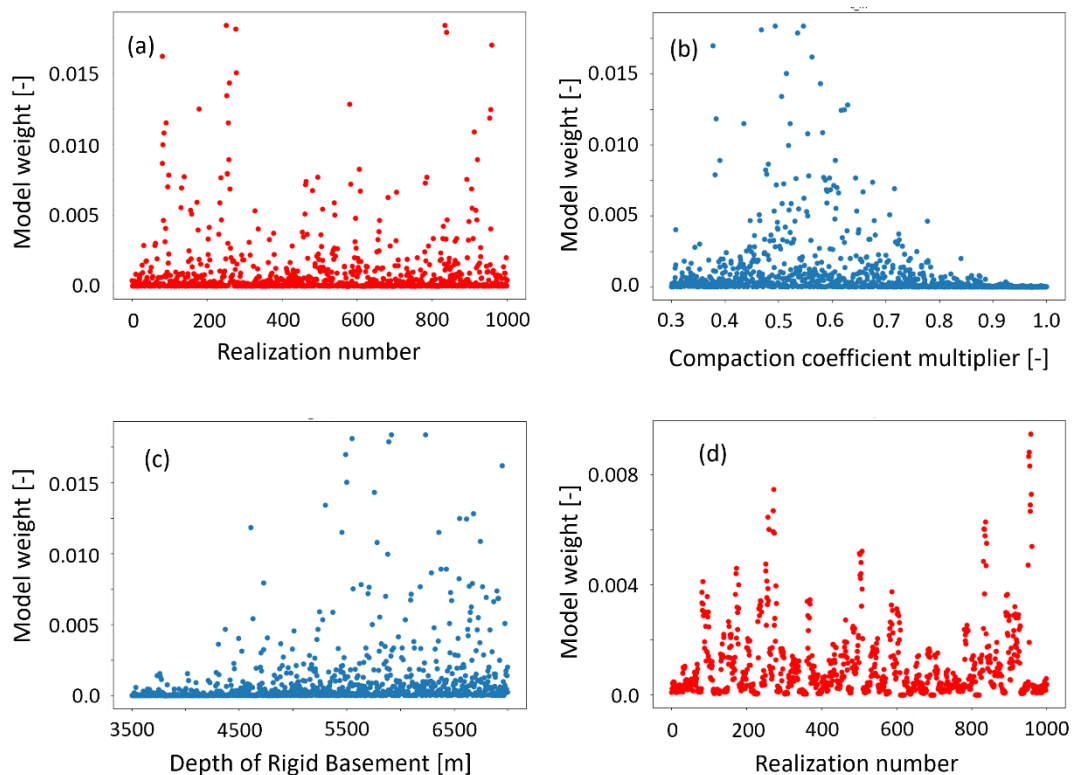

Figure 3-21 Model weights of the model realizations for the linear compaction model plotted against (a) realization number; (b) compaction coefficient multiplication factor; (c) depth of the rigid basement. (d) weights with better constraint starting values
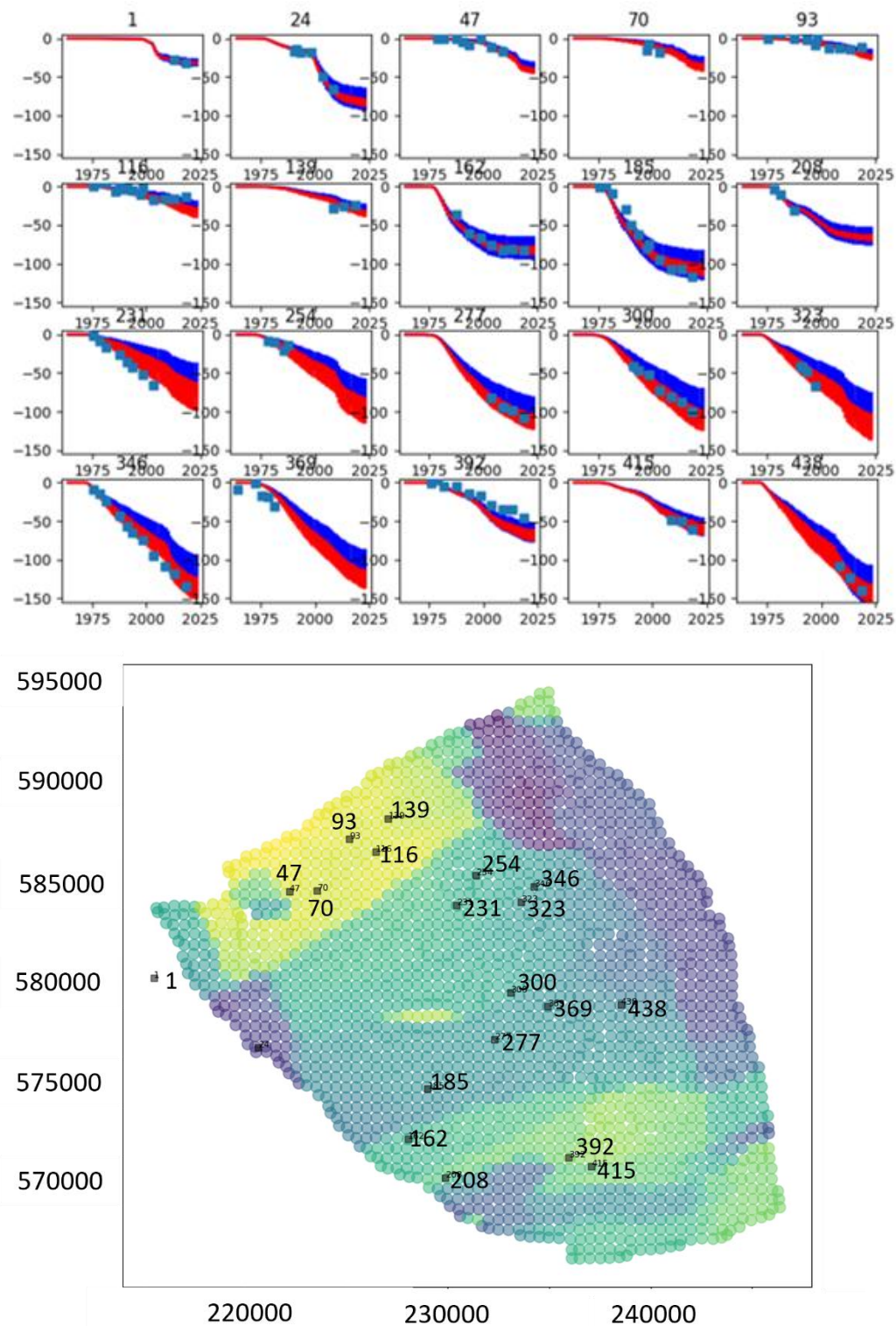
Figure 3-22 Top: Traces of the displacements (in mm) at 20 selected benchmarks. Blue: Prior mean including uncertainty; Red: Posterior mean including uncertainty, based on Red Flag output. Symbols: Measured displacements. Bottom: positions of the represented benchmarks, with the colors indicating the last pressure drawdown of realization 96 (darker colors indicate more drawdown).

3.4.2.2 Alternative models

A similar procedure was followed with the bilinear compaction model, a model with different values for the compaction coefficient for pressures larger and smaller than a transition pressure. Compaction model parameters are here the compaction coefficients f_{cm1} and f_{cm2} for smaller and for larger depletion pressures, and the pressure value P_{trans} at which the transition occurs:

$$\frac{\Delta V_{bilinear}}{V} = \begin{cases} f_{cm1} \cdot c_{m0} \cdot (P_0 - P) & (P \geq P_{trans}) \\ f_{cm1} \cdot c_{m0} \cdot (P_0 - P_{trans}) + f_{cm2} \cdot c_{m0} \cdot (P_{trans} - P) & (P < P_{trans}) \end{cases}$$

We refer the compaction coefficients again to the starting values c_{m0} with a multiplication factors f_{cm1} and f_{cm2}. We found that the first compaction coefficient (the one working at smaller depletion pressures) was similar to the single coefficient in the linear compaction model (f_{cm1} in the range 0.5 – 0.6) and that the rigid basement should be deep. The results were insensitive to the transition pressure and the second compaction coefficient. This is related to the range starting value for the transition pressure, between 180 and 270 bar, which is reached for only very few points in the aquifer. We therefore do not use the bilinear compaction model in the remainder of this study.

The time-decay model employs a delayed action of pressure depletion to compaction (Mossop, 2012). The relative compaction of a grid cell with volume V, subject to a pressure step change dP at time t_0, is given by

$$\frac{\Delta V_{tdecay}}{V} = f_{cm} \cdot c_{m0} \cdot dP \cdot \frac{1}{\tau} \exp\left[-\frac{t - t_0}{\tau}\right]$$

An evolving pressure is included through a time convolution of the pressure development with this function. The model parameters are the multiplication factor for the compaction coefficient c_m and the characteristic time constant τ.

Starting with a broad distribution of f_{cm} and τ of 0.1 – 2 and 0.1 – 40 years we see a clear correlation between them when plotting the ranked probabilities in a cross-plot. The realizations ranking higher are distributed along a band ranging from $(f_{cm}, \tau) \sim (0.5, 0)$ to (2.0, 25) (Figure 3-23). However, a number of resampling exercises led to an optimum range of f_{cm} between 0.5 and 0.6 and τ between 0.1 and 1. This is virtually equivalent to results of the linear compaction model, because a decay of 1 year and less can hardly be seen on the scale of the measurements. Also the results for the rigid basement was similar: it should be deep to the extent that its effect at the surface can not be seen.
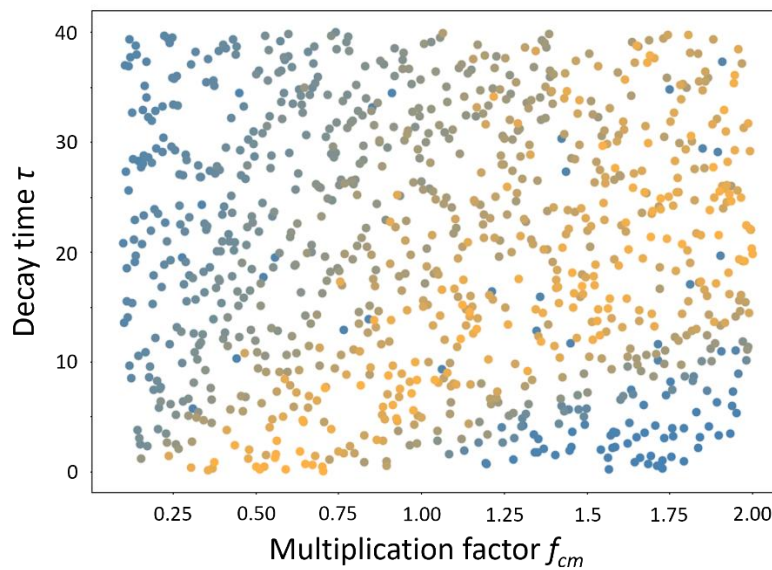
Figure 3-23 Crossplot of decay time vs multiplication factor for the compaction coefficient, with realizations in the broad test of the time decay model. Colors from yellow to blue indicate the ranking from high to low probability.

The rate type compaction model employs two contributions to compaction: an immediate response and a delayed response that depends on the rate of pressure depletion. The model is well documented in Candela et al (2022) and Pruiksma et al (2015) and utilizes three material parameters ($c_{m,ref}, c_{m,d}, b$) and one state parameter ($\dot{\sigma}'_{ref}$ Results of a screening of the parameters yielded values of $c_{m,ref}$ between 0.3 and 0.6; $c_{m,d}$ between 0.6 and 0.9, b between 0.01 and 0.02 and $\log \dot{\sigma}'_{ref}$ between -6 and -3. This is in line with the values reported by NAM (NAM report, 2021). Except for the value of $c_{m,ref}$, the outcome is not discriminating. This is due to the relatively small values for the depletion in the aquifer, while the distinction of the rate type compaction model with regard to the linear compaction model is mainly for larger values of the depletion. We will therefore not use the rate type compaction in the remainder of the report.

3.4.2.3 Synthesis of the Red Flag model results

The Red Flag methodology has been deployed with an inflated variance, in order to avoid ensemble collapse. We judge this allowable since we only use the method to identify the best reservoir model realizations at this stage; and ensemble collapse is known to pose a major problem if many data points are available.

All compaction models yielded reasonable values for their parameters. At the same time the Red Flag approach yielded a clear distinction between reservoir models. The models with the largest probabilities were consequently the same for all compaction models, and the optimal value for the rigid basement was found to be large. The selection of the best realizations to pursue further is documented in Section 3.5.1.

3.5 Forecast of the post-abandonment pressure

3.5.1 Selection of model realizations

Before making the selection for the model realizations to be used for forecasting, first it is discussed why some reservoir models from the ensemble are more probable based on the observed subsidence than others (in other words: fit the data better). Figure 3-24 shows the pressure in the model with the highest probability based on the subsidence (member 96). Comparison with the pressure of the base model in Figure 3-16, shows that the main change is in the aquifer north of the Roden aquifer which is connected to the small gas field Pasop to the west and the Ten Boer area to the east. In particular on the east side of this aquifer (near the Ten Boer area), the pressure is expected to be considerably lower than in the base model. The pressure depletion in the middle of the aquifer is less certain: the posterior ensemble of the subsidence still shows a relatively large range of ~5 cm at the end of the history period (Figure 3-22).
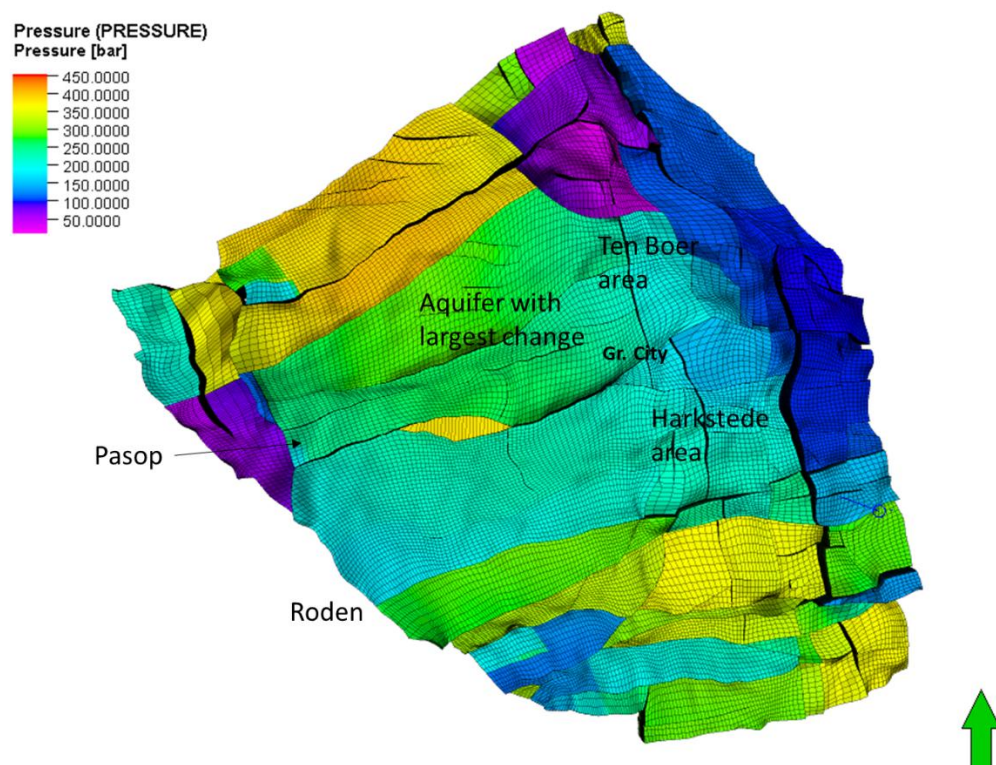
Figure 3-24 Top view of the pressure at the end of the historical period (1 Jan 2022) for the model with the highest probability based on the subsidence (96).

In order to make a selection of the model realizations that fit the observations best, the probability based on the subsidence needs to be combined with a measure for the fit to the pressure data. Therefore the Root Mean Squared Error (RMSE) of the static pressure observations was calculated for the all the wells of the small gas fields and HRS-2A and MLA-1. First the RMSE was calculated per well and then the values per well were averaged to arrive at one RMSE per model realization.

Figure 3-25 shows a plot of both the probability and the RMSE per model realization. This shows no correlation between the two measures. Because the pressure was already used to

tune the base model, it was decided to base the selection of the best fitting models (which are to be used for forecasting) on the fit to the subsidence more than on the fit to the pressure. The following thresholds were used to get a reasonable number of models.
- The threshold for the probability based on subsidence is 0.015
- The threshold for RMSE of the pressure is 51 bar

This means that ensemble members with a probability higher than 0.015 and RMSE lower than 51 bar are selected. The selection is illustrated in Figure 3-25 by the red outline. This results in a selection of 22 models from the total of 100.
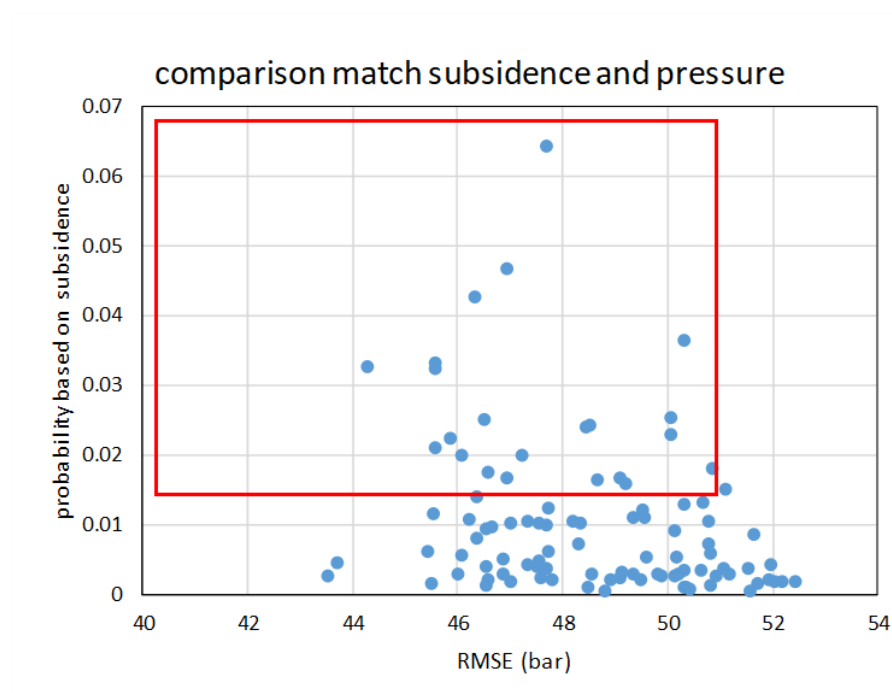
Figure 3-25 Probability of the model realizations based on the subsidence plotted against the averaged RMSE for the reservoir pressure. The red square indicates the model realizations selected for prediction.

3.5.2 Constraints for the forecast period

To simulate the post-abandonment pressure, the selected model realizations need to be run forward in time to the year 2100. To do this, well constraints are required, both for the small gas fields and the Groningen side. For the small gas fields, the constraints are simple. Except for well FAN-01, all wells were closed before 1/1/2024. The production data from 2022 and 2023 are taken from NLOG.nl, where necessary. Based on the publicly available 'Winningsplan' for Faan, well FAN-01 is expected to cease production in 2025. Production as listed in the 'Winningsplan' for the mid case is implemented for 2024 and 2025.

On the east side of the model, constraints need to be decided upon for Bedum and the Groningen wells. The required pressure constraints for the Eemskanaal wells are based on the results of the base case model from the KEM24b project (TNO, 2024), which is based on the NAM Eclipse model. The original KEM24b model was run to 2054, but the run was extended to 2100 for this project. To achieve the pressure decline due to the equilibration with the rest of the Groningen field, the wells were opened for gas production in the model.

For the wells in the western periphery (HGZ-1 and KHM-1), the historical results of the KEM24b model are not in line with the NAM MoReS model and the model developed in this project. Unfortunately, no predictions are available from the NAM MoReS model. So for both wells, a pressure decline was defined based on expert judgement. For HGZ-1 it was assumed that the well will fully equilibrate with the Groningen field, because the pressure was already close to the Groningen pressure (Figure 3-26). For well KHM-1, which probably depletes via the Eemskanaal area rather than the Groningen main field (Landman, 2023), the pressure constraint is set to go down to 125 bar and then further deplete via Eemskanaal.
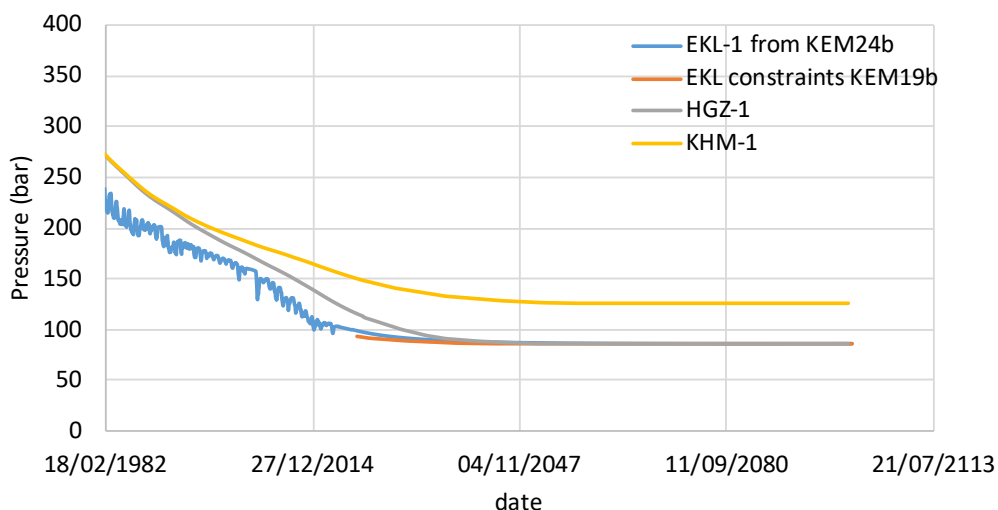
Figure 3-26 Pressure constraints for the Eemskanaal wells (EKL constraints KEM19b), HGZ-1 and KHM-1.

Based on the production plan for Bedum, the abandonment pressure for the field is 35 bar and shutin is expected in 2030. Therefore the pressure constraints for all wells are gradually declined to a pressure of 35 bar and the field is shutin on 1-1-2030. Well BDM-4 had already dropped below 35 bar in 2021, so no more gas was produced from this well.
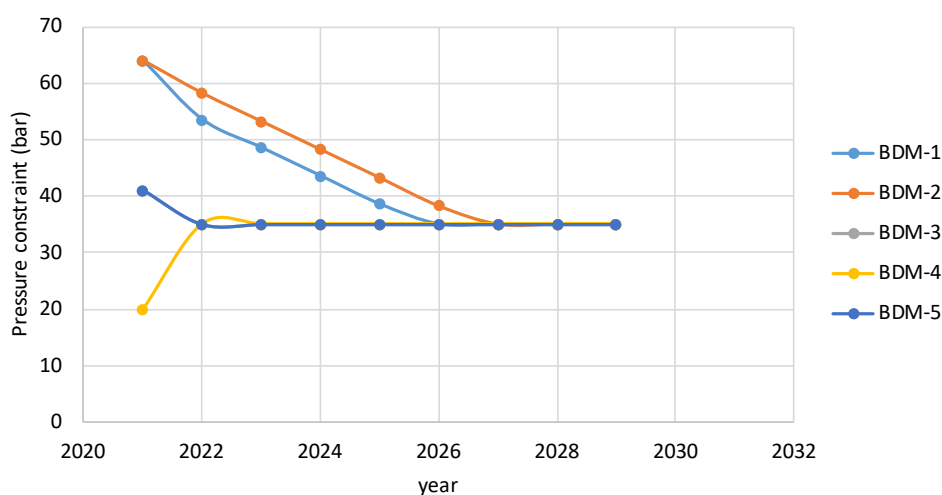
Figure 3-27 Pressure constraints for the Bedum field.

3.5.3 Results

The entire ensemble of 100 members is simulated over the entire time period from 1960 to 2100. The reason for simulating and showing the entire ensemble is that this shows how the selected ensemble members are distributed over the initial ensemble. An example is shown in Figure 3-28 for HRS-2A. Each curve represents the pressure at HRS-2A of one model realization. The blue curves are the model realizations that were not selected for the prediction period. The black curves are the ones that are selected (see Section 3.5.1 for the selection criteria). The red curve is the most probable model realization based on the subsidence (number 96). The vertical blue line marked "2022" indicates the point in time when we move from history to forecast mode. The black curves are distributed over the entire ensemble, which indicates that the ensemble is not biased and the uncertainty cannot be further reduced based on the subsidence observations at the locations where the base model was already tuned using pressure observations. The best overall fitting member (most probable member 96 in the red curve) shows very little drawdown in the early period which conflicts with the pressure observations in the well (see Figure 3-13 and Figure 3-19): a good overall fit doesn't imply a good fit for each individual well.
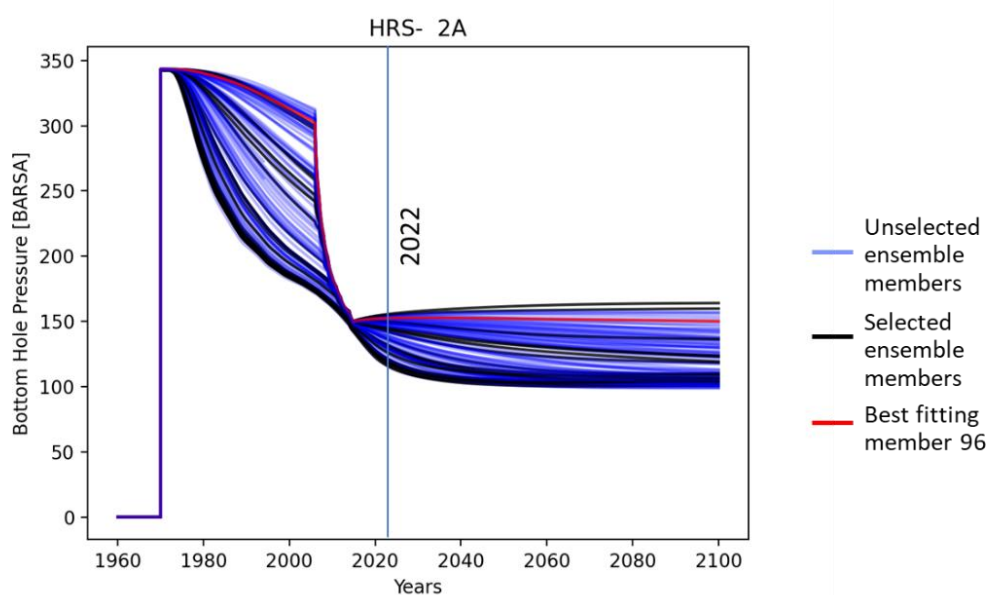

Figure 3-28 Pressure at HRS-2A for the period 1960 to 2100. Black and red curves are the selected model realizations, where the red curve is the best fitting member 96. Blue curves are the model realizations that do not fit sufficiently well to data to be used for prediction.

A second example is shown in Figure 3-29 for the Roden field for the north and south block. For both Roden north and south, the selected ensemble members span the entire range of the ensemble, again indicating no bias. For Roden south a decline in pressure is predicted after the earlier rebound for many of the ensemble members. This is due to slow depletion from adjoining aquifers and gas fields. The results from the other small gas fields and wells are shown in Appendix B.
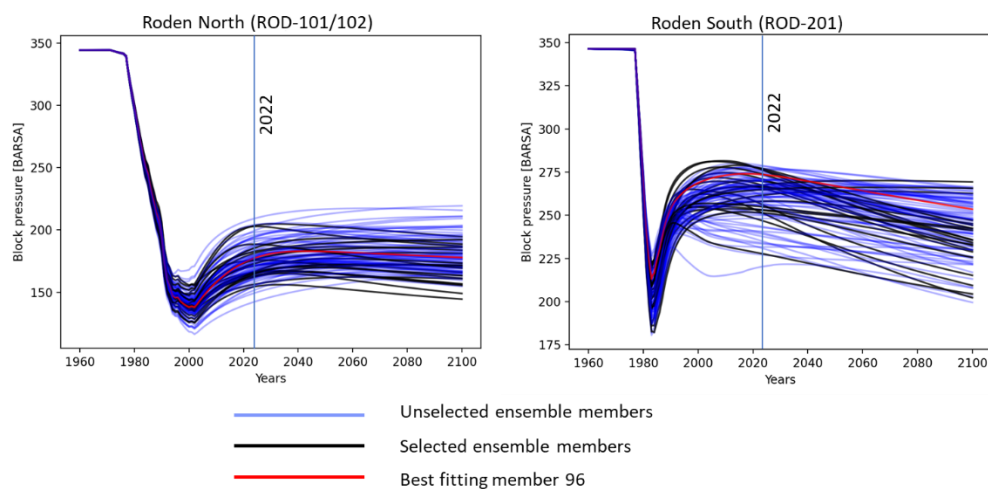
Figure 3-29 Pressure in the Roden field in the north and south blocks for the period 1960 to 2100. Black and red curves are the selected model realizations, where the red curve is the best fitting member 96. Blue curves are the model realizations that do not fit sufficiently well to data to be used for prediction.

Results in the aquifer
Up to this point, all the presented results are from either small gas fields or the Groningen field. To better understand the results within the aquifer, the pressure over time for a series of points from north to south in the aquifer is plotted in Figure 3-30 and Figure 3-31. Figure 3-30 shows the pressure in the northern part of the aquifer, while Figure 3-31 shows the pressure in the southern part. The red dots indicate the position in the aquifer. The map shows the pressure at the end of the history period (in 2022) for the best fitting member 96. The legend of the curves is as in Figure 3-28 and Figure 3-29. The most northerly two points, which are in the aquifer connected to Faan and Bedum, have limited depletion overall (30 to 40 bar) and the ensemble shows no bias. However for the two points to the south ((85,47,4) and (87,56,4)) which are in the aquifer connected to Pasop, the selected model realizations in black are exclusively in the lower part of the graph indicating that the observed subsidence points to more pressure depletion than the prior ensemble. For both points, the best fitting member (in red) is the curve that has most depletion. Clearly in this part, using the subsidence had added value. In Figure 3-29, the two points near Harkstede ((86,96,4) and (110, 100, 4)) are the locations with the largest depletion, which is supported by the subsidence. In fact, most of the selected curves are in the lower part of the graph. The point (110,122,4) further south has the largest spread in the results from any of the points and is poorly constrained both by wells and by subsidence.

In Figure 3-32 the depletion is shown for the best fitting member 96 for the years 2022, 2060 and 2100. All calculated with respect to the pressure before the start of production in 1960. The figure shows the ongoing depletion in the aquifers and some recovery in pressure in some small gas fields like Bedum (in the north-east), Faan (in the north-west) and Vries (south-west). Overall the largest depletion that is reached in the aquifer is around 200 to 220 bar in the Harkstede/Ten Boer area or a decrease of about 60% of the initial pressure. The figure also shows the relatively uniform depletion in the aquifers between the Roden field and Harkstede and the more variable depletion in the south part of the model.
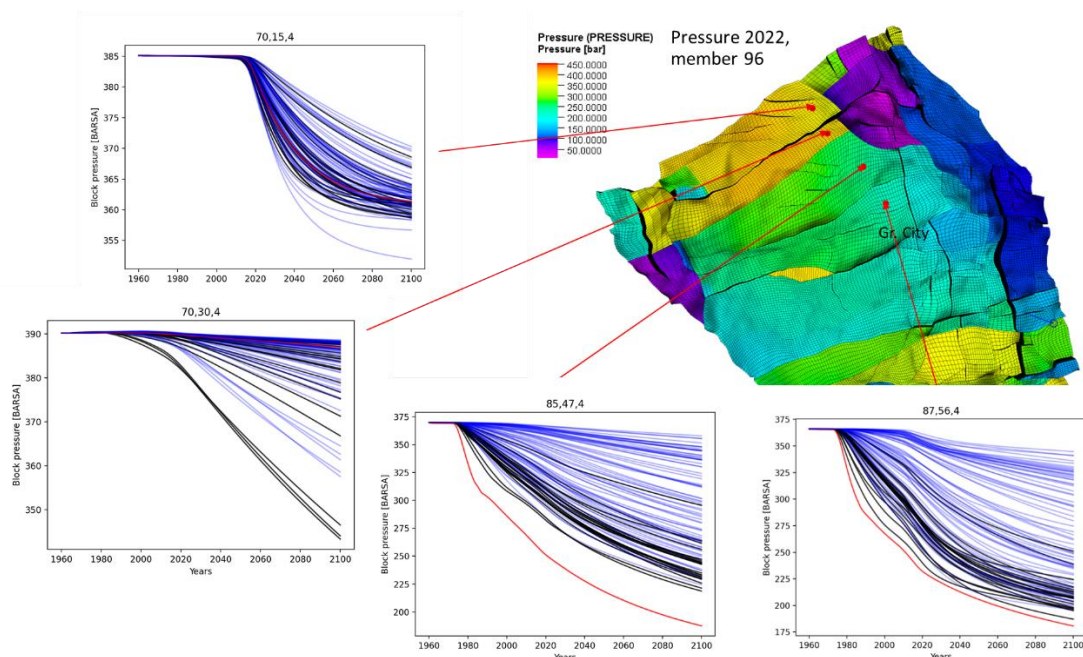
Figure 3-30 Pressure for four locations in the northern part of the aquifer for the period 1960 to 2100. The red dots indicate the position in the aquifer for which the line plots are. The legend of the curves is as in Figure 3-28 and Figure 3-29. The map shows the pressure at the end of the history period (in 2022) for the best fitting member 96. The number on top of the graph is the grid block.
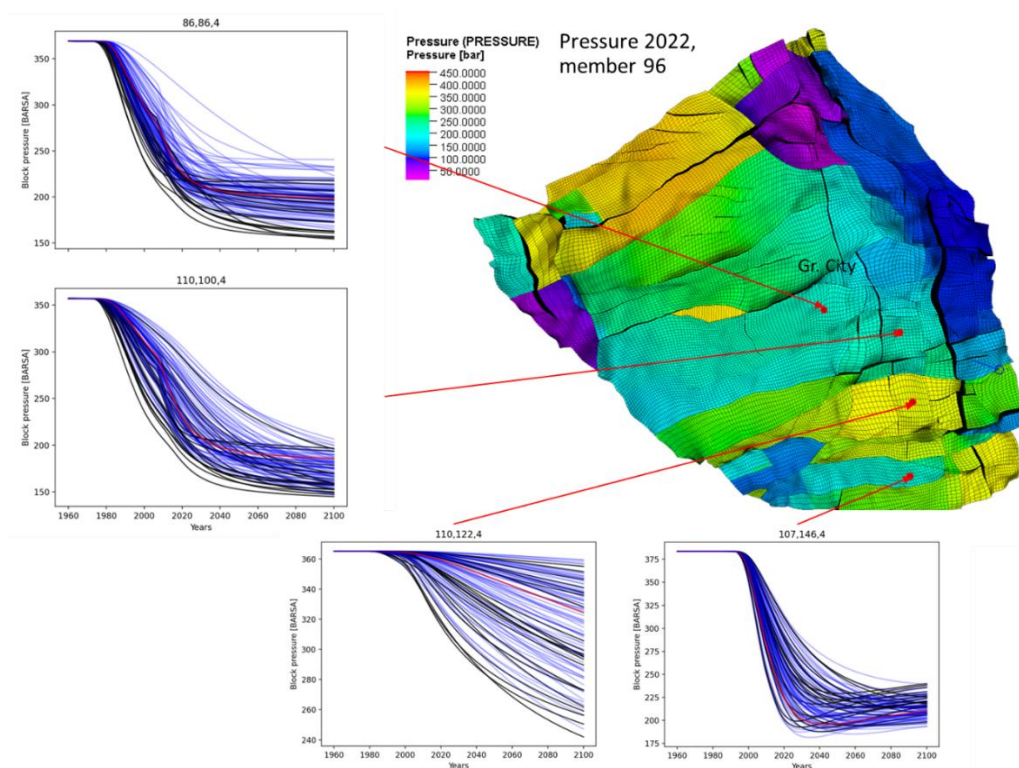

Figure 3-31 Pressure for four locations in the southern part of the aquifer for the period 1960 to 2100. The red dots indicate the position in the aquifer for which the line plots are. The legend of the curves is as in Figure 3-28 and Figure 3-29. The map shows the pressure at the end of the history period (in 2022) for the best fitting member 96. The number on top of the graph is the grid block.
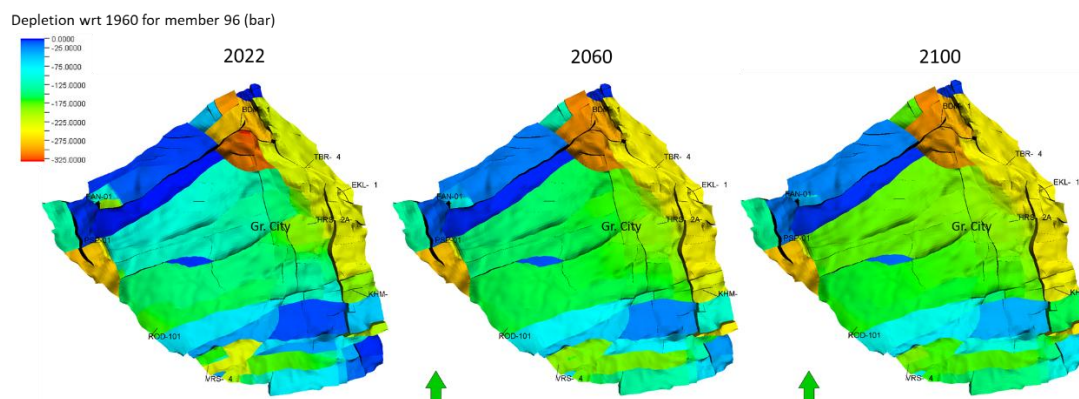
Figure 3.32. Depletion in 2022, 2060 and 2100 with respect to 1960 for the best fitting member 96

3.6 Discussion and conclusions

The current study has resulted in the forecast of pressure depletion for an ensemble of 22 out of 100 members in the SW aquifer of Groningen gas field in the southern Lauwerszee Trough. The ensemble was ranked based on static pressure measurements in the small gas fields and observations of surface movement measurements above the aquifer. The surface movement measurements have helped making this ranking by discriminating the models according to how the calculated surface movements fit the measured ones. The better constrained reservoir properties facilitate a better estimate of seismicity that is still to be expected, as the main outcome of the complete study.

The forecasted depletion on the east side of the aquifer is dominated by the Groningen field (Figure 3-32), although the production from the Roden field likely has caused depletion in this area in the period before 2000 (Figure 3-31 subfigure '86,86,4'). After that the depletion due to production near Harkstede (from EKL-13) dominated the pressure depletion. The aquifer between the small gas field Pasop (just North of Roden) and the Groningen field, also shows considerable depletion, but based on the timing of the drawdown this appears to be caused more by production from the Groningen field, in particular the Eemskanaal cluster, than from Pasop. The other small gas fields appear to have a more local influence.

Reservoir model
During the tuning of the base model, additional faults or baffles were interpreted compared to the faults interpreted during the seismic interpretation. Some of these were small compared to the resolution of the current model, while some were very poorly visible in the seismic data, probably because of small fault offset. This suggests that also in the aquifers, the fault interpretation is not complete.

It should be realised that the focus of this model is the SW aquifer. Even though the small gas fields and the west part of the Groningen model are part of the model area and some effort was made to simulate these parts correctly, the model does not represent this sufficiently well for detailed analysis. In particular, in the Groningen and Bedum gas fields, the pressure predictions from the NAM models are more accurate and better constrained by data.

Although considerable effort was invested in making a reliable estimate of the possible pressure range and constraining the uncertainty, the uncertainty that remains in some areas

is still considerable. Sometimes this is due to model limitations: for example the area near Midlaren is relatively close to the boundary of the model and the surface movement is influenced by the Groningen Main field and the Annerveen gas field (Figure 3-20 and Figure 2-2). This means that only a few surface movement observation points could be included in this area. The impact of the Annerveen field was also not included on the pressure depletion, because the field is separated from the model area by a fault with a very large offset isolating the Annerveen field from the aquifer to the north.

Comparison with NAM results
To guide the history match despite the lack of measurements, NAM assumed that the depletion in SW aquifer should be larger than 90 bar based on the earthquakes in the aquifer at Paddepoel and Eelderwolde (Zeeuw and Geurtsen, 2018b). This is based on the observation in gas fields that the possibility of seismicity is negligible when the pressure drop is less than 28% of the initial pressure (Staatstoezicht op de Mijnen, 2016; Thienen-Visser, 2012) The depletion of the aquifer connected to Roden was expected to be more than 100 bar in the entire aquifer by 2006. In the model developed in this project, depletion in the Roden aquifers in 2006 is estimated around 140 to 160 bar, so in agreement with the assumptions by NAM. For the Groningen Long term Subsidence Forecast (NAM, 2021), NAM has also matched a simplified aquifer model to surface movement data. For the aquifer connected to the Roden North gas field, they estimated a drawdown of around 120 to 140 bar in 2020, which is slightly lower than the estimates in this project (140 to 160 bar depletion for the best fitting member 96). In the Roden south block, the estimated drawdown is 70 to 80 bar for both models. The aquifer connected to the Pasop field is simulated differently in the two models: the connectivity is higher in the KEM19B model than in the NAM model with a drawdown of ~100 bar compared to ~50 bar in the NAM model in the middle of the aquifer. Overall the results align quite well taking into account the overall uncertainty.

Subsidence modelling
For the surface movement estimates there are still steps for improvement possible. These are related to the shortcomings of the present study and we will list them here.

The main problem with the procedure followed in this study is concerned with the Red Flag method itself. It is known that a particle filter (which is the more common name for our Red Flag method) is prone to ensemble collapse if many data points are available (Van Leeuwen, 2009). The 2829 difference measurements that we have is indeed a large number in that respect and a straightforward application of the method resulted in a single ensemble member with all probability collected in it. This was the case for any single compaction model and set of starting parameters that we employed. We have addressed this point in two ways: by reducing the discriminating power of the method through an inflation of the data variance, and by resampling of the parameter space. Inflation of the data variance is not scientifically underpinned but was only meant to identify more than a single realization as the outcome of the procedure. The obvious alternative of increasing the ensemble size in order to obtain a more dense sampling of the parameter space was not feasible because of the associated requirement of making many reservoir model realizations and the large computation times involved. Resampling after first testing a broad distribution and focusing this to a narrower one, on the other hand, is warranted and was successfully deployed.

An alternative would be to use a different data assimilation method. In other studies we have used the Ensemble Smoother with Multiple Data Assimilation (ES-MDA) (Fokker, Wassing et al, 2016; Fokker, Gunnink et al, 2019). ES-MDA uses a linear superposition of the prior models and model parameters to construct an update. We have fixed reservoir simulations that cannot be changed and of which the parameters have not been schematized in the procedure.

Updating only the compaction and geomechanical parameters would therefore be inappropriate since the surface movement data predictions on which these updates are based are originating from different reservoir realizations. The updated parameter values would be applied to the original reservoir model realizations which have not been assimilated.

A single-step Ensemble Smoother could possibly circumvent this shortcoming of the combination of ES-MDA with our ensemble of reservoir models. The single-step Ensemble Smoother does not require a re-run of the model, and assimilated forecasts could be constructed in the same way as the assimilated parameter values. It is certainly a way forward that deserves to be attempted.

The second fruitful way forward that we envisage makes use of the fact that only a small number of realizations of the reservoir model have survived the Red Flag approach of the current study. Each of these can then be treated separately and subjected to a data assimilation or inversion exercise in order to constrain the best set of parameters for that particular realization, in combination with the compaction model selected. Such an exercise is feasible, with some 40 inversion exercises: 4 compaction models for each of the 10 most probable realizations. Upon completion of those exercises the user can decide which combination of reservoir model with compaction model fits best.

In any case, the way forward will involve considerable expert knowledge and expert judgement. This is the fate of the necessary sequence of models ranging from geological to reservoir to compaction finally to surface movement. For the purpose of using surface movement data in order to improve seismicity estimates, however, we deem the approach that was followed in the present study sufficient.

4 Seismicity analysis and seismic hazard assessment

4.1 Objectives

The objective of this part of the study is to provide a forecast of the induced seismicity rate, and the corresponding seismic hazard assessment for the coming decades in the SW aquifer of Groningen. For this purpose, the TNO Model Chain workflow developed for the Groningen field (TNO, 2020) is applied to the SW aquifer. This application requires the spatial extension of the two main building blocks: (1) the seismic source model (SSM) and (2) the ground motion model (GMM). For the Groningen model chain both components have been designed and calibrated specifically for the Groningen field. An extension to include the SW aquifer at depth, and a larger exposed area at the surface, requires both taking into account new (more) data, as well as a (re)calibration.

In Section 4.2 we describe the theory and methodology used to achieve the model extensions and generate the results. The results are presented in Section 4.3, and discussed in Section 4.4.

4.2 Seismicity analysis and hazard

4.2.1 Seismic hazard analysis

In this section we provide a brief summary of seismic hazard analysis and its relation to the seismic source and ground motion models. For more details the reader is referred to TNO(2020) or general introductions such as Baker et al. (2021).

Let us define the seismicity rate λ as the expected number of earthquakes per unit time, per unit space (area, or volume) and per unit magnitude. The seismicity rate function will, in general, depend on time t, spatial dimensions x, representing the location of the hypocentre, and magnitude m, and hence, can be expressed as a parameterized function accordingly: $\lambda(t, x, m)$. Furthermore let us define the distribution of a certain ground motion attribute, such as peak ground acceleration (PGA) or spectral acceleration (SA), say g, at a surface location y, in terms of its survival function (probability of exceedance) S_G. In general, this distribution will depend on the subsurface conditions at the surface location (e.g. the local shear wave velocity profile) represented by a zone-index ζ, the magnitude of the earthquake, and the distance to the earthquake rupture r. The ground motion distribution can thus be presented as a conditional distribution: $S_G(g|\zeta, r, m)$.

Seismic hazard as a consequence of the seismicity rate distribution introduced above can be defined as the rate of exceedance $R_G(g|y,t)$, obtained by integrating over the rupture distance, space and magnitude dimensions:

$$R_G(g|y,t) = \iint S_G(g|\zeta(y),r,m) f_R(r|x,y,m) \lambda(t,x,m) \, dr \, dm \, dx.$$

Here, f_R represents the probability density function of the rupture distance. This distribution quantifies the rupture model, which describes the distribution of possible rupture lengths and orientations extending from the hypocentre conditional on the location and magnitude of the earthquake. For more details on the rupture model the reader is referred to TNO (2020). In the current project, the rupture model is adopted identically from the Groningen model chain. To arrive at an annual probability of exceedance $P_G(g|y)$ two more steps are required. First, the rate needs to be integrated over the span of a year, and then, based on the Poisson assumption, the probability $P_G(g|y)$ of at least one exceedance in this period can be defined as the complement of the probability of no exceedance. Under the assumption that all events are independent (Poisson assumption) the waiting time for the next event follows an exponential distribution. This means that the probability that no event occurs within a year is equal to the probability that the waiting time exceeds one year. Hence, we get:

$$P_G(g|y) = 1 - \exp\left(-\int R_G(g|y,t) \, dt\right),$$

where the integration over time relates to the specific time period of one year. Again, for more details, see TNO (2020) or Baker et al. (2021).

In the following sections we describe how we define the seismicity rate distribution $\lambda(t,x,m)$ using the Seismic Source Model (SSM, Section 4.2.2) and the conditional ground motion distribution represented by survival function $S_G(g|\zeta,r,m)$ using the Ground Motion Model (GMM, Section 4.2.3). Results in the form of seismicity and hazard maps will be provided in the Results (Section 4.3).

4.2.2 Seismic source model

The seismic source model is tasked with providing the seismicity rate λ as the expected number of earthquakes per unit time, per unit area and per unit magnitude. The seismicity rate function depends on time t, spatial dimensions x, representing the location of the hypocentre, and magnitude m. The seismic source model used in his study was developed for the Groningen gas field and has been extensively described in previous publications (Bourne and Oates, 2017; TNO, 2020). Here, rather than applying the model to the SW aquifer only, we spatial *extend* the Groningen source model to include the SW aquifer. This way, we get a spatially continuous seismicity model to incorporate in the seismic hazard calculation. This is desirable from a physical perspective, since seismicity within the bounds of the Groningen gas field affect the hazard calculation above the SW aquifer and vice-versa.
The input needed for the source model consists of:
- Reservoir compressibility
- Reservoir pressures through time
- Fault locations and properties, including the fault throw and reservoir thickness at fault

All these inputs are readily available for the area covered by the Groningen gas field. For the SW aquifer, and ensemble of the reservoir compressibility and reservoir pressures has been obtained in this study. This was covered in Chapter 3. Both the reservoir compressibility and reservoir pressures are described as 2D 'map-view' grids, without accounting for the depth dimension. This follows the 'thin-sheet' geometry assumption that underlies the Groningen source model (Bourne and Oates, 2017).

The structural model used to generate the dynamic model in Chapter 3 contains the fault locations, including the fault throws and reservoir thickness at fault. These were extracted and converted to the same format as the faults in the Groningen reservoir, where faults are represented by their location in map view as a collection of points, with their throw and reservoir thickness as attributes at each point.

With the required inputs available for both the Groningen gas field and the SW aquifer, the next step is to merge them.

For the compressibility and reservoir pressures, there is some overlap between the KEM19b reservoir model and the pressures available for the Groningen gas field. In other words, the original Groningen gas field reservoir model contains a pressure forecast for part of the SW aquifer, and the KEM19b reservoir models contain pressure forecasts for part of the Groningen gas field. For the locations that spatially overlap, we have chosen to populate the combined model according to the following logic: if the location falls within the mapped outline of the Groningen field, the Groningen reservoir model is used, while all locations outside this polygon are populated using the KEM19b model. We believe this choice most closely honors the original purpose of each reservoir model; the Groningen reservoir model was created to model pressures within the gas field, while the KEM19b models were created to model pressures in the aquifer.

Combining the two fault datasets was slightly more involved, due to the nature of fault data. Individual faults are represented as a collection of points. In order to properly incorporate these points in the seismic source model, it is not only important to know which point belongs to each fault, but also the distance to their neighboring point(s) and therefore their 'order' within the fault. A simple way to maintain this structure would be to simply add the two fault databases together. However, this would result in faults that are present in both models to be 'double counted' and since fault density is an important metric for the seismicity model, this is not desirable. We therefore do the following:

1. For each fault in the original Groningen database, we check whether for each of its constituent points whether it falls within the area covered by the KEM19b pressure model. If the fault is fully outside the KEM19b area, we label it *keep*. If it falls fully within the KEM19b area, we label it *dismiss*. If it partially falls within the KEM19b area, we label it for manual checking (Figure 4.1a).
2. Since the faults from the KEM19b fault database only cover the KEM19b area, we can now add the faults from the original Groningen model labelled *keep* and the KEM19b fault database, without any double counted faults (see Figure 4.1b).
3. The faults labelled *check* are inspected individually. For these faults, it is possible that they partially represent a fault that is already included in the KEM19b model, and should therefore be dismissed in the overlapping section. This is done on a fault-by-fault basis (see Figure 4.1c).

The result is a combined fault database that contains all faults that were present in the original Groningen fault model and the KEM19b fault model, but without any 'double' counting of faults or parts of faults.
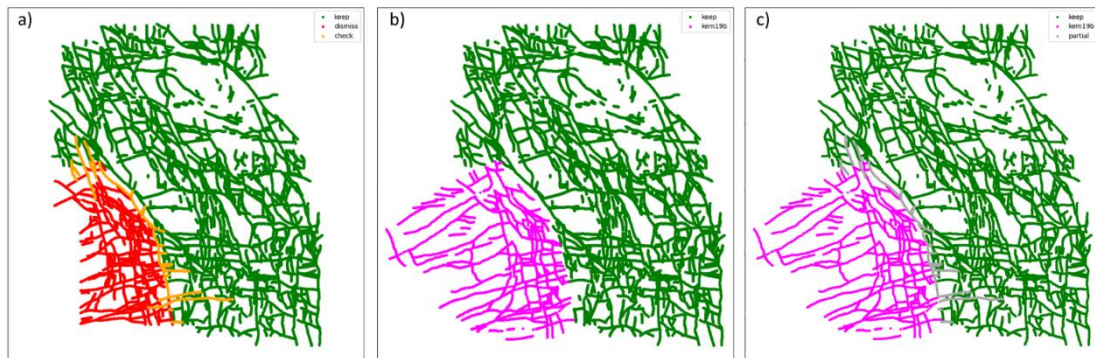
Figure 4-1: Three stages of merging the original Groningen and KEM19b fault databases. Subfigure (a) shows the curation of the original dataset, subfigure (b) the combination of the mutually exclusive sets, and (c) the inclusion of curated faults at the boundary

As described in Section 3.5.1, 22 reservoir models were selected to represent the uncertainty in pressure evolution of the SW aquifer. Each pressure realization comes with its corresponding compressibility realization which need to be multiplied with a factor between 0.5 and 0.6 to obtain the final compressibility map. To represent a low, medium, and high compressibility scenario, we here choose 0.51, 0.55, and 0.59. This means that a total of 66 sub-surface realizations are used for calibration and forecast.

To calibrate the seismic source model, a Bayesian framework is applied (TNO, 2020). The data used to infer the posterior distribution of model parameters consists of all 371 recorded earthquakes of M1.5 and above in the period 1995-01-01 until 2024-04-30 (KNMI, 2024). Of these, 12 events fall within the SW aquifer, while the remaining 359 fall within the Groningen field outline.

The calibration is performed for each reservoir compaction realization (see Chapter 3) independently. For each realization, a well-defined posterior distribution is obtained. Although not identical, the posterior parameter distribution are very similar between the 66 realizations. It's also interesting to note that the posterior parameter distributions that are obtained are fairly similar to the one obtained on the 'base' reservoir model. This means that adding the SW aquifer to the model does not significantly change our understanding of the physical parameters of the seismicity-controlling processes, and conversely, that our understanding of the seismicity based on the Groningen reservoir does a reasonable job of explaining the observed seismicity in the SW aquifer.

4.2.3   Ground motion model

For the ground motion model of KEM19b we adopt the general approach of the GMM-V7 ground motion model for the Groningen field as developed by Bommer et al. (2021). GMM-V7 is a probabilistic model in the sense that it provides probability distributions of ground motion attributes conditional on the three predictor variables, introduced in Section 4.2.1, being the magnitude m, the distance to the rupture plane r and zone-index or -identifier ζ. The latter represents the variety of physical properties associated with a specific geological zone in which the surface point where the ground motion is realized is located. The ground motions attributes of interest are the spectral accelerations, which encode the hypothetical response of idealized buildings with a set of specific resonance periods. In risk assessment practice, the spectral response of actual buildings can be predicted in terms of these idealized spectral accelerations. These assessments, however, are not part of the current work.

The ground motion model (Bommer et al., 2021) consists of two main components:

1. A *reference ground motion* model that expresses the distribution of spectral accelerations at a reference level at approximately 800 m depth below the surface, i.e., the bottom of the North-Sea lithostratigraphic unit. This part of the model is ergodic, in the sense that all lateral and directional variations in ground motions due to heterogeneities in the subsurface properties and rupture processes are summarized in a predictive model conditioned only on earthquake magnitude and rupture distance.

2. A *site response* model that expresses the amplification and/or damping of ground motions propagating upwards from the reference level to the surface. This model is only partially ergodic, in the sense that it does takes into account spatial variations of the physical properties of the local soils by using a regional zonation. For GMM-V7 a total of 160 zones are defined on the basis of geological characterization. See Kruiver et al. (2017a) for het methodology applied for an earlier version of the model.

For the KEM19B project we have made the decision to adopt the first component, the ergodic reference ground motion model, identically from the Groningen GMM-V7. This is warranted because of the proximity of the SW aquifer to the Groningen field and the reality that there is no additional information available to constrain the model beyond that what was used for GMM-V7.

For the second component, the site response model, however, additional information is required since its geographic domain of application explicitly extends beyond the contours considered in GMM-V7.

Figure 4.2 shows the geographic domain of the aquifer in relation to the domain of the Groningen model chain and the GMM-V7 model.

The extension of the site response model involves the following 4-step work plan:

1. Interpretation and characterization of geological features of the shallow subsurface and construction of regional zonation (Kruiver et al., 2017a),
2. Generation of (stochastic) ensembles of representative shear-wave velocity profiles for every zone (Kruiver et al., 2017b),
3. Numerical analysis of wave amplification for all generated shear-wave velocity profiles using a stochastic sample of representative input motions (Kruiver et al., 2017b, Rodriguez-Marek et al., 2017),
4. Calibration of the non-linear amplification model (Rodriquez-Marek et al., 2017, Bommer et al., 2021).
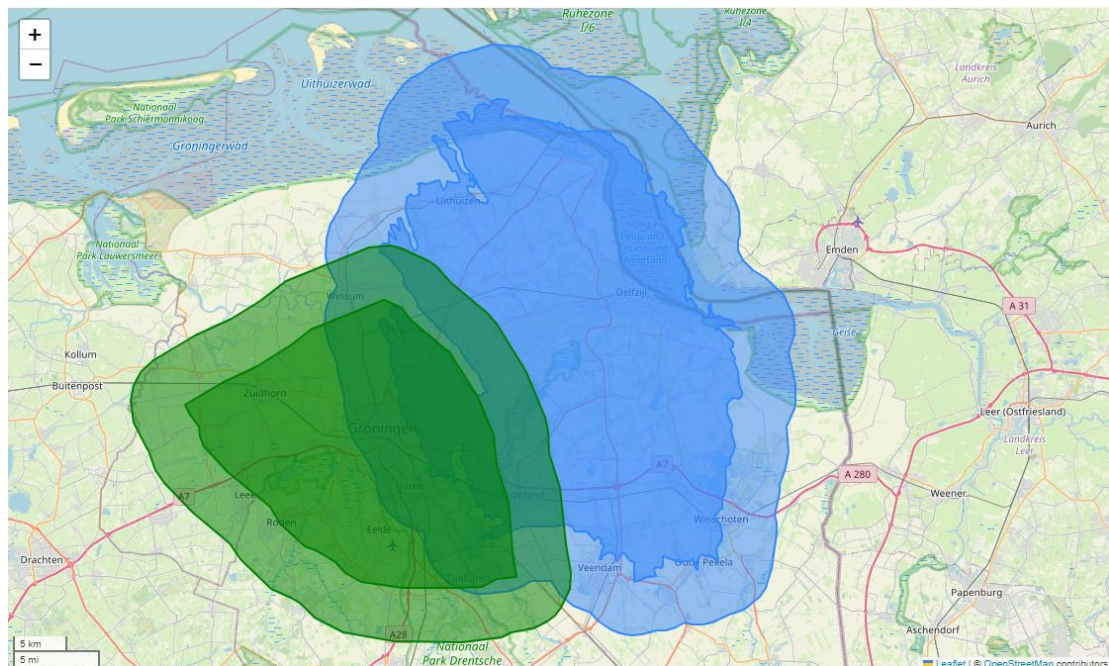
Figure 4-2: Geographic regions involved in the seismic hazard assessment for the Groningen field (blue) and the KEM19-B SW aquifer (green). The darker patches represents the subsurface domains. The lighter areas represent a five km buffer that demarcates the spatial extent of the site response model.

Step 1 above was already completed by the earlier work in the context of the Groningen GMM project. Figure 4.3 shows both the geological zonation obtained for the work described in Kruiver et al. (2017a) and the KEM-19B project area. It shows that a small fraction of the site response region has not yet been covered by a geological zone. We have decided to designate this region a separate zone. A complete KEM-19B zonation has been constructed by first determining the geometric intersection of the geological zonation and the KEM-19B site response area, and second determining the geometric complement with the existing GMM-V7 zonation. The final zonation is displayed in Figure 4.4. It contains 81 new zones in addition to the 160 zones adopted from GMM-V7.
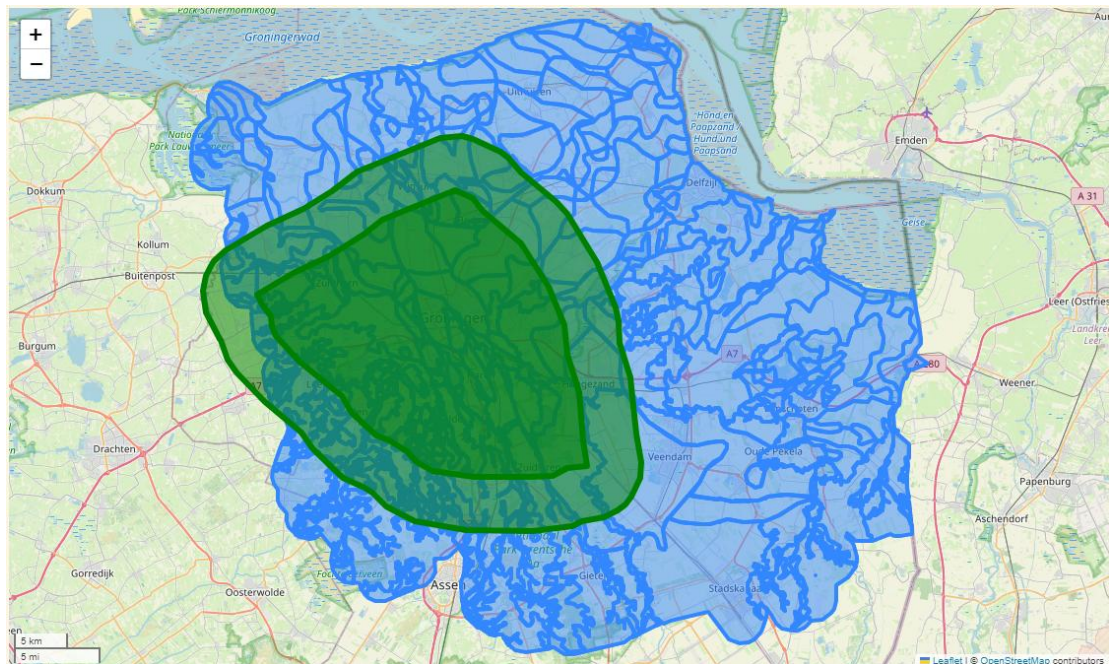
Figure 4-3: Kem 19-B geographic region against in the background the geological zonation obtained for the Groningen GMM project (Kruiver et al., 2017a).
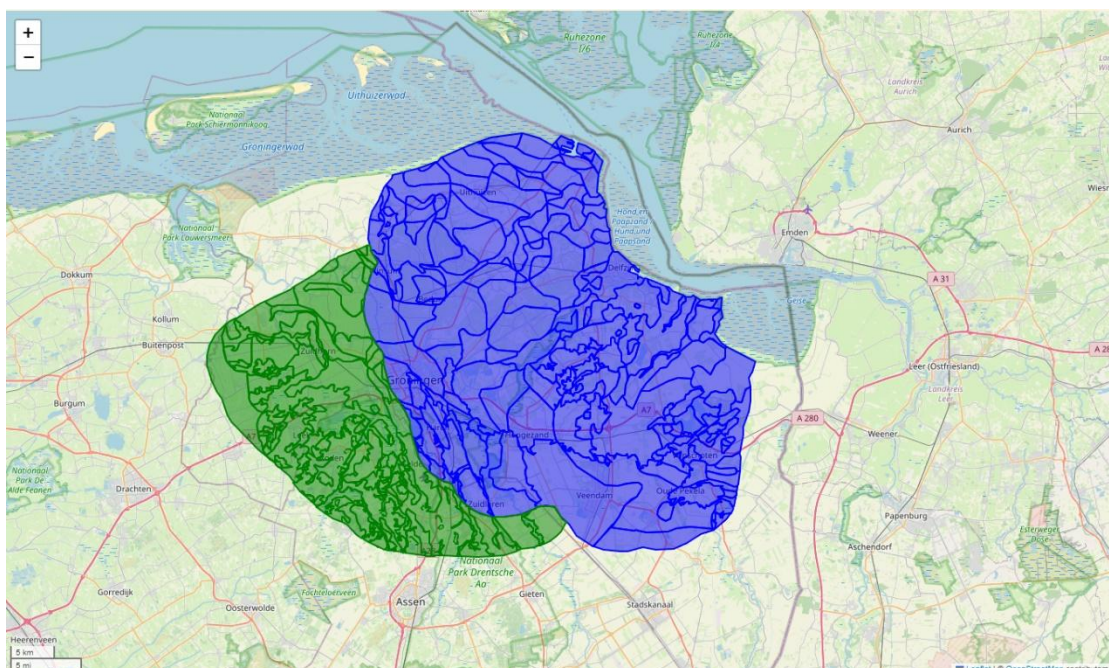
Figure 4-4 Site response zonation of GMM-V7 in blue, and the extension provided by the KEM-19B project in green.

Steps 2 and 3 of the work plan have been executed by Deltares and reported in Appendix E They have largely followed the work flow that they used in their contribution to GMM-V7 (Bommer et al., 2021). As an output of their work they have delivered stochastic sets of synthetic amplification data organised per KEM-19B site response zone.

Step 4 of the work plan involves the calibration of a predictive amplification model using the data obtained in Step 3. During the execution of this step it became clear that it within the

current project we are not able to completely reproduce the workflow of GMM-V7, as described in Bommer et al. 2021 (Chapter 8) for two reasons. First, the description of the workflow in Bommer et al., is insufficient to fully reproduce it as it depends on undocumented algorithmic choices. Second, it turns out that calibration has been by using a combination of both linear and equivalent-linear simulations, where the linear simulations are used to calibrate the linear part of the model and the equivalent-linear simulations for the non-linear. However, for the KEM-19b project only the equivalent-linear simulations have been performed. In principles it is possible to perform an independent calibration, but that will produce inconsistencies between the GMM-V7 and the KEM-19b parts of the ground motion model. Since the main focus of the project is to study effects of changes in the source distribution, a conflation with changes in the ground motion model appears undesired.

Instead of an independent calibration, we have chosen to infer the site amplification model for each KEM-19b zone by selecting the best fitting (maximum likelihood) model out of the 160 GMM-V7 models. This appears a reasonable compromise between adaptation and consistency. An example of the inferred models is shown in Figure 4.5. The fact that the new zone functions are fairly distributed among the original GMM-V7 options provides confidence that the original distribution is sufficiently wide. In addition an example map view of the linear amplification is provided in Figure 4.6.
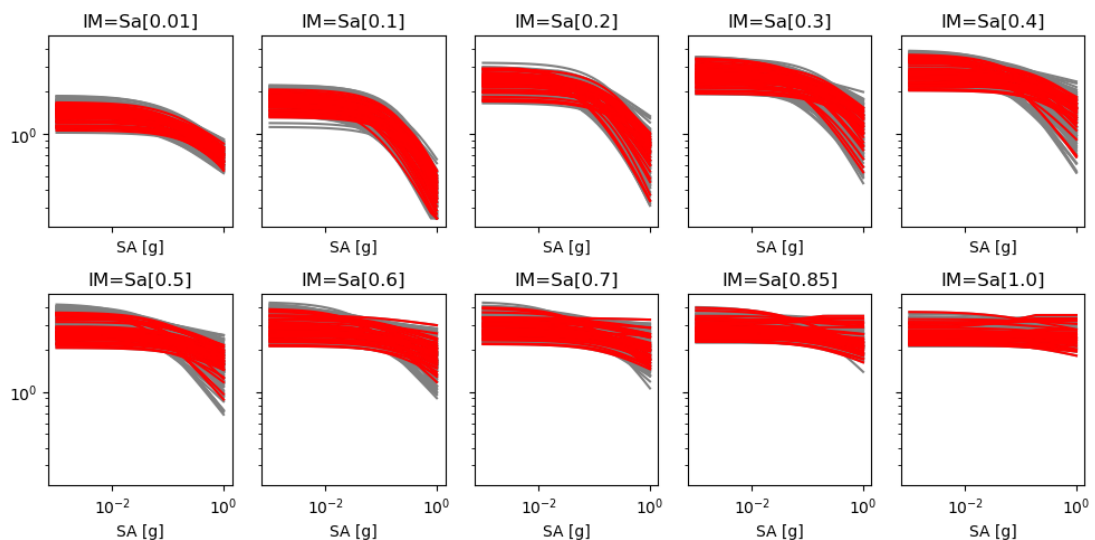
Figure 4-5 Median site amplification as a function of reference spectral acceleration per spectral component for all zones. The grey curves represent the 160 zones of the GMM-V&, while the red curves represent the 81 new zones for KEM-19B. The curves are produces for an earthquake of magnitude 4.5 at distance of 15 km, to be able to compare to Figure 8.8 in Bommer et al. (2021).
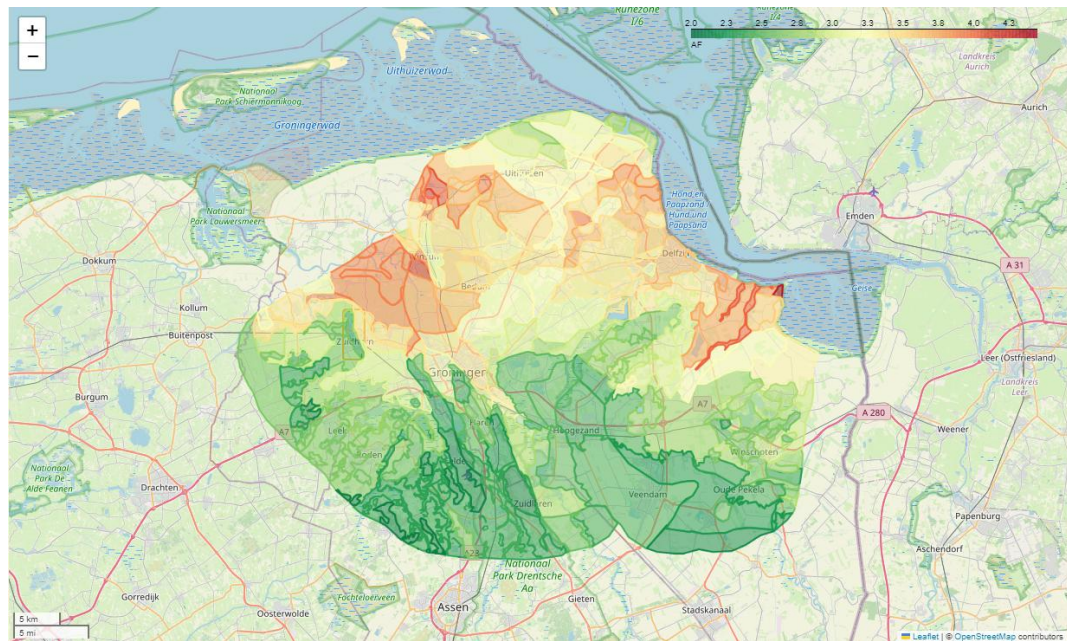
Figure 4-6: Linear amplification response per zone for spectral acceleration at a period of 0.6s (Sa[0.6]), for an earthquake of magnitude 4.5 at 5 km distance.

4.3 Results

The calibrated source models (all 66 realizations) can be used to forecast seismicity into the future, based on the spatio-temporal pressure forecast of each model (see Section 4.2.2 for details). Although there is quite a range of pressure scenarios contained in the ensemble, the ensemble of seismicity forecasts is significantly less wide. In fact, both the spatial and temporal signature of the 66 seismicity forecasts look remarkably similar, not just to each other, but also to the seismicity forecasts generated in the past for the Groningen gas field (TNO, 2023b). It is difficult to strictly speak of 'seismicity in the SW-aquifer' versus 'seismicity in the Groningen field. This is for two reasons. First, the pressures in the SW-aquifer and the Groningen field influence each other, and consequently the resulting vertical strains and seismicity are interconnected as well. Second, the spatial smoothing that is an inherent part of the seismic source model further blurs the clear distinction between the two areas. It is therefore more sensible to view the models as a whole: the Groningen gas field models (TNO, 2023b) on one hand, and the models of the Groningen gas field plus the SW-aquifer on the other hand (this work).

In the calibration period (1995-01-01 until 2024-04-30) a total of 371 M1.5+ events occurred in the area covered by the Groningen gasfield and the SW aquifer (black lines in Figure 4.7). Of these, 12 happened in the SW aquifer, outside the boundaries of the Groningen gas field. The calibrated models hindcast a total of ~5.1 events in this area. It is important to realize that the calibration attempts to find the best fitting model in space and time. Any sub-section of the model, whether in space or time or both, is likely to either overpredict or underpredict compared to the data. However, since this study specifically focusses on the SW aquifer, we believe it's important to further explore the nature of the mismatch between model and data. Of the 12 events observed in the SW aquifer, 6 appear to be directly related to the gas fields of Roden and Vries (see Table 11). Although these gas fields are included in the KEM19b pressure model, our model was aimed at representing the aquifer and the uncertainty in the pressure distribution within the aquifer, rather than the gas fields that are connected to the aquifer. It may therefore be reasonable to expect that our model does not capture these seismic events well. The remaining 6 events do occur within the 'true' aquifer portion of the model. This number compares well to the ~5.1 events hindcasted by our calibrated model.

Table 5: Events in the SW aquifer during the calibration period.

Date	Latitude	Longitude	Magnitude	Description
1996-09-02	53.147	6.422	2.1	Roden (Roden gas field)
1996-12-28	53.107	6.505	1.9	Bunne (Vries gas field)
1996-12-28	53.111	6.502	1.8	Bunne (Vries gas field)
2006-09-06	53.189	6.522	1.8	Aquifer
2009-01-01	53.095	6.718	1.5	Aquifer
2011-06-05	53.176	6.612	1.5	Aquifer
2012-08-09	53.183	6.613	1.5	Aquifer
2013-07-08	53.305	6.542	1.6	Aquifer
2017-03-06	53.327	6.571	1.6	Aquifer
2020-09-27	53.122	6.496	1.8	Winde (Vries gas field)
2023-08-22	53.117	6.495	1.6	Winde (Vries gas field)
2023-08-23	53.117	6.496	1.7	Winde (Vries gas field)

Here, we show the ensemble mean forecast (equal weight applied to all ensemble members, Figure 4.7). Although the SW aquifer is included in the model, it is barely visible due to the small amount of seismicity forecasted. The main reason for the lack of forecasted seismicity in the SW aquifer is the relatively limited pressure decline (and associated vertical strain) in this region. In the seismic source model, there is a linear relation between vertical strain and incremental Coulomb stress. The relation between incremental Coulomb stress and seismicity rate is exponential. This means that the amount of seismicity resulting from a given amount of pressure decline depends heavily on the local reservoir pressure: the lower the pressure, the more seismicity results from a given amount of pressure decline. The slow and limited pressure decline in large parts of the SW aquifer (slow and limited compared to the Groningen gas field) means that the seismicity rate in this region is expected to remain low in the future: in the 30 years that the forecast covers (GY 2024/2025 until GY 2053/2054) the number of expected events of M1.5 and above within the entire region (gas field + SW aquifer) is 43.04 (ensemble standard deviation: 0.55). In the same time period, the total number of expected events of M1.5 and above within the SW aquifer is 2.24 (ensemble standard deviation: 0.17).

Table 6: Forecasted event rates in the entire model, and the SW aquifer area specifically.

Gas year	Total event rate (M1.5+)	SW aquifer event rate (M1.5+)
2024/2025	4.25	0.12
2025/2026	3.70	0.11
2027/2028	3.24	0.11
2028/2029	2.87	0.10
2029/2030	2.54	0.10
2030/2031	2.26	0.09
2031/2032	2.03	0.09
2032/2033	1.82	0.08
2033/2034	1.65	0.08
2034/2035	1.52	0.08
2035/2036	1.40	0.07
2036/2037	1.31	0.07
2037/2038	1.22	0.07
2038/2039	1.14	0.07
2039/2040	1.07	0.07
2040/2041	1.01	0.07
2041/2042	0.95	0.07
2042/2043	0.90	0.07
2043/2044	0.82	0.06
2044/2045	0.82	0.06
2045/2046	0.78	0.06
2046/2047	0.74	0.06
2047/2048	0.71	0.06
2048/2049	0.68	0.06
2049/2050	0.65	0.06
2050/2051	0.63	0.06
2051/2052	0.59	0.06
2052/2053	0.57	0.06
2053/2054	0.55	0.05
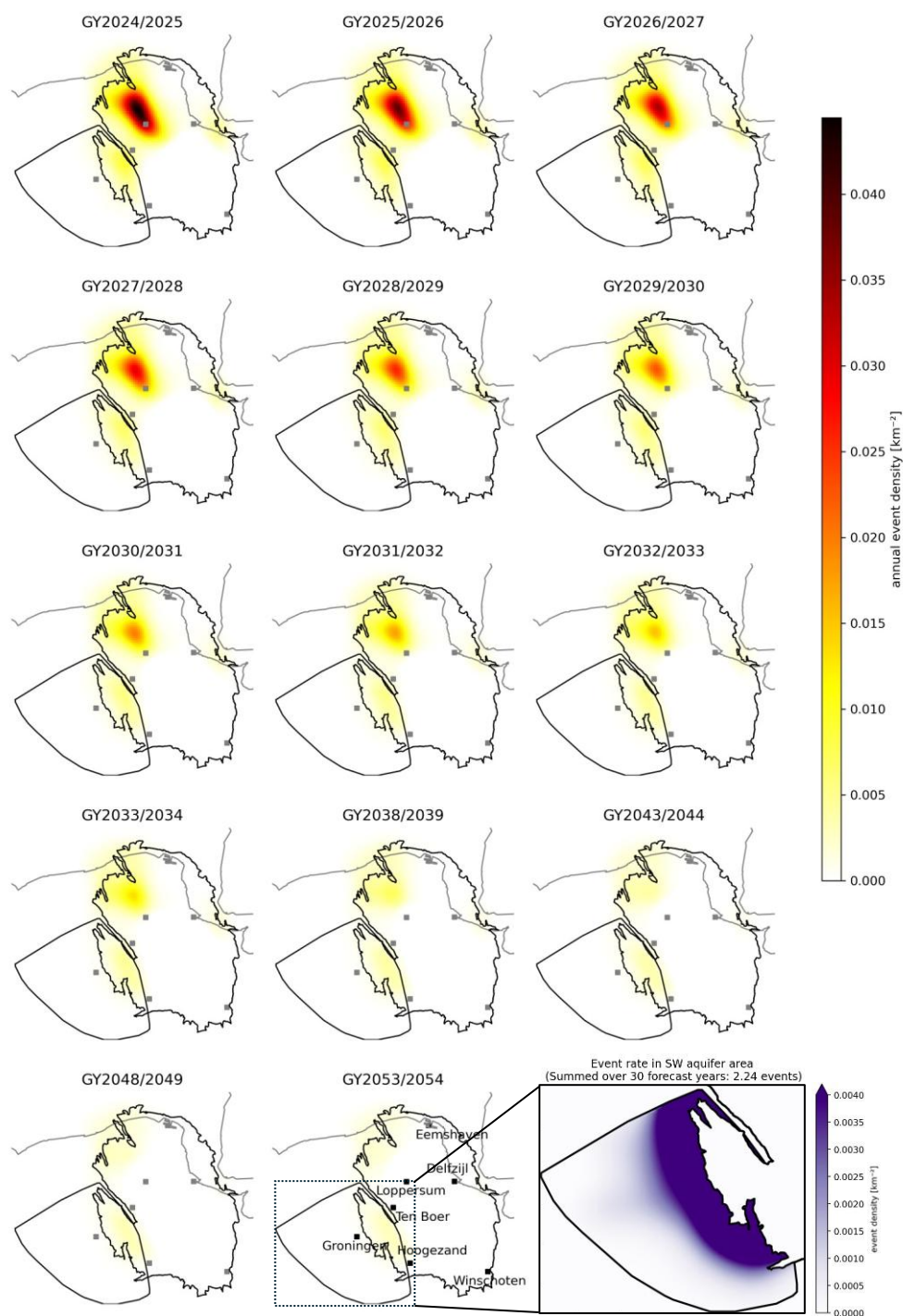
Figure 4-7 Ensemble mean seismicity forecast for the Groningen gas field and the SW aquifer combined. The forecasted seismicity in the SW aquifer is low for all forecasted years and the individual ensemble member forecasts all look very similar to the ensemble mean. The extent of the Groningen field outline and the SW aquifer model is shown in black solid lines. In the bottom-right, we show a zoom-in on the SW aquifer, with a different color scale. This sub-figure shows the total event density over 30 years, indicating that the event rate is highest close to the Groningen gas field. It is important to note that compared to the Groningen gas field, the event rate in the SW aquifer is much lower, as can be seen in the annual figures with the yellow-red color scale.

With the extended ground motion model (including the site-response model) available, the seismic hazard (annual probability of exceedance of spectral accelerations per selected surface point) can be calculated. This is the seismic hazard related to the ongoing pressure development in the aquifer under study, as well as in the Groningen gas field. Conversely, the extended seismic source model also influences the seismic hazard that is calculated for the original area under consideration of the Groningen pSHRA. However, due to the low seismicity rates forecasted in the SW aquifer, the impact of the extended source model is limited, both in the area covered by the original GMM-V7 model and in the area added in this study. In Figure 4.8, we show a comparison between the hazard calculated using the base reservoir model as described in Chapter 2, and the hazard calculated using the spatial extension of the reservoir model including the SW aquifer. Both hazard calculations use the same source model and ground motion model (besides the spatial extension). This comparison conveys that the spatial extension of the source model to include the SW aquifer does not increase the hazard compared to before in the area that was previously already included in the hazard calculation. In fact, in the area west of the city of Groningen, the hazard actually decreases. This is a direct result of the updated source model forecasting less events in this region, which in turn stems from the model being calibrated on a different spatial region (now including the SW aquifer). Although the updated spatial distribution appears to better match the observed events, this is in some way a 'lucky' outcome since no explicit effort was made to improve the spatial match; the underlying source model is unchanged in terms of its representation of physics.

The hazard in the newly considered area above the SW aquifer is very much in line with what could be expected based on simple extrapolation of the pSDRA 2023 results. In Figure 4.9, we include an overview of the hazard maps (PGA, 475 year return period) for up to gas year 2053/2054. The individual hazard maps are included in Appendix D.
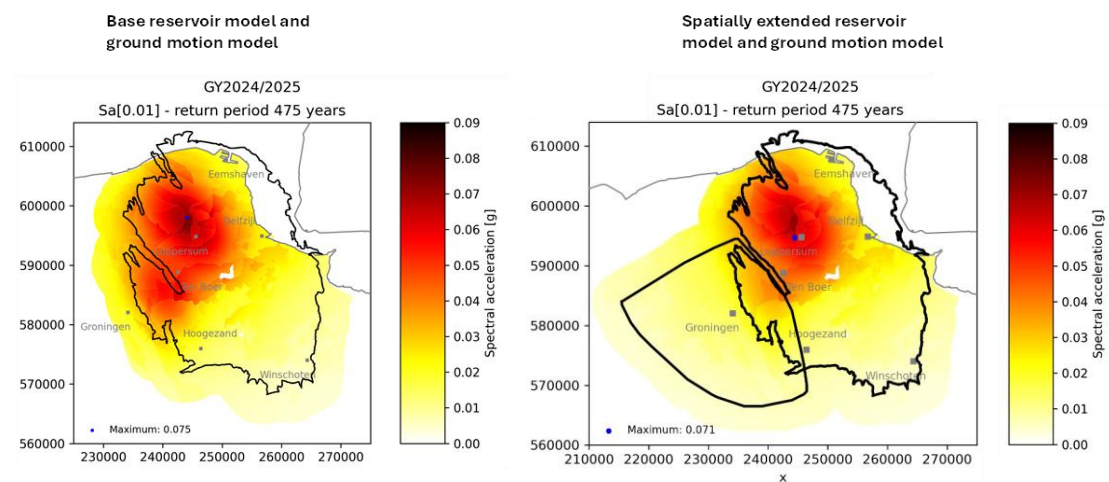
Figure 4-8 Hazard maps for PGA at 475 years from the pSDRA 2023 (TNO, 2023b) and the current study (KEM19b).

Sa[0.01] return period: 475 years
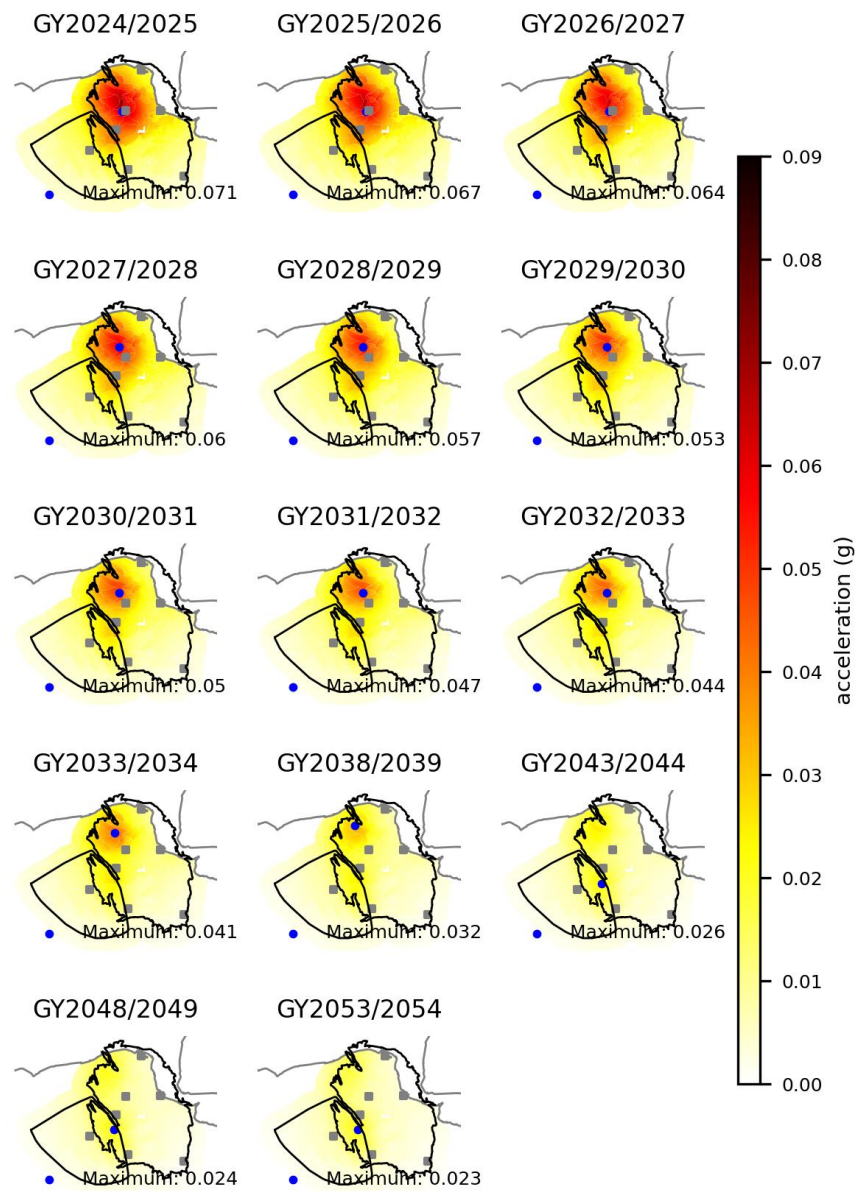
Figure 4-9: Hazard maps for PGA at 475 years for the coming gas years.

4.4 Discussion and conclusions

The work presented in this chapter shows we have been able to successfully extend both the Ground Motion Model and the Seismic Source Model for the Groningen area to include the SW aquifer. Even though this project focusses on the seismicity and seismic hazard resulting from pressure changes in the SW aquifer, an important feature of our modelling throughout is the consistency in approach and models between the original Groningen seismicity & seismic hazard assessment, and those for the SW aquifer. Adding the site response model and extending the subsurface models required some implementation choices to be made. However, we do not expect these choices to significantly impact the results of either the seismicity forecast or the seismic hazard calculations. Using the results from Chapter 3, we incorporate the significant uncertainty in both the past and future pressure evolution of the SW aquifer through an ensemble of pressure models. For each ensemble member, we successfully calibrated the seismic source model for the combined SW aquifer and the Groningen gas field, with a posterior parameter distribution that is similar to that obtained for the Groningen field alone. This means that the model parameters that get significant weight in forecasting the seismicity for the Groningen gas field also get significant weight in the combined model, indicating that the model captures the relevant physics. Despite the considerable uncertainty related to the pressures, once calibrated, the seismicity forecasts of the individual pressure model ensemble members all show very limited seismicity in the SW aquifer when compared to the expected ongoing seismicity in the Groningen field. This relatively small uncertainty surrounding the number of induced events in the SW aquifer stems from the subsidence inversion, which allows us to forecast the expected vertical strain (the product of pressure depletion and compaction coefficient, which in the end drives seismicity in the model) with much more certainty than the pressure depletion itself. This is an important result, as it indicates that the uncertainty in the pressure forecasts does not translate to uncertainty around seismicity. Finally, due to the low level of forecasted seismicity in the SW aquifer, there is a very limited impact of this newly modelled seismicity on the seismic hazard above the SW aquifer. In fact, the hazard in the 81 zones that were added to the site response model in this study is equal or lower than the hazard on the former western edge of the site response model. That means that this study did not identify a 'previously missed' zone of increased seismic hazard due to seismicity in the SW aquifer, but rather that we've identified that the seismic hazard continues to decrease with increasing distance from the Groningen gas field and that the seismicity of the SW aquifer itself is very limited and does not significantly change this general picture.

5 Conclusions and recommendations

This study addressed the following research questions:

1. What will be the pressure depletion of the southwestern aquifer taking into account the depletion of Groningen gas field as well as the smaller gas fields in the Lauwerszee Trough?
2. What are the locations of smaller faults, and their orientation and throw in the southwestern aquifer?
3. What is the expected induced seismicity in the coming decades?
   a. What is the seismic hazard?
   b. How does this compare to the seismic hazard of the Groningen gas field?

These can be answered as follows:

1. The current study has resulted in the forecast of pressure depletion for an ensemble of 22 out of 100 flow models in the SW aquifer of Groningen gas field in the southern Lauwerszee Trough. The model ensemble was ranked based on static pressure measurements in the small gas fields and observations of subsidence above the aquifer. The surface movement measurements have helped making this ranking by discriminating the models according to how the calculated surface movements fit the measured ones. The forecast of the depletion on the east side of the aquifer is dominated by the Groningen field, although the production from the Roden field likely has caused depletion in this area in the period before 2000. After that the depletion due to production near Harkstede (from EKL-13) dominated the pressure depletion. The aquifer between the small gas field Pasop (just North of Roden) and the Groningen field, also shows considerable depletion, but based on the timing of the drawdown this appears to be caused more by production from the Groningen field, in particular the Eemskanaal cluster, than from Pasop. The other small gas fields appear to have a more local influence.

2. The smaller faults in the aquifer, which were interpreted in this project, are mainly short faults with east-west orientation and a small throw of less than 40 m. In general, the large faults (both in length and offset) are oriented west-south-west to east-north-east. Near the Harkstede area (the transition of the Groningen field to the aquifer) has several north-south faults with large off-set.

3. The expected induced seismicity in the SW aquifer, taking into account the considerable uncertainty in the pressure depletion, is low (see Figure 4.7). We obtain a total of 2.24±0.17 expected events of M1.5 and above within the south west aquifer in the 30 years that the forecast covers (GY2024/2025 until GY 2053/2054). For context, the number of expected events of M1.5 and above for that same time period within the entire region is 43.04±0.55.
   a. The seismic hazard in the 81 added site-response regions above is relatively low, with a PGA value of 0.02g or below (see Figure 4.9).

b. These hazard levels are comparable to those in the southeast region of the Groningen earthquake area, or around Hoogezand (see Figure 4.9).

Recommendations
The forecasted seismicity in the SW aquifer and associated seismic hazard at the surface is relatively low, despite the relatively large uncertainty range in the underlying pressure forecasts. Therefore, in the context of this study (seismicity related to pressure changes in the SW aquifer due to its connection to the Groningen gas field), no major effort is currently recommended to further reduce uncertainty. It is recommended to keep monitoring the subsidence above the aquifer, in particular near just west of Harkstede and Ten Boer, to check that the subsidence remains within the ranges forecasted by the ensemble of models.

In case of future activities in the aquifer, however, more detailed analysis might be required. In that case, the workflow could be improved in several ways:
- The largest added value is in particular a joint history match of the reservoir and subsidence model based on pressure and subsidence measurements.
- If a joint history match is not feasible, several improvements to the two step approach are also possible. These are discussed in paragraph 0.
- Future human activities in the aquifer will likely impact the pressure and temperature fields in the aquifer. Assessing the magnitude and spatial footprint of the changes in these fields will be a crucial part of updating the seismicity model and consequently of updating the seismic hazard assessment.
- The current seismic source model uses for both the Groningen gas field and the SW aquifer (in this study), assumes a so called 'thin-sheet' geometry, which is based on the large horizontal extent of the reservoir compared to its thickness, and the relatively smooth spatial changes (small spatial gradients) of pressure and temperature. If future operations lead to violation of these assumptions, for example by introducing relatively large temperature gradients, the source model may need to be updated to account for these changes.

In addition to improvements to the workflow, the low availability of pressure data in the aquifer remains a point of attention, especially in the context of potential future activities in the aquifer.

6   References

Amthor, J.E., Okkerman, J., 1998. Influence of Early diagenesis on reservoir quality of Rotliegende Sandstones, Northern Netherlands. AAPG Bulletin, V2, No.12, p. 2246-2265.

Baker, J., Bradley, B., & Stafford, P. (2021). Seismic Hazard and Risk Analysis. Cambridge: Cambridge University Press.

Bjørlykke, K., Aagaard, P., Egeberg, P.K., Simmons, S.P. 1995. Geochemical constraints from formation water analyses from the North Sea and the Gulf Coast Basins on quartz, feldspar and illite precipitation in reservoir rocks. In: J. Cubitt M., W. England A. (Eds.), The geochemistry of reservoirs, 86, Geological Society, London, pp. 33-50

Bommer, J.J., B. Edwards, P.P. Kruiver, A. Rodriguez-Marek, P.J. Stafford, B. Dost, M. Ntinalexis, E. Ruigrok and J. Spetzler, (2019). V6 Ground-Motion Model (GMM) for Induced Seismicity in the Groningen Field.

Bommer, J.J., B. Edwards, P.P. Kruiver, A. Rodriguez-Marek, P.J. Stafford, M. Ntinalexis, E.Ruigrok and B. Dost (2021). V7 Ground-Motion Model for Induced Seismicity in the Groningen Gas Field. Revision 1, 29 September 2021, 273 pp

Bourne, S. J., Oates, S. J. 2017. Extreme threshold failures within a heterogeneous elastic thin sheet and the spatial-temporal development of induced seismicity within the Groningen gas field. *Journal of Geophysical Research: Solid Earth*, 122, 10,299–10,320

Bouroullec, R., Verreussel, R.M.C.H., Geel, C.R., De Bruin, G., Zijp, M.H.A.A., Körösi, D., Munsterman, D.K., Jansse, N.M.M., Kersholt-Boegehold, S.J., 2018. Tectonostratigraphy of a rift basin affected by salt tectonics: synrift Middle Jurassic–Lower Cretaceous Dutch Central Graben, Terschelling Basin and neighbouring platforms, Dutch offshore. Geological Society, London, Special Publications, 469. In: Kilhams, B., Kukla, P. A., Mazur, S., McKie, T., Mijnlieff, H. F. & Van Ojik, K. (eds) Mesozoic Resource Potential in the Southern Permian Basin. https://doi.org/10.1144/SP469.22

Burkitov, U., H. van Oeveren and P. Valvatne, 2016. Groningen Field Review 2015. Subsurface Dynamic Modelling Report. https://www.nam.nl/feiten-en-cijfers.html.

Candela, T.G.G., Chitu, A.G., Peters, E., Pluymaekers, M.P.D., Hegen, D., Koster, K. and Fokker, P.A., 2022. Subsidence induced by gas extraction: A data assimilation framework to constrain the driving rock compaction process at depth. *Frontiers in Earth Science,* **10**, pp. 1-18.

Carr, N.L., Kobayashi, R., and Burrows, D.B.: 'Viscosity of Hydrocarbon Gases Under Pressure,' Trans. AIME (1954) 201, 264-272

De Jager, J., Visser, C., 2017. Geology of the Groningen field – an overview. Netherlands Journal of Geosciences – Geologie en Mijnbouw. 96-5, s3-s15. Doi: 10.1017/njg.2017.22

[DGM-deep V5 on- and offshore | NLOG](#)

Dranchuk and Abou-Kassem: 'Calculation of z-Factors for Natural Gases Using Equations of State,' JCPT (July-Sept. 1975) 34-36.

Fokker, P.A., Gunnink, J.L., Koster, K. and De Lange, G., 2019. Disentangling and Parameterizing Shallow Sources of Subsidence: Application to a Reclaimed Coastal Area, Flevoland, the Netherlands. *Journal of Geophysical Research: Earth Surface,* **124**(5), pp. 1099-1117.

Fokker, P.A., Wassing, B.B.T., Van Leijen, F.J. and Hanssen, R.F., 2016. Application of an ensemble smoother with multiple data assimilation to the Bergermeer gas field, using PS-InSAR. *Geomechanics for Energy and the Environment,* **5**, pp. 16-28.

Fryberger, S., Knight,R., Hern, C., Moscariello, A. & Kabel, S., 2011. Rotliegend facies, sedimentary provinces and stratigraphy, Southern Permian Basin UK and the Netherlands: A review with new observations. In Grotsch, J. & Gaupp, R., (eds). The Permian Rotliegend Of The Netherlands. SEPM Special Publication 98, pp. 51-88.

Gast, R.E., Dusar, M., Breitkreuz, C., Gaupp, R., Schneider, J.W., Stemmerik, L., Geluk, M.C., Geißler, M., Kiersnowski, H., Glennie, K.W., Kabel, S. & Jones, N.S., 2010. Rotliegend. In: Doornenbal, J.C. and Stevenson, A.G. (editors): Petroleum Geological Atlas of the Southern Permian Basin Area. EAGE Publications b.v. (Houten): 101-121.

Gaupp, R., Okkerman, J.A., 2011. Diagenesis and reservoir quality of Rotliegend sandstones in the Northern Netherlands – A Review. SEPM Special Publications 98:193-226, in the book: The Permian Rotliegend of The Netherlands.

Geluk, M.C., 2007. Permian. In: Wong, Th. E., Batjes, D.A.J. & de Jager, J., (eds). Geology of the Netherlands. Royal Netherlands Academy of Arts and Sciences: 63–83.

Geurtsen, L., A.J. Landman, G. Ketelaar, 2020. Groningen abandonment – Surveillance requirements. Nederlandse Aardolie Maatschappij B.V. EP number: EP202006201318.

Glennie, K.W., 1972. Permian Rotliegendes of Northwest Europe interpreted in light of modern desert sedimentation studies. American Association of Petroleum Geologists Bulletin. 56: 1048–1071.

Hernandez, E.O., 2023. Memo: KEM 19-B: Extended site response analysis to the south-west aquifer of the Groningen gas field. Deltares, 11209407-000-BGS-0001

Howell, J. And Mountney, N., 1997, Climatic cyclicity and accommodation space in arid to semi-arid depositional systems: an example from the Rotliegend Group of the UK southern North Lea, in Ziegler, K., Turner, P., and Daines, S.R., eds., Petroleum Geology of the Southern North Sea: Future Potential: Geological Society of London, Special Publication 123, p. 31–61.

Kestin, Khalifa, & Correia, 'Effect of Pressure on the Viscosity of Aqueous NaCl Solutions in the Temperature Range 20-150degC,' J. Chem. Phys. Ref. Data, Vol 10, No. 1, 1981, p 71.

KNMI 2024, https://rdsa.knmi.nl/abcws/event/query?eventtype=induced&format=csv. Last accessed 2024-12-20.

Kombrink, H., Van Lochem, H., Van der Zwan, K.J., 2010. Seismic interpretation of Dinantian carbonate platforms in het Netherlands; implications for the palaeogeographical and structural development of the Northwest European Carboniferous Basin. Journal of the Geological Society 167: 99-108.

Kortekaas, M., R. Bouroullec, S. Peeters, M. van Unen, M. Swart, D. den Hartog Jager, E. Wiarda, M. Nolten, and K. Beintema. 2023. Play 7 Rotliegend. https://www.geodeatlas.nl/pages/play-7-rotliegend

Kruiver, P.P., van Dedem, E., Romijn, R., de Lange, G., Korff, M., Stafleu, J., Gunnink, J.L., Rodriguez-Marek, A., Bommer, J.J., van Elk, J. &Doornhof, D., 2017b. An integrated shear-wave velocity model for the Groningen gas field, The Netherlands. Bulletin of Earthquake Engineering 15 (9): 3555–3580

Kruiver, P.P., Wiersema, A., Kloosteman, F.H., de Lange, G., Korff, M., Stafleu, J., Buscher, F., Harting, R. & Gunnink, J.L., 2017a. Characterisation of the Groningen subsurface for hazard and risk modelling. Netherlands Journal of Geosciences / Geologie en Mijnbouw.

Landman, A J., 2023. Groningen Dynamic Model Update 2023. NAM. Includes: Landman, A.J. and C. Visser, 2023. Groningen Dynamic Model Update V7. NAM B.V. EP202306200914

Molen, J. van der, E. Peters, F. Jedari-Eyvazi and S.F. van Gessel, 2020. Dual hydrocarbon–geothermal energy exploitation: potential synergy between the production of natural gas and warm water from the subsurface. *Netherlands Journal of Geosciences*, Volume 98, e12. https://doi.org/10.1017/njg.2019.11

Mossop, A., 2012. An Explanation for Anomalous Time Dependent Subsidence, *46th US Rock Mechanics / Geomechanics Symposium*, June 24-27, 2012 2012, pp. 1-8

NAM, 2021. Groningen long term subsidence forecast. NAM-report EP202008201822, version 2.

Nepveu, M., Kroon, I.C. and Fokker, P.A., 2010. Hoisting a Red Flag: An Early Warning System for Exceeding Subsidence Limits. *Mathematical Geosciences,* **42**(2), pp. 187-198.

Opstal, G. H. C. Van, 1974. The effect of base-rock rigidity on subsidence due to reservoir compaction, *Proceeding 3 of the International Society of Rock Mechanics Congress, Advances in Rock Mechanics* 1974.

Patruno, S., Reid, W., Jackson, C.A-L. and Davies, C., 2017. New insights into the unexploited reservoir potential of the Mid North Sea High (UKCS quadrants 35-38 and 41-43): a newly described intra-Zechstein sulphate-carbonate platform complex. In: Petroleum Geology of NW Europe: 50 Years of Learning – Proceedings of the 8th Petroleum Geology Conference. Geological Society, London.

Peeters, S.H.J., Geel, C.R., Garland, J., Bouroullec, R., 2023. Seismic and petrographic characterisation of the Zechstein Hauptdolomit platforms around the Elbow Spit High, Dutch offshore. Journal of Petroleum Geology 46(3): 361-382. https://doi.org/10.1111/jpg.12842

Pruiksma, J.P., Breunese, J.N., Van Thienen-Visser, K. and De Waal, J.A., 2015. Isotach formulation of the rate type compaction model for sandstone. *International Journal of Rock Mechanics and Mining Sciences,* **78**, pp. 127-132.

Reijmer, J.J.G., ten Veen, J.H., Jaarsma, B., Boots, R., 2017. Seismic stratigraphy of Dinantian carbonates in the southern Netherlands and northern Belgium. Netherlands Journal of Geosciences – Geologie en Mijnbouw, 96-4, 353-379. https://doi.org/10.1017/njg.2017.33

Rodriguez-Marek, A., Kruiver, P.P., Meijers, P., Bommer, J.J., Dost, B., van Elk, J. & Doornhof, D., 2017. A regional site-response model for the Groningen gas field. Bulletin of the Seismological Society of America 107 (5): 2067–2077

Smit, J., Van Wees, J-D. and Cloetingh, S., 2018. Early Carboniferous extension in East Avalonia: 350 My record of lithospheric memory. Marine and Petroleum Geology. 92, 1010-1027. Doi: 10.1016/j.marpetgeo.2018.01.004

Spivey, J.P. and McCain, W.D., Jr.: 'Recommended Correlations for Fluid Property Estimation,' unpublished September 2003

Staatstoezicht op de Mijnen (2016) Methodiek voor risicoanalyse omtrent geïnduceerde bevingen door gaswinning. Tijdelijke leidraad voor adressering MBB.24.1.P, versie 1.2

Ten Veen, J.H., van Gessel, S.F., den Dulk, M., 2012. Thin- and thick-skinned salt tectonics in the Netherlands; a quantitative approach. Netherlands Journal of Geosciences – Geologie en Mijnbouw, 91-4, 447-464.

Thienen-Visser, K. van, Nepveu, M. & Hettelaar, J. (2012) Deterministische hazard analyse voor geïnduceerde seismiciteit in Nederland. TNO rapport 2012 R10198.

TNO 2020. Probabilistic Seismic Hazard and Risk Analysis in the TNO Model Chain Groningen. TNO2020 R11052 | 3

TNO 2023b, Publieke Seismische Dreigings- en Risicoanalyse Groningen gasveld 2023. TNO R10682

TNO, 2023a. Berekende bodemdaling ten gevolge van de gaswinning uit het Groningen veld en de gasopslag Norg. TNO 2023 R10900.

TNO, 2024. KEM-24b: Preliminary assessment of beneficial effects of nitrogen injection in depleted reservoirs. TNO 2024 TNO 2024 R11366.

Van Hulten, F.F.N., 2006. Reservoir quality distribution as tool for better exploration prospect evaluation and estimation of the resource base in the Netherlands. In: Hulten, F.F.N. van & Lutgert, J.E. (comp.). Tight gas fields in the Netherlands, workshop EBN-TNO.

Van Leeuwen, P.J., 2009. Particle filtering in geophysical systems. *Monthly Weather Review,* **137**(12), pp. 4089-4114

Van Ojik, K., Böhm, A.R., Cremer, H., Geluk, M.C., De Jong, M.G.G., Mijnlief, H.F. & Nio, S.D., 2012. The rationale for an integrated stratigraphic framework kof the Upper Rotliegend II depositional system in the Netherlands. In: Grötsch, J. & Gaupp, R. (eds): The Permian Rotliegend of the Netherlands. SEPM Special Publication No. 98. SEPM (Tulsa, Oklahoma, USA): 37–48.

Van Wees, J.-D., SEPHENSON, R.A., Ziegler, P.A., Bayer, U., McCann, T., Dadlez, R., Gaupp, R., Narkiewicz, M., Bitzer, F. and Scheck, M., 2000. On the origin of the Southern Permian Basin, Central Europe. Marine and Petroleum Geology, 17, 43-59.

Visser, C.A., 2012. Groningen Field Review 2012; static modelling and hydrocarbon volume determination. Published under 'Feiten en cijfers', available at www.nam.nl

Visser, C.A., Porter, R.J & Solano Viota, J.L, 2016. On the implementation of sedimentological data in porosity modelling of the Groningen field. Published under 'Feiten en cijfers', available at www.nam.nl

Zeeuw, Q. de and L. Geurtsen, 2018a. Groningen Dynamic Model Update 2018. Includes: Zeeuw, Q. de and L. Geurtsen, 2018. Groningen Dynamic Model Update 2018 – V5. NAM B.V. Zeeuw, Q. de and L. Geurtsen, 2018b. Groningen Dynamic Model Update 2019. https://www.nam.nl/feiten-en-cijfers.html. Includes: Zeeuw, Q. de and L. Geurtsen, 2018. Groningen Dynamic Model Update 2018 – V6. NAM B.V. EP201809202872

Signature

TNO ⟩ Energy & Materials Transition ⟩ Utrecht, 7 July 2025

Appendix A Petrophysical results

Calculated log data (porosity, φ, permeability, k, and net-to-grass, NtG)) for wells in the Roden, Pasop, de Vries, Boerakker and Faan fields. .

Each well panel follows similar layout: Track 1 = depth (MD, measured depth, depth along hole); Track 2 = input density log (RHOB/RHOB1) and other relevant logs , e.g. Caliper (CAL) and/or Gamma Ray (GR/GR100), Track 3 = sand/shale as proxy for NtG (clean sand calculated from GR < 60), Track 4 = calculated porosity log, Track 5 = calculated permeability log. Porosity is calculated from the density log (RHOB). Permeability is calculated from the porosity log using field specific poro-perm relationships. See section 2.4 for details.

Well tops follow the Stratigraphic Nomenclature (ZEZ1K = Coppershale member, ROCLT = Ten Boer Member, ROSL = Slochteren Formation, DCCU = Maurits Formation) or the NAM Groningen Model (RO__T, USS_** and LSS_**) naming convention.
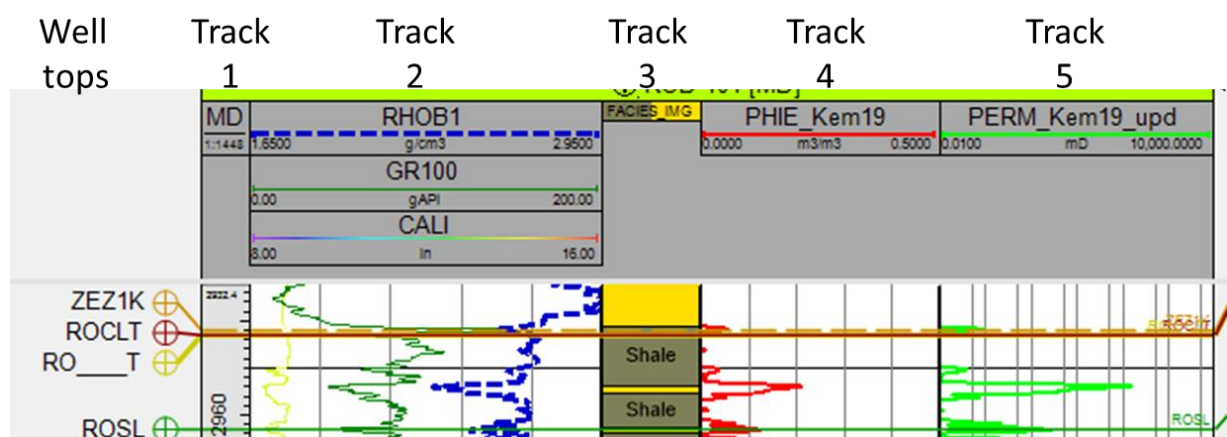
Figure 6-1: Example of a well panel with input and calculated porosity & permeability logs. See text for explanation on well tops and Track 1 – 5.
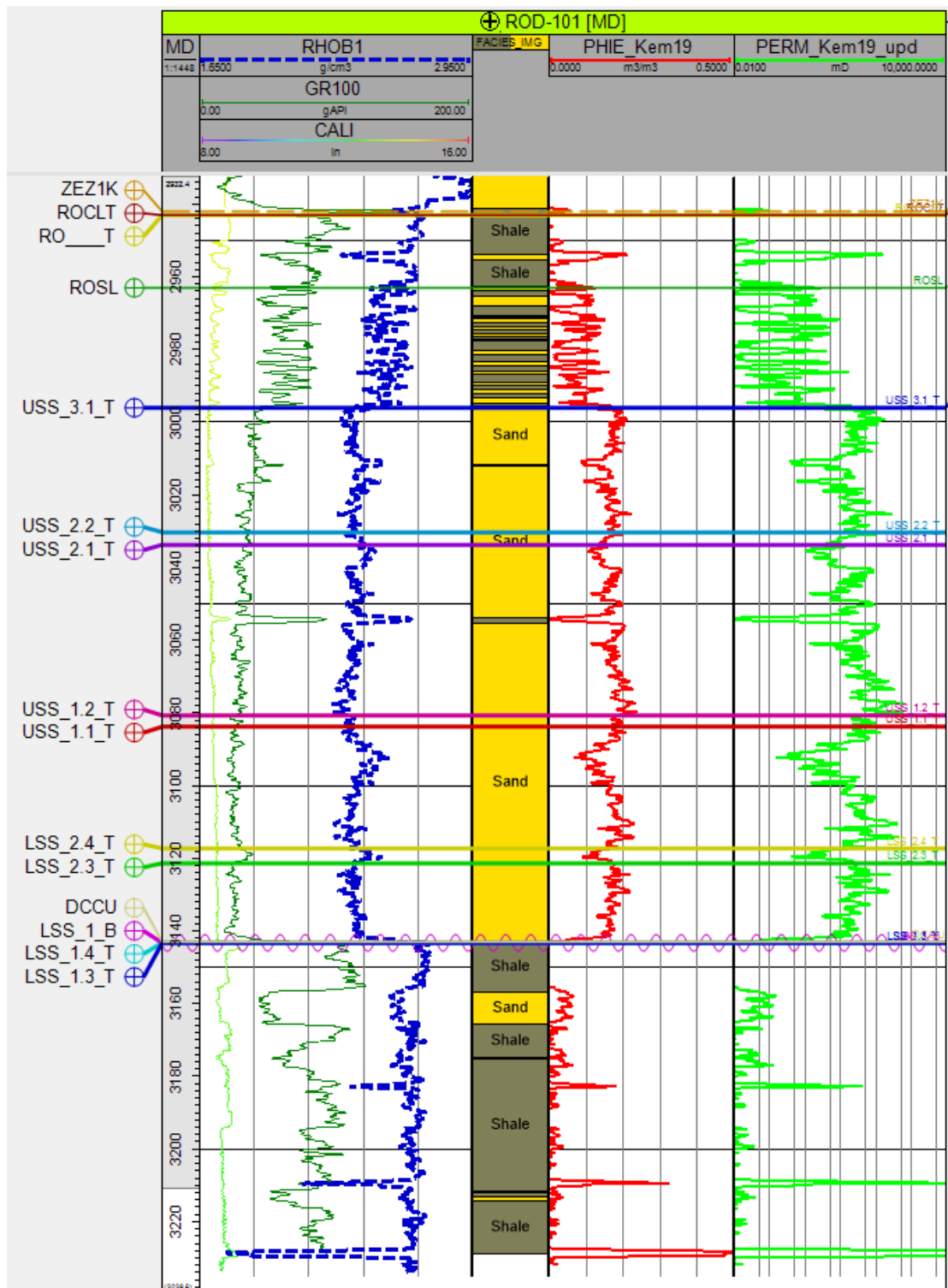
Figure 6-2: Well panel for well ROD-101.
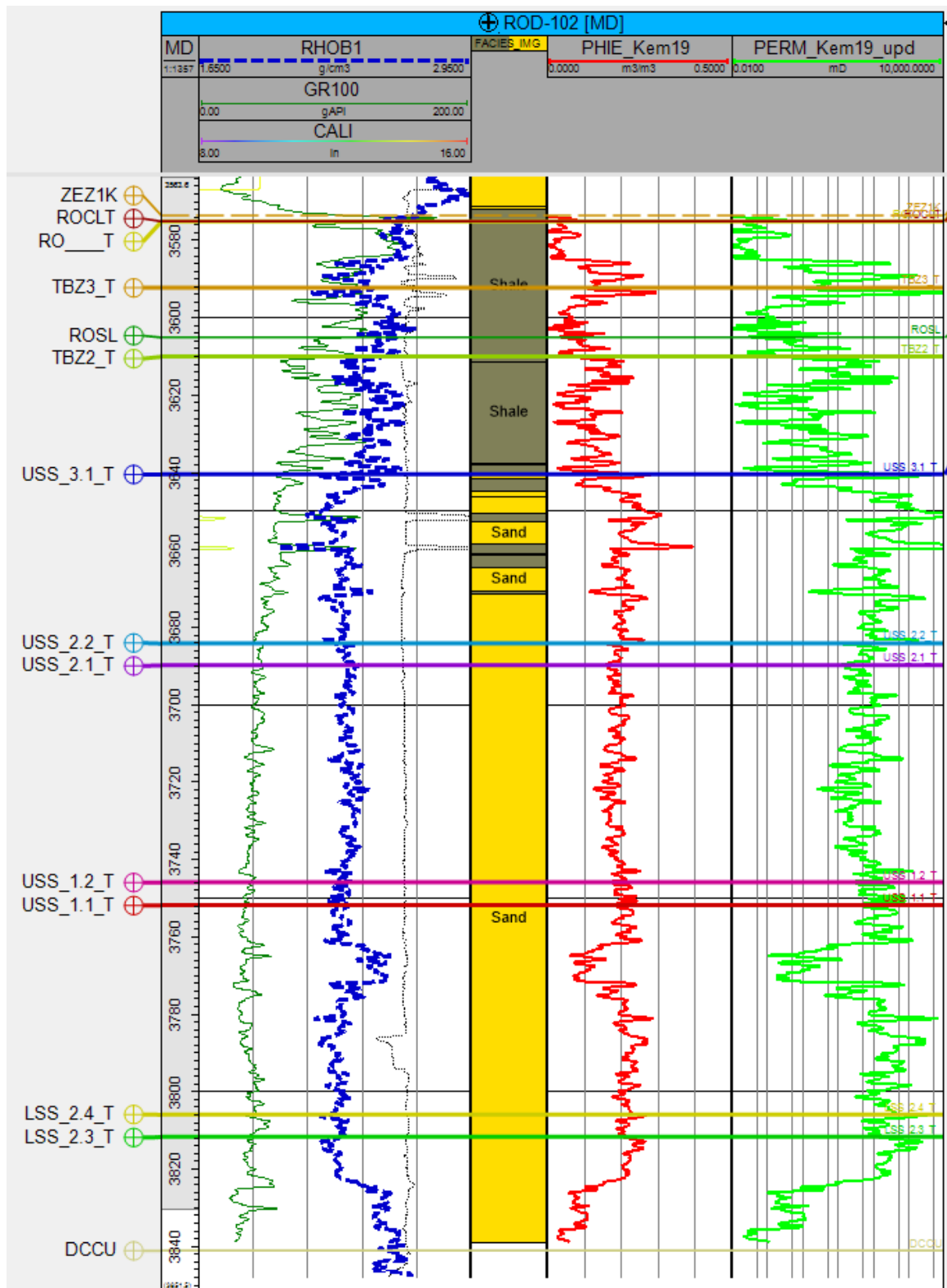
Figure 6-3: Well panel for well ROD-102.
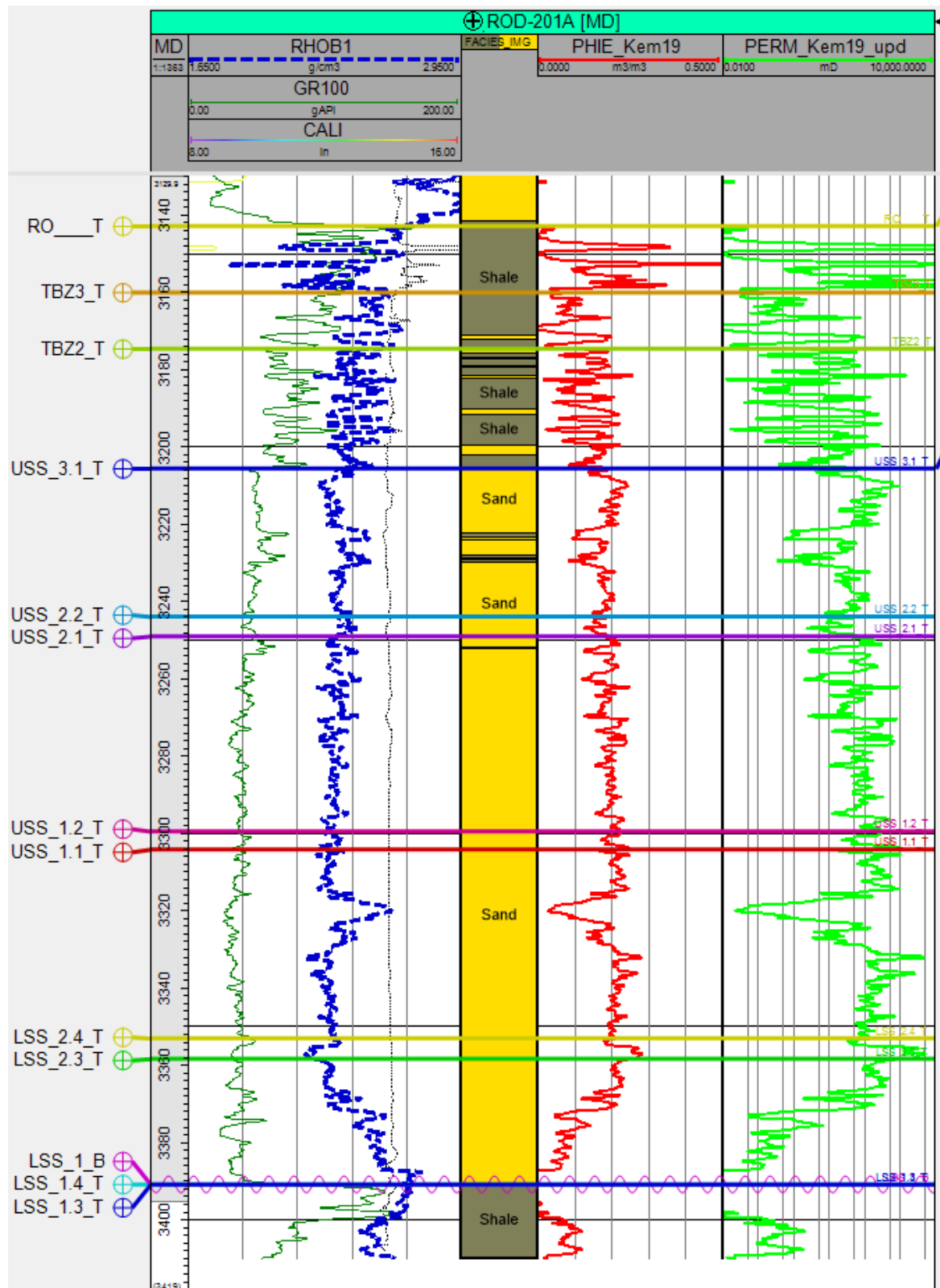
Figure 6-4: Well panel for well ROD-201-S1 (ROD-201A).
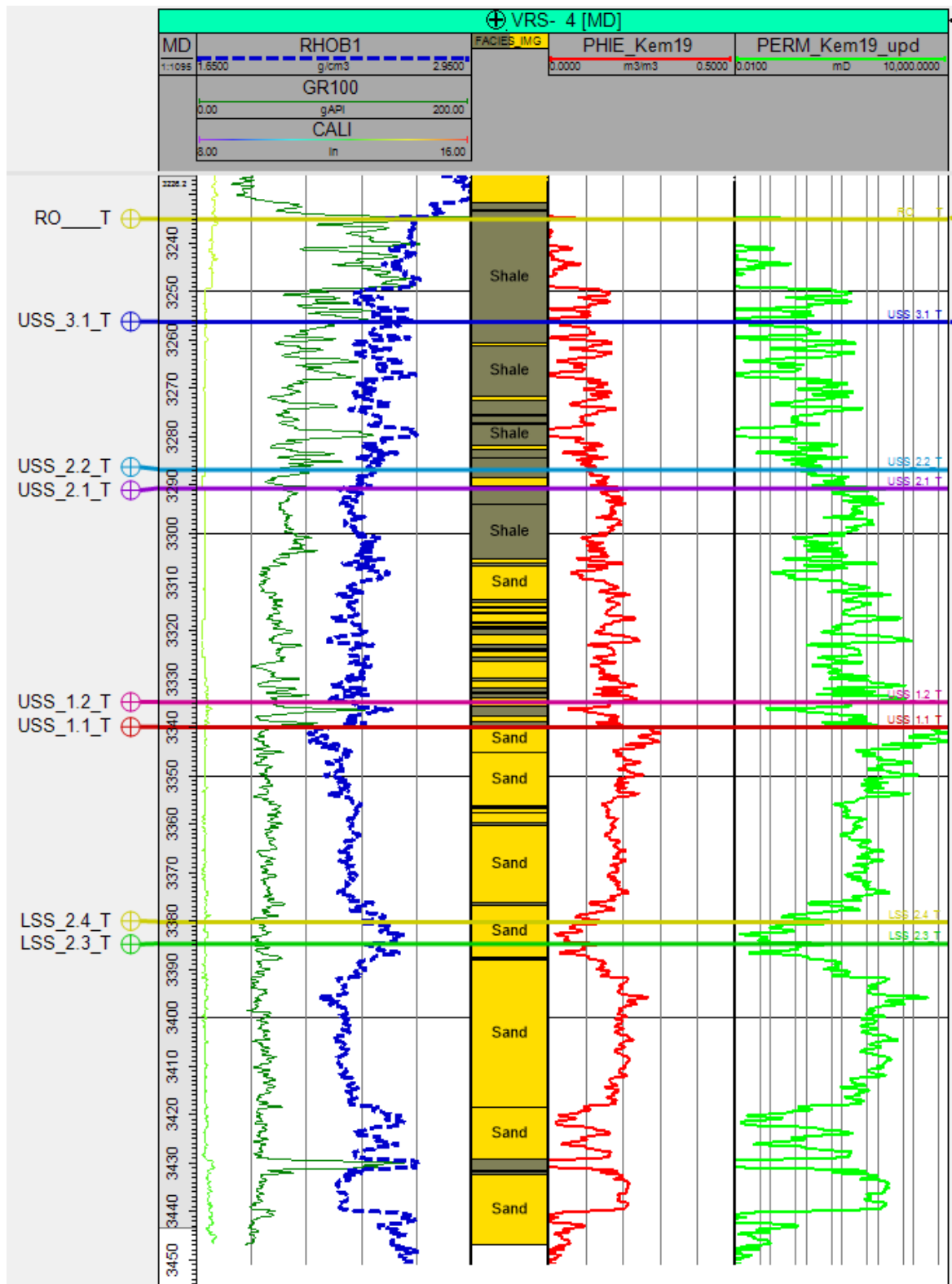
Figure 6-5: Well panel for well VRS-04 (VRS-401).
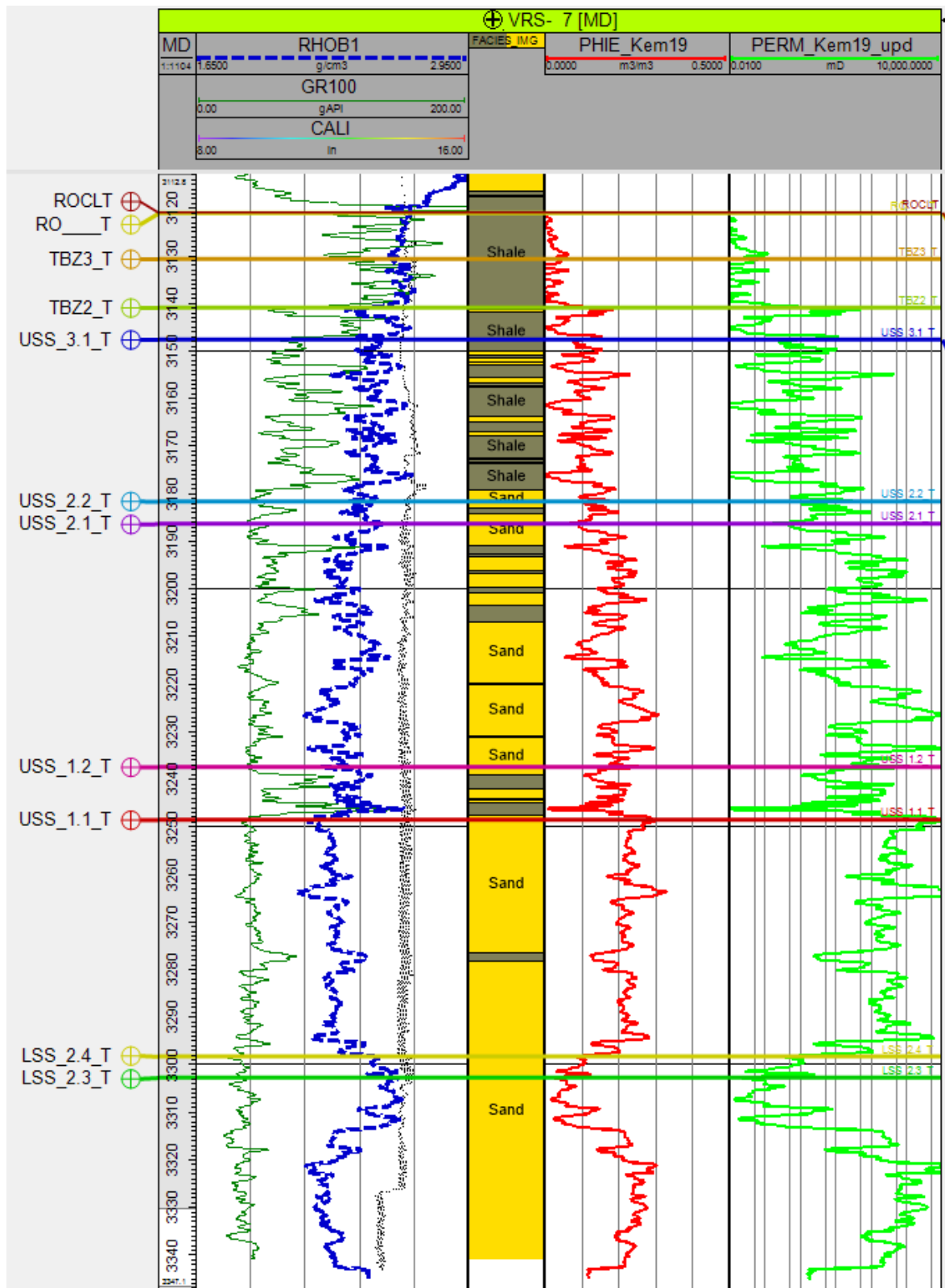
Figure 6-6: Well panel for well VRS-07 (VRS-402).
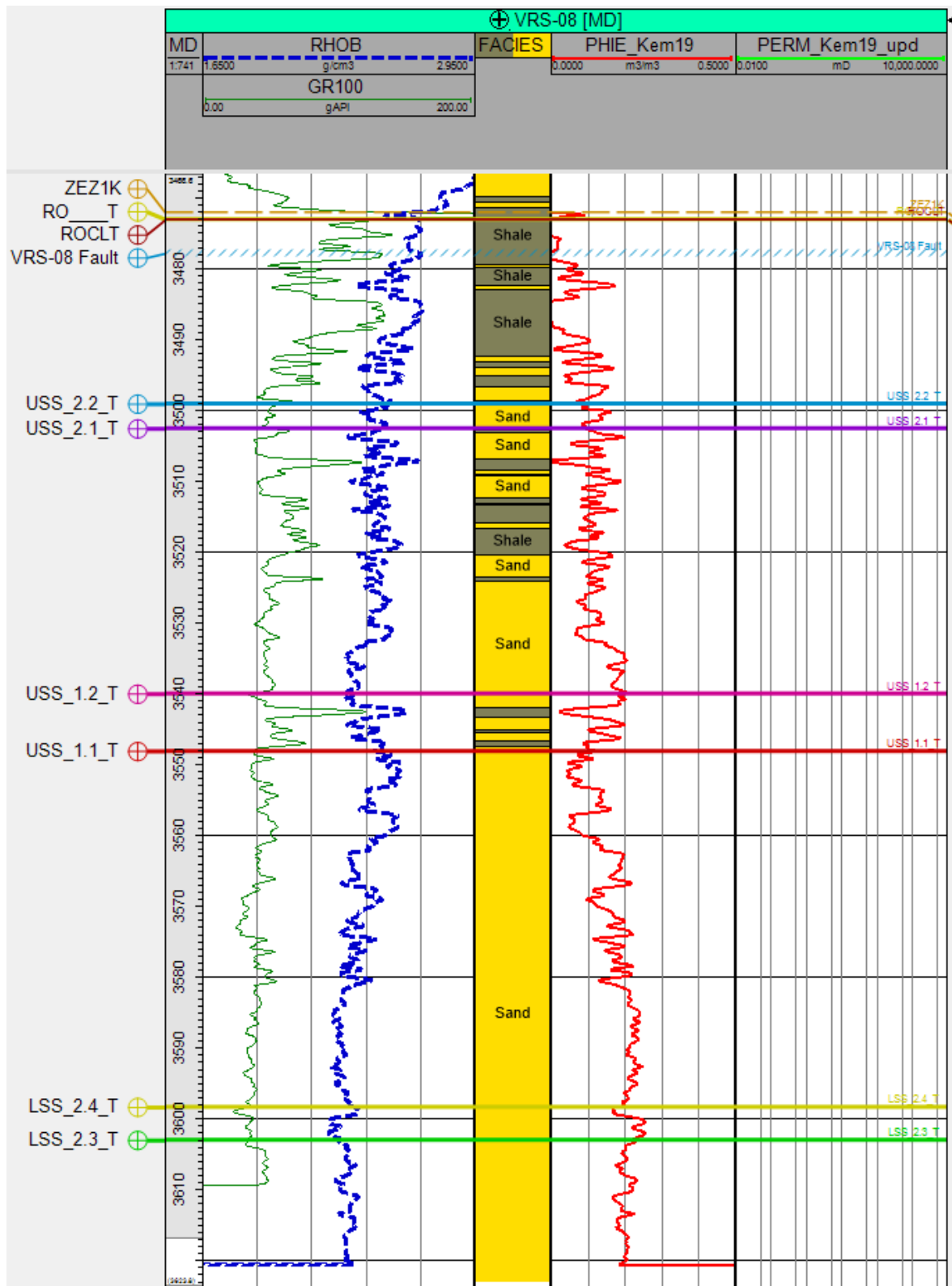
Figure 6-7: Well panel for well VRS-08 (VRS-403).
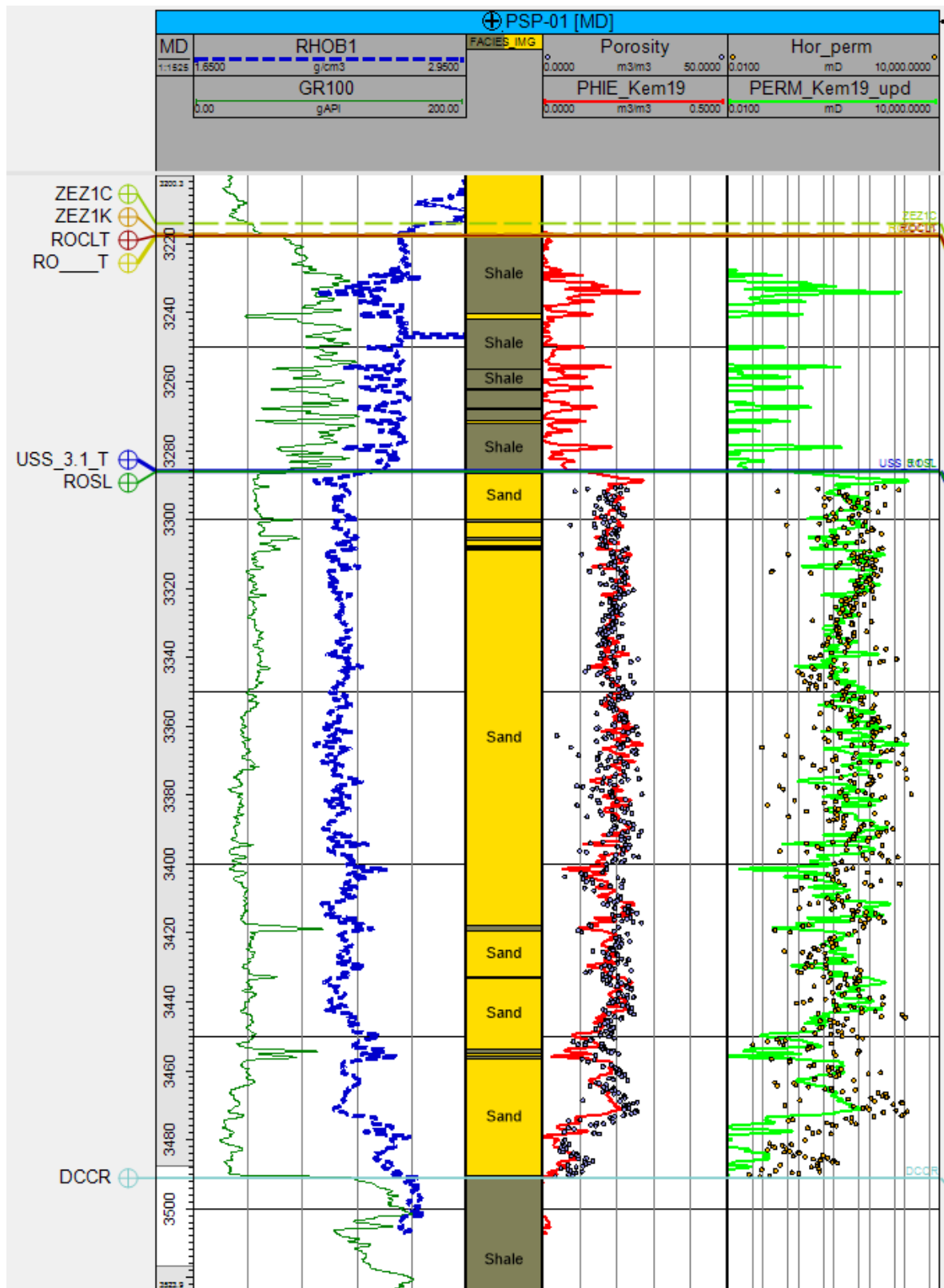
Figure 6-8: Well panel for well PSP-01. In Track 4 and 5, coreplug measurements are plotted, which show a good corelation between calculated log data and measured coreplug data.
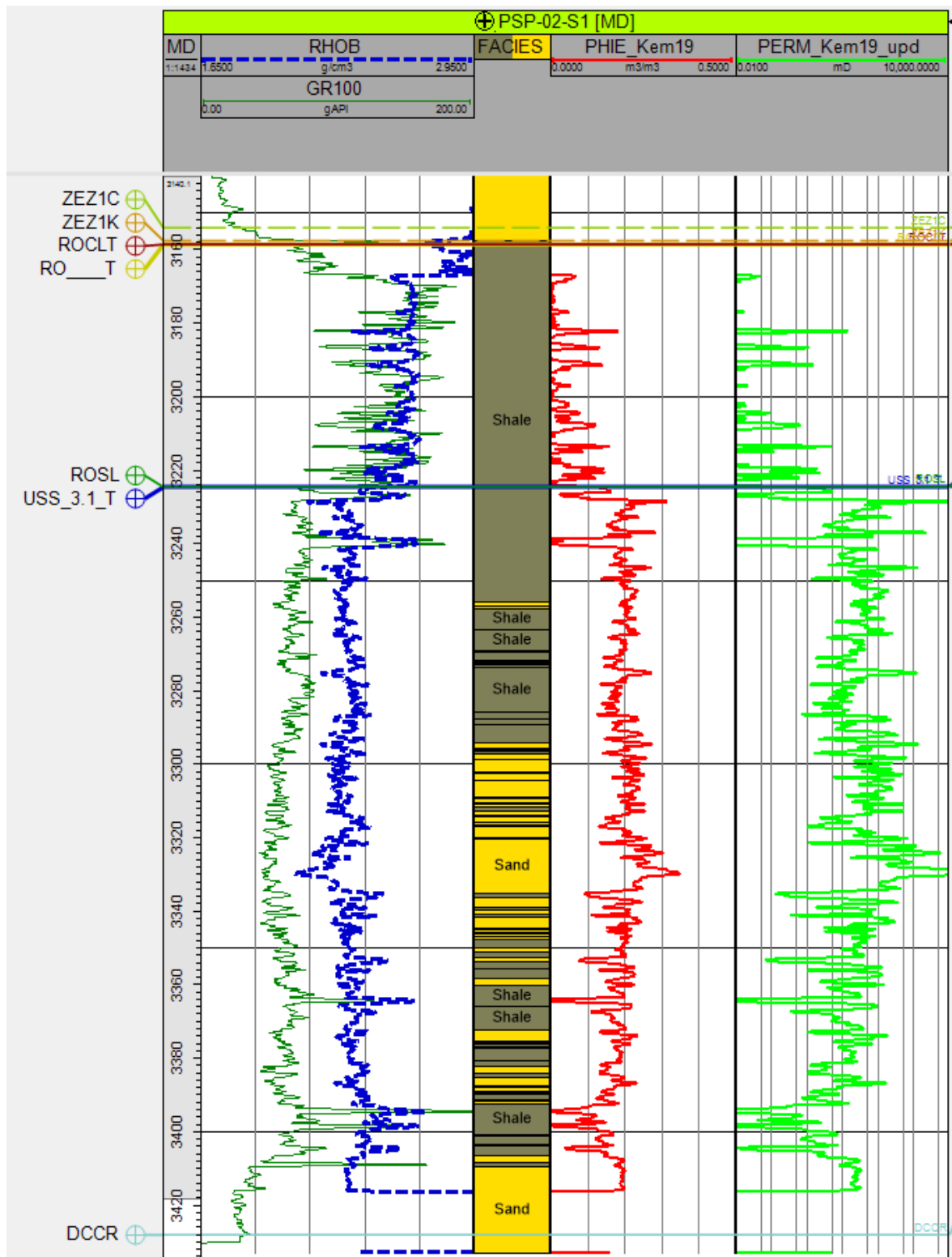
Figure 6-9: Well panel for well PSP-02-S1.
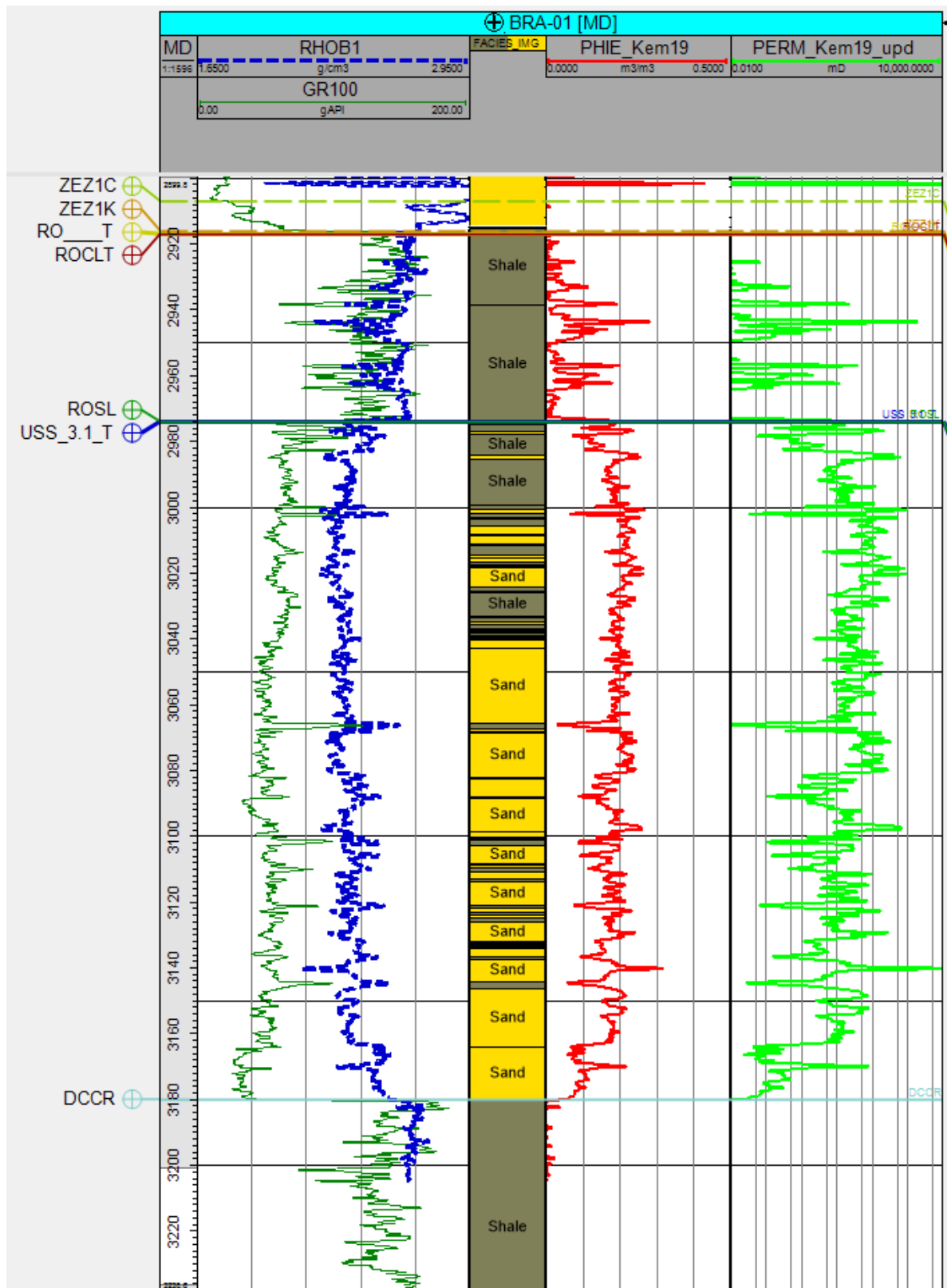
Figure 6-10: Well panel for well BRA-01.
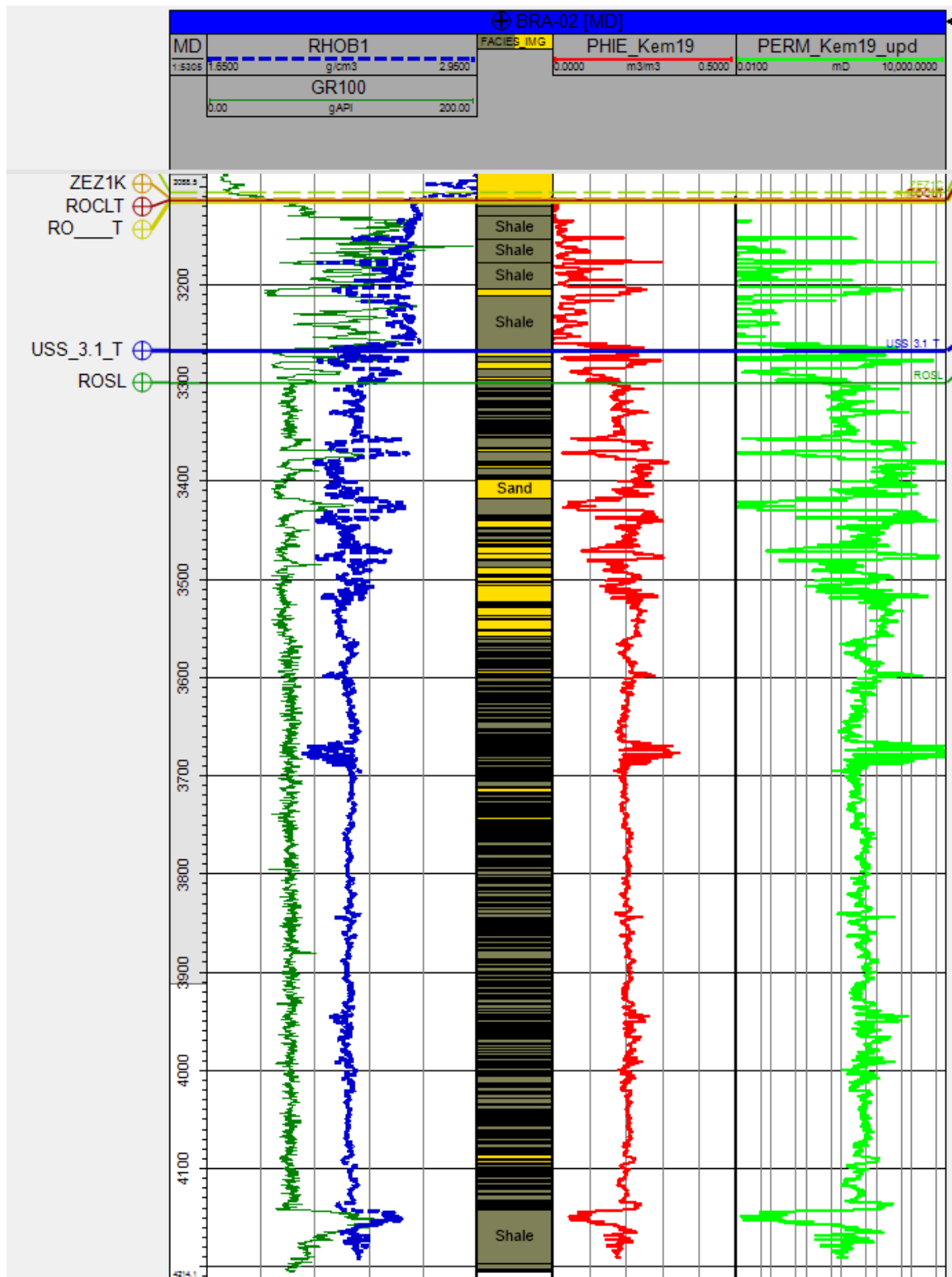
Figure 6-11: Well panel for well BRA-02.
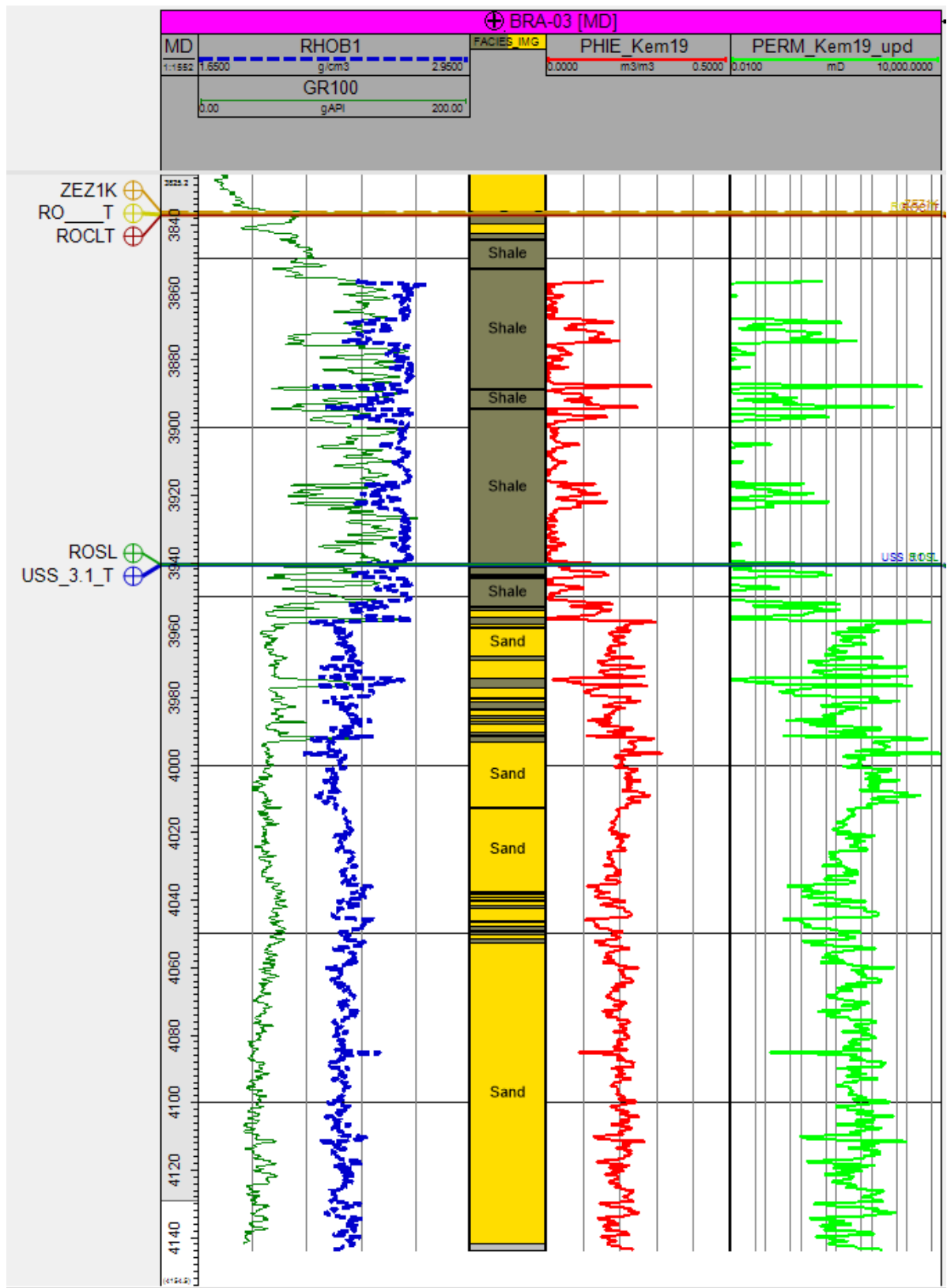
Figure 6-12: Well panel for well BRA-03.
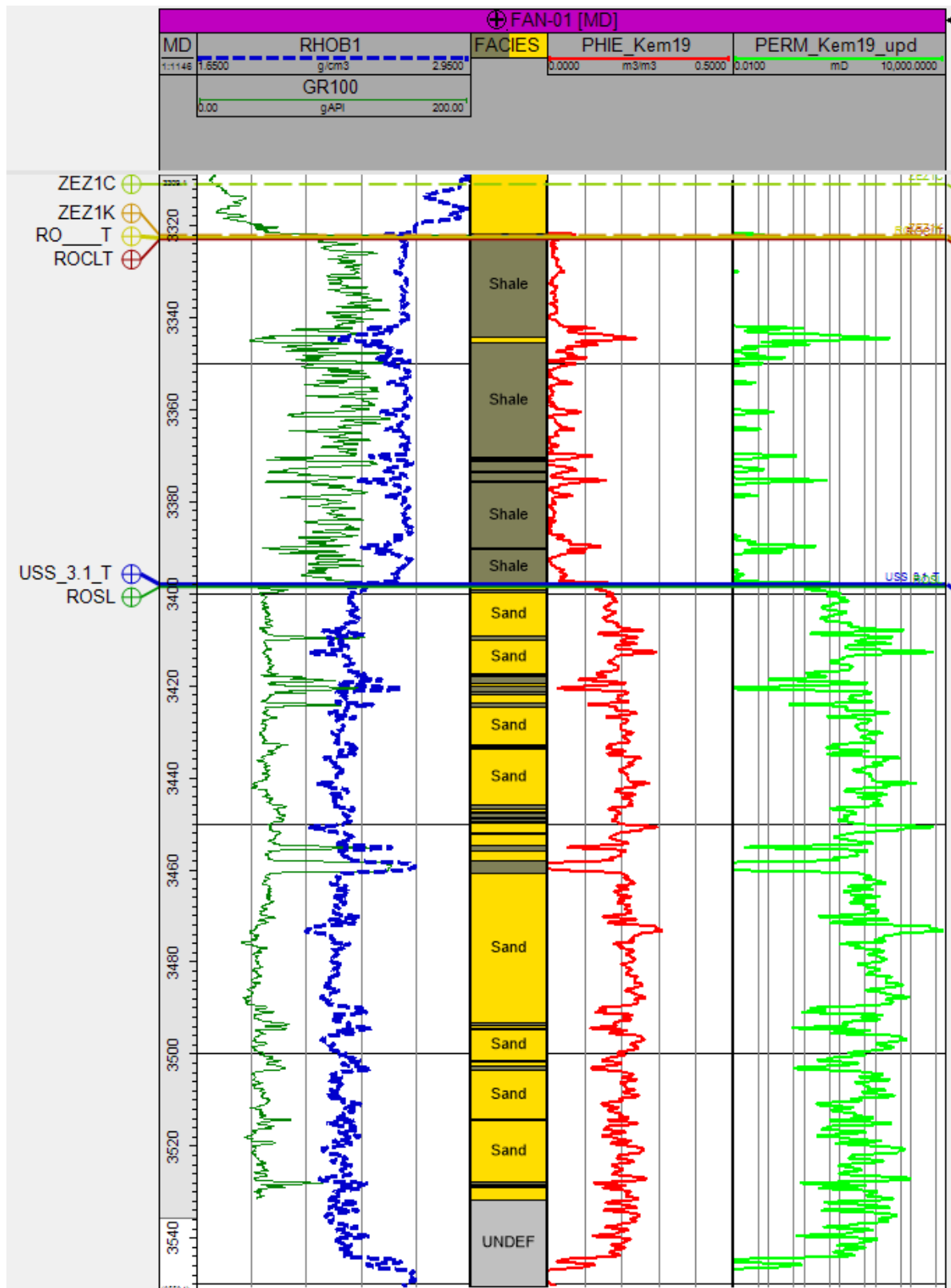
Figure 6-13: Well panel for well FAN-01.

Appendix B Input base model and ensemble

Table B-1 Gas composition used to create tables from correlations

	Roden, Pasop, Boerakker and Faan	Vries Noord	Groningen and Bedum
Methane (C1)	0.8119	0.8735	0.86
Ethane (C2)	0.0411	0.0409	-
Propane (C3)	0.0155	0.011	-
Iso-butane (iC4)	-	0.0036	-
Normal-butane (nC4)	0.0068	-	-
Iso-pentane (iC5)	-	0.0015	-
Normal-pentane (nC5)	0.0025	-	-
Hexanes (C6)	0.0013	0.0005	-
Heptanes plus (C7+)	0.0009	-	-
Carbon dioxide (CO_2)	0.01	0.007	-
Nitrogen (N_2)	0.11	0.062	0.14
Gravity (sg air)	0.667	0.625	0.644

Table B-2 Free water levels of the small gas fields and east side of the Groningen field.

	Free water level (m TVDSS)	Pressure at FWL (bar)
Areas without gas	2500	286.28
Roden	3021	346.42
Vries-Noord block 4	3108	356.47
Vries-Noord block 5 (with well VRS-08)	3075	352.66
Pasop	3123	358.20
Boerakker	2949	338.11
Faan	3346	383.94
Bedum	3002	344.23
Eemskanaal	2996	343.54
Harkstede and Kolham area	3016	345.85
Hoogezand	3030	347.46
Midlaren	3173	363.97

Table B-3 Overview of the faults in the model, including the Fault Group and multiplier of the base model (please note that in the Petrel fault names, some duplicates appear in this table, because the folder structure is not included here)

Name Petrel	Name Eclipse	Group	Multiplier
INT_29	'INT_29'	0	0.1
fault interpretation 5	'FAULTINT'	0	0.1
Fault 2	'FAULT2'	0	0.1
mFS18_Fault_52	'MFS18_FA'	5	1
mFS18_Fault_20	'MFS18__1'	0	0.1
mFS18_Fault_6	'MFS18__2'	0	0.1
mFS18_Fault_5	'MFS18__3'	0	0.1
Fault 3	'FAULT3'	0	0.001
mFS18_Fault_21	'MFS18__4'	0	0.1
B31	'B31'	0	0.00001
B35	'B35'	3	0.06
B36	'B36'	0	0.00001
B37	'B37'	5	0.03
B39	'B39'	3	0.03
B52a	'B52A'	0	0.00001
B53	'B53'	0	0.1
B55	'B55'	0	0.00001
B56	'B56'	0	0.00001
B58	'B58'	0	0.00001
B59a	'B59A'	0	0.00001
B60	'B60'	2	0.01
B64	'B64'	0	0.00001
INT 31	'INT31'	0	0.001
INT 32	'INT32'	0	0.00001
INT_24	'INT_24'	3	0.1
INT_25	'INT_25'	3	0.1
INT_26	'INT_26'	10	0.00001
INT_27	'INT_27'	11	0.00001
M10	'M10'	12	0.1
M11	'M11'	5	0.003
M12	'M12'	3	0.1
M16	'M16'	0	0.1
M19	'M19'	0	0.1
M22	'M22'	7	0.00001

Name Petrel	Name Eclipse	Group	Multiplier
M23	'M23'	0	0.001
M24	'M24'	0	0.00001
M27	'M27'	4	0.003
M28	'M28'	0	0.1
M29	'M29'	11	0.00001
M33	'M33'	0	0.00001
M35	'M35'	0	0.1
M74	'M74'	10	0.00001
M9	'M9'	5	0.001
M9b	'M9B'	10	0.00001
B57	'B57'	4	0.1
mFS9_Fault_9	'MFS9_FAU'	0	0.1
M30	'M30'	6	0.1
M68_E	'M68_E'	0	0.02
M31_E	'M31_E'	0	0.00001
M31_W	'M31_W'	11	0.0001
mFS17_Fault_5	'MFS17_FA'	3	0.1
mFS17_Fault_14	'MFS17__5'	12	0.1
mFS17_Fault_1	'MFS17__6'	3	0.1
mFS18_fault 21a	'MFS18__7'	6	0.1
mFS18_Fault_1	'MFS18__8'	0	0.1
mFS18_Fault_11	'MFS18__9'	0	0.1
mFS18_Fault_18	'MFS18_10'	12	0.1
mFS18_Fault_3	'MFS18_11'	0	0.1
mFS18_Fault_31	'MFS18_12'	6	0.06
mFS18_Fault_34	'MFS18_13'	12	0.1
mFS18_Fault_35	'MFS18_14'	0	0.1
mFS18_Fault_36	'MFS18_15'	0	0.1
mFS18_Fault_45	'MFS18_16'	0	0.1
mFS18_Fault_7	'MFS18_17'	0	0.1
mFS18_Fault_9	'MFS18_18'	0	0.1
mFS18_Fault_22_(See comments)	'MFS18_19'	0	0.1
mFS16_Fault_2	'MFS16_FA'	1	0.03
mFS16_Fault_20	'MFS16_20'	3	0.1
mFS16_Fault_24	'MFS16_21'	3	0.1
mFS16_Fault_25	'MFS16_22'	3	0.1
mFS16_Fault_26	'MFS16_23'	3	0.1
mFS16_Fault_32	'MFS16_24'	0	0.1

Name Petrel	Name Eclipse	Group	Multiplier
mFS16_Fault_41	'MFS16_25'	0	0.1
mFS16_Fault_43	'MFS16_26'	3	0.1
mFS16_Fault_45	'MFS16_27'	9	0.00001
mFS16_Fault_50	'MFS16_28'	0	0.1
mFS15_Fault 56	'MFS15_FA'	0	0.1
mFS15_Fault_10	'MFS15_29'	0	1
mFS15_Fault_107	'MFS15_30'	0	0.1
mFS15_Fault_11	'MFS15_31'	3	0.1
mFS15_Fault_112	'MFS15_32'	4	0.01
mFS15_Fault_12	'MFS15_33'	0	0.1
mFS15_Fault_16	'MFS15_34'	0	1
mFS15_Fault_17	'MFS15_35'	0	0.1
mFS15_Fault_18	'MFS15_36'	0	0.1
mFS15_Fault_19	'MFS15_37'	0	0.1
mFS15_Fault_21	'MFS15_38'	0	0.1
mFS15_Fault_22	'MFS15_39'	0	1
mFS15_Fault_26	'MFS15_40'	0	0.1
mFS15_Fault_27	'MFS15_41'	0	0.1
mFS15_Fault_3	'MFS15_42'	3	0.1
mFS15_Fault_31	'MFS15_43'	0	0.1
mFS15_Fault_33	'MFS15_44'	0	0.1
mFS15_Fault_35	'MFS15_45'	0	0.1
mFS15_Fault_36	'MFS15_46'	0	0.1
mFS15_Fault_4	'MFS15_47'	3	0.1
mFS15_Fault_43	'MFS15_48'	0	1
mFS15_Fault_44	'MFS15_49'	4	0.1
mFS15_Fault_44a	'MFS15_50'	0	0.1
mFS15_Fault_49	'MFS15_51'	0	0.1
mFS15_Fault_5	'MFS15_52'	3	0.1
mFS15_Fault_50	'MFS15_53'	0	1
mFS15_Fault_9	'MFS15_55'	0	0.1
mFS15_Fault_Extra 3	'MFS15_56'	0	0.1
mFS15_Fault_Extra2	'MFS15_57'	0	0.1
mS15_Fault_63	'MS15_FAU'	0	0.1
mFS15_Fault_48 (See comments)	'MFS15_58'	0	1
mFS15_Fault_15	'MFS15_59'	0	1
mFS15_Fault 34	'MFS15_60'	0	0.1
mFS10_fault_46	'MFS10_FA'	0	0.1

Name Petrel	Name Eclipse	Group	Multiplier
mFS10_Fault_47	'MFS10_61'	0	0.04
mFS10_Fault_48	'MFS10_62'	0	0.1
mFS10_Fault_49	'MFS10_63'	0	0.1
mFS9_Fault_20	'MFS9__64'	0	0.1
mFS9_Fault_22	'MFS9__65'	0	0.1
mFS9_Fault_27	'MFS9__66'	0	0.00001
mFS9_Fault_28	'MFS9__67'	0	0.00001
mFS9_Fault_29	'MFS9__68'	0	0.1
mFS9_Fault_31	'MFS9__69'	0	0.1
mFS9_Fault_37	'MFS9__70'	0	0.1
mFS9_Fault_44	'MFS9__71'	0	0.1
Bedum Aquifer fault 1	'BEDUMAQU'	7	0.00001
M68_W (delete)	'M68_W(DE'	7	0.00001
Fault interpretation 2	'FAULT_72'	9	0.00001
Fault interpretation 3	'FAULT_73'	9	0.00001
Fault interpretation 4	'FAULT_74'	9	0.00001
Fault interpretation 5	'FAULT_75'	0	0.1
Fault interpretation 7	'FAULT_76'	8	0.1
Fault interpretation 8	'FAULT_77'	8	0.1
Fault interpretation 10	'FAULT_78'	8	0.1
Fault interpretation 11	'FAULT_79'	12	0.001
Fault interpretation 12	'FAULT_80'	11	0.00001
Fault interpretation 13	'FAULT_81'	0	0.01
Fault interpretation 24	'FAULT_82'	0	0.1
Fault interpretation 29	'FAULT_83'	10	0.00001
Fault interpretation 30	'FAULT_84'	10	0.00001
Fault interpretation 32	'FAULT_85'	9	0.00001
Fault interpretation 29 (Depth 1)	'FAULT_87'	9	0.00001
Fault interpretation 35 (Depth 1)	'FAULT_89'	0	0.00001
Fault interpretation 39 (Depth 1)	'FAULT_91'	0	0.0003
Fault interpretation 40 (Depth 1)	'FAULT_92'	0	0.1
Fault 8	'FAULT8'	9	0.00001
Fault 9	'FAULT9'	0	0.1
Fault 15	'FAULT15'	0	0.1
Fault interpretation 1	'FAULT_94'	0	0.01
Fault interpretation 2	'FAULT_95'	0	0.01
Fault interpretation 6	'FAULT_96'	0	0.01
Fault interpretation 4	'FAULT_97'	0	0.00001

Name Petrel	Name Eclipse	Group	Multiplier
Fault 1_VRS-08	'FAULT1_V'	11	0.00001
Fault 4_VRS-08	'FAULT4_V'	11	0.00001
PSP EBF	'PSPEBF'	13	0.00001
Fault 1	'FAULT1'	0	0.00001
Riedel 1	'RIEDEL1'	0	0.01
Riedel 2	'RIEDEL2'	0	0.01
Riedel 3	'RIEDEL3'	0	0.01
Faan fault	'FAANFAUL'	0	0.00001
Fault 4	'FAULT4'	0	0.01
Fault 5	'FAULT5'	0	0.01
Fault 6	'FAULT6'	0	0.00001
Fault 7	'FAULT7'	1	0.01

Table B-4 Definition of the fault groups for applying multipliers in the ensemble.

Group	Description	Faults (Petrel name)
0	Don't vary	All faults not listed below
1	Between BDM/HRS –aq	Fault 7, mFS16_Fault_2
2	Gron-HRS	B60
3	HRS-Rod-aquifer	B35, INT_24, M12, INT_25, mFS16_Fault_20, mFS16_Fault_24, mFS16_Fault_25, mFS16_Fault_26, mFS17_Fault_1, mFS16_Fault_43, mFS15_fault_11, mFS15_fault_3, mFS15_fault_4, mFS15_fault_5, B39, mFS17_Fault_5
4	EKL-HRS block	M27, B57, mFS15_Fault_112, mFS15_Fault_44
5	KHM,HAR block E-W	B37, M9, mFS18_Fault_52, M11
6	HGZ-MLA connection	mFS18_fault_21a, M30, mFS18_Fault_31
7	BDM-Aq	M22, Bedum Aquifer fault 1, M68_W (delete)
8	N-S faults ROD/PSP aq	Fault interpretation 7, Fault interpretation 8, Fault interpretation 10
9	Large E-W faults, N	Fault interpretation 29 (Depth 1), Fault interpretation 32, Fault interpretation 4, Fault 8, Fault interpretation 2, Fault interpretation 3, mFS16_Fault_45
10	Large E-W faults, M	Fault interpretation 29, Fault interpretation 30, INT_26, M74, M9b

11	Large E-W faults, S	M29, M31_W, Fault 1_VRS-08, Fault 4_VRS-08, Fault interpretation 12
12	Vries aq dir. west	Fault interpretation 11, mFS17_Fault_14, M10, mFS18_Fault_34, mFS18_Fault_18
13	PSP EBF	PSP_EBF

Ranges of the uniform distribution from which the fault multipliers per group are samples for creating the ensemble

Table B-5 Ranges of the uniform distribution from which the fault multipliers per group are samples for creating the ensemble.

Group	range min	range max
0	n.v.t.	n.v.t
1	-1	1
2	-1	1
3	-1	1
4	-1	1
5	-1	1
6	-1	1
7	-1	1
8	-3	1
9	-1	2
10	-1	2
11	-1	2
12	-1	1
13	-1	1
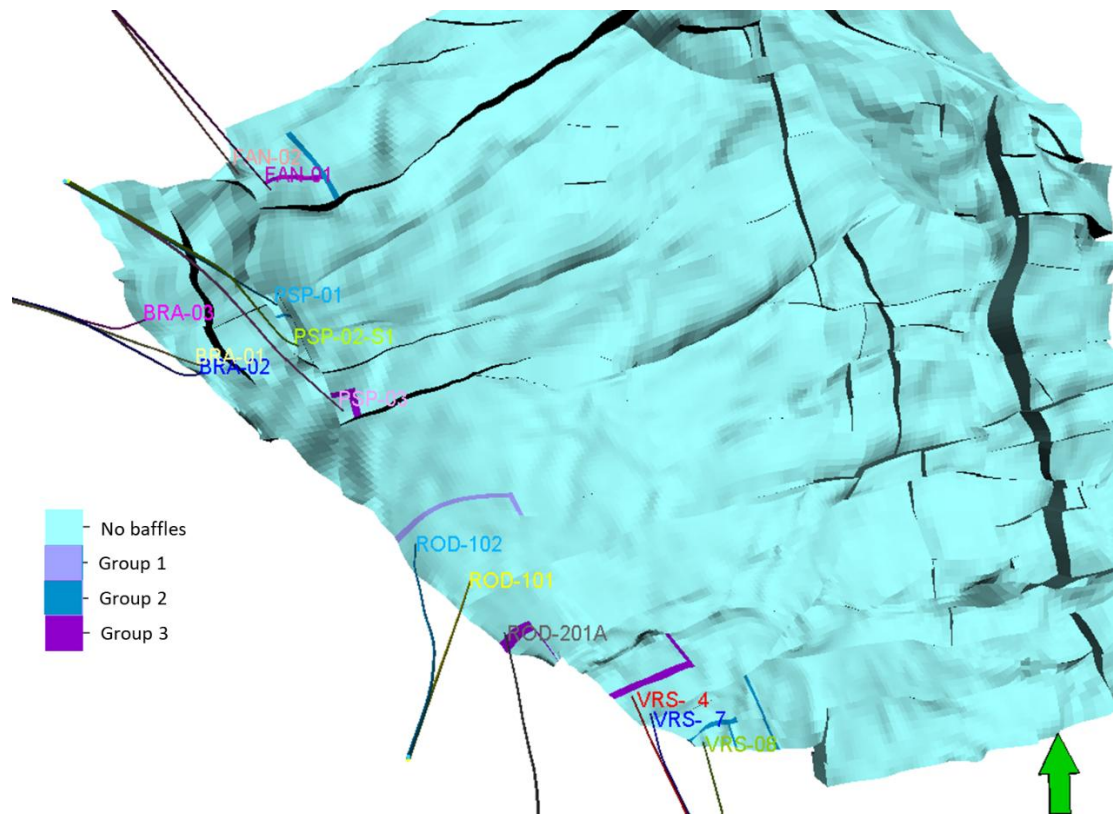
Figure B-14 Baffles implemented in the small gas fields during tuning. See Table 3-3 for the permeability values used for the base model and the ensemble.

Appendix C Results ensemble

C.1　Ensemble results history

Per block or small gas field the block pressure (BPR) is plotted:
Roden north block (ROD-101/ROD-101B and ROD-102): 7, 100, 4
Roden south block (ROD-201A): 7, 109, 4
Vries Noord (block with VRS-4 and VRS-7): 24, 140, 3
Vries Noord (block with VRS-8): 24, 151, 4
PSP-01: 13, 43, 4
PSP-02-S1: 13, 47, 4
PSP-03: 15, 66, 4
FAN-01: 14, 22, 4
FAN-02: 13, 16, 4
BRA-1 and BRA-2: 6, 39, 4
BRA-3 (listed as A-3-OPM): 1, 28, 4
Well Bottom hole pressure (WBHP) for HRS-2A and MLA-1.
Water production rate is plotted for all wells of the small gas fields

Every line represent a model realization. Crosses indicate measurements.
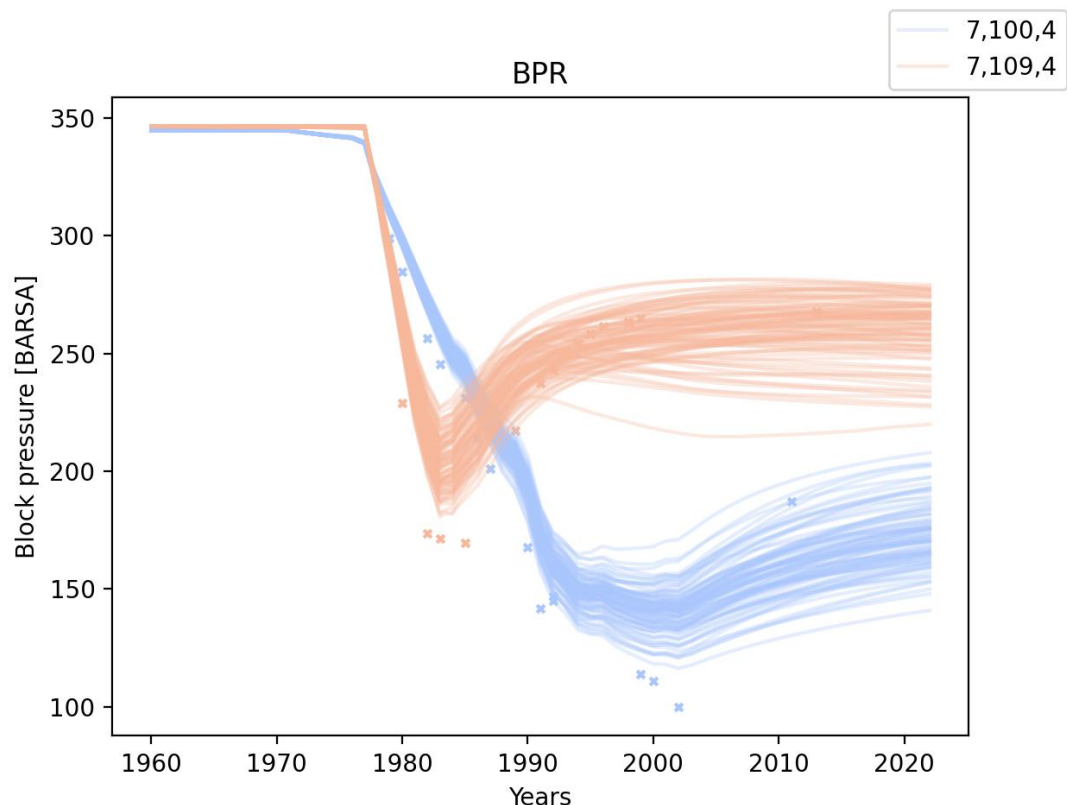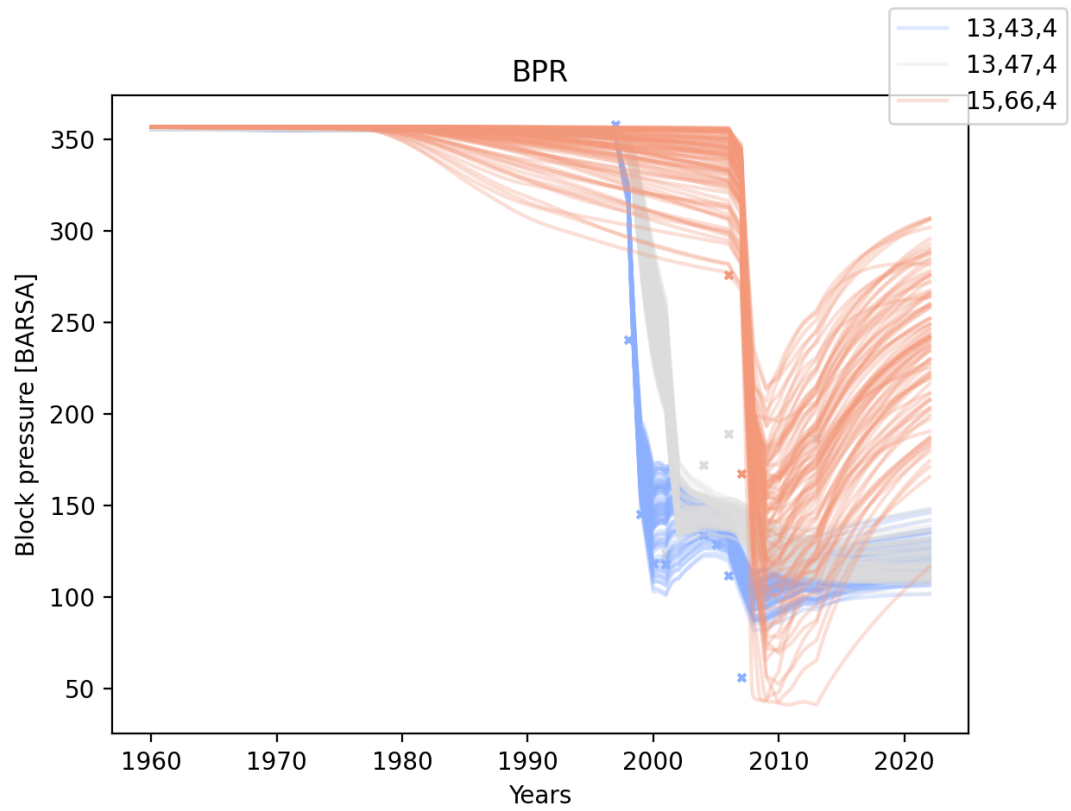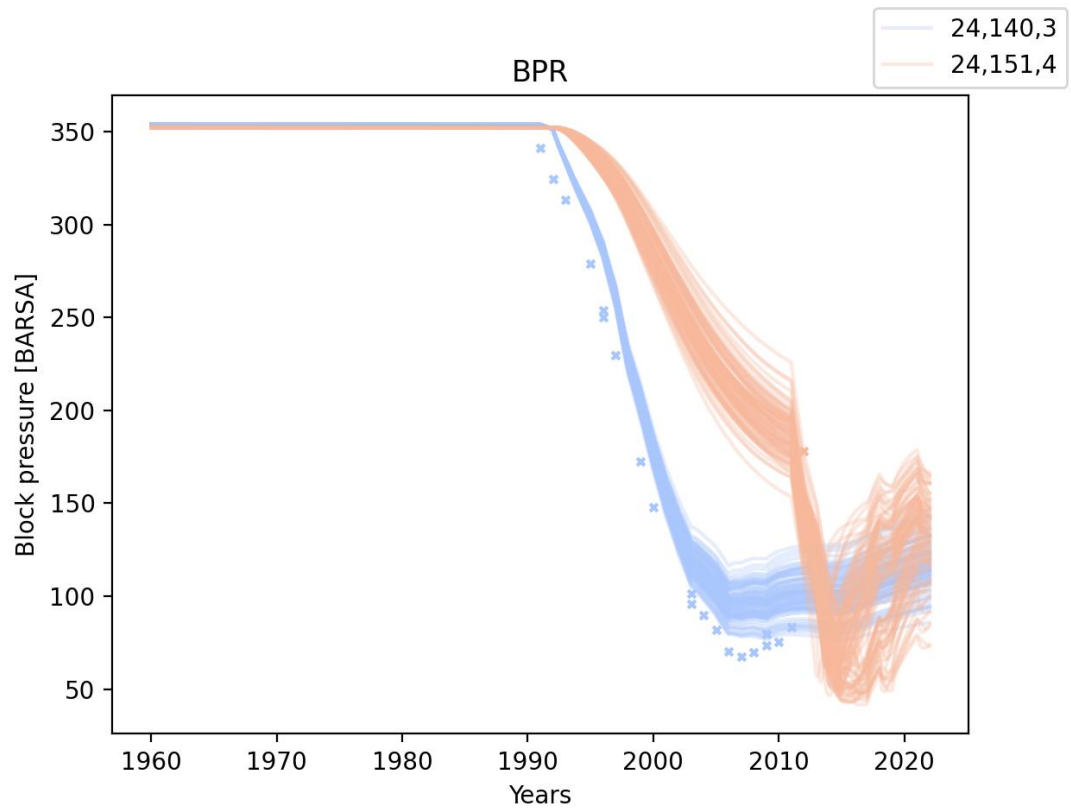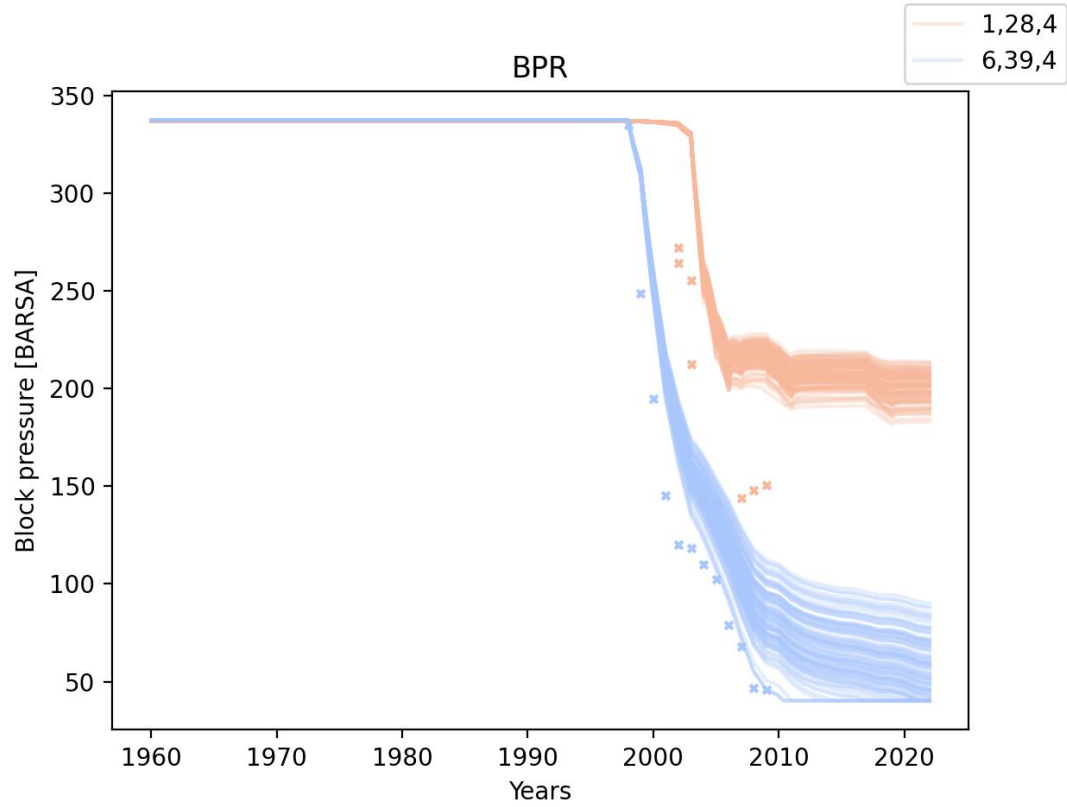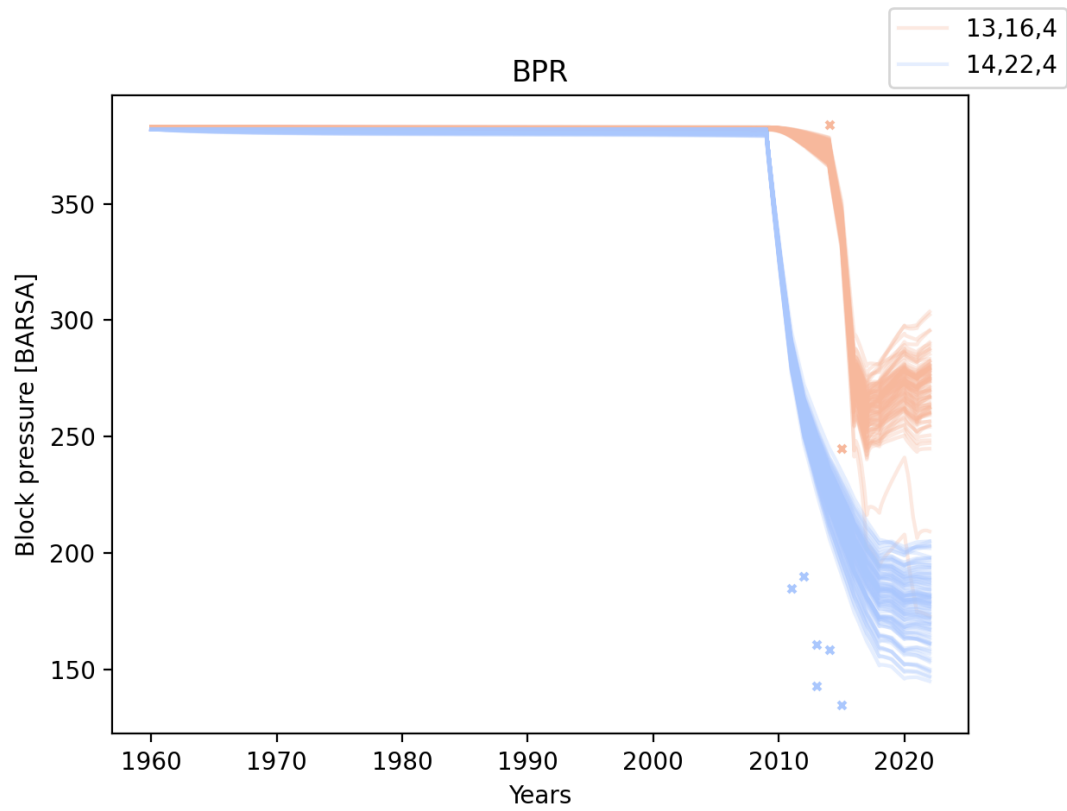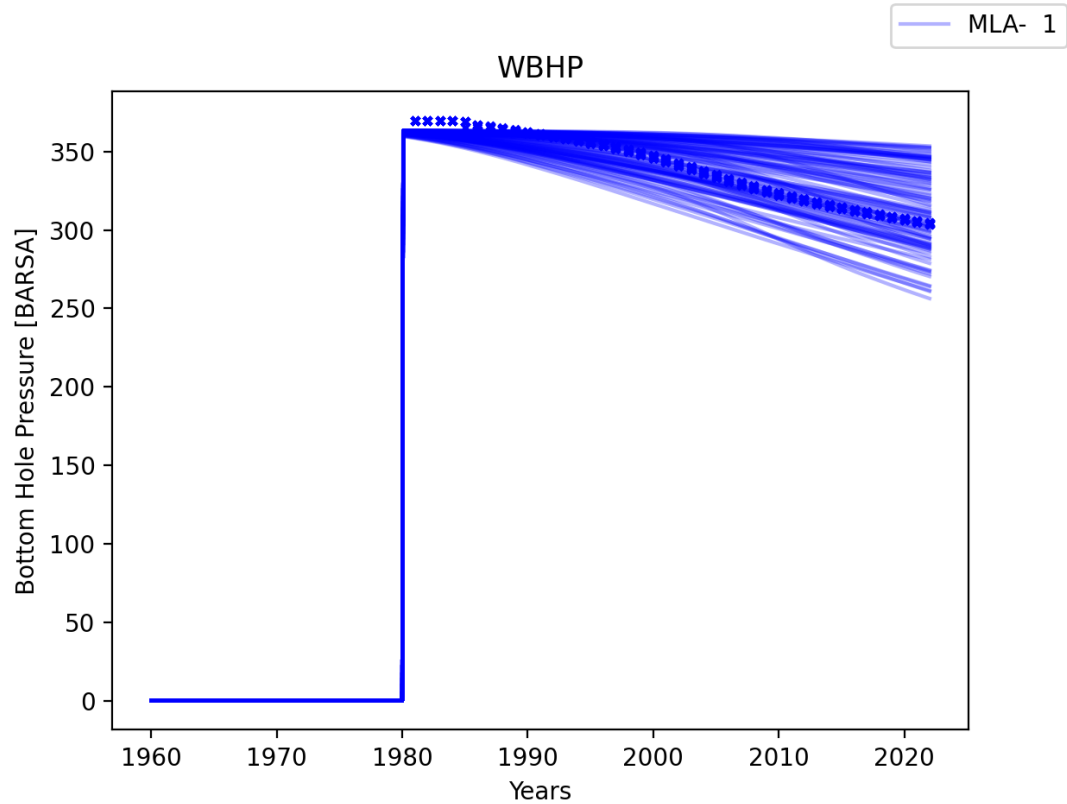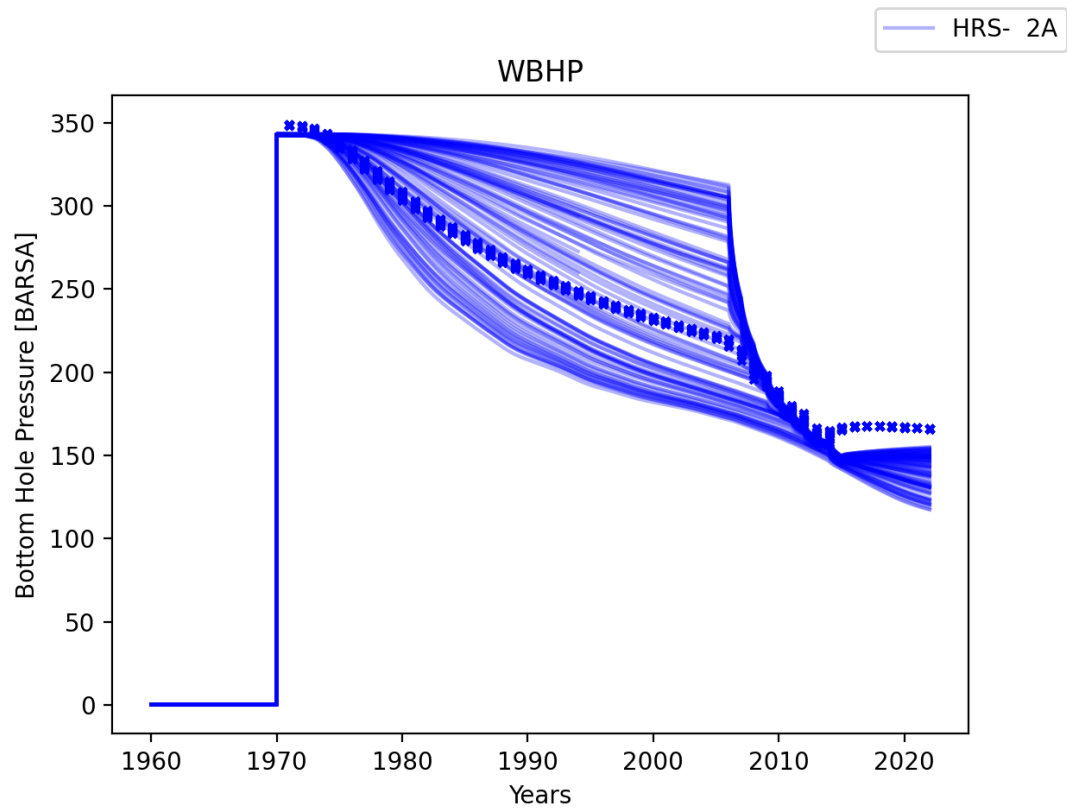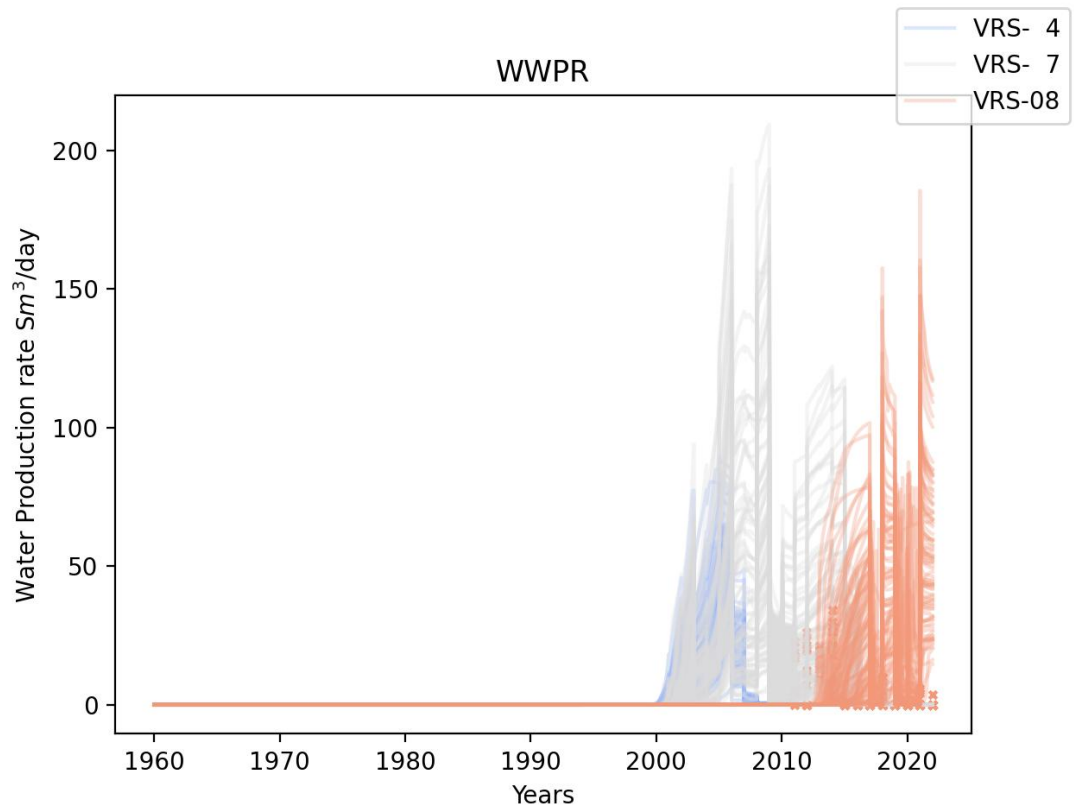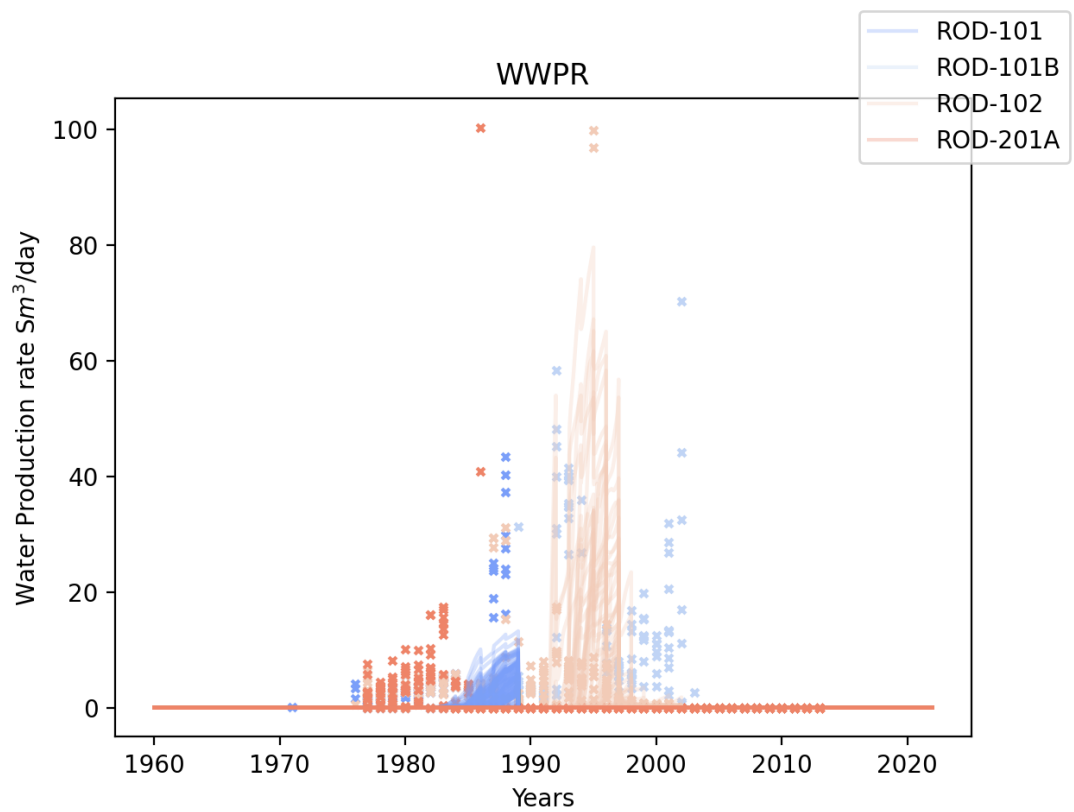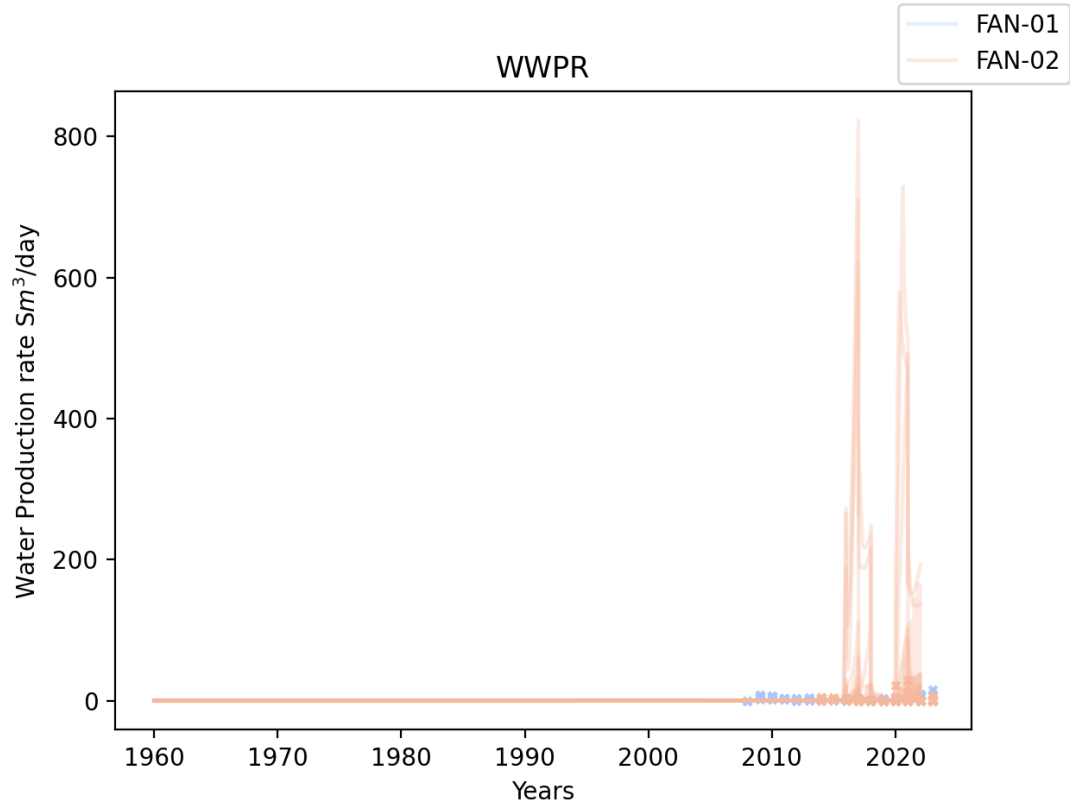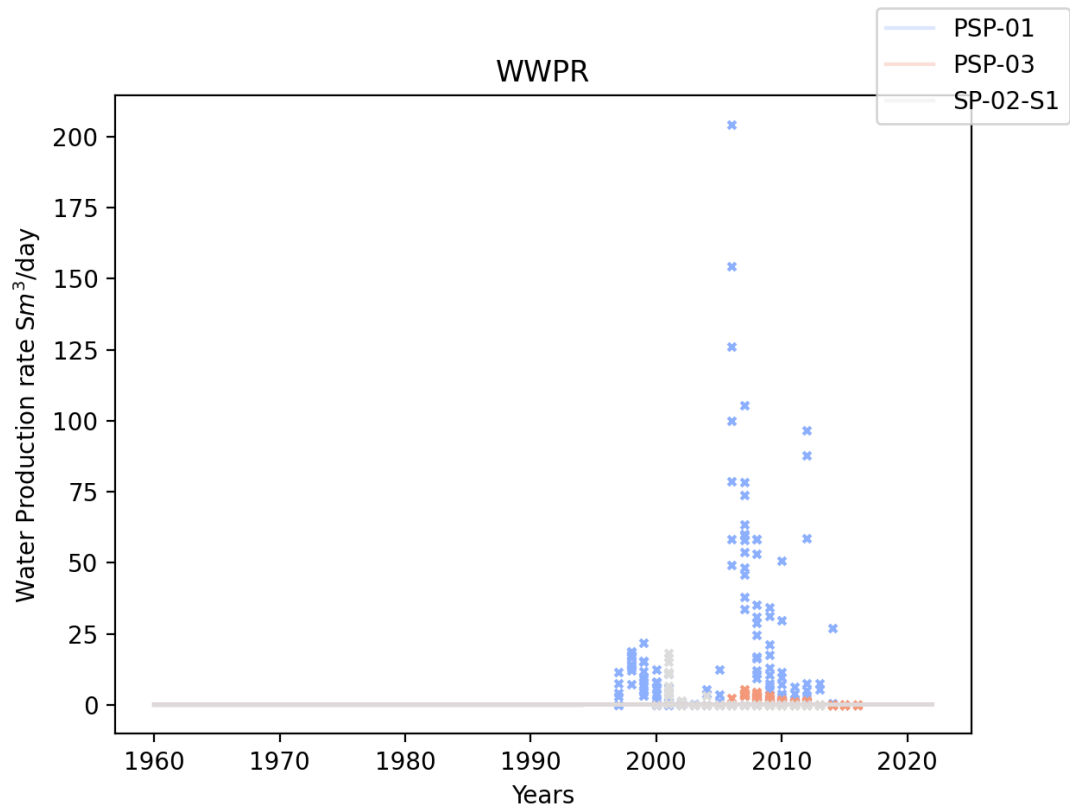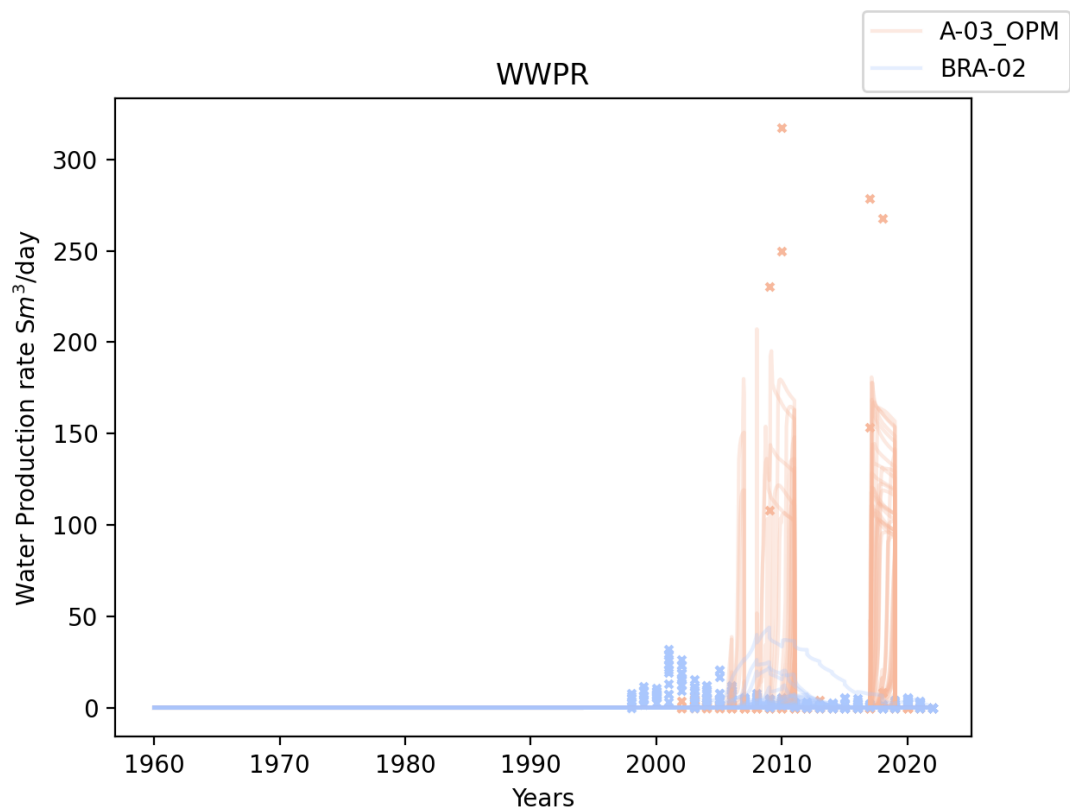
C.2　Ensemble results prediction

Ensemble results for both the historical and prediction period of the pressure. Black and red curves are the model realizations from which the predictions will be used ifor the seismicity analyses because they fit better to the observations (pressure and subsidence). The red curve is the best fitting member 96. Blue curves are the model realizations that do not fit sufficiently well to data to be used for the seismicity analysis. See the start of the appendix which block represents which field.

7,100,4

7,109,4

24,140,3

24,151,4

13,43,4

13,47,4

15,66,4

14,22,4

13,16,4

6,39,4

1,28,4
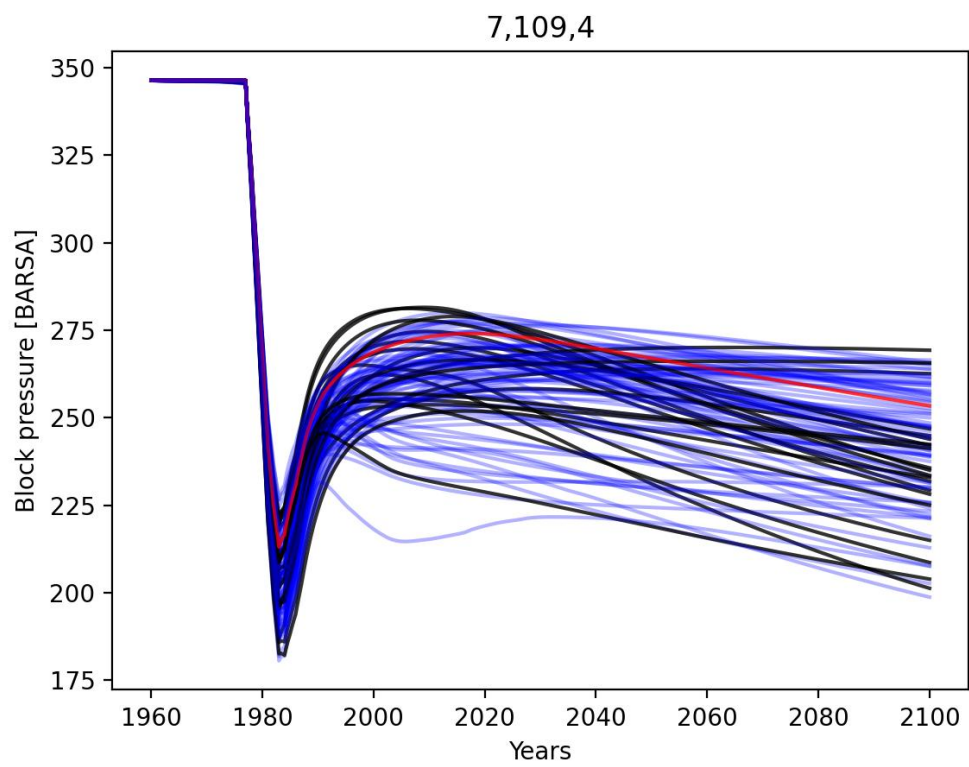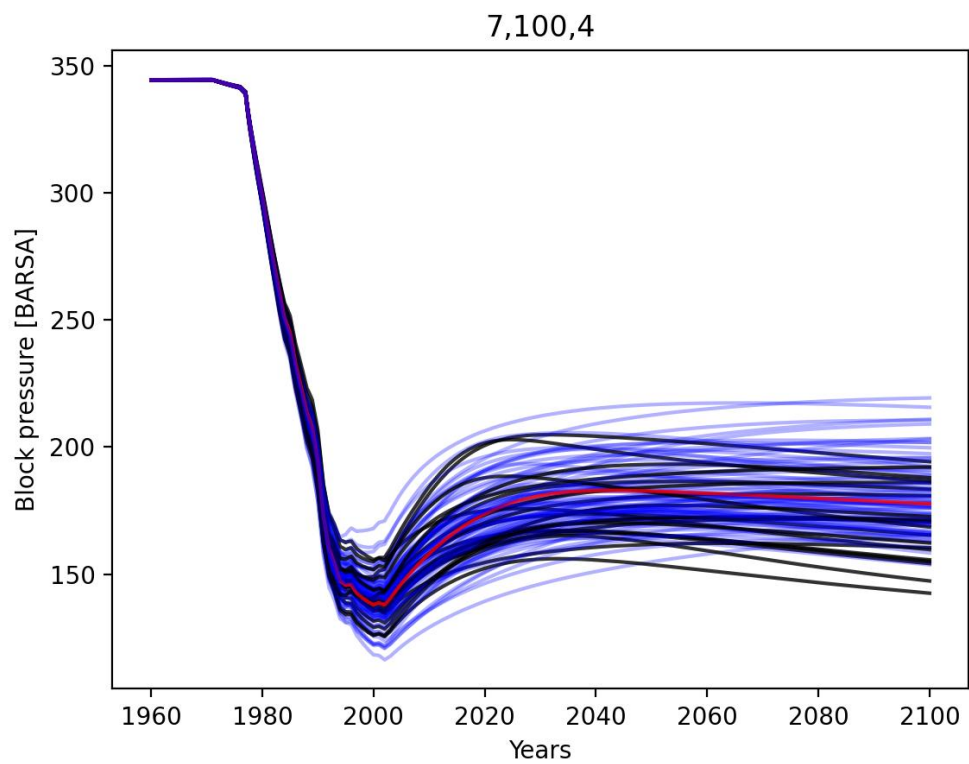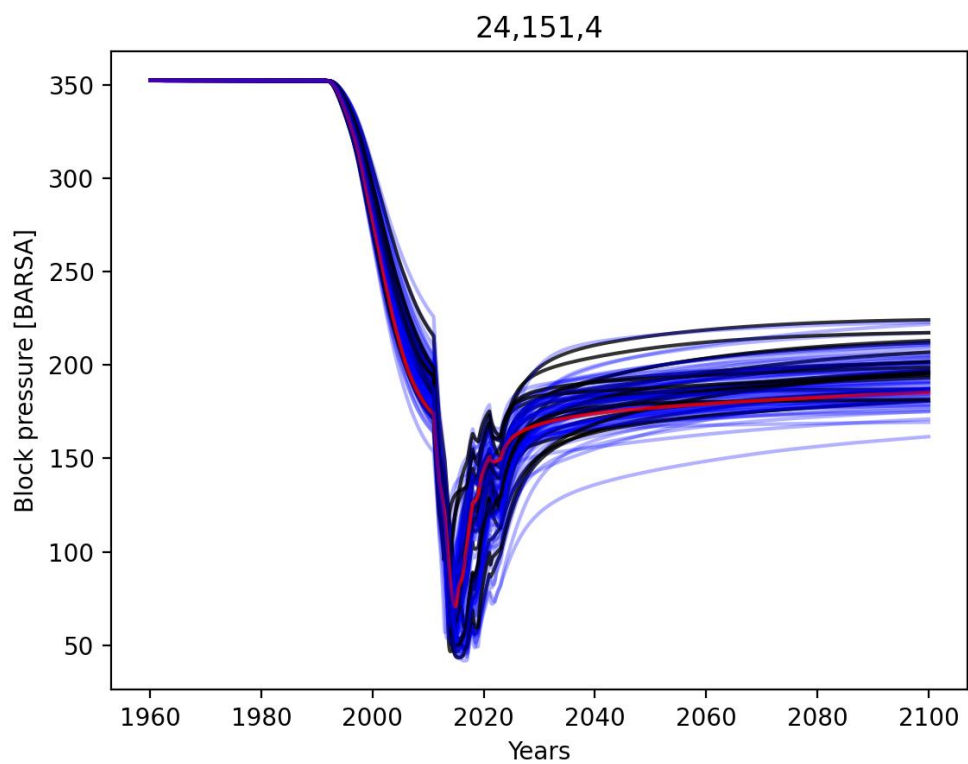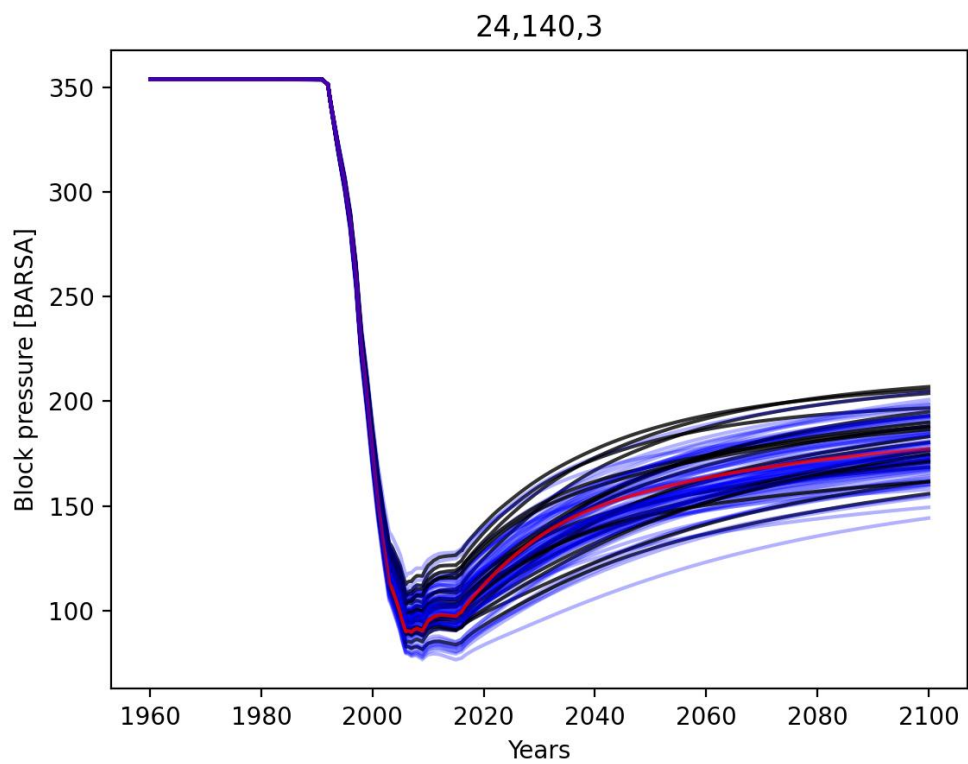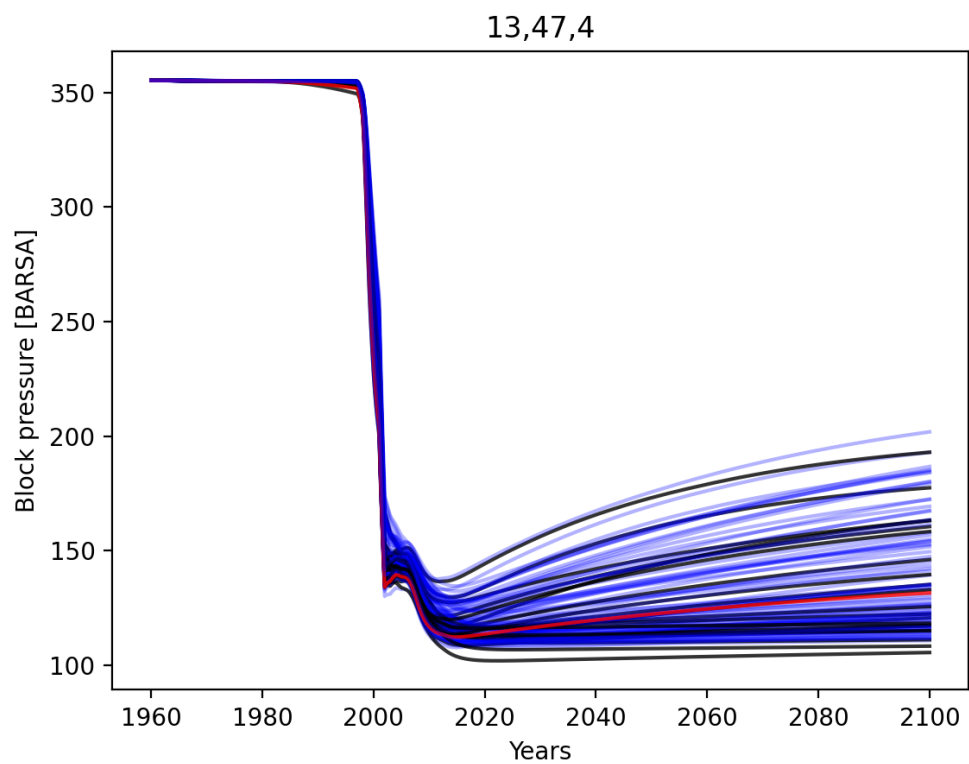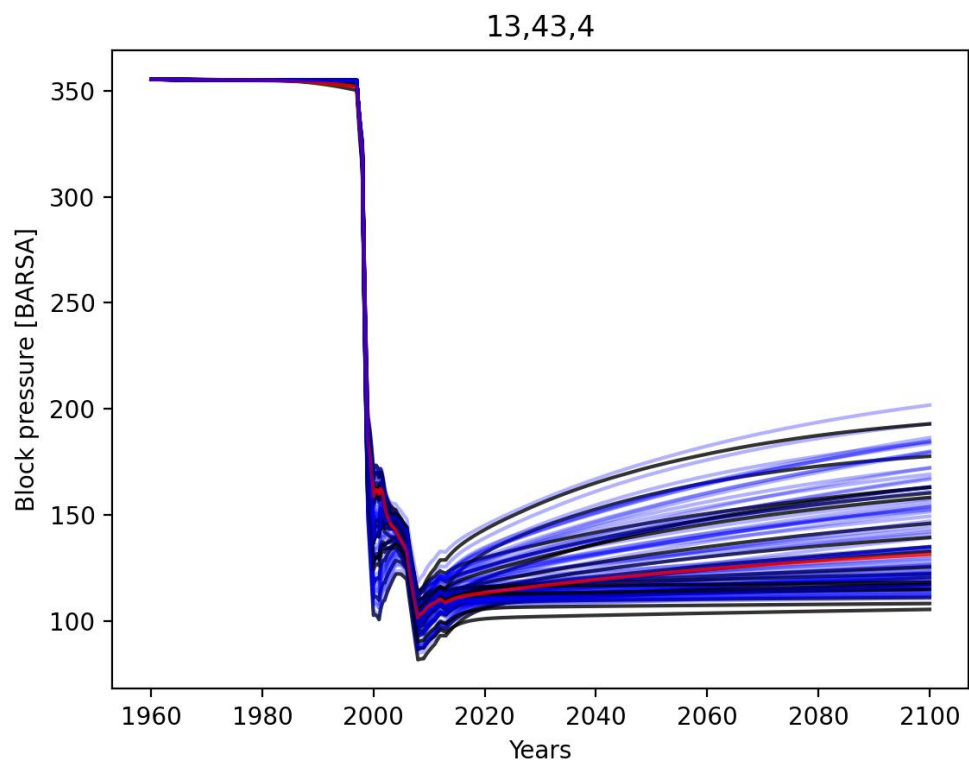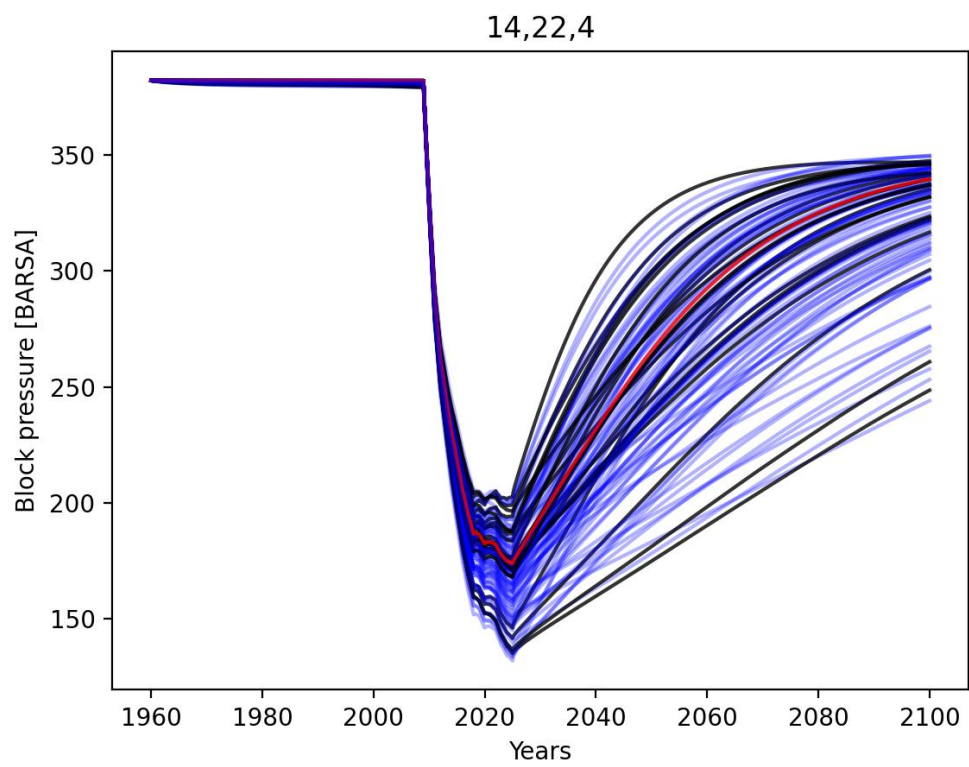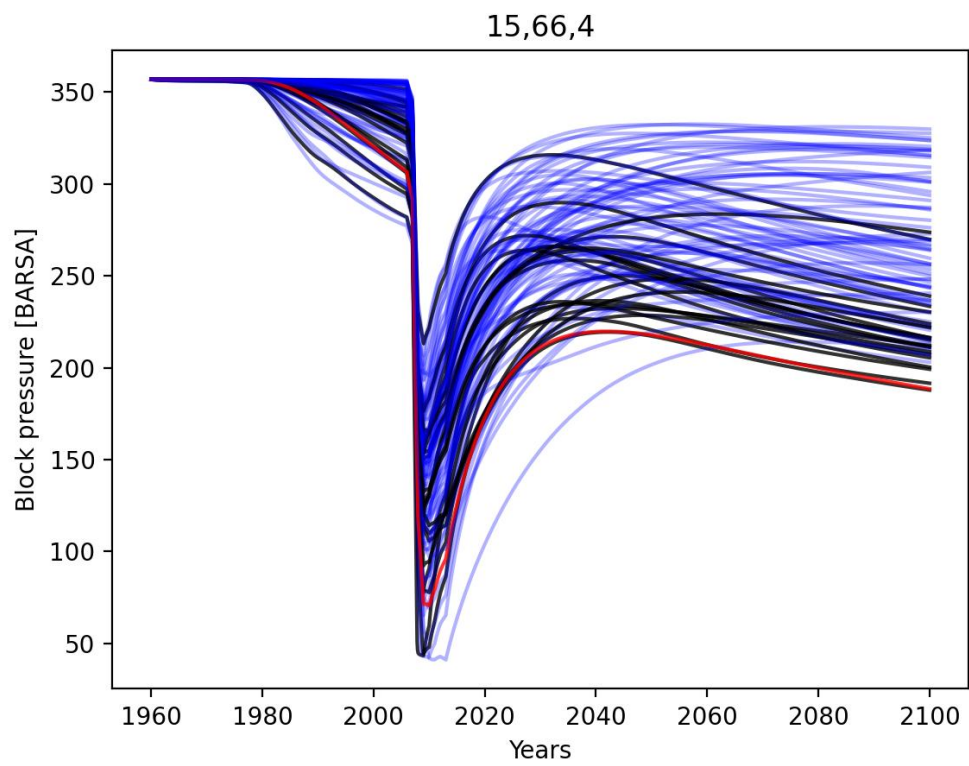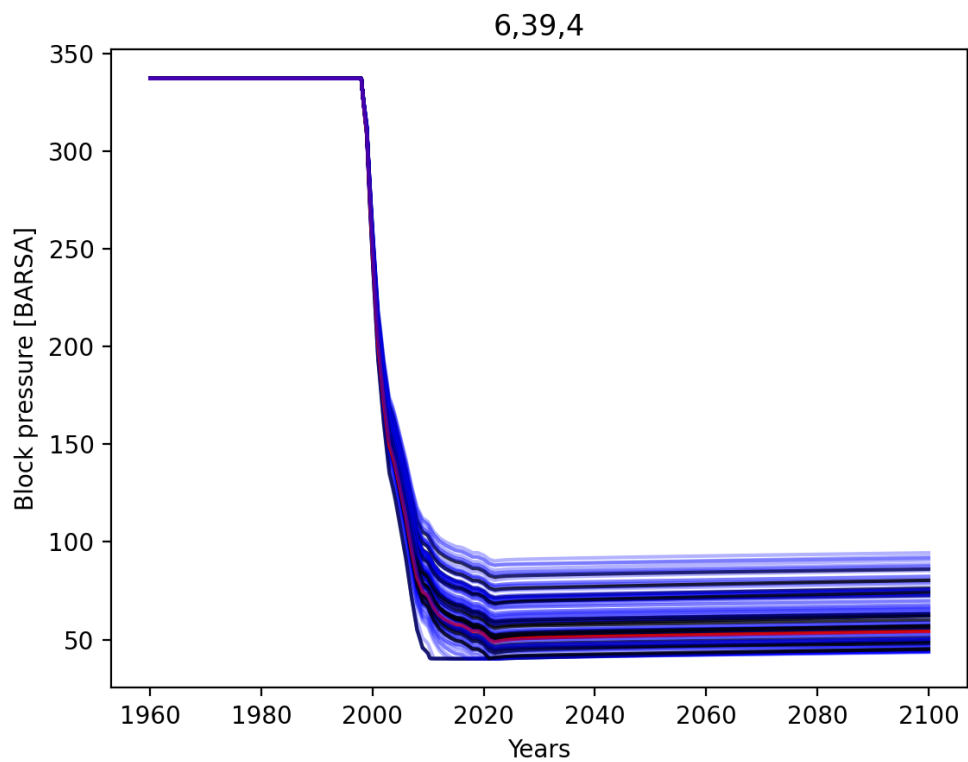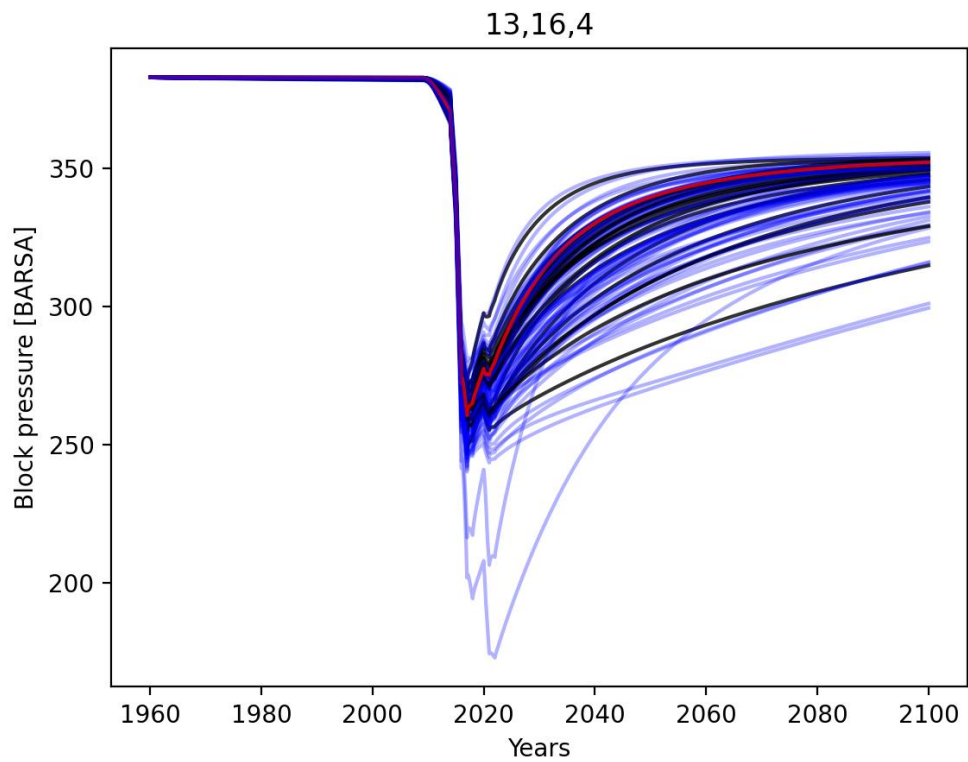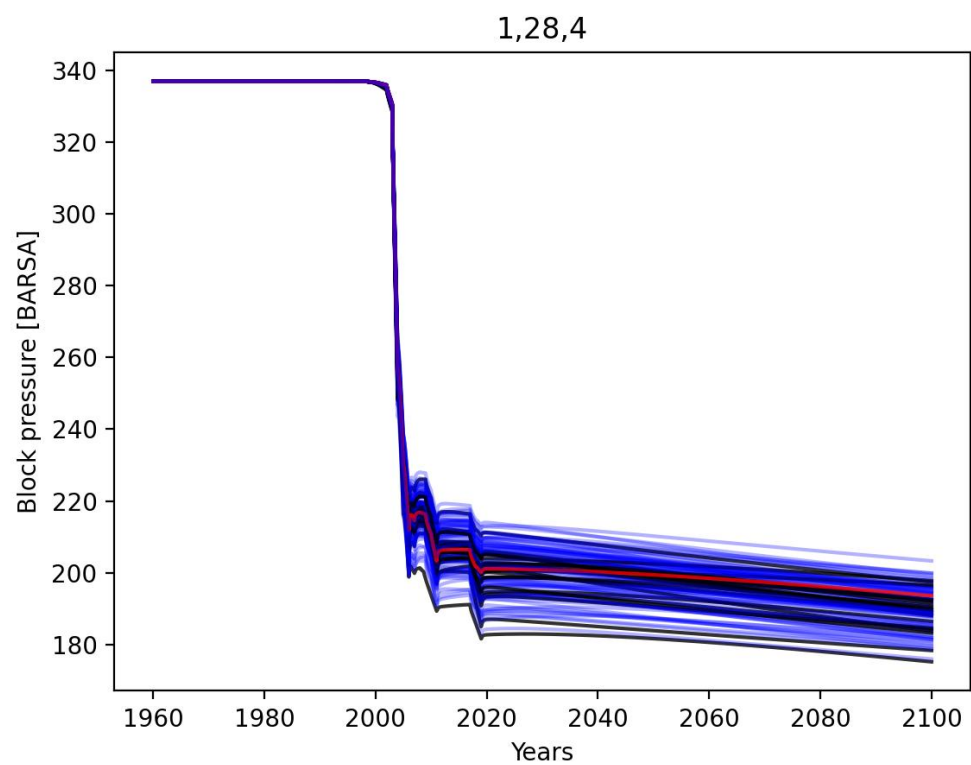
Appendix D Hazard results for individual years
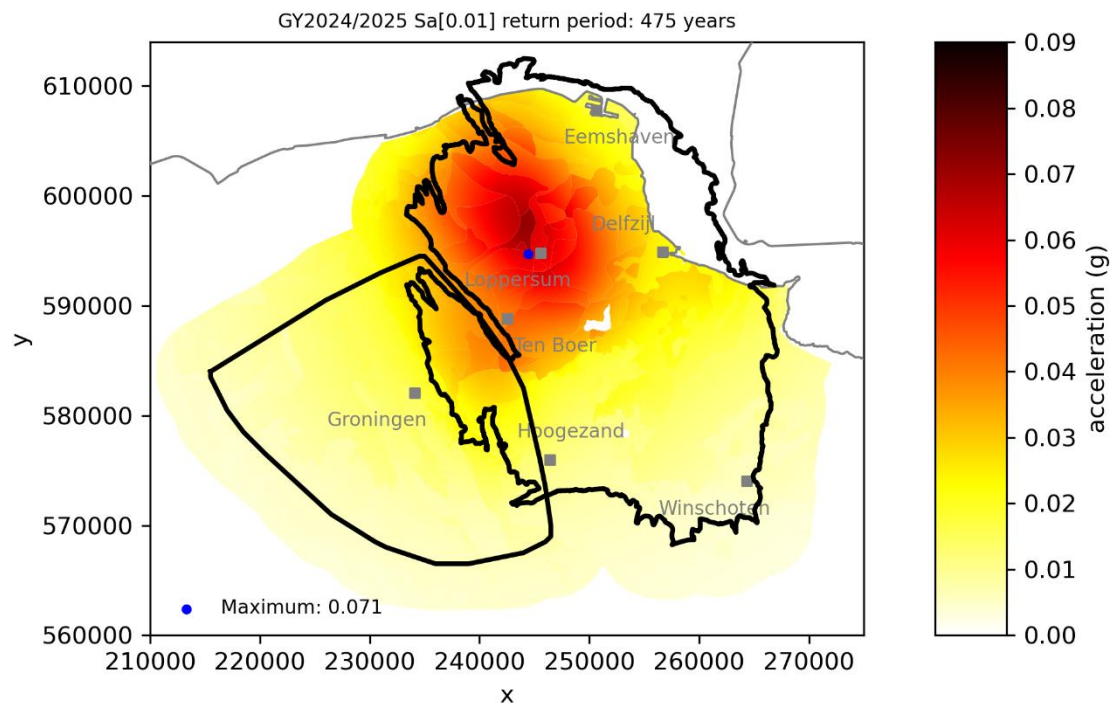
Figure D.1: Hazard maps for PGA at 475 years for gas year 2024/2025
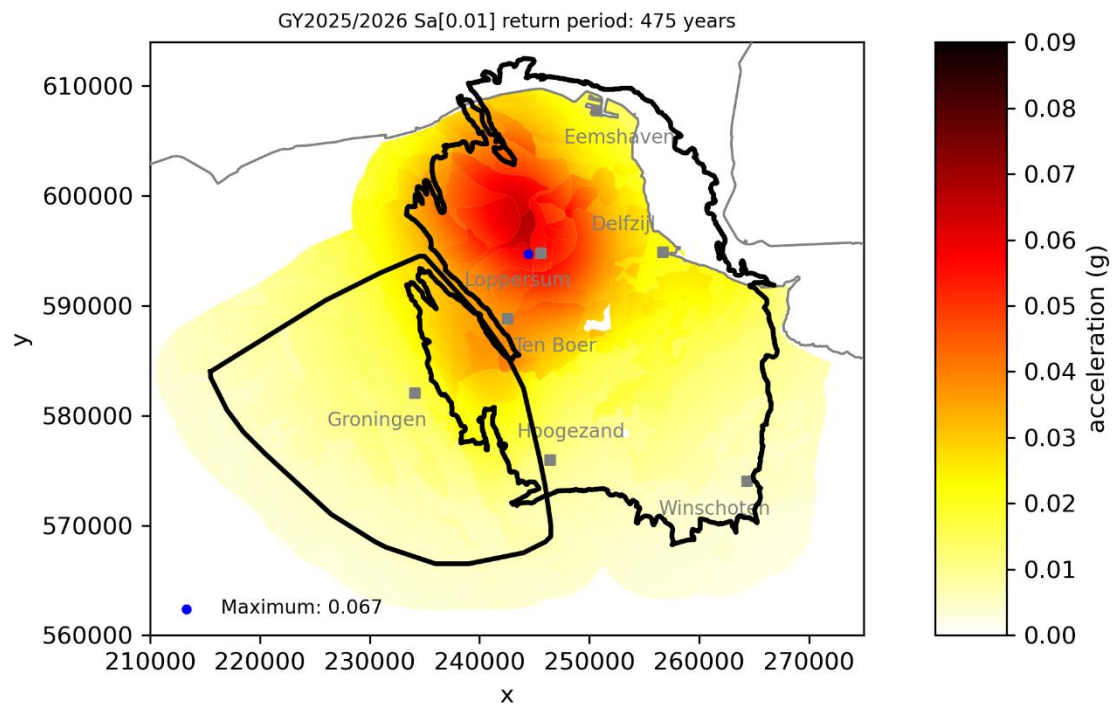
Figure D.2: Hazard maps for PGA at 475 years for gas year 2025/2026
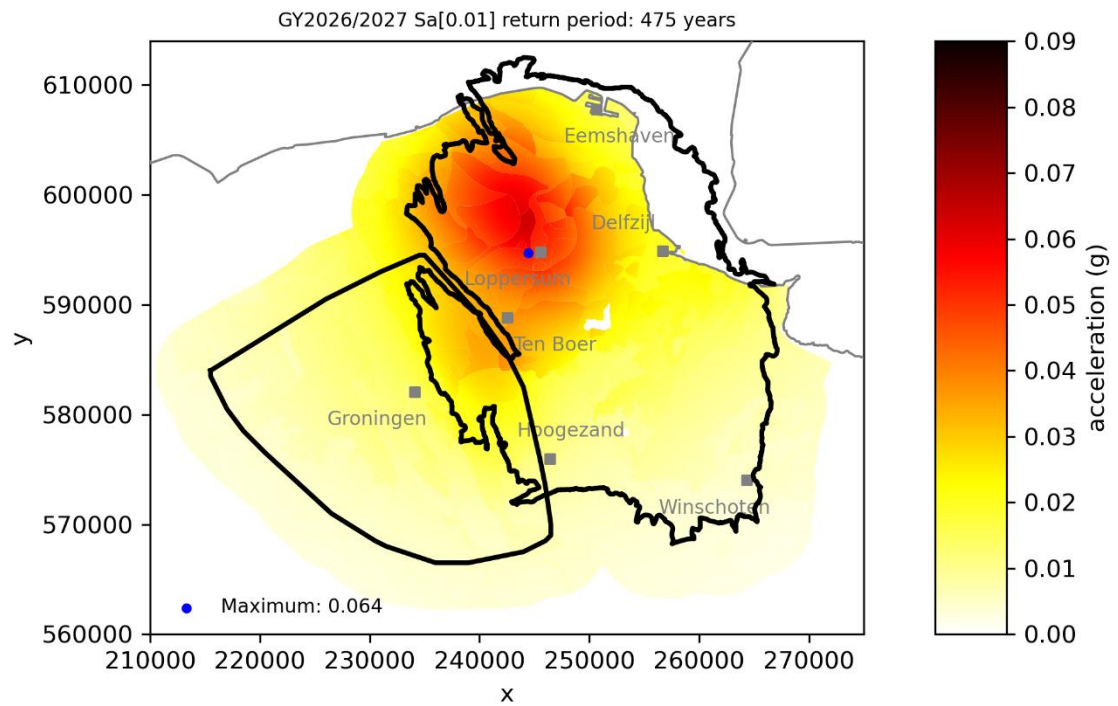
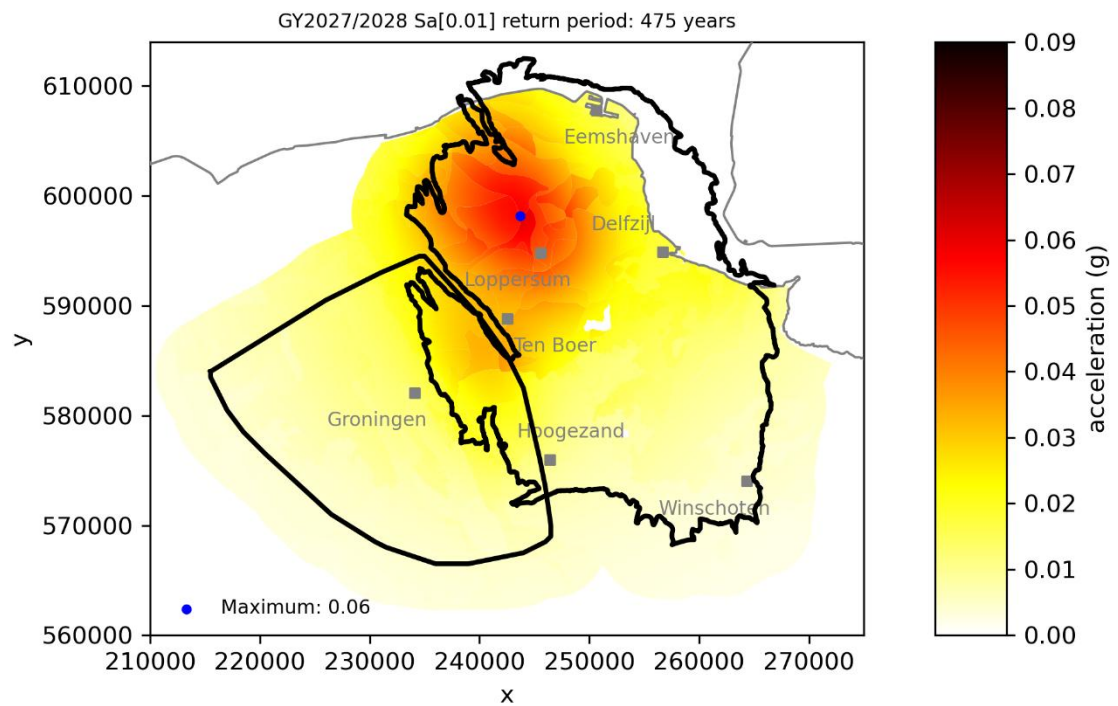Figure D.3: Hazard maps for PGA at 475 years for gas year 2026/2027

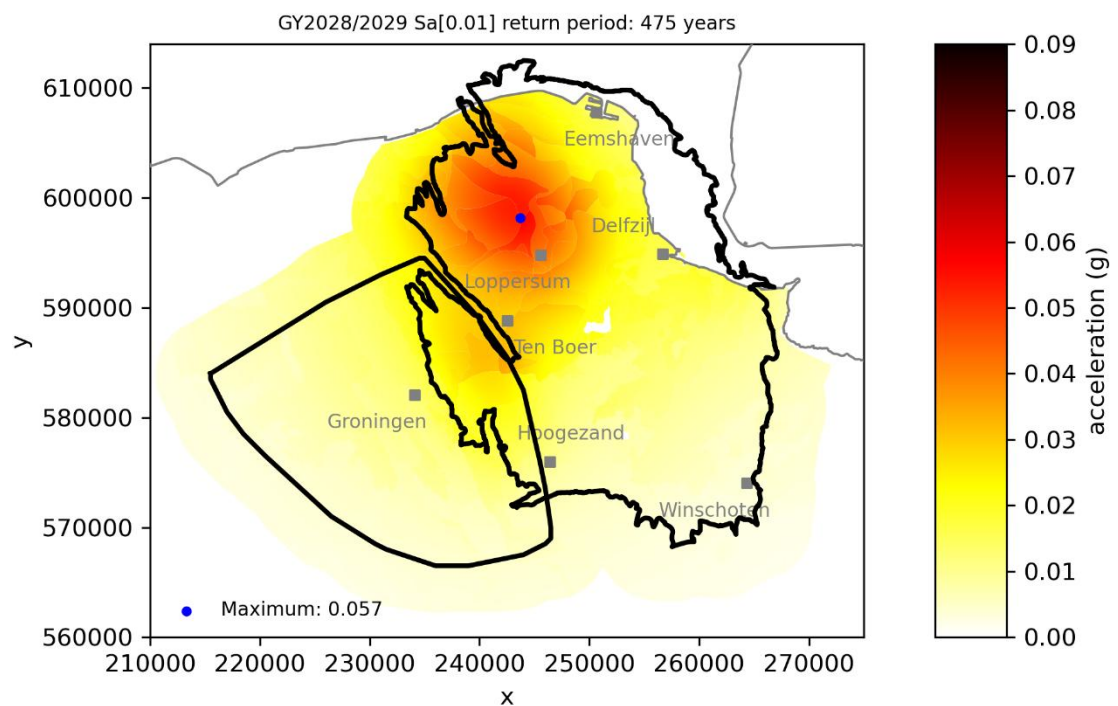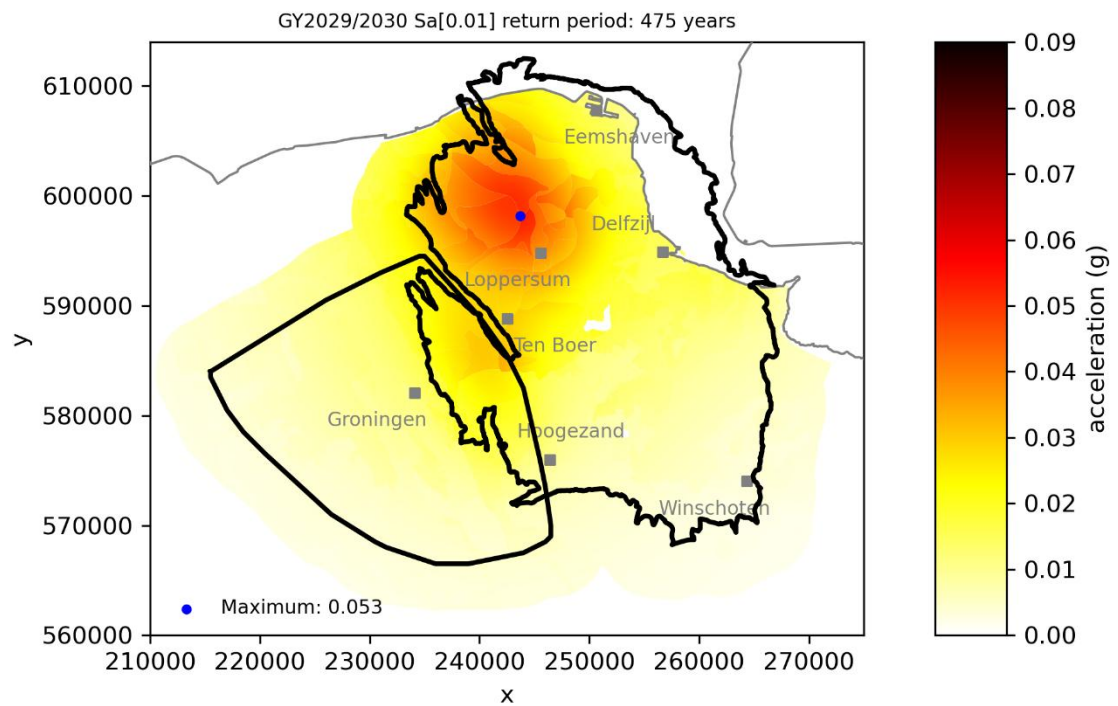Figure D.4: Hazard maps for PGA at 475 years for gas year 2027/2028

Figure D.5: Hazard maps for PGA at 475 years for gas year 2028/2029

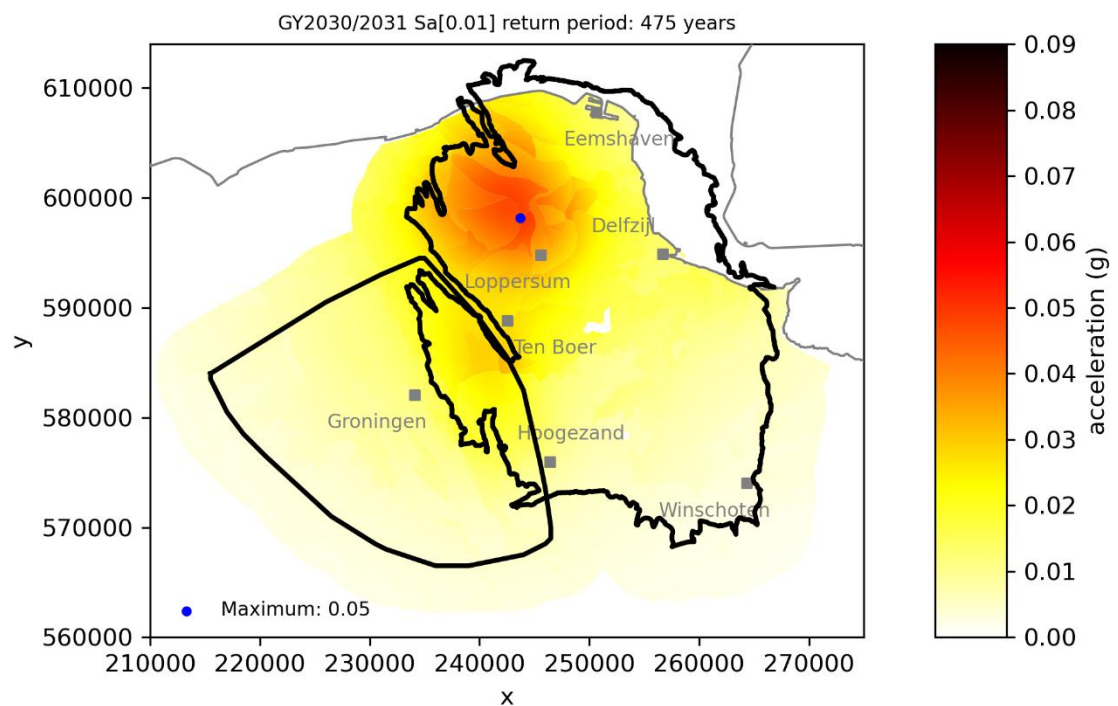Figure D.6: Hazard maps for PGA at 475 years for gas year 2029/2030

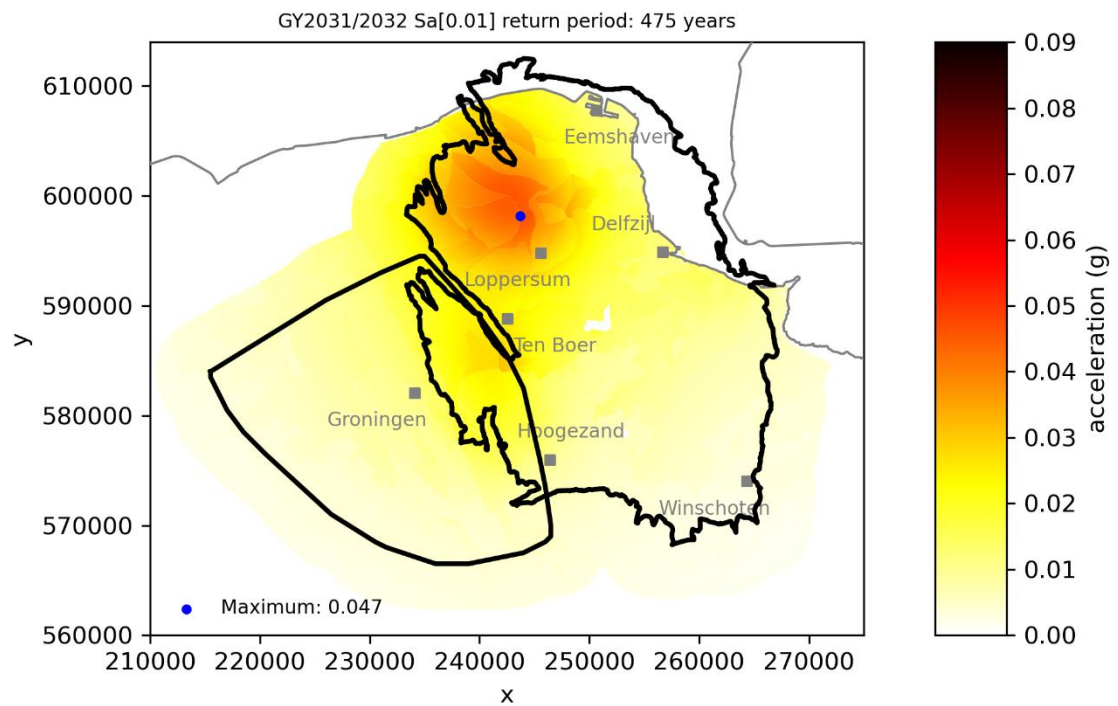Figure D.7: Hazard maps for PGA at 475 years for gas year 2030/2031

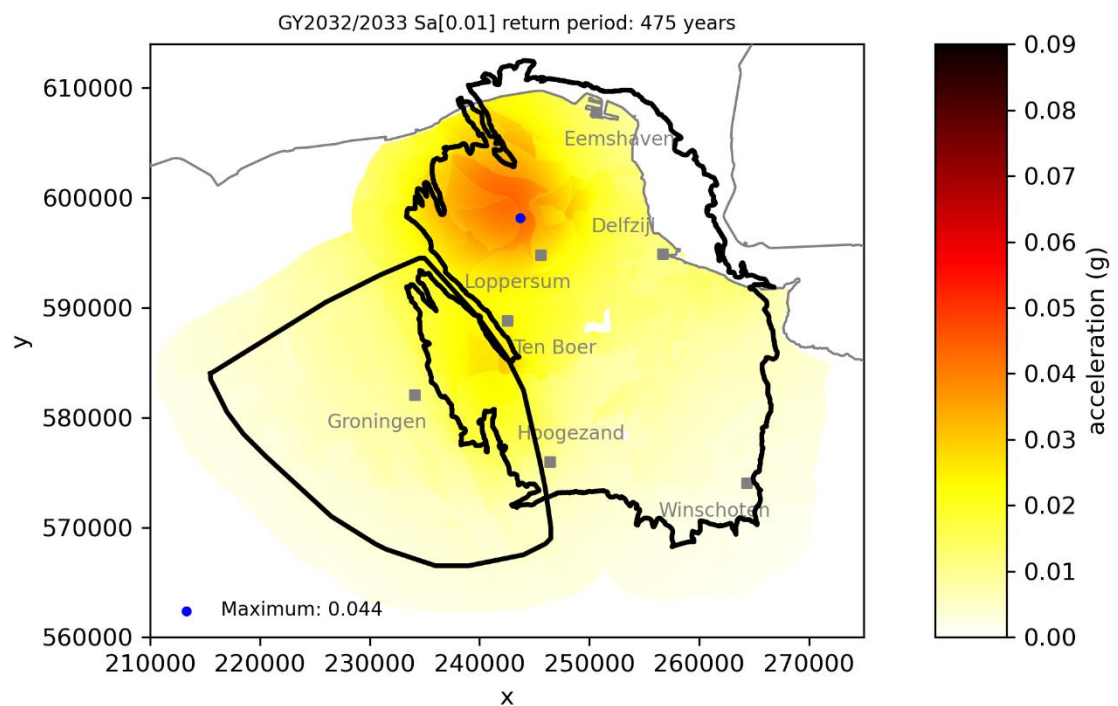Figure D.8: Hazard maps for PGA at 475 years for gas year 2031/2032

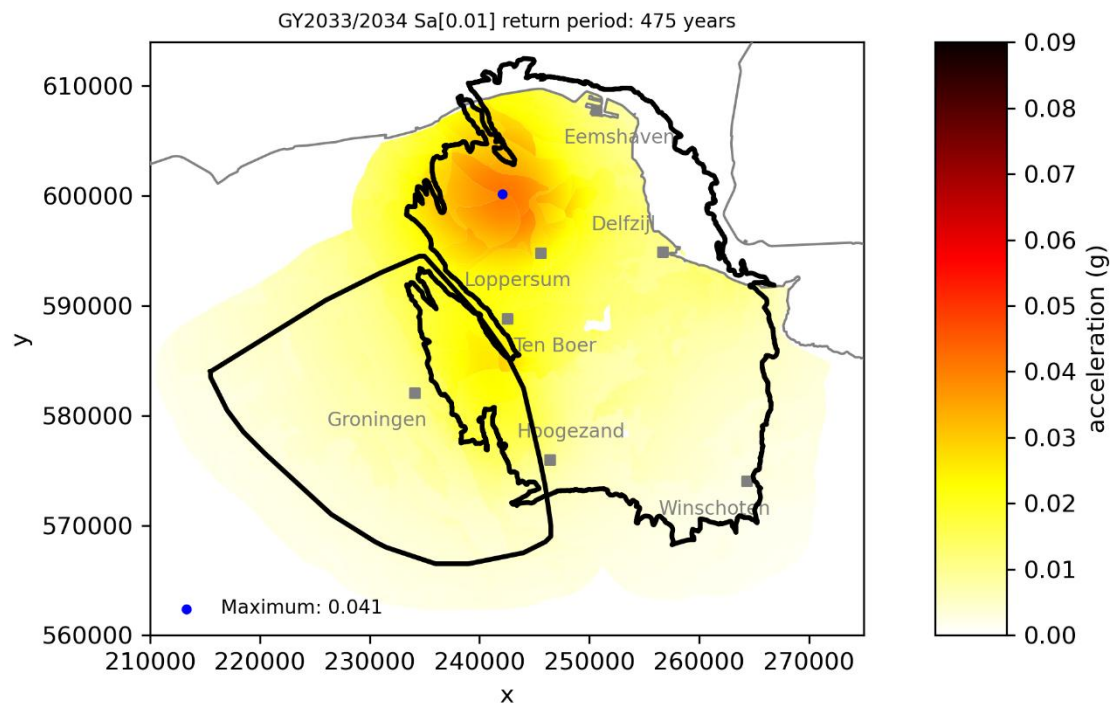Figure D.9: Hazard maps for PGA at 475 years for gas year 2032/2033

Figure D.10: Hazard maps for PGA at 475 years for gas year 2033/2034
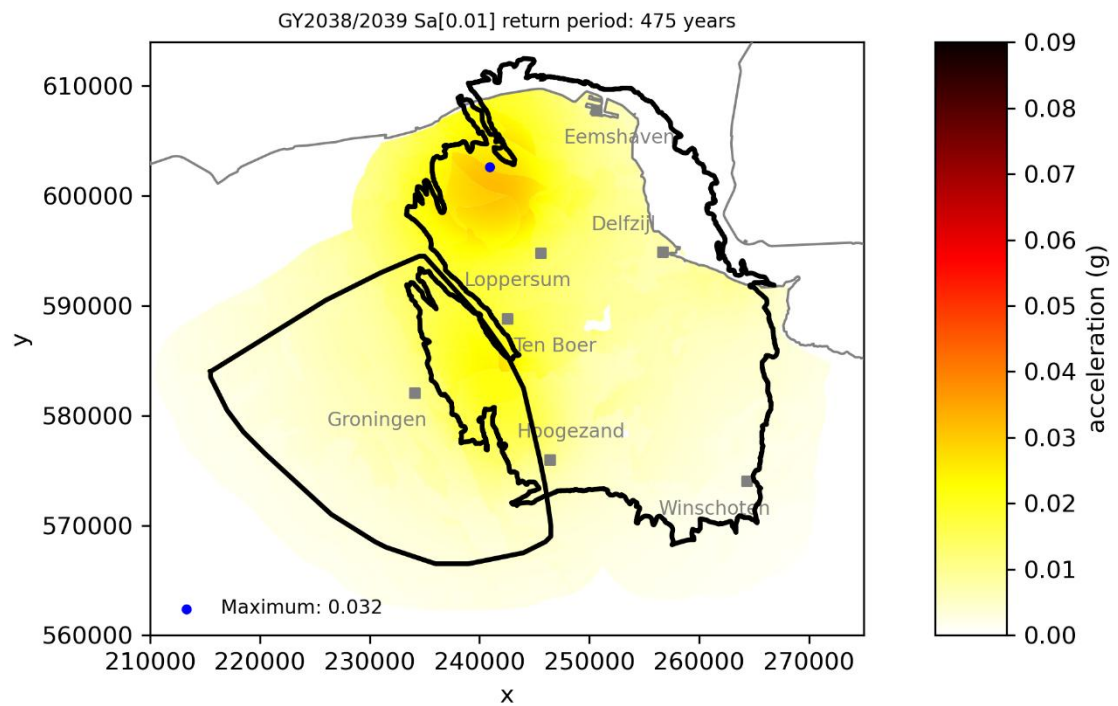

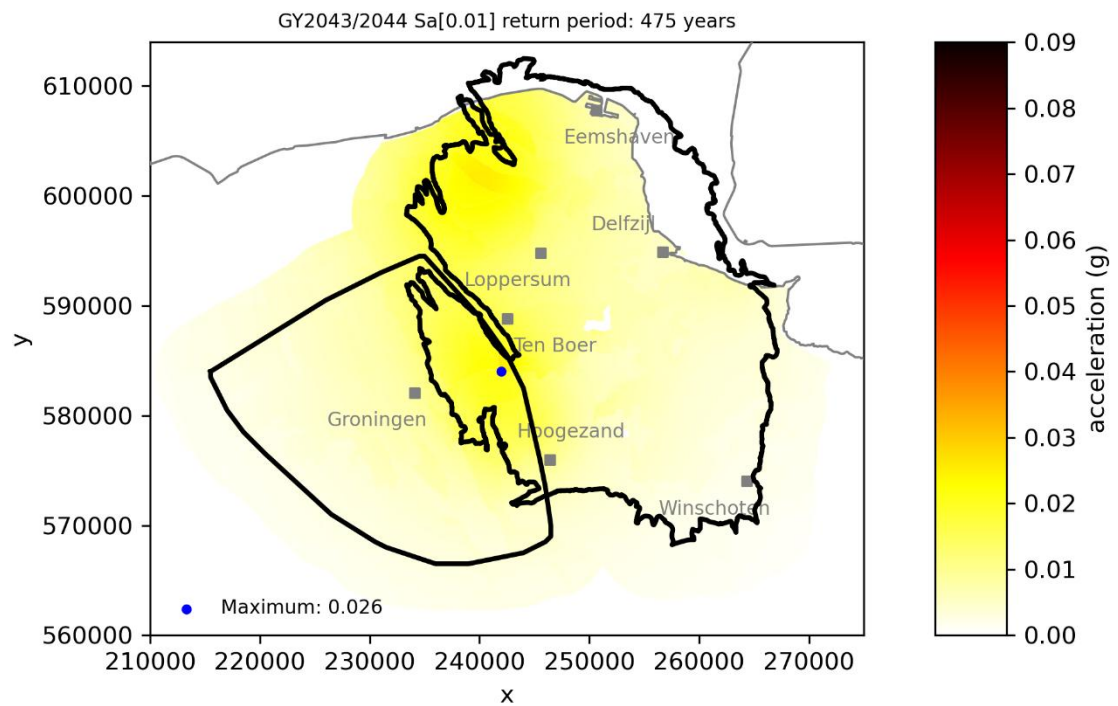Figure D.11: Hazard maps for PGA at 475 years for gas year 2038/2039

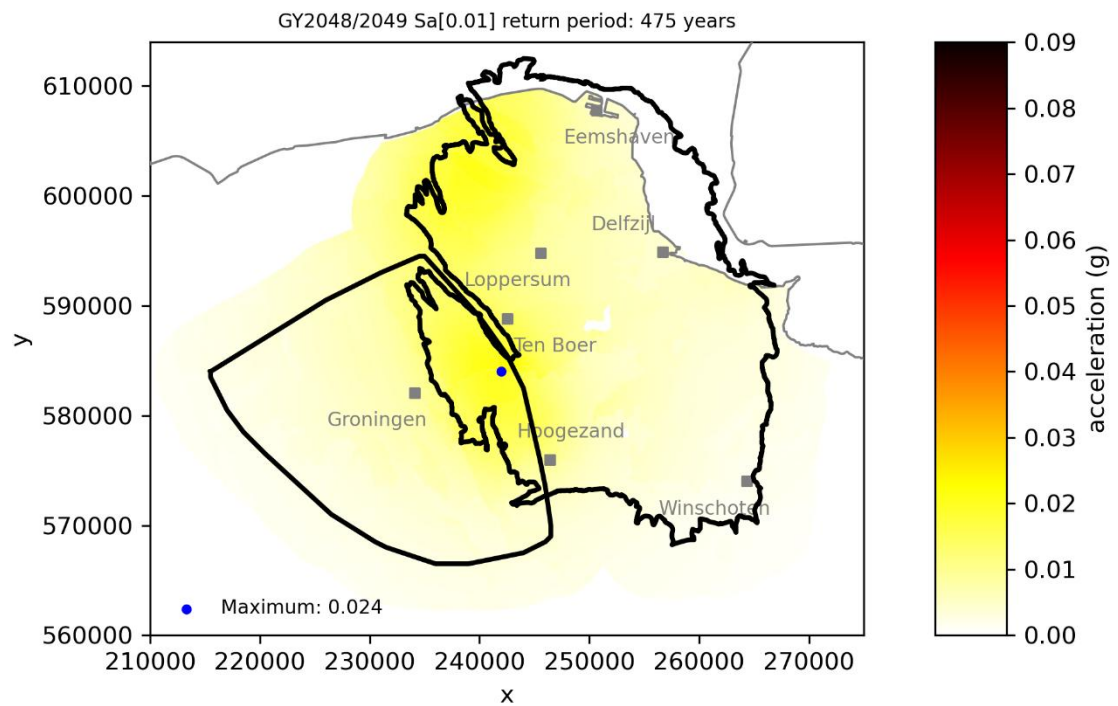Figure D.12: Hazard maps for PGA at 475 years for gas year 2043/2044

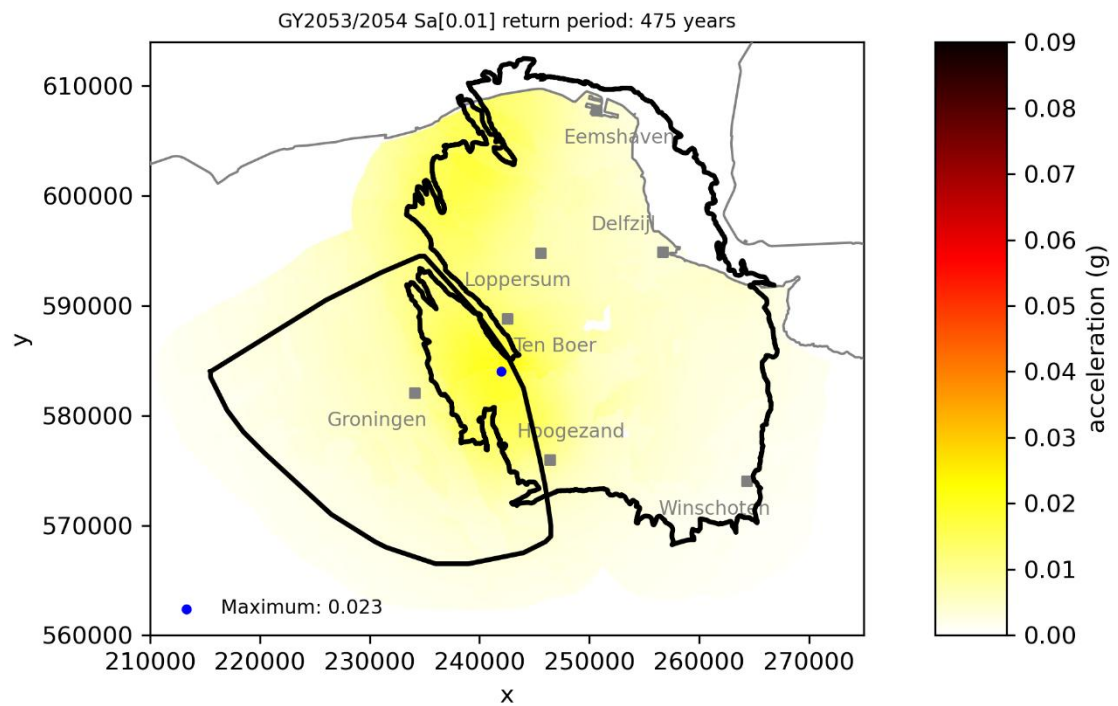Figure D.13: Hazard maps for PGA at 475 years for gas year 2048/2049

Figure D.14: Hazard maps for PGA at 475 years for gas year 2053/2054

Appendix E Extended site response analysis to the SW aquifer of the Groningen gas field

This work has been conducted and reported by Deltares as part of the KEM-19b project.

E.1　Introduction

In this memo we describe the methodology followed to produce the geological model including the data sources and criteria established for merging the different model sections. The report also contains a description and explanation of the shear-wave velocity profile (Vs) construction and the choices made regarding the available data sources. Finally, we summarize of the parameters used to produce the amplification factors through STRATA.

E.2　Methodology

E.2.1　Shear-wave velocity profiles (Vs)

The profiles used need the following information to calculate the amplification factor: mean Vs value, sampled Vs value and 'soil type': a combination of stratigraphy and lithology.

In the Groningen Ground Motion Model (GMM) Vs profiles were reconstructed using the following approach and data (for details see Bommer et al. 2021):
From surface level to NAP -50 m, soil type and Vs were derived from and related to the GeoTOP model from TNO Geological Survey Netherlands (TNO-GSN).
Soil type below NAP -50 m: is related to an expert schematization of the subsurface per geological zone with a stochastic approach, till the base of the Breda Formation (this is the base of the Upper North Sea Group). The Middle and Lower North Sea group were treated as one soil type; at the base of this unit, the top of Cretaceous, bedrock was modelled.
Vs below NAP -50 m: is based on two models: MEI – till 125 m - and Sonic – till bedrock. MEI values are used till the depth where it is higher than the Vs from the Sonic data, below that depth Sonic values are used. Vs at bedrock was fixed 1400 m/s.

For the KEM-19b area the MEI and Sonic models of the Vs values are not available – only in the overlapping area – and no expert schematization is available or part of the current study. Therefore, an alternative approach is followed to construct the profiles in the KEM-19b area, which is described in Section E.2.1.1 and E.2.1.2.

E.2.1.1　Shear-wave velocity profiles (Vs) for KEM-19b area

For the KEM study area the MEI and Sonic data are not available, except for the overlapping area with the Groningen GMM (Figure E 2.1). Therefore, in the entire KEM area, Vs profiles have been based on the values from the Groningen area. No correlation was found between soil type and Vs in the Groningen GMM, however, until the base of the Breda Formation there is a relatively small variation in the Vs values. The Vs shows a linear relation with depth, with an inflection point at NAP -350 m (Figure E 2.2). For the profiles in the KEM-19b area the mean Vs values up to the base of the Breda Formation uses the average values (blue line), for the sampled Vs value a random draw from a normal distribution is used, using presented averages

and standard deviations. In Table E1 and Table E2 all values for the MEI and Sonic Vs can be found.

Below the base of the Breda Formation, the Vs values don't show a linear relationship with depth. They show a typical pattern where Vs increases from the base of the Breda Formation to the top of the Brussels Sand Formation – a subunit within the Middle and Lower North Sea group. From the top to the base of the Brussels Sand Formation the Vs decreases. Below the base the Brussels Sand Formation, till the bedrock, the Vs has an almost constant value with relatively small spread (Figure E 2.3).
For the KEM-19b area the Vs value at the top of the Brussels Sands is related to the Vs value at the base of the Breda Formation, based on the values in the overlapping area this is a factor 1.077 (so Vs is 7.7% higher). The Vs is increased linearly between the base of the Breda Formation and the top of the Brussels Sands. The Vs below the Brussels Sands has an average Vs of 594.52 (m/s) with a standard deviation of 24.78. From the top to the base of the Brussels Sands the Vs is decreased linearly (to 594.52 m/s). Below the Brussels Sands the average value is used till bedrock, where Vs is fixed at 1400 m/s.

On four selected Vs profiles from the Groningen GMM the linear transfer function is calculated for 1) the mean Vs profile, 2) the sampled Vs profile and 3) the Vs profile as reconstructed using the above described method (see Figure E 2.4). These results show that the reconstructed profiles, even if deviating from the Vs mean profile, give a very similar transfer function, and show less variation than the sampled Vs profile. The latter has largest differences with the mean Vs in the upper part, which is based on GeoTOP (this part of the profile is constructed by TNO-GSN).

E.2.1.2 Soil type for the KEM19-b area

For the KEM area the vertical boundaries and soil type are based on three geological models from TNO-GSN: Digital Geological Model (DGM), REGIS II and DGM Deep. The Brussels Sands Formation boundaries were only used to reconstruct the Vs values (see previous section). The DGM model was adjusted by TNO-GSN for the KEM area including newly mapped base of the Peelo Formation.
The DGM has information on the stratigraphical units up to the base of the Breda Formation. The lithology is not available, but for most formations only one type of lithology is expected like in the schematization for the Groningen GMM. Only in the Peelo Formation and the Oosterhout Formation both a sandy lithology and a clayey lithology is expected. To include these, the clayey units from REGIS II were included: Peelo clay unit 1 and unit 2 (lithology 'clay' used for soil type), Oosterhout complex unit and clayey unit 1 (lithology 'clayey sand' used for soil type). For the depth of the bedrock, the DGM deep boundary of base of the Middle and Lower North Sea group was used.

Between the different geological models (minor) inconsistencies were present at some locations in the study area. These were corrected as follows:
The REGIS II units were corrected with the updated DGM boundaries: either units were entirely removed if the Peelo base was deeper, otherwise the top or base were adjusted to the Peelo base depth;
At locations where the Brussels Sands base is absent but the top is present, the unit was assumed absent;
Where Brussels Sands top is shallower than the base of the Breda Formation, the top is changed to the same depth as the base of the Breda Formation;

Where the bedrock depth is shallower than the base of the Breda Formation, the top is changed to the same depth as the base of the Breda Formation.
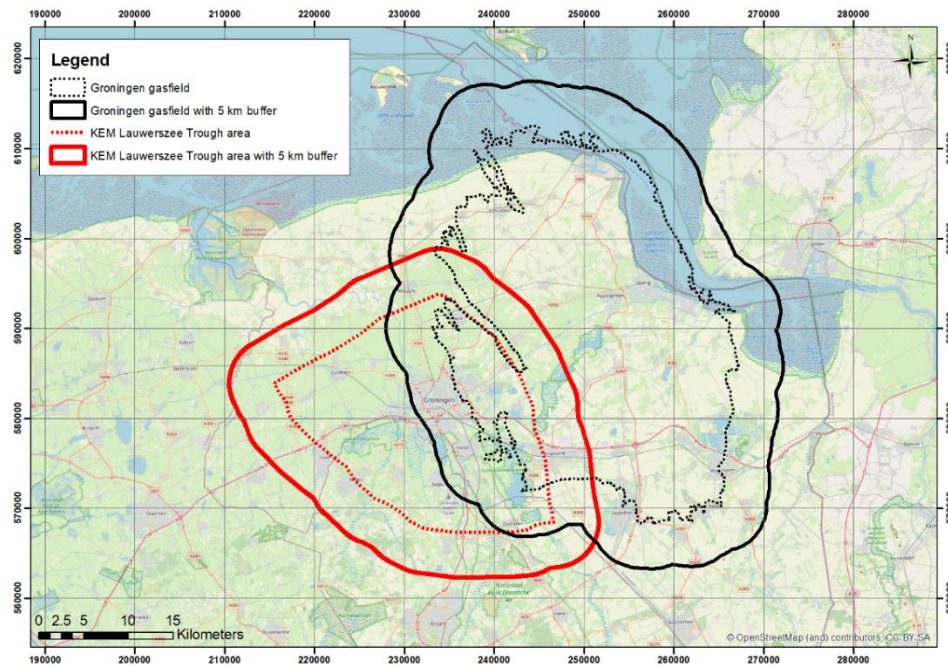

Figure E 2.1: Map of the KEM Lauwerszee Trough, study area in this report, and the Groningen area
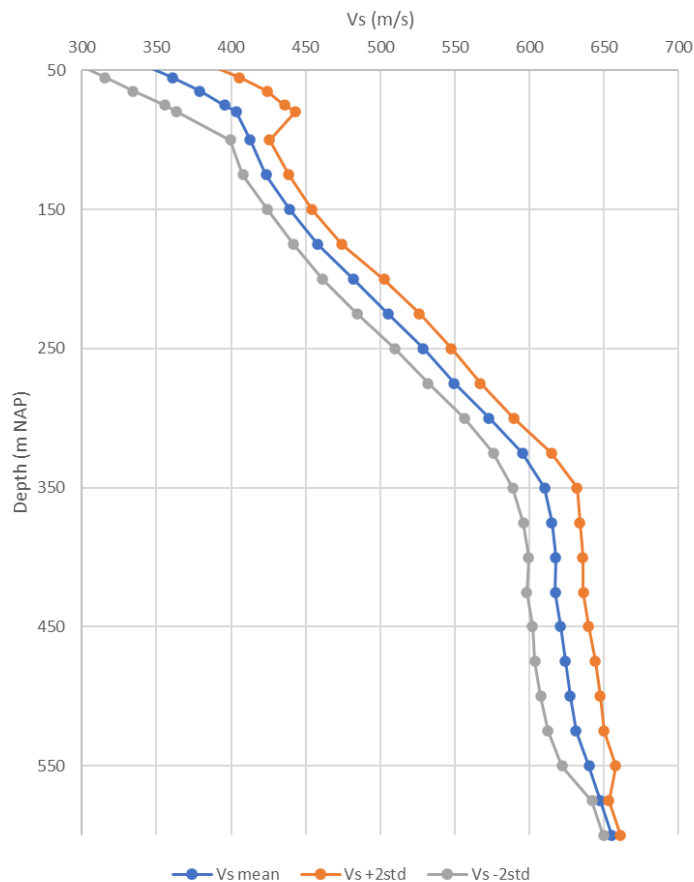
Figure E 2.2: Vs profile based on MEI and Sonic data, the blue line is the average Vs at specified depth, grey and orange lines are respectively average minus two standard deviations and average plus two standard deviations.
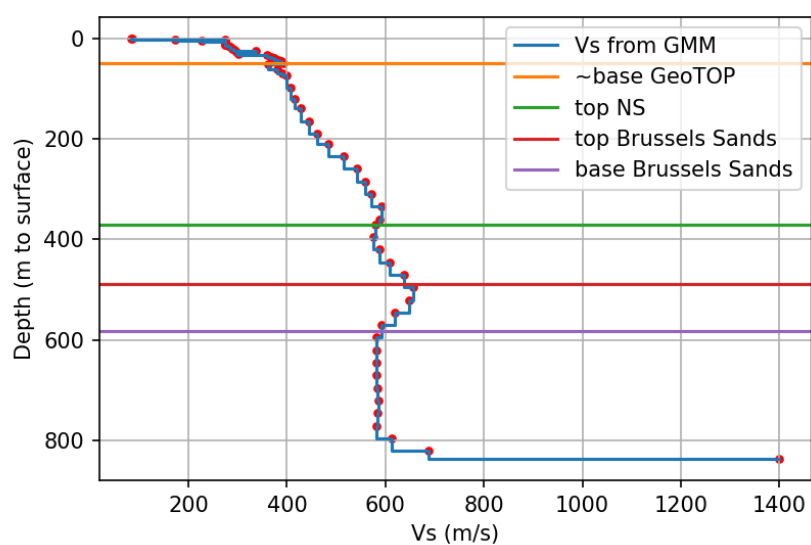

Figure E 2.3: Example of a Vs profile from the Groningen GMM (at x=236050, y=574250). NS is the Middle and Lower North Sea group, depth taken from the DGM Deep geological model (TNO-GSN). Top and base of Brussels Sands are based on the mapped surfaces from TNO-GSN
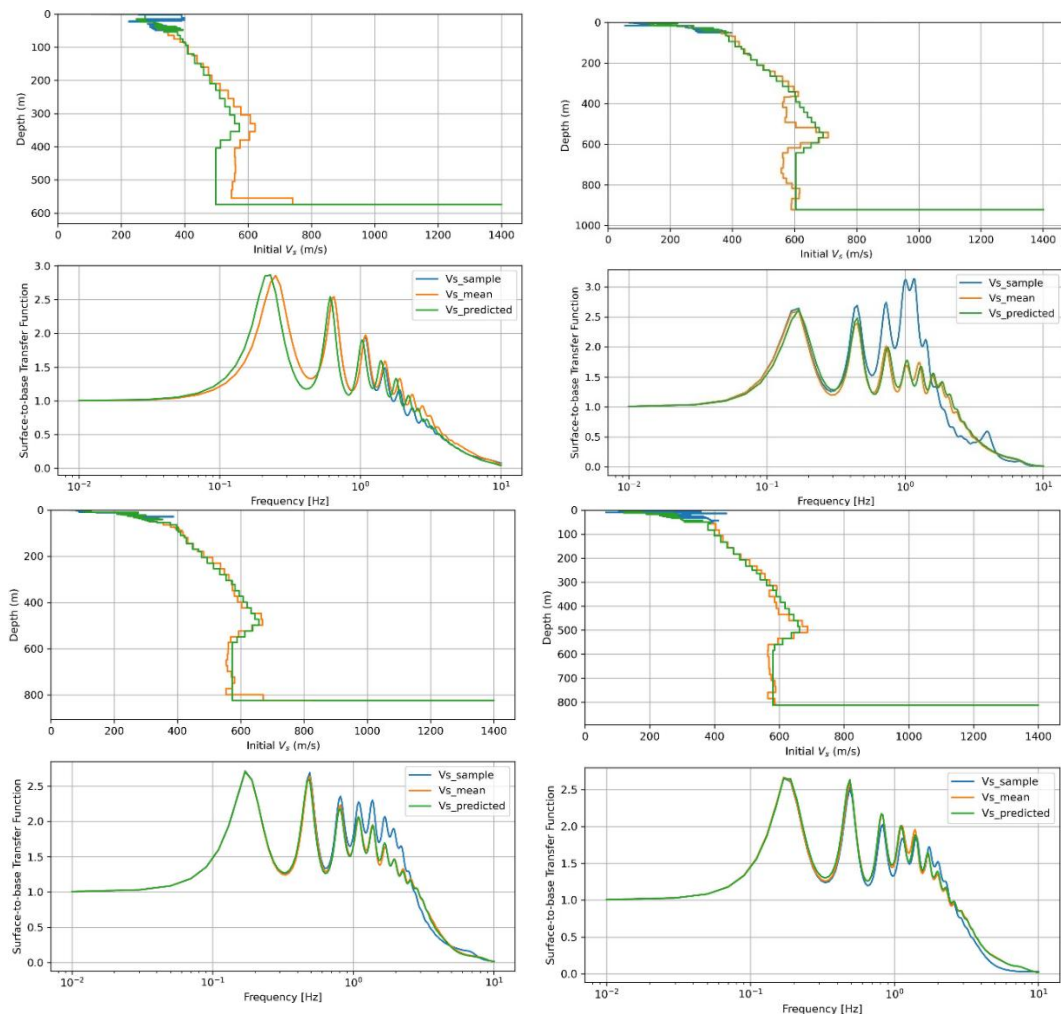
Figure E 2.4: Effect of four selected profiles on the linear transfer function.

E.2.1.3 Geological zonation

The boundaries of the geological zonation have been created by TNO-GSN and delivered as a shapefile. These zones are used to group the final results of the STRATA calculations, but have no influence on the creation of the Vs profiles or the calculation of the amplification factor. Since the results are analyzed per zone, a minimum number of profiles should be within each zone. In the Groningen GMM zonation the smallest zone had 45 locations, this was used as a minimum for the new study area. Zones with less locations were therefore merged with neighboring zones based on expert judgement, taking into account a.o. the general geological sequence. In Table E3 the remapped zones are given.

E.2.2　Summary of input parameters for STRATA calculations

The site response calculations are performed using the STRATA workflow version 7 implemented in Groningen area. The main output are the amplification factors computed for all profiles per zone. The computations are carried out considering two scenarios, namely: (1) Vs mean and (2) Vs sample. In the study area one soil type is present which is absent in the Groningen GMM: the Maassluis Formation. This formation occurs in the western part of the study area between the Peize-Waalre Formation and the Oosterhout Formation. Within the study area the formation has a limited thickness. The soil properties for this formation are taken from those of the Oosterhout Formation and Breda Formation.

Calculation Dmin per geological zone:

$$
D_{fact} = \begin{cases} 1.7 & \text{for } V_{S30} \leq 119.6\,m/s \\ \exp\left(5.2874 - 0.9942\ln\left(V_{S30}\right)\right) & \text{for } 119.6\,m/s < V_{S30} \leq 204.0\,m/s \\ 1 & \text{for } V_{S30} > 204.0\,m/s \end{cases}
$$

Equation from Bommer et al. (2021).

E.3　Summary of results

E.3.1　Description of Vs profiles derived for the new area

In total 105,192 profiles in the study area were created till the bedrock. Visual inspection of the final results is performed on the locations overlapping with the Groningen GMM. The new approach give a good match for the upper part of the profile, up to the base of the Breda Formation. The part below shows larger deviations from the original profile, but still resembles it quite well and good enough to have relatively small effect on the linear transfer function (see also Section E.2.1.1). Some differences are caused by a different depth of the base of the Breda and the depth of the bedrock between the values used in this study and in the Groningen GMM. These surfaces were remapped for the Groningen GMM area specifically and not available for the entire KEM study area. Three examples of profiles are given in Figure E 3.1.
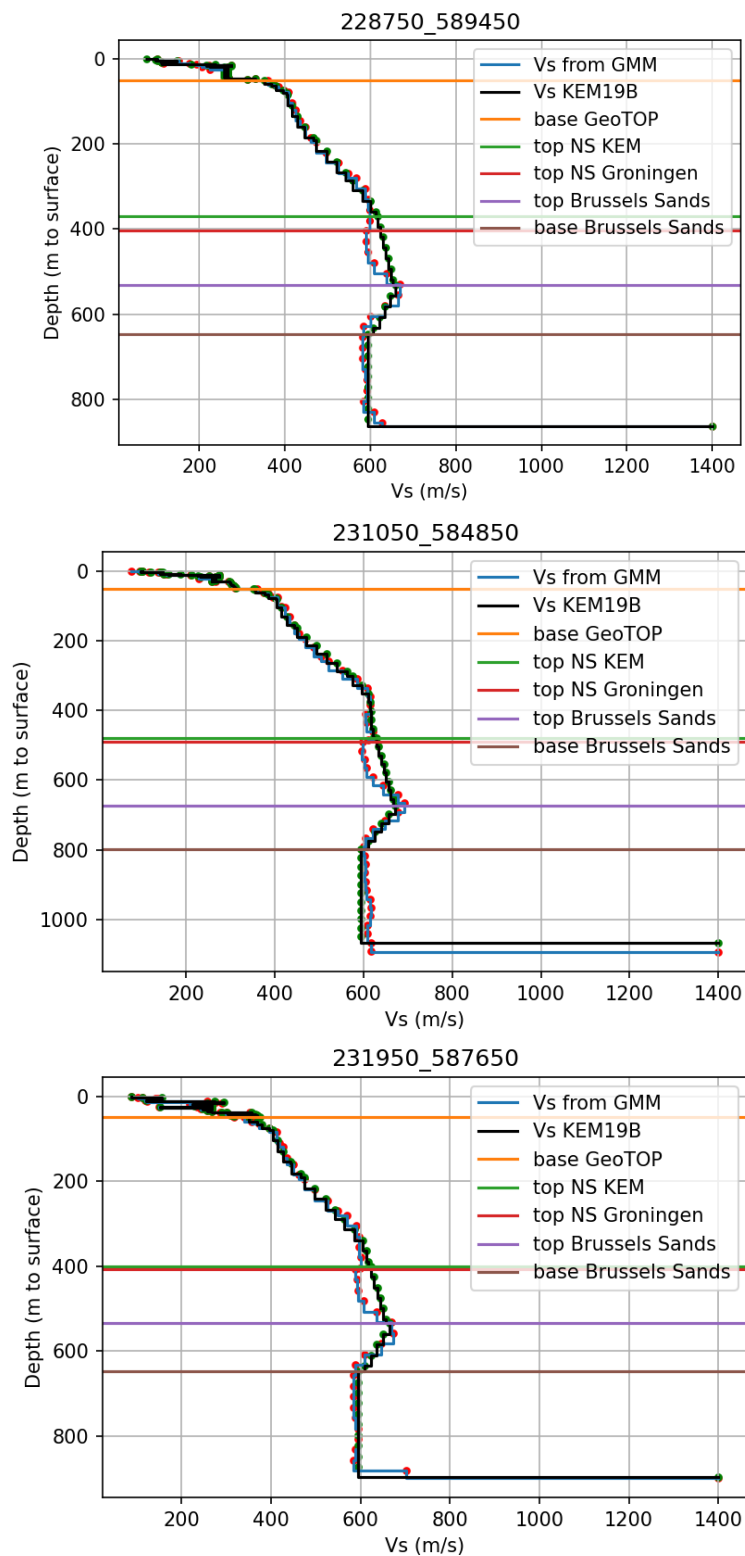
Figure E 3.1: Examples of reproduced Vs profiles (showing Vs mean) for three locations (coordinates in titles)

E.3.2 Description of STRATA input files

The STRATA outputs are generated with Python. The Python generated STRATA file is a combination of multiple data sources:
- GeoTOP model from TNO Geological Survey Netherlands.
- Digital Geological Model (DGM), REGIS II and DGM Deep.
- Derived VS profiles (paragraph E2).

The STRATA file is a .csv file that contains the following data columns:
- Location', 'X', 'Y': X and Y coordinates of the data location.
- Thickness: The thickness of individual layers.
- Depth: All data is interpolated or calculated for this depth interval.
- Stratigraphy, Lithology, and Soil Type: Formations are described in 'Stratigraphy'. The lithology that corresponds to this 'Stratigraphy' is set in the 'Lithology' and the 'Soil Type' is a combination of both.
- Vs mean: The mean S-wave velocity for each depth is dependent on the Soil Type. For the first 50 meters, this mean S-wave velocity comes from GeoTop. For the data below GeoTop, the mean VS is derived as described in paragraph 2.
- Vs sample: The sample S-wave velocity is a random draw from a normal distribution generated using the VS mean and the standard deviation. For the first 50 meters, this data is from GeoTop, for the deeper data, these values are derived as described in Section E.2.

The STRATA file is built up using the following workflow:
- GeoTop data is split for every unique location. The GeoTop data is translated into the STRATA file format and forms the first framework of the output.
- For every location, the depth is interpolated until the bedrock formation. Until the depth of the boundary between the MEI and Sonic data, the depth resolution of the data is set to 10 meters. Below, the resolution of the data is set to 25 meters. Every formation boundary is added in between the interpolated depths.
- The S-wave velocity is interpolated based on the depth of the key formation boundaries.
- Using the mean velocity data and the standard deviation, the sample VS is calculated for every given depth.
- Formation markers are interpolated between their base and top, corresponding lithologies are assigned and the soil type can be constructed using both values.
- Because of possible mismatches in the Geotop and MEI dataset for geological boundaries, it is possible that an unrealistic geological sequence is generated: Peelo-Appelscha-Peelo. From a geological viewpoint, this sequence is impossible and therefore, the Appelscha formation is removed from the dataset and replaced by Peelo.
- The output is generated per location and saved per geological zone defined by TNO.

E.3.3 Description of STRATA output files

The STRATA output files consists of text files that contain amplification factors per zone, computed for Vs mean and Vs sample. Each file contains the following relevant information: the name of the zone, X and Y coordinates, Earthquake Magnitude, epicentral distance, spectral acceleration of outcrop rock for various periods, and amplification factors for 24

structural periods between 0.01 – 5.0 seconds. An example of amplification factors for a single structural period is provided in Figure E 3.2.
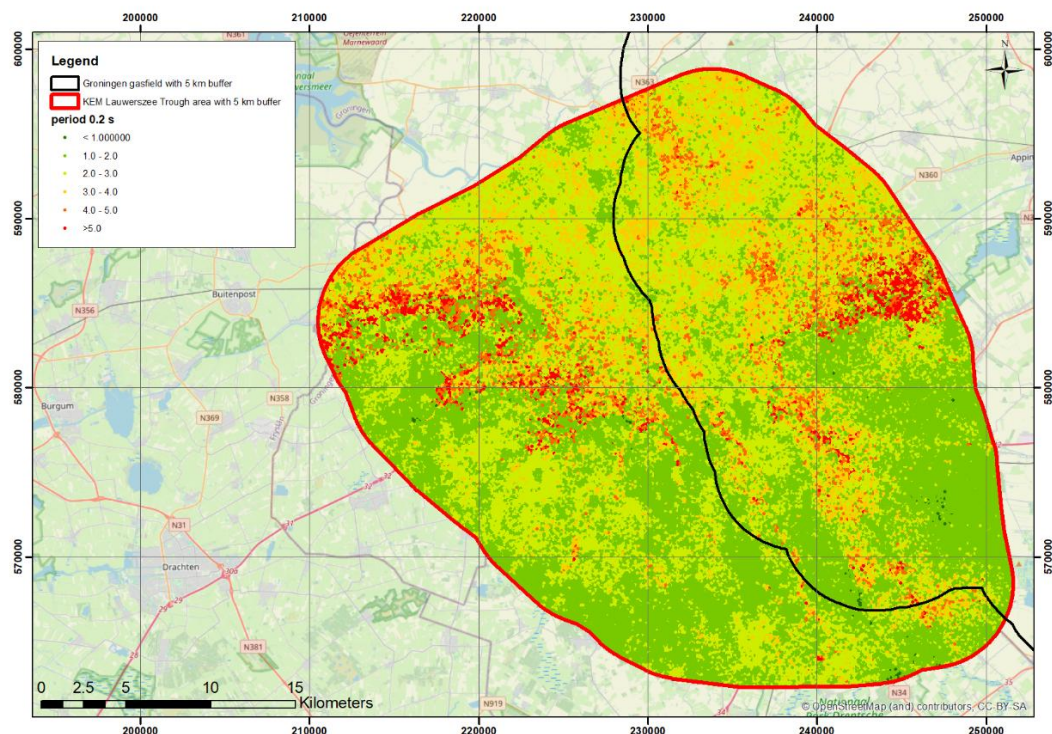

Figure E 3.2: Amplification factor based on mean Vs profiles for a period of 0.2 seconds.

Table E 1   Mean values and standard deviations of the MEI Vs model

Depth	Vs mean	Vs standard deviation
25	270.70	14.98
35	305.90	18.97
45	339.60	21.60
55	360.53	22.48
65	379.17	22.44
75	395.71	19.96
85	411.81	17.12
95	431.52	13.78
105	451.32	10.70
115	474.34	8.14

Table E 2 Mean values and standard deviations of the Sonic Vs model

Depth	Vs mean	Vs standard deviation
50	388.73	4.50
75	401.06	4.76
100	412.61	6.53
125	423.33	7.75
150	439.33	7.49

175	458.07	8.14
200	482.05	10.30
225	505.26	10.49
250	528.67	9.45
275	549.52	8.70
300	572.81	8.25
325	595.22	9.72
350	610.28	10.83
375	614.93	9.45
400	617.60	9.10
425	617.19	9.46
450	620.76	9.40
475	623.95	10.07
500	627.48	9.96
525	631.13	9.40
550	639.87	9.04
575	647.58	2.83

Table E 3 Remapped geological zones

Old zone ID	New zone ID
5	504
7	93
38	309
40	308
43	310
100	155
191	185
193	185
224	189
225	189
229	587
277	25
486	517
491	560
493	553
494	494
497	564
500	558
502	567
503	567
506	567
513	504

516	504
518	504
519	505
534	484
535	484
537	498
538	498
539	498
540	498
545	498
546	498
551	504
552	494
554	498
555	504
557	505
561	504
565	507
572	498
574	495
584	564
585	564
586	558

TNO innovation for life